Durham E-Theses

Proton structure from deep inelastic and diffractive scattering

Gehrmann, Thomas

How to cite:

Use policy

Proton Structure from Deep Inelastic and Diffractive Scattering

Thomas Gehrmann

Department of Physics
University of Durham

A thesis submitted to the University of Durham
for the degree of Doctor of Philosophy
August 1996

3 0 OCT 1996

Declaration

I declare that the material presented in this thesis has not been submitted for a degree at this or any other university.

Much of the research work presented in Chapters 4 to 8 of this thesis has been carried out in collaboration with Professor W.J. Stirling. It has largely appeared in the following publications:

- *Spin–dependent Parton Distributions from Polarized Structure Function Data*
  T. Gehrmann and W.J. Stirling, Z. Phys. **C65** (1995) 461.

- *Analytic approaches to the Evolution of Polarized Parton Distributions at Small x*
  T. Gehrmann and W.J. Stirling, Phys. Lett. **B365** (1996) 347.

- *Polarized Parton Distributions in the Nucleon*
  T. Gehrmann and W.J. Stirling, Phys. Rev. **D53** (1996) 6100.

- *Drell–Yan asymmetries at HERA-$\vec{N}$*
  T. Gehrmann and W.J. Stirling, Proceedings of the workshop "Future Physics at HERA", DESY, Hamburg, September 1995 - May 1996, eds. A. De Roeck, G. Ingelman and R. Klanner, to appear.

- *Production of J/ψ–pairs at HERA-$\vec{N}$*
  T. Gehrmann, Phys. Rev. **D53** (1996) 5310.

- *Deep Inelastic Electron–Pomeron Scattering at HERA*
  T. Gehrmann and W.J. Stirling, Z. Phys. **C70** (1996) 89.

- *The Effects of a New Vector Boson on the Top Quark Cross Section at the Tevatron*
  T. Gehrmann and W.J. Stirling, Phys. Lett. **B381** (1996) 221.

Extracts from these publications are furthermore contained in the following conference proceedings:

- *Spin–dependent Parton Distributions*

  T. Gehrmann and W.J. Stirling, Proceedings of the "XXVII Int. Conf. on High Energy Physics", Glasgow, 1994, eds. P.J. Bussey and I.G. Knowles, IOP Publishing (Bristol, 1995), Vol. II, p.667.

- *Present Status of Polarized Parton Distributions*

  T. Gehrmann and W.J. Stirling, Proceedings of the "Workshop on the Prospects of Spin Physics at HERA", DESY Zeuthen, 1995, eds. J. Blümlein and W.D. Nowak, DESY report 95-200 (Hamburg, 1995), p.295

- *J/ψ–pairs: A physics case for HERA–$\vec{N}$?*

  T. Gehrmann, Proceedings of the "2nd Meeting on Possible Measurements of Singly Polarized $p\vec{p}$ and $p\vec{n}$ Collisions at HERA", DESY Zeuthen, 1995, eds. H. Böttcher and W.D. Nowak, DESY Zeuthen report 95-05 (Zeuthen, 1995), p.55

- *Working Group Report on the Structure of the Proton*

  B. Badelek, J. Bartels, N. Brook, A. De Roeck, T. Gehrmann, M. Lancaster, A.D. Martin and A. Vogt, Proceedings of the workshop "HERA Physics: Proton, Photon and Pomeron Structure", Durham, 1995, J. Phys. **G22** (1996) 815.

- *Polarized Parton Distributions from a Global NLO–QCD Analysis*

  T. Gehrmann and W.J. Stirling, Proceedings of the "Workshop on Deep Inelastic Scattering and Related Phenomena (DIS '96)", Rome, 1996, to appear.

Statement of Copyright

Acknowledgements

Firstly and most important of all, I would like to thank James Stirling for his excellent supervision, for encouragement and fruitful collaboration.

I am very grateful to Ewald Reya and Horst Gerlach from Dortmund University and to Ingrid Czolbe from the Studienstiftung des deutschen Volkes for supporting my plans to work in Durham and for continuous encouragement throughout the last three years.

Numerous people have contributed to my understanding of theoretical and experimental physics. I would like to thank especially Barbara Badelek, John Dainton, Nigel Glover, Alan Martin, Ewald Reya, Dick Roberts, Misha Ryskin, Werner Vogelsang and Rüdiger Voss for many stimulating insights and interesting discussions.

The Particle Physics group of Durham University provided a friendly working environment and excellent facilites. In particular, I would like to thank Mike Whalley for sharing his knowledge and enthusiasm on the computer system with me.

During the past year, I have participated in two workshops on future physics at HERA (DESY, Hamburg) and GSI (Darmstadt). I would like to express my gratitude to Andreas Schäfer, who invited me to these workshops and who made every working group meeting enjoyable and motivating.

This work would not have been possible without financial support from the Gottlieb Daimler– und Karl Benz–Stiftung and the Studienstiftung des deutschen Volkes, which is hereby gratefully acknowledged.

Finally, I would like to thank my dear wife Aude for her invaluable help and encouragement in the preparation of this thesis and, most important of all, for her love and kindness.

Thomas Gehrmann

A thesis submitted to the University of Durham
for the degree of Doctor of Philosophy
August 1996

Proton Structure from Deep Inelastic and Diffractive Scattering

Abstract

We investigate various aspects of the proton structure in this thesis. The first addresses the distribution of the proton spin among its constituents, quarks and gluons. We derive the framework of distribution functions for these constituents and study the properties of the polarized distributions which describe the spin structure of the proton. A determination of the polarized distributions on the basis of present experimental data is presented and options for future measurements are critically evaluated. A second aspect under consideration is the phenomenology of hard diffractive electron–proton scattering. We show how diffractive interaction and hard scattering can be disentangled and suggest experimental tests for this interpretation. Finally, we illustrate how the knowledge on the proton structure can be used for the computation of observables in proton–antiproton collisions, confirming or extending our knowledge of the physics of elementary particles.

Contents

Chapter 1

Introduction

One of the primary objectives of physics is the understanding of the fundamental constituents of matter and their interactions. The historical development of physics has taught us that particles, which appear to be fundamental at first sight, display a rich substructure if looked at closely enough. Even the smallest crystal is made out of millions of atoms; an atom consists of a nucleus surrounded by a cloud of electrons; any atomic nucleus contains a certain number of protons and neutrons, and even protons and neutrons are not yet fundamental. If probed at sufficiently small scales, they display a complex internal structure. Some aspects of this structure are studied in this thesis.

In the remainder of this chapter, we will outline a formalism which enables us to describe the form and structure of the proton. A model for the structure of the proton and the nature of its constituents will be outlined in Chapters 2 and 3. In the framework of this model, we will study the distribution of the proton's spin among its constituents in Chapters 4 to 6. An extension of this model to the diffractive scattering of electrons on protons is attempted in Chapter 7. We will furthermore demonstrate in Chapter 8, how precise knowledge on the proton structure can be used to compute observables in collider experiments, which can confirm or extend our present understanding of particle physics. Finally, Chapter 9 summarizes the main results presented in this thesis. Two appendices contain mathematical and computational methods used to obtain these results.

1.1 Probing the proton structure

A microscope can help us to resolve objects which are too small to be seen with the naked eye, such as the cellular structure of plants and tissue. It therefore appears to be natural to assume, that even the structure of atoms, nuclei or protons can be studied under a microscope with sufficient resolution. This resolution is however limited by the wavelength of the light used in the microscope, as described by Rayleigh's criterion [1]. If the object lens covers an angle 2Θ when viewed from the probe, a minimum separation of

$$\Delta l_{min} = 0.61 \frac{\lambda}{\sin \Theta}$$

can be resolved with light of wavelength λ. To resolve structure in the proton, a microscope would have to operate with wavelengths at least a billion times smaller than visible light. Light at such small wavelengths cannot be deflected by lenses anymore, making a study of protons under a microscope unfeasible.

Electrons of these wavelengths, corresponding to beam energies $E_{beam} \gtrsim 1$ GeV, can be focused with magnetic fields, scattered electrons are relatively easy to detect. Furthermore, electrons appear to have no internal structure up to the smallest scales probed at present, their dynamics are well understood. The proton structure can therefore be probed by scattering an electron beam off a proton target. Two substantially different cases of electron–proton scattering have to be distinguished[1]:

1.1.1 Elastic scattering: Form factors

An electron scattering elastically off a proton has interacted with the proton as a whole, not just with one of its constituents. The distribution of elastically scattered electrons therefore contains information on the *form* of the proton, not on its internal structure.

The electromagnetic vertex for the interaction of a point-like proton (mass M) with a

---

[1]The dynamics of electron–proton scattering are discussed in most textbooks on particle physics, the treatment presented here follows the book of Halzen and Martin [2].

virtual photon of momentum q is
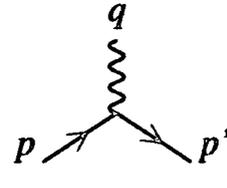
$$\mathord{\text{[diagram]}} = -ie\left[\gamma^\mu + \frac{\kappa}{2M}i\sigma^{\mu\nu}q_\nu\right],$$

(1.1)

where the second term takes account of the anomalous magnetic moment of the proton $\mu_p = (1+\kappa)\,e/(2M)$, $\kappa = 1.8$. Using this vertex, the elastic electron–proton cross section per unit of solid angle in the proton rest frame can be calculated:

$$\frac{d\sigma}{d\Omega} = \frac{\alpha^2}{4E^2\sin^4\frac{\theta}{2}}\frac{E'}{E}\left\{\left(1-\frac{\kappa^2 q^2}{4M^2}\right)\cos^2\frac{\theta}{2} - \frac{q^2}{2M^2}(1+\kappa)^2\sin^2\frac{\theta}{2}\right\},$$

(1.2)

where $\alpha \simeq 1/137$ is the electromagnetic coupling constant, and the energies of the incoming (outgoing) electron are denoted by $E(E')$. The angle Θ is defined between incoming and outgoing electron directions, the invariant momentum transfer to the proton can be measured by $q^2 = -2EE'(1-\cos\theta)$. Deviations from the above prediction were observed in 1955 [3], only two years after the first measurement [4] of elastic electron–proton scattering. This observation provided the first experimental evidence for a finite size of the proton.

The vertex (1.1) can be generalized for an object of finite size by introducing two independent form factors F_1 and F_2, which depend on the invariant momentum transfer q^2:
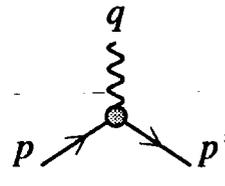
$$\mathord{\text{[diagram]}} = -ie\left[F_1(q^2)\gamma^\mu + \frac{\kappa}{2M}F_2(q^2)i\sigma^{\mu\nu}q_\nu\right].$$

(1.3)

The scattering cross section (1.2) reads then [5]:

$$\frac{d\sigma}{d\Omega} = \frac{\alpha^2}{4E^2\sin^4\frac{\theta}{2}}\frac{E'}{E}\left\{\left(F_1^2-\frac{\kappa^2 q^2}{4M^2}F_2^2\right)\cos^2\frac{\theta}{2} - \frac{q^2}{2M^2}(F_1+\kappa F_2)^2\sin^2\frac{\theta}{2}\right\}.$$

(1.4)

The above result is simplified by introducing electric and magnetic form factors [6]

$$G_E = F_1 + \frac{\kappa q^2}{4M^2}F_2$$

3

$$G_M = F_1 + \kappa F_2, \tag{1.5}$$

yielding

$$\frac{d\sigma}{d\Omega} = \frac{\alpha^2}{4E^2 \sin^4 \frac{\theta}{2}} \frac{E'}{E} \left(\frac{G_E^2 + \tau G_M^2}{1 + \tau} \cos^2 \frac{\theta}{2} + 2\tau G_M^2 \sin^2 \frac{\theta}{2} \right), \tag{1.6}$$

with $\tau = -q^2/4M^2$. These form factors can be interpreted as Fourier transformations of the radial charge and angular momentum density in the proton.

The above scattering cross section has been measured up to momentum transfers of $-q^2 \simeq 10$ GeV^2. The results [7] can be well parametrized in the simple form

$$(1 + \kappa)G_E = G_M = \left(1 - \frac{q^2}{0.7 \text{ GeV}^2} \right)^{-2},$$

a good approximation of the vertex factors is hence given by

$$F_1(q^2) = \frac{4M^2 - 2.8q^2}{4M^2 - q^2} \left(\frac{1}{1 - q^2/(0.7 \text{ GeV}^2)} \right)^2,$$

$$F_2(q^2) = \frac{4M^2}{4M^2 - q^2} \left(\frac{1}{1 - q^2/(0.7 \text{ GeV}^2)} \right)^2. \tag{1.7}$$

Using the above form factors, one can estimate the mean charge radius of the proton to be about $0.88 \cdot 10^{-15}$m [7].

1.1.2 Inelastic scattering: Structure functions

The inelastic scattering of an electron on a proton target can – in analogy to inelastic scattering in classical mechanics – have two different outcomes. If the energy deposited inside the proton is smaller than the typical binding energy of its constituents, the proton will only be *deformed*, i.e. excited to resonant state (electro-excitation of nucleon resonances). Provided the energy deposit exceeds the typical binding energy of the constituents, the proton will be *destroyed*, yielding a final state with several particles.

The first process allows an indirect, spectroscopic study of the proton as a bound state of its constituents. It does not yield conclusive information on the nature of the constituents and on their dynamics. This information can only be obtained from the second process, which is called *"Deep Inelastic Scattering (DIS)"*.

4
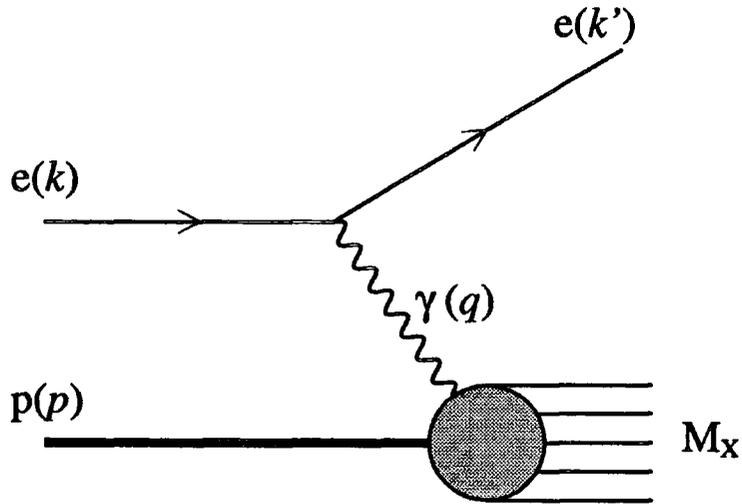
Figure 1.1: Kinematics of deep inelastic scattering

Definition	Experimental Observable	Description
$s \equiv (P + k)^2$	$s = M^2 + 2ME$	Invariant centre-of-mass energy
$Q^2 \equiv -q^2 = (k - k')^2$	$Q^2 = 4EE' \sin^2 \frac{\theta}{2}$	Invariant momentum transfer
$\nu \equiv (p \cdot q)/M$	$\nu = E - E'$	Energy of the virtual photon
$M_X^2 \equiv (P + q)^2$	$M_X^2 = M^2 + 2M\nu - Q^2$	Invariant mass of the final state
$x \equiv Q^2/(2P \cdot q)$	$x = Q^2/(2M\nu)$	'Scaling variable'
$y \equiv (P \cdot q)/(P \cdot k)$	$y = (E - E')/E$	Fractional photon energy

Table 1.1: Kinematical variables in deep inelastic scattering

The kinematical situation [8] of deep inelastic scattering is illustrated in Fig. 1.1. The commonly used DIS variables are listed in Table 1.1. It should be noted that, given a fixed

centre-of-mass energy $\sqrt{s}$, only two of the remaining variables are independent. These are usually chosen to be x and Q^2, for reasons which will become clear in Section 2.4. It should be noted that all experimental definitions of the kinematical variables refer to a setup with an electron beam onto a fixed proton target.

The differential scattering cross section for inelastic electron–proton scattering can be expressed as the product[2] of a leptonic tensor $L_{\mu\nu}$ and a hadronic tensor $W^{\mu\nu}$

$$\frac{d\sigma}{dE'd\Omega} = \frac{\alpha^2}{16\,E^3\,E'\sin^4\frac{\Theta}{2}} L_{\mu\nu}W^{\mu\nu}. \qquad (1.8)$$

The leptonic tensor describes the emission of a virtual photon off the incoming electron, it can be calculated from first principles and reads for an electron of given helicity λ:

$$L_{\mu\nu} = 2\left(k_\mu k'_\nu + k_\nu k'_\mu - \frac{1}{2}Q^2 g_{\mu\nu} - i\,\lambda\,\epsilon_{\mu\nu\rho\sigma}k^\rho k'^\sigma\right). \qquad (1.9)$$

The hadronic tensor contains all information on the proton structure. Its most general decomposition contains all possible combinations of the four-vectors characterising the photon–proton interaction: the proton momentum P, the proton spin S and the photon momentum q:

$$P = \begin{pmatrix} M \\ 0 \\ 0 \\ 0 \end{pmatrix}, \qquad S = \begin{pmatrix} 0 \\ \sin\psi\cos\phi \\ \sin\psi\sin\phi \\ \cos\psi \end{pmatrix}, \qquad q = \begin{pmatrix} E - E' \\ -E'\sin\Theta \\ 0 \\ E - E'\cos\Theta \end{pmatrix}.$$

Current conservation and invariance under charge conjugation, parity and time reversal reduce the number of independent functions, such that

$$W^{\mu\nu} = -\left(g^{\mu\nu} + \frac{q^\mu q^\nu}{Q^2}\right)W_1(\nu,Q^2) + \frac{1}{M^2}\left(P^\mu + \frac{P\cdot q}{Q^2}q^\mu\right)\left(P^\nu + \frac{P\cdot q}{Q^2}q^\nu\right)W_2(\nu,Q^2)$$

$$+\frac{i}{M^2}\epsilon^{\mu\nu\rho\sigma}q_\rho\left(S_\sigma\left(G_1(\nu,Q^2) + \frac{P\cdot q}{M^2}G_2(\nu,Q^2)\right) - \frac{S\cdot q}{M^2}P_\sigma G_2(\nu,Q^2)\right). \quad (1.10)$$

---

[2]Note that the normalization of the hadronic tensor is a matter of convention. We adopt the convention of [2, 8], such that the hadronic tensor of a *point–like* target would be $L^{\mu\nu}/(4\pi M)$.

The functions $W_{1,2}(\nu, Q^2)$ are called unpolarized structure functions, $G_{1,2}(\nu, Q^2)$ are polarized structure functions.

The differential cross section (1.8) can then be expressed in terms of these structure functions. For future convenience, we decompose the cross section into a spin averaged and a spin dependent part:

$$d\sigma = d\bar{\sigma} + \frac{1}{2}\lambda\,\Delta\sigma$$

The unpolarized cross section can then be written as [9]

$$\frac{d\bar{\sigma}}{dE'd\Omega} = \frac{\alpha^2}{4E^2 \sin^4\frac{\Theta}{2}}\left[2W_1(\nu, Q^2)\sin^2\frac{\Theta}{2} + W_2(\nu, Q^2)\cos^2\frac{\Theta}{2}\right]. \tag{1.11}$$

The polarized cross section can be further decomposed into longitudinal and transverse contributions, depending on the spin orientation of the proton. The angle formed by the proton spin and the electron spin is denoted by ψ, the projections of the outgoing electron momentum and the proton spin onto the plane perpendicular to the incoming electron direction form the angle ϕ. The polarized cross section reads then:

$$\Delta\sigma = -\frac{1}{2}\cos\psi\Delta\sigma_L + \frac{1}{2}\sin\psi\Delta\sigma_T$$

$$\frac{d\Delta\sigma_L}{dE'd\Omega} = \frac{4\alpha^2}{M^3Q^2}\frac{E'}{E}\left[(E + E'\cos\Theta)MG_1(\nu, Q^2) - Q^2G_2(\nu, Q^2)\right] \tag{1.12}$$

$$\frac{d\Delta\sigma_T}{dE'd\Omega} = -\cos\phi\frac{2\alpha^2}{M^3Q^2}\frac{E'^2}{E}\sin\Theta\left[MG_1(\nu, Q^2) + 2EG_2(\nu, Q^2)\right] \tag{1.13}$$

Instead of measuring the absolute cross sections for different spin configurations, it is more convenient to perform asymmetry measurements. The longitudinal spin asymmetry is defined as the difference between the cross sections for antiparallel ($\psi = \pi$) and parallel ($\psi = 0$) spin orientations

$$A_{\parallel} \equiv \frac{\Delta\sigma_L}{2\bar{\sigma}}. \tag{1.14}$$

The transverse spin asymmetry is the difference between opposite transverse orientations of the proton spin for fixed lepton helicity:

$$A_{\perp} \equiv \frac{\Delta\sigma_T/\cos\phi}{2\bar{\sigma}}. \tag{1.15}$$

7

We will give explicit expressions for these asymmetries in section 4.1.

The first unpolarized DIS experiments were carried out with the 20 GeV electron beam at SLAC in 1967/68. First results from these experiments [10] displayed a behaviour which was significantly different from the results of the earlier elastic scattering experiments.

The elastic cross section (1.6) falls rapidly below the cross section expected for a point-like proton (1.2) as Q^2 increases. On the contrary, the cross section for deep inelastic electron–proton scattering at sufficiently large ν appeared to be proportional to the cross section for a pointlike target at all Q^2. This *scaling behaviour* was the first evidence for point-like constituents in the proton. The nature of these constituents will be discussed in the following two chapters.

Similar measurements can be carried out with muon or neutrino beams. The cross sections for electron–proton and muon–proton scattering are identical, they probe the electromagnetic structure functions. Neutrino–proton scattering probes the weak structure functions of the proton, which are different from the above.

Soon after these first observations, a large programme of deep inelastic scattering experiments was launched at SLAC, CERN and Fermilab. These experiments studied proton, deuterium and nuclear targets, determining the unpolarized structure functions to a high level of accuracy. Reviews of these experiments can be found in [11, 12].

A different kinematical configuration for the study of deep inelastic scattering is given at the HERA electron–proton collider at DESY, where electron and proton beams are collided at $\sqrt{s} = 300$ GeV, compared to $\sqrt{s} < 30$ GeV at fixed target experiments. This allows one to study the proton structure in a different kinematical regime and enables dedicated studies of the final state of DIS events. A final state configuration unique to HERA, diffractive DIS, will be discussed in Chapter 7.

The experimental knowledge on the polarized proton structure is far more incomplete than in the unpolarized case. First measurements of the longitudinal asymmetry (1.14) were made at SLAC in 1976 [13], a first study of the transverse asymmetry (1.15) followed only in 1994 [14]. An overview of the present experimental situation will be given in Section 4.1. The experimental data available at present are used to estimate the distribution

8

of the proton's spin amongst its constituents in Chapter 5. We will furthermore study, in Chapter 6, how future experiments can yield a more precise understanding of the spin structure of the proton.

Chapter 2

Quarks, Quantum Chromodynamics and the parton model

The stability of the atomic nucleus – built up of positively charged protons and uncharged neutrons – cannot be explained as the effect of the two macroscopic forces in nature: the gravitational attraction between its constituents is far too small to compensate the electromagnetic repulsion among the protons. Therefore a new, *strong interaction* has to be present in the nucleus. A first formulation of the theory of the strong interaction [15] predicted three massive particles $(\pi^{\pm}, \pi^0)$, which mediate the strong forces in the nucleus, much like the massless photon mediates the electromagnetic interaction. The discovery of the $\pi^{\pm}$ [16] and π^0 [17] around 1950 gave strong support to this picture.

Soon after the discovery of the pion, experiments began to observe an increasing number of different strongly interacting particles with properties similar to the proton, neutron and pion. This large number of new, apparently fundamental particles raised the question whether these are made up from a smaller number of fundamental particles in different configurations.

We illustrate in Section 2.1 how the spectrum of strongly interacting particles can be explained in the static quark model. The dynamical interaction of quarks – the theory of Quantum Chromodynamics (QCD) – is described in Section 2.2. QCD forms one of the

10

building blocks of the Standard Model of particle physics, which will be briefly sketched in Section 2.3.

Taking the quark model literally, one could identify quarks with the point-like proton constituents observed in DIS experiments. This identification is the basis of the naïve quark parton model, as described in Section 2.4, its implications on other experimental observables are discussed in Section 2.5.

2.1   The static quark model

By the year 1960, about 25 strongly interacting particles (hadrons) were observed experimentally. Their interaction laws and decay properties could be described approximately by requiring conservation of three quantum numbers – isospin T_3, baryon number B and strangeness S – under strong interactions. The isospin is related to the symmetry between proton ($T_3 = +1/2$) and neutron ($T_3 = -1/2$) and among the pions ($T_3 = 0, \pm1$), baryon number discriminates between strongly interacting fermions (baryons, like $p; n$, $B = 1$) and bosons (mesons, like $\pi^{\pm,0}$, $B = 0$). The third quantum number, strangeness, was introduced to explain the anomalously large lifetimes of certain hadrons, justifying why their decays can not be mediated by strong interactions.

It was shown independently by Gell-Mann and Ne'eman in 1961, that hadrons with identical spin and parity quantum numbers could be classified into particular representations (multiplets) of the symmetry group SU(3) [18], their places within the multiplet determined by their isospin T_3 and hypercharge $Y = B + S$ (Fig. 2.1).

An explanation of this complicated multiplet structure is given by the quark model [19], which postulates the existence of three quark flavours (up, down and strange), which form the fundamental triplet representation of the symmetry group SU(3)$_f$ (Fig. 2.2). All mesons can then be interpreted as quark–antiquark bound states, all baryons are bound states of three quarks (Fig. 2.1).

The SU(3)$_f$ symmetry of hadrons is in fact only approximate, as the hadron masses within a multiplet vary. This behaviour can be explained in the quark model, if the s

11
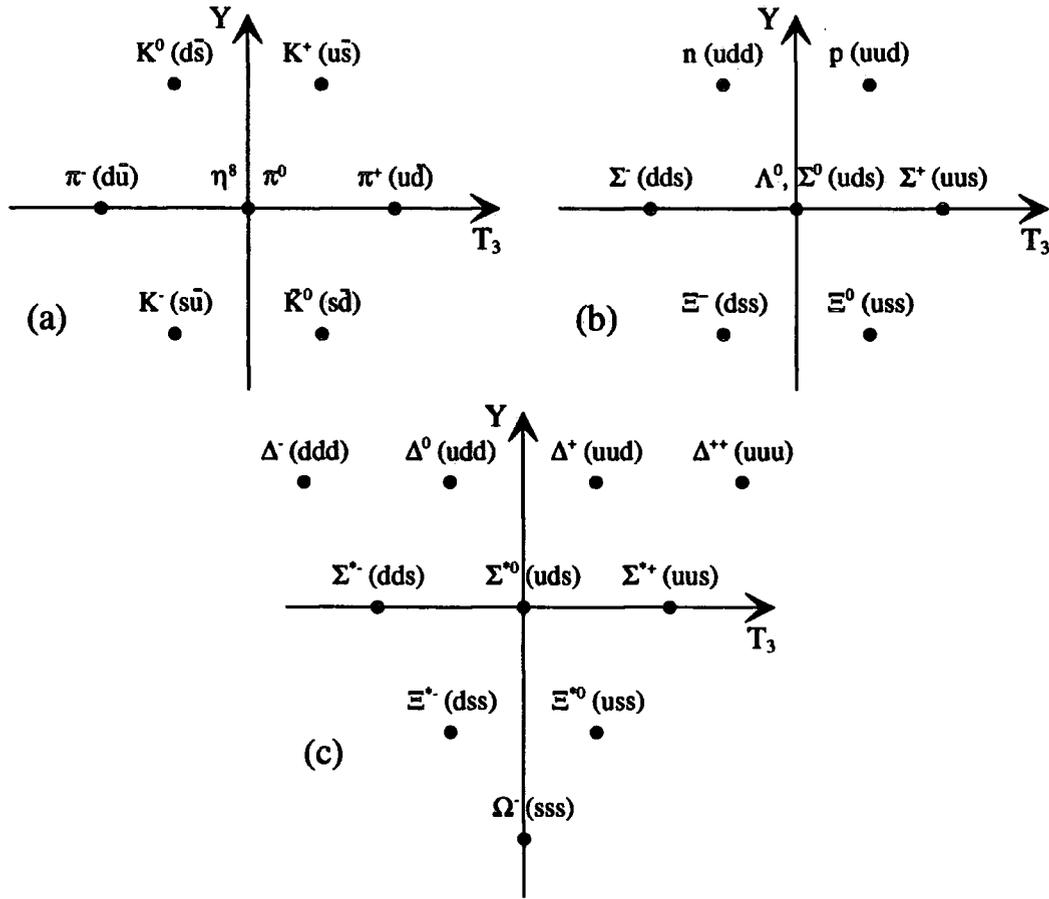
Figure 2.1: Multiplets of the $J^P = 0^-$ mesons (a), the $1/2^+$ baryons (b) and the $3/2^+$ baryons (c) and their interpretation in the quark model. The $T_3 = 0$, $Y = 0$ states in (a) are superpositions: $\pi^0 = (u\bar{u} - d\bar{d})/\sqrt{2}$, $\eta^8 = (u\bar{u} + d\bar{d} - 2s\bar{s})/\sqrt{6}$, where η^8 and the singlet combination $\eta^1 = (u\bar{u} + d\bar{d} + s\bar{s})/\sqrt{3}$ mix to give the physical states η and η'.

quark is heavier than the u and d quarks. Since the invention of the quark model, three more quarks (charm, bottom and top) have been discovered, all being heavier than u, d, s. Due to the large mass differences, it does not make sense to extend the $SU(3)_f$ symmetry to include these heavier flavours.

The interpretation of hadron multiplets as products of fundamental $SU(3)_f$ quark triplets is, however, not without conceptual problems. Having spin–1/2, the quarks must

12
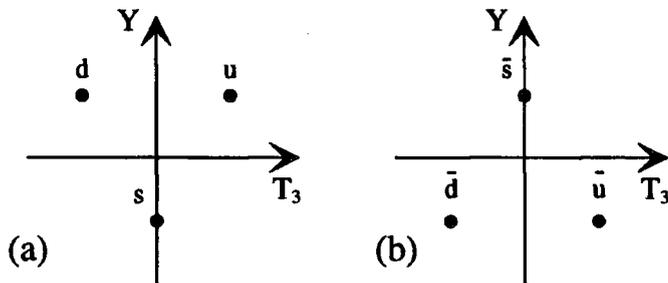
Figure 2.2: Fundamental representations of SU(3)$_f$: quark (a) and antiquark (b) triplets.

obey Fermi–Dirac statistics, i.e. they are forbidden to coincide in all their quantum numbers inside a hadron. Looking at the $3/2^+$ baryon decuplet (Fig. 2.1c), we find that the particles on the three edges (Δ^{++}, Δ^-, Ω^-) seem to contradict this principle, each of them consists of three identically flavoured quarks, the quark spins pointing into identical directions. This conceptual difficulty can only be overcome by introducing a new quantum number, *colour* [20].

Quarks are assumed to carry one of three colours (red, green or blue), antiquarks one of the corresponding anticolours. Hadrons are only formed of colour singlet combinations of quarks and antiquarks: baryons consist of three quarks with different colours, mesons of a quark–antiquark pair with identical colours.

2.2 Dynamical properties of quarks: QCD

The conservation of colour in quark–quark interactions gives rise to a new interaction, which is described by the theory of Quantum Chromodynamics (QCD) [21]. Interactions of quarks are mediated by the exchange of the gauge bosons of QCD, the *gluons*. The structure of the colour symmetry group SU(3)$_c$ is more complicated than the structure of the electromagnetic symmetry group U(1): while the quantum theory of electromagnetic interactions (QED) only requires one uncharged gauge boson, the photon, QCD has 8 gluons which carry different combinations of colour charge. Apart from a coupling between

gluons and quarks, QCD predicts the self-coupling of gluons.

The Lagrangian density of QCD[1] is given by

$$\mathcal{L} = -\frac{1}{4} F^a_{\mu\nu} F^{\mu\nu}_a + \sum_q \bar{\psi}_q \left[i\gamma^\mu D_\mu - m_q \right] \psi_q \,, \tag{2.1}$$

with

$$\begin{aligned} F^a_{\mu\nu} &= \partial_\mu A^a_\nu - \partial_\nu A^a_\mu - g f^{abc} A^b_\mu A^c_\nu, \\ D_\mu &= \partial_\mu + i g A^a_\mu T_a. \end{aligned} \tag{2.2}$$

The $SU(3)_c$ symmetry determines the algebra of the T^a matrices, in fixing the structure constants f_{abc}:

$$\left[T^a, T^b \right] = i f^{abc} T^c.$$

From the above, we can read off the QCD interactions: the covariant derivative D_μ gives rise to a quark–gluon vertex, the contraction of the field strength tensors $F^a_{\mu\nu} F^{\mu\nu}_a$ yields 3-gluon and 4-gluon vertices. The parameter g in the above expression is the QCD coupling, it can only be determined experimentally.

The colour structure of QCD is contained in the T^a matrices and their algebra. These can be factored out in practical calculations, yielding overall colour factors. The most common colour factors are:

$$\sum_{k=1}^{3} \sum_{a=1}^{8} \quad \underset{T^a_{ik} \quad T^a_{kj}}{\overset{i \quad k \quad j}{\cdots}} \quad \equiv \quad C_F \delta_{ij} = \frac{4}{3} \delta_{ij} \,,$$

$$\sum_{i,j=1}^{3} \quad \underset{T^a_{ij} \quad T^b_{ji}}{\overset{i}{\underset{j}{\cdots}}} \quad \equiv \quad T_F \delta^{ab} = \frac{1}{2} \delta^{ab} \,,$$

$$\sum_{c,d=1}^{8} \quad \underset{f_{acd} \quad d \quad f_{bcd}}{\overset{c}{\cdots}} \quad \equiv \quad C_A \delta^{ab} = 3 \delta^{ab} \,, \tag{2.3}$$

and furthermore $T_f \equiv n_f T_F$.

---

[1] We will only give a brief outline of QCD in what follows, a more formal and complete treatment can for example be found in [22]

14

Like any other quantum field theory, QCD faces the problem that only the computation of the most simple (leading-order) contribution to a particular process yields a finite result, whereas all higher orders contain infinities. These infinities are always associated with an (unphysical) parameter μ^2, which has the dimension (mass)^2 and appears either as cut-off in momentum integrals or as normalization constant in dimensional regularization. Apart from infinities associated with particular configurations of particles in the initial and final state, one finds certain infinities which appear to be process independent and are associated with the QCD vertex functions. The universal infinities can be removed by redefining the QCD coupling constant g in (2.1). This procedure is called renormalization. The new, *renormalized* coupling is the sum of the original, *bare* coupling and terms containing infinities. As both the bare and the renormalized coupling are required to be dimensionless while the infinite terms contain the unphysical μ^2, one has to introduce a renormalization scale μ_R^2, at which the renormalized coupling is evaluated. Requiring the bare coupling to be independent of μ_R^2 yields a differential equation for the renormalized coupling. If we denote $\alpha_s(\mu_R^2) = 4\pi g(\mu_R^2)$, this reads [23]

$$\mu_R^2 \frac{\partial \alpha_s(\mu_R^2)}{\partial \mu_R^2} = \beta\left(\alpha_s(\mu_R^2)\right) \equiv -\alpha_s(\mu_R^2)\left[\frac{\alpha_s(\mu_R^2)}{4\pi}\beta_0 + \left(\frac{\alpha_s(\mu_R^2)}{4\pi}\right)^2 \beta_1 + \left(\frac{\alpha_s(\mu_R^2)}{4\pi}\right)^3 \beta_2\right],$$
(2.4)

where the right hand side has been calculated in [24]. In the remainder of this thesis, we will use only the solution of the above equation up to β_0 for quantities evaluated at leading order and up to β_1 for quantities evaluated at next-to-leading order.

Introducing a parameter Λ as constant of integration, one can solve (2.4):

$$\alpha_s(\mu_R^2) = \frac{4\pi}{\beta_0 \ln(\mu_R^2/\Lambda^2)}\left(1 - \frac{\beta_1}{\beta_0^2}\frac{\ln\left(\ln(\mu_R^2/\Lambda^2)\right)}{\ln(\mu_R^2/\Lambda^2)}\right),$$
(2.5)

where

$$\beta_0 = 11 - \frac{2\,n_f}{3}, \qquad \beta_1 = 102 - \frac{38\,n_f}{3}.$$
(2.6)

Measurements of the strong coupling constant yield $\Lambda \approx 200$ MeV for five active quark flavours.
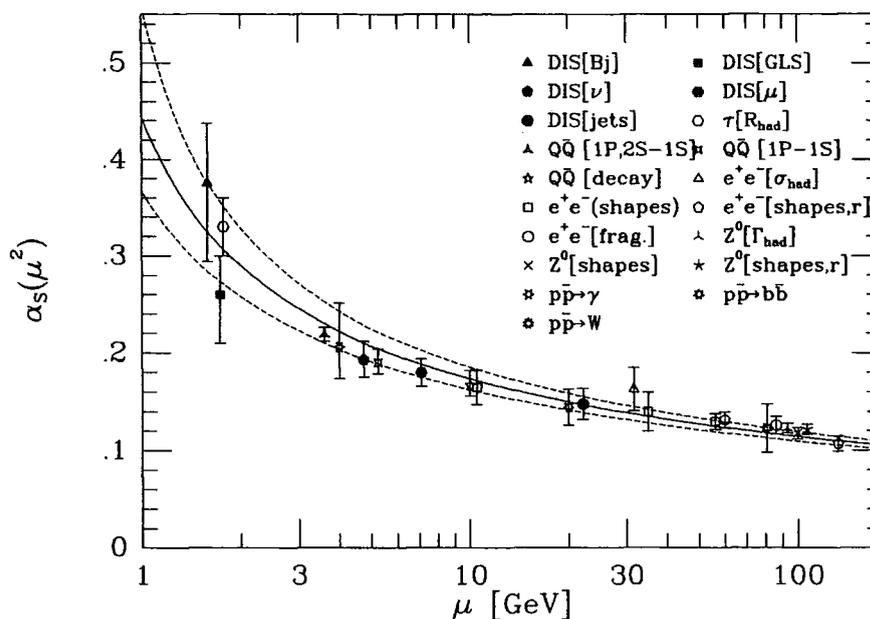
Figure 2.3: The strong coupling constant $\alpha_s(\mu^2)$ as function of the renormalization scale μ, compared to experimental measurements. The curves correspond to $\alpha_s(M_Z^2) = 0.116 \pm 0.005$. Figure taken from [25].

The running of α_s is illustrated in Fig. 2.3, two characteristic features of QCD can be read off:

Asymptotic freedom at high energies

At large scales the QCD coupling constant becomes small, i.e. quarks only interact very weakly with each other and can be treated as free particles. This feature allows one to calculate high energy processes in a perturbative expansion – a series in powers of α_s.

Confinement at low energies

The rise of the QCD coupling towards small scales makes the theory uncalculable with perturbative methods, as no small expansion parameter is present anymore. This strong

coupling at low scales binds quarks together into hadrons. This phenomenon is presently not yet understood theoretically, as no reliable method for precise non–perturbative QCD calculations is available.

2.3 The other fundamental interactions: the Standard Model

Apart from QED and QCD, a third interaction is present on the level of elementary particles: the weak interaction. This interaction is mediated by three gauge bosons: $W^{\pm}$ and Z^0, which couple to a quantum number called weak isospin[2].

The electroweak gauge bosons have masses ($M_W \sim 80$ GeV, $M_Z \sim 91$ GeV) due to the breaking of the high-energy symmetry between electromagnetic and weak interactions (Higgs mechanism). Although the weak coupling is larger than the electromagnetic coupling, all low-energy effects of the weak interaction are strongly suppressed by the large gauge boson masses, this interaction is only visible in nuclear β-decay. The effective weak coupling at low energies is given by

$$G_F = \frac{\pi\alpha}{\sqrt{2}M_W^2 \sin^2\Theta_W} \simeq \frac{1}{(300 \text{ GeV})^2} ,$$

where $\sin^2\Theta_W = 0.232$ is the ratio of electromagnetic and weak coupling constants.

A particular feature of the W and Z bosons is their coupling structure to fermions. The W only couples to the left-handed fermions, and the couplings of the Z to left-handed and right-handed fermions are different. This is expressed in couplings with vector and axial vector contributions.

These three interactions form the basis of our current understanding of particle physics, the Standard Model. Up to the smallest scales accessible at present ($\approx 10^{-18}$ m), the Standard Model appears to be in very good agreement with experimental observations.

---

[2]We will only give a brief outline of basic features of the Standard Model, more complete treatments are in the standard literature, e.g. [2]

	e_f	v_f	a_f	Particles		
Quarks	$\frac{2}{3}$	$\frac{1}{2} - \frac{4}{3}\sin^2\Theta_W$	$\frac{1}{2}$	u	c	t
	$-\frac{1}{3}$	$-\frac{1}{2} + \frac{2}{3}\sin^2\Theta_W$	$-\frac{1}{2}$	d	s	b
Neutrinos	0	$\frac{1}{2}$	$\frac{1}{2}$	ν_e	ν_μ	ν_τ
Leptons	-1	$-\frac{1}{2} + 2\sin^2\Theta_W$	$-\frac{1}{2}$	e	μ	τ

Table 2.1: Particle content of the Standard Model, electric charges e_f, vector- and axialvector-couplings v_f, a_f. All particles are spin–1/2 fermions.

Only very recently, some evidence for deviations from the Standard Model has been reported. These deviations will be discussed in more detail in Chapter 8.

The particle content of the Standard Model can be grouped into three generations of quarks and leptons, which are listed in Table 2.1. The particles of different generations have – despite their different mass – identical properties.

2.4 The naïve quark parton model

The scaling behaviour of the DIS cross section indicated the existence of point-like constituents ('partons') in the proton. With the quark model successfully describing hadron spectroscopy, it would be natural to assume that these partons are in fact one d and two u quarks, each carrying about a third of the proton's mass.

R.P. Feynman developed a model for the proton structure which does not make any assumptions on the *nature* of these proton constituents, the *parton model*. Using the quantitative predictions of this model for the proton structure functions, one can test the above interpretation of the proton structure in terms of quark constituents.

The kinematics of deep inelastic scattering are characterized by [26]

$$Q^2 \to \infty, \quad \nu \to \infty \qquad \text{with } x = \frac{Q^2}{2M\nu} \text{ fixed.}$$

The parton model is formulated by choosing a frame, in which the longitudinal momentum

of the proton approaches infinity in the above limit. Such a frame is given by the *infinite momentum frame*, in which

$$
P = \begin{pmatrix} \sqrt{P_B^2 + M^2} \\ 0 \\ 0 \\ P_B \end{pmatrix}, \qquad q = \begin{pmatrix} 0 \\ 0 \\ 0 \\ -\sqrt{Q^2} \end{pmatrix},
$$

with $P_B = M\nu/\sqrt{Q^2} = \sqrt{Q^2}/(2x)$. In this particular frame, one can make several assumptions on the proton as seen by the electron. These assumptions form the concept of the parton model for the structure of the proton; they are summarized in [27]:

> [In the infinite momentum frame]..., *we visualize the intermediate state from which the electron scatters as follows:*
>
> (a) *It consists of a certain number N of free partons (with probability P_N).*
>
> (b) *The longitudinal momentum of the ith parton is a fraction x_i of the total momentum of the proton:*
>
> $$p_i = x_i P .$$
>
> (c) *The mass of the parton, before and after the collision is small (or does not significantly change).*
>
> (d) *The transverse momentum of the parton before the collision can be neglected, in comparison with* $\sqrt{(Q^2)}$, *the transverse momentum imparted as $p \to \infty$.*
>
> *With these assumptions, it should be a good approximation to write, at infinite momentum,*
>
> $$p_i^\mu \cong x_i P^\mu .$$

At the time of interaction, the virtual photon therefore 'sees' one parton carrying a fraction x_i of the proton's momentum, while the proton remnant carries a fraction $(1 - x_i)$, as illustrated in Fig. 2.4. Although this state is not stable, its lifetime is much longer than the time it takes the photon to interact with the parton.

Assuming the partons to be spin-1/2 particles, one can compute (1.11) for the elastic scattering of the electron off the i-th parton, given a partonic charge e_i. Comparison of the expression obtained with (1.11) yields the following partonic contributions to the

19
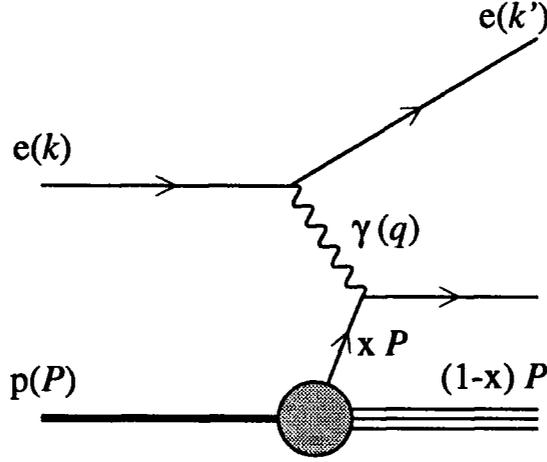
Figure 2.4: Deep inelastic scattering in the parton model.

proton structure functions:

$$W_{1,i}(\nu, Q^2) = e_i^2 \frac{Q^2}{4x_i^2 M^2} \delta\left(\nu - \frac{Q^2}{2x_i M}\right),$$

$$W_{2,i}(\nu, Q^2) = e_i^2 \delta\left(\nu - \frac{Q^2}{2x_i M}\right). \tag{2.7}$$

We have to sum over all species i of different partons to obtain the structure functions of the proton. Furthermore, we must integrate the above expression over x_i, weighted by the probability $f_i(\xi)$ of finding a parton in the interval $[\xi; \xi + d\xi]$:

$$W_2(\nu, Q^2) = \sum_i e_i^2 \int_0^1 d\xi f_i(\xi) \delta\left(\nu - \frac{Q^2}{2\xi M}\right)$$

$$= \frac{x}{\nu} \sum_i e_i^2 f_i(x).$$

The above equation shows the scaling behaviour of structure functions: $\nu W_2(\nu, Q^2)$ only depends on the scaling variable x in the deeply inelastic limit $Q^2 \to \infty$, $\nu \to \infty$. It can be interpreted as charge weighted sum of *parton distributions* $f_i(x)$.

Similar scaling properties hold for the other proton structure functions [26]

$$MW_1(\nu, Q^2) \to F_1(x) = \frac{1}{2} \sum_i e_i^2 f_i(x),$$

$$\nu W_2(\nu, Q^2) \quad \rightarrow \quad F_2(x) = \sum_i e_i^2 x f_i(x) \,,$$

$$\frac{\nu}{M} G_1(\nu, Q^2) \quad \rightarrow \quad g_1(x) = \frac{1}{2} \sum_i e_i^2 \Delta f_i(x) \,,$$

$$\frac{\nu^2}{M^2} G_2(\nu, Q^2) \quad \rightarrow \quad g_2(x) \,, \tag{2.8}$$

where $\Delta f_i(x) \equiv f_i^\uparrow(x) - f_i^\downarrow(x)$ denotes the difference between the distributions of partons f_i with spins parallel and antiparallel to the proton spin. The structure function $g_2(x)$ cannot be interpreted in terms of parton distributions.

If the quark model is sufficient to describe the proton, one would expect distributions for u and d quarks, which are both peaked around $x \approx 1/3$, with

$$\int_0^1 f_u(x) \mathrm{d}x = 2 \quad \text{and} \quad \int_0^1 f_d(x) \mathrm{d}x = 1 \,.$$

Comparing these model predictions with data from the first DIS experiments [10] shows already the failure of this simple picture. The data on νW_2 appear to be constant for $x \rightarrow 0$ while the integrability of the distributions requires $F_2(x) \rightarrow 0$ for $x \rightarrow 0$.

This apparent discrepancy can be explained by assuming that the three *valence* quarks predicted by the quark model are accompanied by a *sea* of quark–antiquark pairs [27]. The sea does not contribute to the macroscopic quantum numbers of the proton and can therefore contain an arbitrary number of pairs of different flavours.

As the proton and neutron are related by isospin symmetry, one can obtain the parton distributions in the neutron from the distributions in the proton by interchanging u and d quarks:

$$f_{d/n}(x) = f_{u/p}(x), \quad f_{u/n}(x) = f_{d/p}(x), \quad f_{\bar{d}/n}(x) = f_{\bar{u}/p}(x), \quad f_{\bar{u}/n}(x) = f_{\bar{d}/p}(x).$$

A common simplification of notation is the labelling of parton distributions by the symbol of the parton species, i.e. $u(x) \equiv f_u(x)$, $\Delta u(x) \equiv \Delta f_u(x)$, etc. Both notations will be used in the remainder of this thesis.

When the quark parton model was postulated in 1969, the dynamics of quarks were not yet understood; QCD only followed in 1973. Although QCD introduces corrections

to the parton model, the global picture as derived in this section still remains intact. We will discuss these corrections in Chapter 3.

2.5 Implications of the parton model

If the partonic interpretation of the proton structure is correct, it should not only describe the proton structure function, but also other observables in electron–hadron and hadron–hadron collisions. The parton model predictions for these observables are given by:

$$\sigma_{e+h \to F} = \sum_i \int dx\, f_{i/h}(x)\, \hat{\sigma}_{e+i \to F}(x)\,, \qquad (2.9)$$

$$\sigma_{h_1+h_2 \to F} = \sum_i \sum_j \int dx_1\, dx_2\, f_{i/h_1}(x_1)\, f_{j/h_2}(x_2)\, \hat{\sigma}_{i+j \to F}(x_1, x_2)\,, \qquad (2.10)$$

where F denotes the particular final state under consideration, $f_{i/h}$ is the distribution of parton i in hadron h and $\hat{\sigma}$ is the cross section on the parton level

The first observable of this type was suggested by Drell and Yan [28]: the production of lepton pairs in hadron–hadron collisions due to quark–antiquark annihilation (Fig. 2.5). One usually studies this process as a function of the invariant mass of the lepton pair M^2. The parton level cross section is given by

$$\frac{d\hat{\sigma}}{dM^2} = \frac{4\pi\alpha^2}{9\hat{s}}\, e_q^2 \delta(\hat{s} - M^2), \qquad (2.11)$$

where $\hat{s} = x_1 x_2 s$ is the centre-of-mass energy of the quark–antiquark pair. Introducing a scaling variable $\tau = M^2/s$ and considering the asymptotic limit

$$M^2 \to \infty, \quad s \to \infty \quad \text{with } \tau \text{ fixed},$$

the proton–proton cross section can be written as

$$M^4 \frac{d\sigma}{dM^2} = \frac{4\pi\alpha^2}{9} \tau \int_0^1 dx_1\, dx_2\, \delta(x_1 x_2 - \tau) \sum_q e_q^2 \{f_q(x_1) f_{\bar{q}}(x_2) + (q \leftrightarrow \bar{q})\}$$

$$= \frac{4\pi\alpha^2}{9} \tau \mathcal{F}(\tau), \qquad (2.12)$$

22
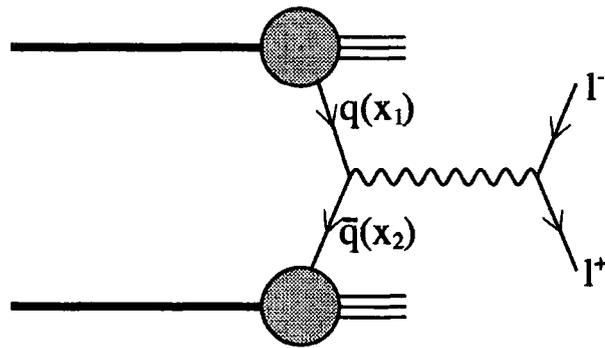
Figure 2.5: The parton model description of the Drell–Yan process.

where the last relation demonstrates the scaling behaviour of the Drell–Yan cross section in the parton model.

The experimental observation [29] of this process in 1970 was the first success of the parton model. Nowadays, a multitude of other observables in collider experiments can be described in a similar way, an overview can be found in [25].

Chapter 3

The evolution of parton distributions

So far, we have considered the quarks of the parton model to be static noninteracting objects. This naïve picture can, however, not be true anymore in QCD, where quarks are constantly interacting by emission and absorption of gluons.

The naïve quark parton model picture can be largely maintained even in QCD, although some corrections have to be applied. Apart from the quark distributions, a sizable distribution of gluons is found in the proton. Quarks and gluons are dynamically interacting inside the proton; if the distributions are probed at increasing values of Q^2, more and more of these interactions will be resolved: the scaling behaviour of the naïve quark parton model is violated in QCD.

We will quantify these effects in the following chapter. Section 3.1 motivates QCD corrections to structure functions using a particular example and demonstrates how these corrections lead to *scaling violations*. These scaling violations yield *evolution equations* for unpolarized and polarized parton distributions which will be presented in section 3.2. Expanding quark and gluon contributions to the structure functions order by order, one obtains a consistent picture of deep inelastic scattering in QCD; the relevant formulae for a treatment of cross sections and structure functions at next-to-leading order are

summarized in Section 3.3. Finally, we will describe in Section 3.4 how the distribution functions for quarks and gluons in the proton can be determined from experimental data.

3.1 QCD corrections to the naïve parton model

In the QCD–improved parton model, we have to consider a more complicated photon–parton subprocess than in the naïve parton model (cf. Fig. 2.4). We will illustrate this in the case of the structure function F_2, a similar argumentation applies to all other structure functions.

A parton i of momentum p_i carrying a fraction ξ of the proton's longitudinal momentum can contribute to $F_2(x, Q^2)$ via a parton level subprocess. This subprocess

$$\hat{F}_{2,i}(z, Q^2)(\gamma^* + i \to X)$$

is characterized by two invariant variables: Q^2, the virtuality of the photon and the photon–parton centre-of-mass energy, more conveniently denoted by the dimensionless variable $z = Q^2/(2q \cdot p_i)$. The subprocess can be projected out of the hadronic tensor [30]. Integrating over all allowed values for ξ and z, we obtain the structure function

$$\frac{1}{x} F_2(x, Q^2) = \sum_i \int_0^1 d\xi \, dz \, \delta(x - z\xi) \, f_i(\xi) \, \hat{F}_{2,i}(z, Q^2) \, . \tag{3.1}$$

In the QCD–improved parton model, this parton can be a quark as well as a gluon: $f_i(\xi) = q(\xi), \bar{q}(\xi), G(\xi)$. We will elaborate the structure of the QCD corrections for the quark-initiated $\hat{F}_{2,q}(z, Q^2)$ process in what follows. The process $\hat{F}_{2,g}(z, Q^2)$ can be described in the same formalism, only the lowest order contribution is absent, as gluons do not couple directly to the photon.

At lowest order, one finds (Fig. 3.1.a)

$$\hat{F}_{2,q}^{(0)}(z, Q^2) = e_q^2 \delta(1 - z) \, ,$$

recovering the parton model result of (2.7). The QCD corrections from real gluon emission and virtual gluon exchange are due to the diagrams in Fig. 3.1.b-d. Integration of these
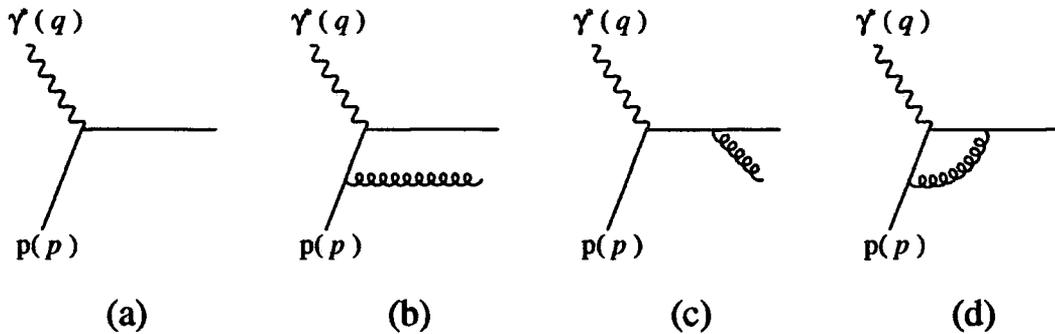
Figure 3.1: Partonic contribution to deep inelastic structure functions: lowest order quark subprocess (a) and its $\mathcal{O}(\alpha_s)$ corrections (b-d).

contributions over the appropriate phase space yields at first sight an infinite result: the virtual contribution (d) diverges, if the gluon momentum becomes small; contributions (b/c) diverge, if the gluon momentum becomes collinear to the incoming/outgoing quark or small. In order to regulate these divergencies, one can evaluate the above contributions in $d = 4 + 2\epsilon$ dimensions, which yields the following contribution [30] to the structure function

$$\hat{F}_{2,q}^{(1)}(z, Q^2) = e_q^2 \frac{\alpha_s}{2\pi} \frac{1}{\Gamma(1+\epsilon)} \left(\frac{4\pi Q^2}{\mu^2}\right)^{\epsilon} \left(\frac{1}{\epsilon} P_{qq}^{(0)}(z) + c_{2,q}^{(1)}(z) + \mathcal{O}(\epsilon)\right), \qquad (3.2)$$

where an arbitrary mass parameter μ^2 has been introduced to maintain a dimensionless coupling constant. Explicit forms for $P_{qq}^{(0)}$ and $c_{2,q}^{(1)}$ will be given later. It is apparent from the above equation that only a partial cancellation of singular terms has taken place. The leftover $1/\epsilon$-term can be identified with the initial quark/gluon collinear divergence, which is not canceled by any other contribution to this process.

As the left hand side of (3.1) is a finite, experimentally observable quantity, this divergence has to be compensated by a similar divergence in the *bare* quark distribution $q(\xi)$. We can decompose[1] the bare quark distribution $q(\xi)$ into a finite, *renormalized*

---

[1] This decomposition is not unambiguous, as one could add an arbitrary finite term into the bare parton distribution. The particular choice of finite term defines the renormalization/factorization scheme. The results given below correspond to the so-called modified minimal subtraction ($\overline{MS}$)-scheme.

parton distribution and an infinite contribution. To keep both distributions dimensionless, a *mass factorization* scale μ_F^2 has to be introduced, compensating the unphysical scale μ^2,

$$q(\xi) = q(\xi, \mu_F^2) - \frac{1}{\epsilon} \frac{1}{\Gamma(1 + \epsilon)} \left(\frac{4\pi\mu_F^2}{\mu^2} \right)^\epsilon \frac{\alpha_s}{2\pi} \int_\xi^1 \frac{dz}{z} P_{qq}^{(0)}(z) q(\xi/z). \tag{3.3}$$

The renormalized parton distribution $q(\xi, \mu_F^2)$ now depends on the chosen mass factorization scale.

The mass factorization procedure removes all infinities from the right hand side of (3.1), in the case of a quark in the initial state, it yields the replacement

$$q(\xi) \, \hat{F}_{2,i}(z, Q^2) \quad \rightarrow \quad q(\xi, \mu_F^2) e_q^2 C_{2,q}(z, Q^2, \mu_F^2),$$

where the *coefficient function*

$$C_{2,q}(z, Q^2, \mu_F^2) = \delta(1 - z) + \frac{\alpha_s}{2\pi} \left(P_{qq}^{(0)}(z) \ln \frac{Q^2}{\mu_F^2} + c_{2,q}^{(1)}(z) \right)$$

contains two contributions at $\mathcal{O}(\alpha_s)$: a left-over term from the mass factorization procedure, which vanishes if $\mu_F^2 = Q^2$, and a term containing the finite corrections from (3.2).

Requiring the bare parton distribution $q(x)$ to be independent of the mass factorization scale chosen yields an *evolution equation* for the renormalized parton distribution

$$\mu_F^2 \frac{\partial}{\partial \mu_F^2} q(x, \mu_F^2) = \int_x^1 \frac{dz}{z} \frac{\alpha_s}{2\pi} P_{qq}^{(0)}(z) q(x/z, \mu_F^2). \tag{3.4}$$

The above equation is the most simple of the "Dokshitzer–Gribov–Lipatov–Altarelli–Parisi" (DGLAP) [31] evolution equations. Its solution depends on the boundary conditions imposed at a certain scale Q_0^2. These are typically given in the form of an initial distribution $q(x, Q_0^2)$. An explicit solution for these boundary conditions will be derived in the appendix.

The DGLAP evolution equation has a simple probabilistic interpretation. As Q^2 increases, the available final state phase space volume becomes larger. It becomes therefore more likely that the incoming quark emits a gluon into the final state, losing a fraction $1 - z$

27
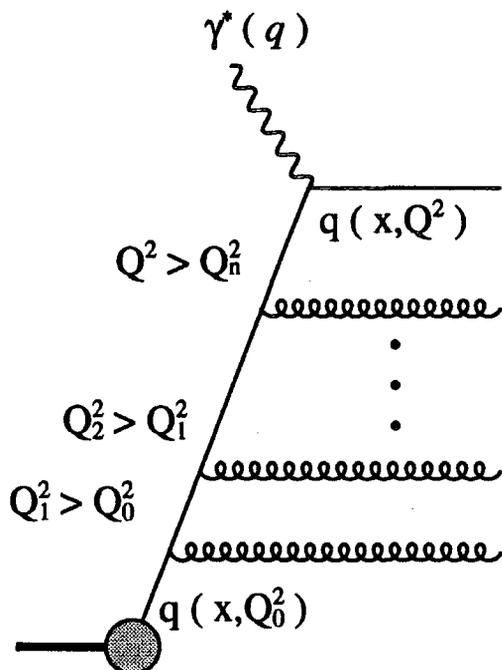
Figure 3.2: Interpretation of the DGLAP evolution equation: ladder of gluon emissions.

of its initial longitudinal momentum before interacting with the photon. The probability for such a single *parton splitting* grows like

$$\frac{\alpha_s}{2\pi}\, P_{qq}^{(0)}(z) \ln \frac{Q_j^2}{Q_i^2}$$

if Q^2 is increased from Q_i^2 to Q_j^2. The function

$$\frac{\alpha_s}{2\pi}\, P_{qq}^{(0)}(z)$$

quantifying this probability is called *splitting function*, it is related to the $q \to q$ splitting process illustrated in Fig. 3.3.

If we consider a given initial distribution $q(x, Q_0^2)$ with $Q_0^2 \ll Q^2$, a large number of these splittings can occur, resulting in a *ladder* of gluon emissions (Fig. 3.2). A ladder with n rungs contributes to the structure function with terms of $\mathcal{O}(\alpha_s^n \ln^n Q^2)$ and less

singular terms, as the phase space for these contributions takes the form

$$\int^{Q^2} \frac{dk_{Tn}}{k_{Tn}^2} \cdots \int^{k_{T3}} \frac{dk_{T2}}{k_{T2}^2} \int^{k_{T2}} \frac{dk_{T1}}{k_{T1}^2} \sim \frac{\ln^n Q^2}{n!}.$$

The solution of (3.4) resums only the most singular contributions from ladders with any n. The resulting distribution $q(x, Q^2)$ therefore contains all QCD corrections which are proportional to $\mathcal{O}(\alpha_s^n \ln^n Q^2)$.

The first subleading corrections to the above formalism are of the order $\mathcal{O}(\alpha_s^n \ln^{n-1} Q^2)$. These can be resummed into $q(x, Q^2)$ by solving (3.4), if the next-to-leading order corrections to the splitting function are included:

$$\frac{\alpha_s}{2\pi} P_{qq}^{(0)}(z) \quad \rightarrow \quad \frac{\alpha_s}{2\pi} P_{qq}^{(0)}(z) + \left(\frac{\alpha_s}{2\pi}\right)^2 P_{qq}^{(1)}(z).$$

It has to be kept in mind that the resummation at next-to-leading order only contains terms accompanied by $\ln Q^2$, i.e. $n \geq 2$. The $n = 1$ term is in fact the $c_{2,q}(z)$ from (3.2). A description of $F_2(x, Q^2)$ at next-to-leading order in this formalism is therefore only consistent if the splitting functions are truncated to $\mathcal{O}(\alpha_s^2)$ and the coefficient functions are truncated to $\mathcal{O}(\alpha_s)$.

The most important consequence of these QCD corrections to the naïve parton model is the violation of the scaling behaviour of parton distributions. These *scaling violations* – the explicit dependence of the parton distributions on Q^2 – can be understood as due to multiple emission of collinear particles off the incoming parton and yield correction terms of $\mathcal{O}(\alpha_s \ln Q^2)$. The experimental observation [32] of these scaling violations was one of the first confirmations of the theory of QCD.

3.2 Evolution equations

The evolution equation (3.4) is strictly speaking only valid for non-singlet combinations of quark distributions, such as the valence quark distributions $q_v = q - \bar{q}$. A more rigorous treatment must include the possibility of any parton species (quark, antiquark or gluon) splitting into any other parton species. At $\mathcal{O}(\alpha_s)$, only the splittings denoted in Fig. 3.3

29
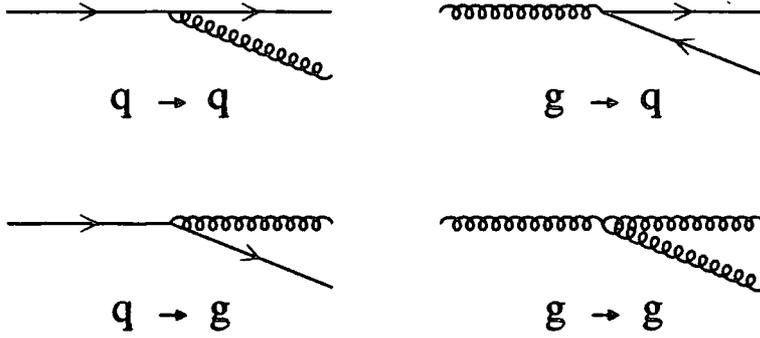
Figure 3.3: Parton splitting processes at leading order. Splitting processes involving antiquarks can be trivially obtained from the above and are not shown.
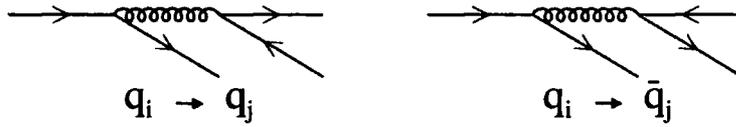
Figure 3.4: Parton splitting processes only occuring in higher orders, i and j can denote identical or different flavours.

are possible. The splitting of a quark of certain flavour into a quark of different flavour or into an antiquark are only possible at $\mathcal{O}(\alpha_s^2)$ (Fig. 3.4).

Including all possible splitting processes, the evolution equation (3.4) generalizes into a set of coupled evolution equations:

$$
Q^2 \frac{\partial}{\partial Q^2}
\begin{pmatrix}
q_1(x, Q^2) \\
\vdots \\
\bar{q}_n(x, Q^2) \\
G(x, Q^2)
\end{pmatrix}
= \int_x^1 \frac{dz}{z}
\begin{pmatrix}
P_{q_1 q_1}(z) & \cdots & P_{q_1 \bar{q}_n}(z) & P_{q_1 g}(z) \\
\vdots & \ddots & \vdots & \vdots \\
P_{\bar{q}_n q_1}(z) & \cdots & P_{\bar{q}_n \bar{q}_n}(z) & P_{\bar{q}_n g}(z) \\
P_{g q_1}(z) & \cdots & P_{g \bar{q}_n}(z) & P_{gg}(z)
\end{pmatrix}
\begin{pmatrix}
q_1(x/z, Q^2) \\
\vdots \\
\bar{q}_n(x/z, Q^2) \\
G(x/z, Q^2)
\end{pmatrix},
$$

(3.5)

where

$$
P_{ji}(z) = \frac{\alpha_s}{2\pi} P_{ji}^{(0)}(z) + \left(\frac{\alpha_s}{2\pi} \right)^2 P_{ji}^{(1)}(z) + \dots
$$

and n denotes the number of quark flavours active in the evolution (see the discussion in

30

Appendix B.3.1).

The above set of $2n + 1$ coupled equations can be simplified to $2n - 1$ uncoupled and 2 coupled equations by introducing the following combinations of quark distributions:

$$
\begin{aligned}
Q_{1,+}(x,Q^2) &= q_1(x,Q^2) + \bar{q}_1(x,Q^2) - q_2(x,Q^2) - \bar{q}_2(x,Q^2), \\
&\vdots \qquad \vdots \\
Q_{n-1,+}(x,Q^2) &= \sum_{i=1}^{n-1} \left(q_i(x,Q^2) + \bar{q}_i(x,Q^2) \right) - \frac{1}{n-1} \left(q_n(x,Q^2) + \bar{q}_n(x,Q^2) \right), \\
Q_{1,-}(x,Q^2) &= q_1(x,Q^2) - \bar{q}_1(x,Q^2), \\
&\vdots \qquad \vdots \\
Q_{n,-}(x,Q^2) &= q_n(x,Q^2) - \bar{q}_n(x,Q^2), \\
\Sigma(x,Q^2) &= \sum_{i=1}^{n} \left(q_i(x,Q^2) + \bar{q}_i(x,Q^2) \right).
\end{aligned}
\tag{3.6}
$$

The $Q_{i,+}(x,Q^2)$ are called *flavour non-singlet* distributions and $Q_{j,-}(x,Q^2)$ are called *valence non-singlet* distributions, alternatively denoted by the name of the corresponding quark species: $u_v(x,Q^2) \equiv u(x,Q^2) - \bar{u}(x,Q^2), \ldots$. The sum of all quark distributions $\Sigma(x,Q^2)$ is called the *quark singlet* distribution.

In terms of these combinations, one can write the DGLAP equations [31] as

$$
Q^2 \frac{\partial}{\partial Q^2} Q_{i,+}(x,Q^2) = \int_x^1 \frac{dz}{z} P_{qq,+}(z) Q_{i,+}(x/z,Q^2) \qquad (i = 1 \ldots n-1),
$$

$$
Q^2 \frac{\partial}{\partial Q^2} Q_{j,-}(x,Q^2) = \int_x^1 \frac{dz}{z} P_{qq,-}(z) Q_{j,-}(x/z,Q^2) \qquad (j = 1 \ldots n),
$$

$$
Q^2 \frac{\partial}{\partial Q^2} \begin{pmatrix} \Sigma(x,Q^2) \\ G(x,Q^2) \end{pmatrix} = \int_x^1 \frac{dz}{z} \begin{pmatrix} P_{qq,S}(z) & P_{qg}(z) \\ P_{gq}(z) & P_{gg}(z) \end{pmatrix} \begin{pmatrix} \Sigma(x/z,Q^2) \\ G(x/z,Q^2) \end{pmatrix}.
\tag{3.7}
$$

The leading order splitting functions $P_{ji}^{(0)}(z)$ have been calculated in [31], the next-to-leading order corrections $P_{ji}^{(1)}(z)$ were derived in [33]. Their explicit form is stated in Appendix B.2. With given initial distributions for all quark flavours and the gluon, these equations can be solved as described in Appendix B.3.

31

The quantitative effects of QCD evolution on the unpolarized parton can be understood from simple dynamical arguments: With increasing Q^2, all distributions decrease in the large-x region and increase in the small-x region, as more and more partons with small momenta are radiated off. This rise is particularly emphasized in the sea quark and gluon distributions at small x. The small-x rise of the gluon distribution is due to the generation of a large number of soft gluons in the evolution process. A fraction of these gluons splits into quark–antiquark pairs, causing the rise in the sea quark distribution.

3.2.1 Extension to polarized deep inelastic scattering

The treatment of the polarized structure function $g_1(x, Q^2)$ in perturbative QCD is very similar to the treatment of the unpolarized structure function $F_2(x, Q^2)$. Like in the unpolarized case, we can denote the contribution of a parton i to $g_1(x, Q^2)$ by

$$\hat{g}_{1,i}(z, Q^2)(\gamma^* + i \to X),$$

defined by an appropriate projection onto the hadronic tensor [34]. The structure function then reads

$$2g_1(x, Q^2) = \sum_i \int_0^1 d\xi \, dz \, \delta(x - z\xi) \, \Delta f_i(\xi) \, \hat{g}_{1,i}(z, Q^2) \,,$$

where $\Delta f_i(\xi) = \Delta q(x), \Delta \bar{q}(x), \Delta G(x)$ is a bare polarized parton distribution. The contributions from the quark initiated subprocesses in Fig. 3.1 take the form [34]

$$\hat{g}_{1,q}^{(0)}(z, Q^2) = e_q^2 \delta(1 - z) \,,$$

$$\hat{g}_{1,q}^{(1)}(z, Q^2) = e_q^2 \frac{\alpha_s}{2\pi} \frac{1}{\Gamma(1 + \epsilon)} \left(\frac{4\pi Q^2}{\mu^2}\right)^\epsilon \left(\frac{1}{\epsilon} \Delta P_{qq}^{(0)}(z) + \Delta c_q^{(1)}(z) + \mathcal{O}(\epsilon)\right).$$

Carrying out the mass factorization procedure on the above expressions yields a renormalized quark distribution $\Delta q(\xi, \mu_F^2)$ and a coefficient function $\Delta C_q(z, Q^2, \mu_F^2)$. The polarized quark distribution obeys the DGLAP evolution equation (3.4) with a polarized splitting function $\Delta P_{qq}(z)$.

Like in the unpolarized case, a complete treatment has to incorporate all splitting processes displayed in Fig. 3.3 and Fig. 3.4, resulting in coupled evolution equations

32

(3.7) for the polarized quark, antiquark and gluon distributions $\Delta q(x, Q^2)$, $\Delta \bar{q}(x, Q^2)$, $\Delta G(x, Q^2)$. These equations are controlled by polarized splitting functions $\Delta P_{ij}(z)$, which have been derived in [31] at leading order and in [35] at next-to-leading order in QCD. Explicit expressions for the polarized splitting functions are summarized in Appendix B.2. The qualitative aspects of the polarized evolution will be studied in detail in sections 4.3 and 4.4.

3.3 Structure functions in the QCD corrected parton model

The previous sections have demonstrated that the description of deep inelastic scattering in QCD is most convenient in the variables x and Q^2. In these variables, the DIS cross sections (1.11), (1.12) and (1.13) read

$$\frac{d\bar{\sigma}}{dx\,dQ^2} = \frac{4\pi\alpha^2}{xQ^4}\left[\left(1 - y - \frac{\gamma^2 y^2}{4}\right) F_2(x, Q^2) + xy^2 F_1(x, Q^2)\right] , \qquad (3.8)$$

$$\frac{d\Delta\sigma_L}{dx\,dQ^2} = \frac{16\pi\alpha^2 y}{Q^4}\left[\left(1 - \frac{y}{2} - \frac{\gamma^2 y^2}{4}\right) g_1(x, Q^2) - \frac{\gamma^2 y}{2} g_2(x, Q^2)\right] , \qquad (3.9)$$

$$\frac{d\Delta\sigma_T}{dx\,dQ^2\,d\phi} = -\cos\phi \frac{8\alpha^2 y\gamma}{Q^4}\sqrt{1 - y - \frac{y^2\gamma^2}{4}}\left[\frac{y}{2} g_1(x, Q^2) + g_2(x, Q^2)\right] , \qquad (3.10)$$

where $\gamma = 2Mx/\sqrt{Q^2}$ is a target mass correction factor.

Deep inelastic scattering can be viewed as the absorption of a virtual photon by the proton. The DIS cross section can then be decomposed into absorption cross sections for the longitudinal and transverse components of the virtual photon. The transverse cross section is proportional to F_1, the longitudinal cross section to $F_L = (1 + \gamma^2)F_2 - 2xF_1$. The ratio of longitudinal and transverse absorption cross sections is commonly abbreviated by $R = F_L/(2xF_1)$. Replacing

$$F_1(x, Q^2) = \frac{1}{2x}\left[(1 + \gamma^2)F_2(x, Q^2) - F_L(x, Q^2)\right]$$

$$= \frac{1}{2x\,(1 + R(x, Q^2))}(1 + \gamma^2)F_2(x, Q^2), \qquad (3.11)$$

33

the unpolarized cross sections expressed in terms of F_2 and F_L (or R) read:

$$\frac{d\bar{\sigma}}{dx\,dQ^2} = \frac{4\pi\alpha^2}{xQ^4}\left[\left(1 - y + \frac{y^2(2+\gamma^2)}{4}\right)F_2(x,Q^2) + \frac{y^2}{2}F_L(x,Q^2)\right],$$

$$= \frac{4\pi\alpha^2}{xQ^4}\left[1 - y + \frac{y^2}{2(1+R(x,Q^2))} + \frac{y^2\gamma^2(1-R(x,Q^2))}{4(1+R(x,Q^2))}\right]F_2(x,Q^2) \quad (3.12)$$

In practice, the target mass correction factor γ is small, terms proportional to it can be neglected.

The structure functions $F_2(x,Q^2)$, $F_L(x,Q^2)$ and $g_1(x,Q^2)$ are expressed in terms of quark and gluon distributions by convoluting these with the appropriate coefficient functions:

$$F_{(2,L)}(x,Q^2) = x\int_x^1 \frac{dz}{z}\sum_q e_q^2\left\{C_{(2,L),q}\left(z,\frac{Q^2}{\mu_F^2}\right)\left[q\left(\frac{x}{z},\mu_F^2\right) + \bar{q}\left(\frac{x}{z},\mu_F^2\right)\right]\right.$$

$$\left. + \frac{1}{n_f}C_{(2,L),g}\left(z,\frac{Q^2}{\mu_F^2}\right)G\left(\frac{x}{z},\mu_F^2\right)\right\}, \quad (3.13)$$

$$g_1(x,Q^2) = \frac{1}{2}\int_x^1 \frac{dz}{z}\sum_q e_q^2\left\{\Delta C_q\left(z,\frac{Q^2}{\mu_F^2}\right)\left[\Delta q\left(\frac{x}{z},\mu_F^2\right) + \Delta\bar{q}\left(\frac{x}{z},\mu_F^2\right)\right]\right.$$

$$\left. + \frac{1}{n_f}\Delta C_g\left(z,\frac{Q^2}{\mu_F^2}\right)\Delta G\left(\frac{x}{z},\mu_F^2\right)\right\}, \quad (3.14)$$

where the coefficient functions read in the $\overline{\text{MS}}$ scheme [36, 37, 38][2]

$$C_{2,q}\left(z,\frac{Q^2}{\mu_F^2}\right) = \delta(1-z) + \frac{\alpha_s}{2\pi}C_F\left\{\left[\left(\frac{2}{1-z}\right)_+ - 1 - z + \frac{3}{2}\delta(1-z)\right]\ln\frac{Q^2}{\mu_F^2}\right.$$

$$+ 2\left(\frac{\ln(1-z)}{1-z}\right)_+ - \frac{3}{2}\left(\frac{1}{1-z}\right)_+ - (1+z)\ln(1-z) - \frac{1+z^2}{1-z}\ln z$$

$$\left. + 3 + 2z - \left(\frac{9}{2} + 2\zeta_2\right)\delta(1-z)\right\},$$

$$C_{2,g}\left(z,\frac{Q^2}{\mu_F^2}\right) = \frac{\alpha_s}{2\pi}T_f\left[2(1-2z+2z^2)\ln\frac{(1-z)Q^2}{z\mu_F^2} - 16z^2 + 16z - 2\right]; \quad (3.15)$$

---

[2]The coefficient functions as given here are truncated up to $\mathcal{O}(\alpha_s)$, which is sufficient for a treatment of the structure functions at next-to-leading order. The $\mathcal{O}(\alpha_s^2)$ corrections [30, 34] and parts of the $\mathcal{O}(\alpha_s^3)$ corrections [39] are known as well.

$$C_{L,q}\left(z,\frac{Q^2}{\mu_F^2}\right) = \frac{\alpha_s}{2\pi}C_F\,2z,$$

$$C_{L,g}\left(z,\frac{Q^2}{\mu_F^2}\right) = \frac{\alpha_s}{2\pi}T_f\,8z(1-z);$$

(3.16)

$$\Delta C_q\left(z,\frac{Q^2}{\mu_F^2}\right) = \delta(1-z) + \frac{\alpha_s}{2\pi}C_F\left\{\left[\left(\frac{2}{1-z}\right)_+ - 1 - z + \frac{3}{2}\delta(1-z)\right]\ln\frac{Q^2}{\mu_F^2}\right.$$

$$+2\left(\frac{\ln(1-z)}{1-z}\right)_+ - \frac{3}{2}\left(\frac{1}{1-z}\right)_+ - (1+z)\ln(1-z) - \frac{1+z^2}{1-z}\ln z$$

$$\left. +2 + z - \left(\frac{9}{2} + 2\zeta_2\right)\delta(1-z)\right\},$$

$$\Delta C_g\left(z,\frac{Q^2}{\mu_F^2}\right) = \frac{\alpha_s}{2\pi}T_f\left[2(2z-1)\ln\frac{(1-z)Q^2}{z\mu_F^2} + 6 - 8z\right].$$

(3.17)

All information on perturbative QCD corrections to the naïve quark parton model is contained in these coefficient functions and in the factorization scale dependence of the parton distributions, determined by the splitting functions. Perturbative QCD is however only able to predict the *change* of the parton distributions with increasing scale, not their explicit form at a particular scale Q^2.

3.4 Parton distributions

The dynamics of quarks and gluons at scales corresponding to the mass scale of the proton cannot be described with perturbative methods anymore, and non-perturbative techniques are not yet sufficiently developed to give reliable predictions. The distributions of partons in the proton, reflecting these bound state dynamics, can hence not be computed with present methods. In recent times, some progress towards a calculation of these distributions has been made. Using a formulation of QCD on a discrete space-time lattice, the authors of [40] were able to estimate some moments (cf. Section 4.2) of the polarized and unpolarized quark distributions.

Instead of attempting to compute these distributions from first principles, one can parametrize the present lack of understanding of QCD at low scales in the form of initial
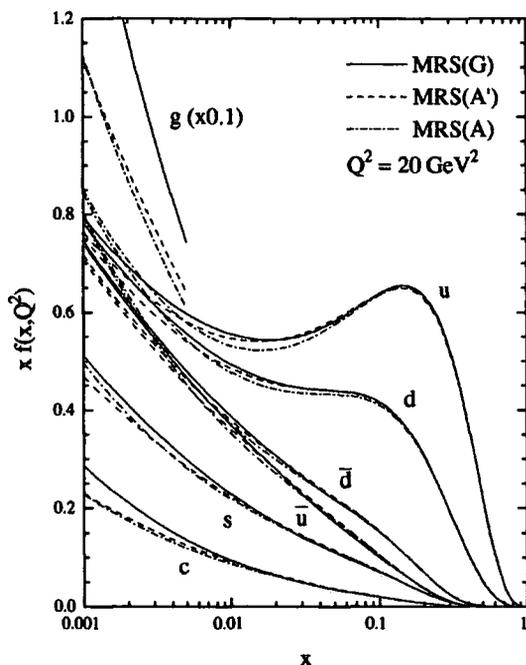
Figure 3.5: Unpolarized parton distributions obtained from a global fit to experimental data [41]. The sets (G) and (A') correspond to different estimates for the behaviour of the gluon distribution at small x, set (A) is from a previous analysis [42] and shown for reference. Figure taken from [41].

distributions at some scale Q_0^2. In the case of the unpolarized distributions, these are characterized by ~ 20 parameters. Using the distribution at Q_0^2 as input to the evolution equations, the parameters are then fitted to experimental data on structure functions and related quantities at higher values of Q^2.

Global fits of unpolarized parton distributions are available from two groups [41, 43], which differ slightly in their data selection criteria and in the functional form chosen to parametrize their initial distributions at $Q_0^2 \sim (1 \ldots 4)\, m_p^2$. A somewhat different approach ('dynamical parton model') is presented in [44]: the distributions are fitted at a scale far below $(Q_0^2 \sim 0.3\, m_p^2)$ the proton mass scale, requiring both quark and gluon distributions to be valence-like. The singular behaviour of the sea quark and gluon distributions for

$x \rightarrow 0$ is then generated purely by perturbative evolution. All three sets [41, 43, 44] differ only within a few percent, which reflects the high precision of the experimental data entering into the fit. We will demonstrate in Chapter 8 how these distributions can be used to make precise predictions for observables in proton–antiproton collisions. As an example, Fig. 3.5 shows the parton distributions obtained in [41].

A determination of the polarized distributions $\Delta q(x, Q^2)$, $\Delta \bar{q}(x, Q^2)$ and $\Delta G(x, Q^2)$ has to rely on fewer, less accurate data. A global fit of these distributions has therefore to be supplemented with additional constraints on the distributions. We will motivate these constraints in the following chapter and apply them in a global fit of polarized parton distributions in Chapter 5.

Chapter 4

The spin structure of the proton

The treatment of the proton structure in the previous chapters always included the unpolarized as well as the polarized structure functions and parton distributions. In this and the following two chapters, we will focus on the polarized proton structure. This chapter introduces some of the specific features of the spin structure of the proton, while the following two will focus on the determination of polarized parton distributions from present and future experiments.

The polarized structure function $g_1(x, Q^2)$ is measured far less accurately than the unpolarized structure function $F_2(x, Q^2)$. We summarize the experimental results available at present in Section 4.1. An important aspect of the spin structure of the proton are the Bjorken and Ellis–Jaffe sum rules. Their origin and implications will be discussed in Section 4.2. Some basic properties of the polarized parton distributions will be summarized in Section 4.3. Finally, we will discuss the behaviour of polarized parton distributions in the limit $x \to 0$ in Section 4.4.

4.1 Experimental results

Experimental measurements of polarized deep inelastic structure functions require both the incoming lepton beam and the proton target to be polarized. While lepton beams

are often polarized naturally, proton polarization inside the target can only be obtained with dedicated target setups. Polarized targets are usually at least an order of magnitude smaller in size and density than unpolarized targets. Measurements of the polarized DIS cross section are therefore far less accurate than their unpolarized counterparts. The accuracy of polarized structure function measurements can be increased, if the polarized cross section is evaluated by multiplying the experimental asymmetries (1.14) and (1.15) with the known unpolarized cross section.

If the asymmetry measurement is carried out at sufficiently large Q^2, target mass corrections can be largely neglected. The asymmetries are then directly related to the ratios of structure functions. Keeping only the dominant target mass terms, (1.14) and (1.15) read:

$$A_{\parallel}(x, Q^2) = D \left(A_1(x, Q^2) + \gamma \frac{2 - 2y}{2 - y} A_2(x, Q^2) \right),$$

$$A_{\perp} = D \frac{2\sqrt{1 - y}}{2 - y} \left(A_2(x, Q^2) - \gamma \frac{2 - y}{2} A_1(x, Q^2) \right),$$

where

$$A_1(x, Q^2) \equiv \frac{g_1(x, Q^2) - \gamma^2 g_2(x, Q^2)}{F_1(x, Q^2)}, \tag{4.1}$$

$$A_2(x, Q^2) \equiv \frac{\gamma \left(g_1(x, Q^2) + g_2(x, Q^2) \right)}{F_1(x, Q^2)}, \tag{4.2}$$

$$D \equiv \frac{y(2 - y)}{y^2 + 2(1 - y)(1 + R(x, Q^2))}. \tag{4.3}$$

D is the fraction of lepton polarization transferred to the virtual photon. If target mass corrections can be neglected completely, one obtains a simple form for the longitudinal asymmetry

$$A_{\parallel}(x, Q^2) \simeq DA_1(x, Q^2) \quad \text{with} \quad A_1(x, Q^2) \simeq \frac{g_1(x, Q^2)}{F_1(x, Q^2)}, \tag{4.4}$$

which is normally used to extract the structure function $g_1(x, Q^2)$ from experimental data.

Experiment	Beam	Beam energy	Target	Q^2 (GeV^2)	x	Results
E80/E130 (SLAC)	e	20 GeV	p	3.5–10	0.180–0.7	[13]
EMC (SLAC)	μ	280 GeV	p	1.5–70	0.010–0.7	[45]
SMC (SLAC)	μ	100–200 GeV	p, d	1–60	0.003–0.7	[46, 47, 48]
E142 (SLAC)	e	30 GeV	n	1–10	0.030–0.6	[49]
E143 (SLAC)	e	30 GeV	p, d	1–30	0.029–0.8	[50, 51]

Table 4.1: Fixed target experiments on polarized deep inelastic scattering.

The measurements of the structure function $g_1(x, Q^2)$ off proton, neutron and deuteron targets which have been carried out so far are summarized in Table 4.1. These experimental results will be used in Chapter 5 to fit the polarized parton distributions in the nucleon. Another experiment, HERMES (DESY) has recently presented [52] its first, preliminary results on the neutron spin structure function $g_1^n(x, Q^2)$. Apart from the above $g_1(x, Q^2)$ measurements, SMC and E143 have performed a measurement of the transverse asymmetry [14, 53], which has been used for a first determination of $g_2(x, Q^2)$. Furthermore, E143 has studied the asymmetry $A_1(x, Q^2)$ in the region $Q^2 < 1$ GeV^2 [54].

So far, the polarized proton structure has only been probed in deep inelastic scattering. Various future experiments intend to study other hard processes involving polarized protons. An overview of these experiments will be given in Chapter 6.

4.2   Sum rules

Neither polarized nor unpolarized parton distributions can be calculated from first principles with present techniques. Certain aspects of the distributions can however be inferred from the properties of the proton as a whole, such as its quantum numbers and its properties in the hyperon multiplet (Fig. 2.1.b).

These macroscopic properties can be related to integrals of the structure functions or

the parton distributions over the scaling variable x. These integrals, weighted by a certain power of x are called *moments*, the n-th moment of a function $f(x)$ is defined as

$$f_n \equiv \int_0^1 x^{n-1} f(x) \mathrm{d}x.$$

A simple example of the physical content of certain moments are the second moments of the unpolarized quark and gluon distributions. To conserve energy and momentum of the proton, these should add up to unity

$$\int_0^1 x \left(\Sigma(x, Q^2) + G(x, Q^2) \right) \mathrm{d}x = 1, \tag{4.5}$$

which has to be imposed at Q_0^2 and is preserved under perturbative evolution. Unfortunately, no similar relation can be constructed for the polarized distributions, as the proton spin receives contributions from polarization and orbital angular momentum of the partons

$$\frac{1}{2} = L_{z,\Sigma}(Q^2) + L_{z,G}(Q^2) + \int_0^1 \left(\frac{1}{2} \Delta\Sigma(x, Q^2) + \Delta G(x, Q^2) \right) \mathrm{d}x. \tag{4.6}$$

No experimental or theoretical information on $L_{z,\Sigma}(Q^2)$ and $L_{z,G}(Q^2)$ is available at present, this equation can consequently not help to constrain the first moments of the polarized quark and gluon distributions.

Information on the first moments of the polarized quark distributions can be gained from two *sum rules* [55, 56, 57] relating the first moment of the polarized structure function

$$\Gamma_1^{p,n}(Q^2) \equiv \int_0^1 g_1^{p,n}(x, Q^2) \mathrm{d}x \tag{4.7}$$

to the weak decay constants of hadrons in the $1/2^+$ multiplet (Fig. 2.1). Due to the chiral coupling of the W-boson, these weak decays receive contributions from hadronic vector and axial vector currents in the $SU(3)_f$ octet. All axial vector currents within the octet can be expressed as combinations of the two diagonal octet currents a_3 and a_8, which are measured to be [58, 59]

$$a_3 = 1.2573 \pm 0.0028,$$

$$a_8 = 0.579 \pm 0.011.$$

The precision on a_3 is naturally higher, as it can be determined from the neutron β-decay only.

The first moment of $g_1(x, Q^2)$ probes the axial vector current between two *identical* nucleon states, which contains contributions from octet *and* singlet currents

$$\Gamma_1^{p,n} = \pm \frac{1}{12} a_3 + \frac{1}{36} a_8 + \frac{1}{9} a_0 . \tag{4.8}$$

The quark model interpretation of the $\mathrm{SU}(3)_f$ octet relates these currents to the first moments of the polarized parton distributions

$$
\begin{aligned}
a_3 &= \int_0^1 \left(\Delta u(x) + \Delta \bar{u}(x) - \Delta d(x) - \Delta \bar{d}(x) \right) \, \mathrm{d}x , \\
a_8 &= \int_0^1 \left(\Delta u(x) + \Delta \bar{u}(x) + \Delta d(x) + \Delta \bar{d}(x) - 2\Delta s(x) - 2\Delta \bar{s}(x) \right) \, \mathrm{d}x , \\
a_0 &= \int_0^1 \left(\Delta u(x) + \Delta \bar{u}(x) + \Delta d(x) + \Delta \bar{d}(x) + \Delta s(x) + \Delta \bar{s}(x) \right) \, \mathrm{d}x = \int_0^1 \Delta \Sigma(x) \mathrm{d}x .
\end{aligned}
\tag{4.9}
$$

According to (3.14), two different QCD corrections apply to (4.8). The first moment of the coefficient function is a power series in α_s and the first moments of the parton distributions can have a non-zero Q^2-dependence due to scaling violations. Due to the vanishing first moment of $\Delta P_{qq,+}$ (B.33), the flavour non-singlet combinations a_3 and a_8 are unaffected by these scaling violations. On the contrary, a_0 is only scale independent at leading order, the next-to-leading order splitting processes (Fig. 3.4) induce a non-vanishing scale dependence

$$a_0(Q^2) = \left(1 - \frac{16 n_f}{2\beta_0} \frac{\alpha_s(Q_0^2) - \alpha_s(Q^2)}{4\pi} \right) a_0(Q_0^2). \tag{4.10}$$

Taking the difference between the proton and neutron structure functions, one obtains the *Bjorken sum rule* [55]

$$\Gamma_1^p(Q^2) - \Gamma_1^n(Q^2) = \left[1 - \frac{\alpha_s}{\pi} + \mathcal{O}(\alpha_s^2) \right] \frac{1}{6} a_3, \tag{4.11}$$

where only the first term of the QCD corrections has been included; the corrections are known up to $\mathcal{O}(\alpha_s^3)$ [60]. This sum rule is a fundamental prediction from the $\mathrm{SU}(2)_T$

isospin symmetry between proton and neutron, and it is confirmed by the experimental measurements listed in Table 4.1.

The first moments of the proton and neutron spin structure function are usually called the Ellis–Jaffe sum rule. Including QCD corrections, [61] they read

$$
\begin{aligned}
\Gamma_1^{p,n}(Q^2) \;=\; & \left[1 - \frac{\alpha_s}{\pi} + \mathcal{O}(\alpha_s^2)\right]\left(\pm\frac{1}{12}a_3 + \frac{1}{36}a_8\right) \\
& + \left[1 - \frac{\alpha_s}{\pi} + \mathcal{O}(\alpha_s^2)\right]\frac{1}{9}a_0(Q^2).
\end{aligned}
\tag{4.12}
$$

They can only be predicted separately if a certain model assumption for the a priori unknown singlet current $a_0(Q^2)$ is made. Two such estimates *in the framework of the naïve quark parton model* (cf. Section 2.4) can be found in the literature. Attributing the whole proton spin to quark polarization, Gourdin [56] finds $a_0 = 1$, while Ellis and Jaffe [57] obtain $a_0 = a_8 \approx 0.579$, assuming no contribution to the proton spin from the sea of strange quarks. Both these estimates are not stable under QCD corrections as they identify a non-conserved quantity with a constant.

All experiments listed in Table 4.1 have measured the Ellis–Jaffe sum rule. Although the errors on the results are still sizable and the extrapolation of the measurement into the region of small values of x is not unambiguous (cf. Section 4.4), these measurements seem to indicate that $a_0 \approx 0.15 - 0.3$ in the range $3\ \mathrm{GeV}^2 < Q^2 < 12\ \mathrm{GeV}^2$. Figure 4.1 displays the values of $a_0(Q^2)$ as extracted from the experimental results using (4.12), together with the next-to-leading order QCD prediction (4.10) normalized to $a_0(Q^2 = 4\ \mathrm{GeV}^2) = 0.219$, the global average obtained from a fit described in the following chapter.

The first precision measurement of the Ellis–Jaffe sum rule [45] initiated a long discussion on the origin of this apparent deviation from the naïve quark parton model. In this model, the discrepancy between the expectation of Ellis and Jaffe and the experimental results could only be explained by a negative contribution from the strange quark sea to the proton spin. There is however a certain ambiguity in the decomposition of the singlet axial vector current a_0, as soon as QCD corrections to the naïve quark parton model are taken into account. Only a_3 and a_8 can unambiguously be identified with the flavour

43
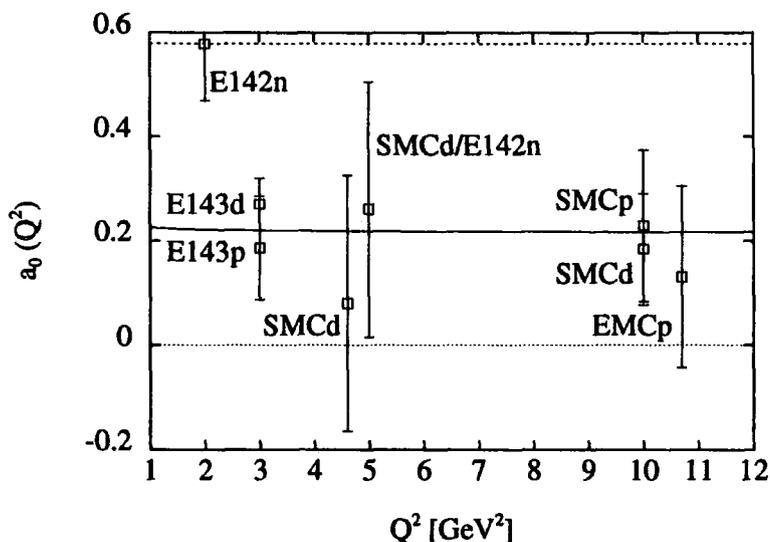
Figure 4.1: The singlet axial vector current determined from measurements of the Ellis–Jaffe sum rule. The solid line is the QCD prediction normalized to a fit at $Q_0^2 = 4\ \mathrm{GeV^2}$, the dashed line shows the Ellis–Jaffe prediction in the quark parton model.

non-singlet combinations in (4.9), the decomposition of a_0 into contributions from quark singlet and gluon distribution depends on the renormalization scheme used.

In the $\overline{\mathrm{MS}}$-scheme, this current is identified with the first moment of the polarized quark singlet only,

$$a_0^{\overline{\mathrm{MS}}}(Q^2) = \eta_\Sigma^{\overline{\mathrm{MS}}}(Q^2)\,, \qquad (4.13)$$

where we have introduced the abbreviations

$$\eta_\Sigma(Q^2) \equiv \int_0^1 \Delta\Sigma(x, Q^2)\mathrm{d}x\,, \qquad \eta_G(Q^2) \equiv \int_0^1 \Delta G(x, Q^2)\mathrm{d}x\,.$$

In this scheme, $\eta_\Sigma(Q^2)$ varies with the scale Q^2, as the first moment of $P_{qq,S}^{(1)}(z)$ is non-zero. The scale dependence of $\eta_\Sigma(Q^2)$ in the $\overline{\mathrm{MS}}$-scheme can be trivially inferred from (4.10), the violation of the Ellis–Jaffe sum rule implies a negative polarization of the sea of strange quarks.

44

Alternatively, one can construct another scheme [62], usually called the Adler–Bardeen (AB) scheme [63], in which $\eta_\Sigma(Q^2)$ becomes independent of Q^2. The appropriate scheme transformation introduces a contribution of the first moment of the polarized gluon distribution to the Ellis–Jaffe sum rule,

$$a_0^{\text{AB}}(Q^2) = \eta_\Sigma^{\text{AB}} - n_f \frac{\alpha_s}{2\pi} \eta_G(Q^2) \,. \qquad (4.14)$$

If viewed in this scheme, the violation of the Ellis–Jaffe sum rule *can* be attributed entirely to the effects of gluon polarization, a polarization of the strange quark sea is not necessary. It is however likely that both gluons and strange quarks contribute to give the overall observed effect.

The transformation between $\overline{\text{MS}}$ and AB scheme only redefines the polarized sea quark distributions while leaving the gluon distribution unchanged [34]. Both schemes are equivalent descriptions of the physical observable $g_1(x, Q^2)$, if implemented consistently at next-to-leading order. Such a consistent treatment at NLO was not possible until very recently, as the complete NLO corrections to the polarized splitting functions $\Delta P_{ji}^{(1)}$ had not been known [35].

Earlier studies of the spin structure of the proton often introduced an *ad-hoc* gluonic contribution to the polarized structure function at leading order (see for example the discussion in [64, 65]) in order to obtain at least an order-of-magnitude estimate of the polarized gluon distribution. This approach faces conceptual problems if the resulting distributions are applied to other quark-initiated processes, such as the production of Drell–Yan-pairs.

The information gained from the Bjorken and Ellis–Jaffe sum rules can be incorporated into a consistent LO or NLO($\overline{\text{MS}}$) determination of the polarized parton distributions by using a_3 and a_8 from the hyperon decay constants and a_0 from the Ellis–Jaffe sum rule measurements to fix the first moments of the polarized u, d and s quark distributions. If further assumptions on the flavour structure of the polarization of the light quark sea are made, this information can be used for a separate determination of the first moments of the polarized valence and sea quark distributions. We will apply this in Chapter 5.

45

4.3 Qualitative features of polarized parton densities

This section collects information on the behaviour of the polarized parton distributions that can be obtained without a fit to experimental data. The asymptotic behaviour of the initial distributions for large and small values of x approaches simple power-like forms, which will be discussed in the following. Furthermore, we will elaborate the qualitative effects of the perturbative evolution on these distributions.

4.3.1 Initial distributions at large and small x

If a valence quark carries a large fraction of the proton's momentum, i.e. $x \to 1$, it should also be expected to carry a significant fraction of the helicity of the proton. The distribution of quarks with spin anti-aligned to the proton's spin is therefore suppressed at large x, the behaviour of polarized and unpolarized distributions becomes qualitatively identical in this limit. With the unpolarized valence quark distributions falling off like $(1 - x)^\beta$ ($\beta \approx 3 \dots 5$) for $x \to 1$, this property can be implemented into the polarized distributions by imposing the same value for the large-x parameter β. A formal proof of this behaviour can be obtained from quark counting rules and is given in [66].

The behaviour of the initial distributions in the limit $x \to 0$ is by far less well understood. In general, one should expect each of them to be proportional to x^α, although neither magnitude nor sign of α are predictable. Even the small-x limit of the unpolarized parton distribution at typical starting scales of a few GeV is not yet understood at present [67], in particular for the gluon and sea quark distributions.

4.3.2 Effects of the DGLAP evolution

Several qualitative features of the polarized parton densities can already be determined by inserting simple test distributions $t(x)$ in the right-hand side of Eq. (3.7). For a qualitative understanding it is sufficient to truncate the splitting functions only to $\mathcal{O}(\alpha_s)$ and to fix

the number of flavours to $n_f = 3$.

The resulting elements of the evolution matrix

$$A_{ji} \equiv \int_x^1 \frac{dy}{y} \, \Delta P_{ji}(y) \, t\left(\frac{x}{y}\right) \tag{4.15}$$

determine the local change of the parton densities with increasing $\ln(Q^2)$. Furthermore, for Q^2/Q_0^2 not too large one can approximate the solution of the DGLAP equations by

$$\begin{pmatrix} \Delta\Sigma(x, Q^2) \\ \Delta G(x, Q^2) \end{pmatrix} = \begin{pmatrix} \Delta\Sigma(x, Q_0^2) \\ \Delta G(x, Q_0^2) \end{pmatrix}$$

$$+ \frac{\alpha_s(Q_0^2)}{2\pi} \int_x^1 \frac{dy}{y} \begin{pmatrix} \Delta P_{qq}(y) & \Delta P_{qg}(y) \\ \Delta P_{gq}(y) & \Delta P_{gg}(y) \end{pmatrix} \begin{pmatrix} \Delta\Sigma(x/y, Q_0^2) \\ \Delta G(x/y, Q_0^2) \end{pmatrix} \ln\left(\frac{Q^2}{Q_0^2}\right).$$

A realistic choice of test distribution is

$$t(x) = x^\alpha (1-x)^\beta \qquad \text{with} \quad (-1 < \alpha < 0, \ \beta > 0),$$

which is similar to the analytic forms of the parton densities at Q_0^2 used in recent fits to the polarized structure function data [65, 68, 69]. The exponent α determines the behaviour of the distribution in the small-x regime, whereas the large-x behaviour is controlled by β, as explained in the previous section.

The elements of the evolution matrix can be computed analytically. Inspection of the leading order splitting functions (B.25) shows that all A_{ji} can be expressed in terms of the four functions

$$\begin{aligned} A_1(x) &= \int_x^1 \frac{dy}{y} \frac{1}{(1-y)_+} \left(\frac{x}{y}\right)^\alpha \left(1 - \frac{x}{y}\right)^\beta \\ &= x^\alpha (1-x)^\beta [\ln(1-x) + \frac{\alpha+\beta+1}{\beta+1}(1-x) \, {}_3F_2(2+\beta+\alpha, 1, 1; 2, 2+\beta; (1-x)) \\ &\quad - \psi(\beta+1) - \gamma_E], \\ A_2(x) &= \int_x^1 \frac{dy}{y} \left(\frac{x}{y}\right)^\alpha \left(1 - \frac{x}{y}\right)^\beta \\ &= (1-x)^{\beta+1} \frac{1}{\beta+1} \, {}_2F_1(1-\alpha, 1+\beta; 2+\beta; (1-x)), \end{aligned}$$

47

$$A_3(x) = \int_x^1 \frac{dy}{y} \, y \left(\frac{x}{y}\right)^\alpha \left(1 - \frac{x}{y}\right)^\beta$$

$$= x(1-x)^{\beta+1} \left[\frac{1}{1-\alpha} x^{\alpha-1} - \frac{\alpha+\beta}{(1-\alpha)(\beta+1)} \, _2F_1(1-\alpha, 1+\beta; 2+\beta; (1-x))\right],$$

$$A_4(x) = \int_x^1 \frac{dy}{y} \, \delta(1-y) \left(\frac{x}{y}\right)^\alpha \left(1 - \frac{x}{y}\right)^\beta$$

$$= x^\alpha (1-x)^\beta, \tag{4.16}$$

where the hypergeometric function $_nF_p$ can be found in [70]. The elements of the evolution matrix read in terms of these functions:

$$A_{qq}(x) = \frac{4}{3} \left[2A_1(x) - A_2(x) - A_3(x) + \frac{3}{2} A_4(x)\right],$$

$$A_{qg}(x) = 3 \left[-A_2(x) + 2A_3(x)\right],$$

$$A_{gq}(x) = \frac{4}{3} \left[2A_2(x) - A_3(x)\right],$$

$$A_{gg}(x) = 3 \left[2A_1(x) + 2A_2(x) - 4A_3(x) + \frac{3}{2} A_4(x)\right]. \tag{4.17}$$

Figure 4.2 shows all $xA_{ji}(x)$ for $\alpha = -0.25$, $\beta = 4$. Several effects of the evolution can be read off: the quark-to-quark and gluon-to-gluon splittings decrease the corresponding distributions at large x while increasing them at small x. This effect is easily understood: the emission of soft particles diminishes the distributions of either helicity at large x, while increasing them at small x. The gluon-to-quark splitting A_{qg} generates a positive contribution to the polarized quark density at large x and a negative contribution at small x. The quark-to-gluon splitting enhances the polarized gluon density over the whole range in x.

It is however not possible to draw quantitative conclusions from the above, as the relative size of each of these corrections depends on the relative normalization of quark and gluon distributions.
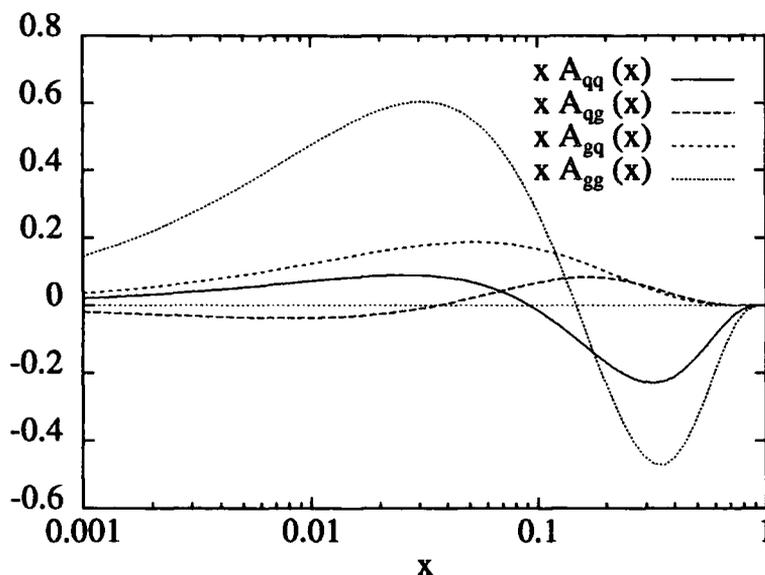
Figure 4.2: Elements of the evolution matrix for a test distribution with $\alpha = -0.25$, $\beta = 4$.

4.4 Asymptotic behaviour at small x

The behaviour of parton distributions and structure functions, both unpolarized and polarized, at small x has been a matter of discussion over the last years. Various approaches in the polarized case can be found in [68, 71, 72, 73] and references therein. In this section, we will discuss analytic methods to determine the behaviour of polarized parton distributions at small x from the DGLAP evolution equations.

We begin with a summary of the present experimental and theoretical knowledge on the polarized proton structure at small x in Section 4.4.1. Various approximations to the leading order DGLAP splitting functions at small x will be compared in Section 4.4.2 on the basis of the evolution matrix described above. Furthermore, we will derive a new approach in Section 4.4.3 and discuss its domain of applicability. Finally, Section 4.4.4 contains conclusions and implications of this study.

4.4.1 Motivation

In the recent past, various authors have attempted to calculate the asymptotic behaviour of $g_1(x)$ at small x. At scales of low momentum transfer ($Q^2 \approx 1$ GeV^2), a non-perturbative calculation [71] of the flavour singlet contribution to g_1 shows good agreement with g_1^p, but it should be noted that the normalization of this non-perturbative contribution is highly sensitive to the only approximately known value of the vacuum quark condensate. The experimental discrepancy between g_1^p and g_1^d in the small-x region seems to contradict the above result. As the singlet distribution is identical for both targets, this discrepancy indicates a sizable valence-quark contribution in this region.

With increasing Q^2, perturbative corrections become more and more important. These corrections affect both the valence and the singlet contributions to g_1 and give rise to an evolution of the corresponding parton densities. A first detailed discussion of the asymptotic behaviour of $g_1(x)$ due to these corrections was presented in [74].

In experimental measurements, perturbative corrections are incorporated by rescaling the value of g_1 to the average Q^2 of the experiment. This rescaling procedure relies on the assumption that the asymmetry $g_1(x)/F_1(x)$ satisfies exact Bjorken scaling, i.e. that the Q^2-dependence of g_1 coincides with that of F_1. Although this assumption is consistent with the present data (which cover only a small range of Q^2 values at fixed x), there is no theoretical justification for it. In particular, examination of the polarized and unpolarized splitting functions [31] shows that $g_1(x)/F_1(x)$ should indeed show only a very weak Q^2 dependence in the large-x region, where both structure functions are dominated by the valence quark content, as $\Delta P_{qq}(x)$ and $P_{qq}(x)$ are identical. In contrast to this, the splitting functions in the singlet sector, which dominates the small-x behaviour of F_1, are different. The unpolarized $P_{gq}(x)$ and $P_{gg}(x)$ have a soft gluon singularity at $x = 0$, which causes the steep rise of F_1 in the small-x region. As this singularity is absent in the polarized splitting functions (soft gluon emission does not change the spin of the parent parton), one would expect the ratio $|g_1(x)/F_1(x)|$ to decrease with increasing Q^2.

With the exact splitting functions it is not possible to find an analytic solution to (3.7)

with realistic boundary conditions for the whole range of x. By restricting themselves to small values of x (although it is not *a priori* clear which values of x can be regarded as small), various authors have attempted to determine the asymptotic behaviour of g_1 in the limit $Q^2 \to \infty$. One possible approach [72] is to assume that all the Q^2 dependence is dominated by the evolution of the gluon, i.e. by $\Delta P_{gg}(x)$. This method gives successful predictions for the unpolarized structure functions, due to the $1/x$ pole in the unpolarized P_{gg}. As this pole is not present in ΔP_{gg}, the validity of this approach needs to be examined more carefully.

Another possible approach [68] to the asymptotic small-x behaviour is to transform (3.7) into moment space and to expand around the rightmost singularity at $N = 0$:

$$\langle \Delta P \rangle_N = \frac{A}{N} + B + O(N) \Rightarrow \Delta P(x) \approx A + B\delta(1 - x).$$

This procedure yields the following approximate splitting functions[1]:

$$\Delta P_{qq}^{(l)}(x) = \frac{4}{3} \left[1 + \frac{1}{2}\delta(1 - x) \right],$$

$$\Delta P_{qg}^{(l)}(x) = 2n_f \frac{1}{2} \left[-1 + 2\delta(1 - x) \right],$$

$$\Delta P_{gq}^{(l)}(x) = \frac{4}{3} \left[2 - \delta(1 - x) \right],$$

$$\Delta P_{gg}^{(l)}(x) = 3 \left[4 - \frac{13}{6}\delta(1 - x) \right] - \frac{n_f}{3}\delta(1 - x). \tag{4.18}$$

With these simplified splitting functions, one can analytically solve (3.7) for asymptotic values of Q^2 with realistic boundary conditions in the small-x region. This approach is based on the fact that the behaviour of the parton distributions at small x is governed by the region around $N = 0$ in moment space. This property can be understood from the N-singularity structure of the initial distributions: a logarithmic ($\sim 1/x$) singularity coincides with a pole at $N = 0$ in the moment transform, a power-like singularity of the form x^α transforms into $\Gamma(\alpha + N)$, which has a singularity at $N = -\alpha$. It is important

---

[1]Similar splitting functions containing only the residue at $N = 0$ were studied in [75], giving qualitatively comparable results to [68]

to notice, however, that the expansion around the $N = 0$ pole in moment space agrees with the full splitting function only within a circle of unit radius. Outside this circle, the series might still be convergent, but its value will be different from that given by the full splitting function. This especially affects the reliability of this approach for low values of α. In the extreme case α could approach -1 giving rise to a pole close to the boundary of the circle of convergence.

4.4.2 Study of the evolution matrix

The evolution matrix introduced in Section 4.3.2 provides us with a tool to study the quality of the approaches introduced above, as it reflects the local effects of perturbative evolution at particular values of x. We will again work with simple test distributions of the form

$$t(x) = x^{\alpha}(1 - x)^{\beta} \quad \text{with} \quad (-1 < \alpha < 0, \ \beta > 0).$$

It is worth recalling that α determines the behaviour of the distribution in the small-x regime, while the large-x behaviour is controlled by β. Variations of β should therefore not affect any predictions of the small-x behaviour of the parton distributions. This property can be used to define the range of validity of these predictions, i.e. to indicate if x can be regarded as small or not.

The leading-pole expanded [68] splitting functions of (4.18) yield the following elements for the evolution matrix:

$$A_{qq}^{(l)}(x) = \frac{4}{3}\left[A_2(x) + \frac{1}{2}A_4(x)\right],$$

$$A_{qg}^{(l)}(x) = 3\left[-A_2(x) + 2A_4(x)\right],$$

$$A_{gq}^{(l)}(x) = \frac{4}{3}\left[2A_2(x) - A_4(x)\right],$$

$$A_{gg}^{(l)}(x) = 3\left[4A_2(x) - \frac{5}{2}A_4(x)\right], \quad (4.19)$$

which have to be compared to the full $A_{ji}^{(f)}$ given in (4.17).

A closer inspection of the A_{ji} shows that all of them diverge like x^α as $x \to 0$. The different contributions (4.16) show the following behaviour:

$$A_1(x) \xrightarrow{x \to 0} x^\alpha \left[-\psi(-\alpha) - \gamma_E\right],$$

$$A_2(x) \xrightarrow{x \to 0} \frac{1}{-\alpha} x^\alpha,$$

$$A_3(x) \xrightarrow{x \to 0} \frac{1}{1-\alpha} x^\alpha,$$

$$A_4(x) \xrightarrow{x \to 0} x^\alpha. \tag{4.20}$$

The behaviour in the limit $x \to 0$ can therefore be written as

$$\lim_{x \to 0} A_{ji}(x) = a_{ji} x^\alpha. \tag{4.21}$$

Provided that both the initial quark singlet and the initial gluon distributions have power-like boundary conditions in the limit $x \to 0$, these most singular terms will dominate the right-hand side of (3.7). The replacement of the $A_{ji}^{(f)}$ by the above expressions (4.21) in (3.7) should therefore enable us to find an analytic solution for $\Delta\Sigma(x, Q^2)$ and $\Delta G(x, Q^2)$, which becomes exact for $x \to 0$. This exercise will be performed in the following section.

The a_{ji} coefficients for the full and the leading-pole expanded splitting functions are *not* identical:

$$a_{qq}^{(f)} = \frac{4}{3} \left[2(-\psi(-\alpha) - \gamma_E) + \frac{1 - 2\alpha}{\alpha(1-\alpha)} + \frac{3}{2}\right], \qquad a_{qq}^{(l)} = \frac{4}{3} \frac{-2 + \alpha}{2\alpha},$$

$$a_{qg}^{(f)} = 3 \frac{1 + \alpha}{\alpha(1-\alpha)}, \qquad a_{qg}^{(l)} = 3 \frac{1 + 2\alpha}{\alpha},$$

$$a_{gq}^{(f)} = \frac{4}{3} \frac{-2 + \alpha}{\alpha(1-\alpha)}, \qquad a_{gq}^{(l)} = \frac{4}{3} \frac{-2 - \alpha}{\alpha}, \tag{4.22}$$

$$a_{gg}^{(f)} = 3 \left[2(-\psi(-\alpha) - \gamma_E) - \frac{2 + 2\alpha}{\alpha(1-\alpha)} + \frac{3}{2}\right], \qquad a_{gg}^{(l)} = 3 \frac{-8 - 5\alpha}{2\alpha}.$$

Figure 4.3 shows examples of the $A_{ji}^{(f)}$ for $\beta = 4, 9$, together with the approximate forms $A_{ji}^{(l)}$ and the limits $a_{ji}^{(f)} x^\alpha$. This figure displays the following important features of the evolution matrix in the small-x region:

53
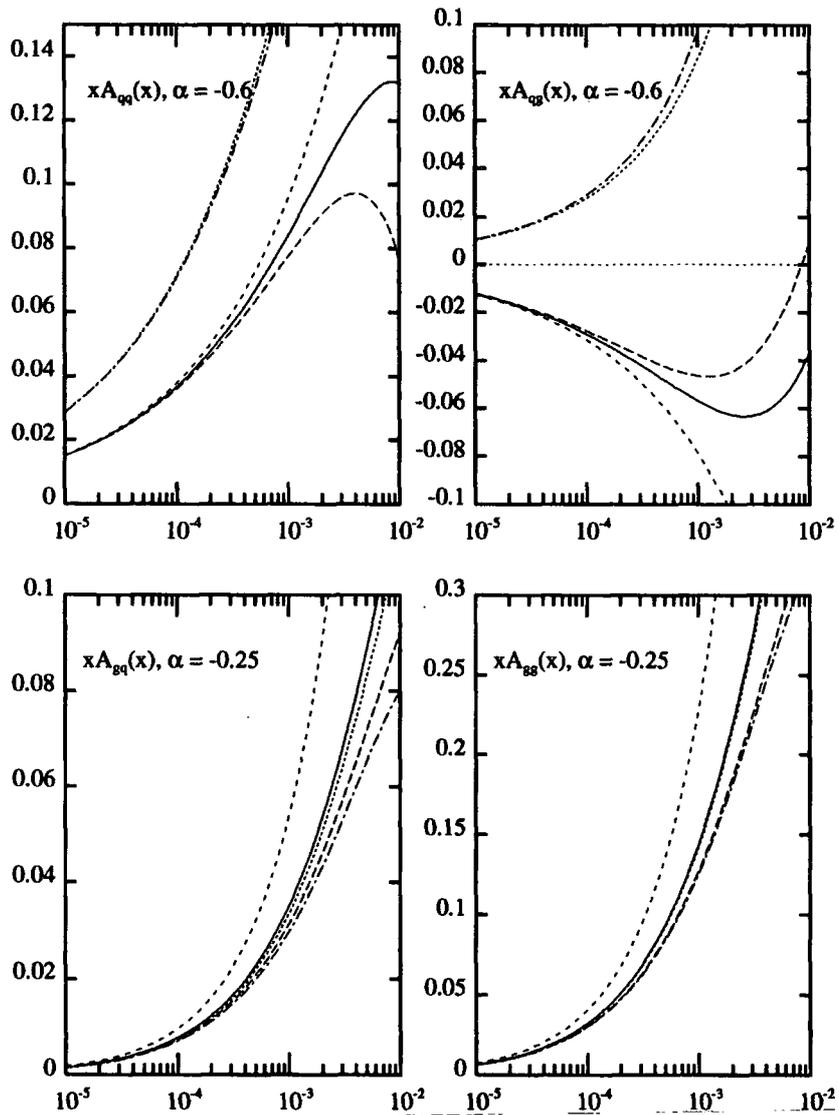
Figure 4.3: Examples of elements of the splitting matrix for the test distribution $x^\alpha(1-x)^\beta$. Solid line: full splitting functions for $\beta = 4$, long-dashed line: same for $\beta = 9$, short-dashed line: most singular x^α contribution, dotted line: leading-pole expanded splitting functions for $\beta = 4$, dot-dashed line: same for $\beta = 9$. For better visibility, all elements are multiplied by x.

(i) Although the test distributions $x^\alpha(1-x)^4$ and $x^\alpha(1-x)^9$ differ by less than 5% for

54
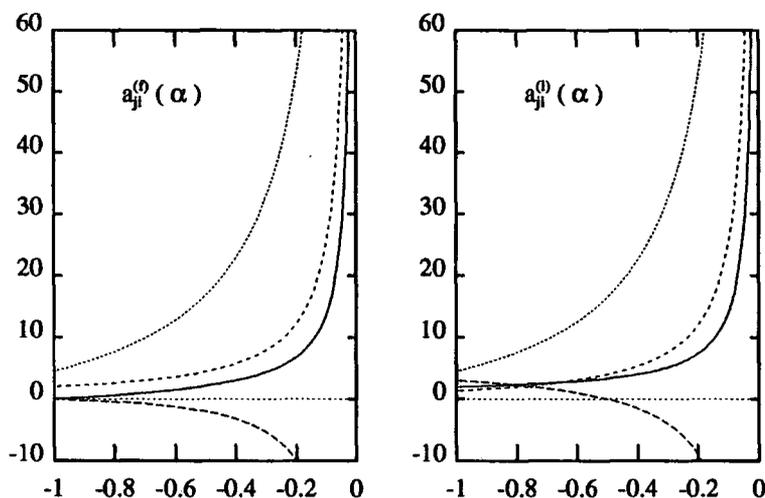
Figure 4.4: Coefficients of the most singular pieces in the splitting matrix for the full (left) and the leading-pole expanded (right) splitting functions. Solid line: a_{qq}, long-dashed line: a_{qg}, short-dashed line: a_{gq}, dotted line: a_{gg}.

$x \leq 0.01$, the corresponding $A_{ji}^{(f)}$ differ by up to a factor of 2 in the same range. This clearly demonstrates that even at $x = 0.01$ and below the evolution is sensitive to the behaviour of the parton distributions in the large-x region. The sensitivity of the $A_{ji}^{(f)}$ to variations of β can furthermore be used to define whether x can be regarded as small. For example, by requiring $A_{ji}^{(f)}$ to vary by less than 30% for all combinations in i and j and both values of α, we find that only $x \leq 0.001$ can be regarded as small, and the more conservative bound of less than 10% deviation yields $x \leq 0.0001$. It should therefore be clear that the mere knowledge of g_1 at the lowest x values accessible with fixed-target experiments is insufficient to predict the asymptotic behaviour of g_1 in the small-x limit, as the behaviour of the parton distributions at these values of x is still closely correlated with the distributions in the large-x region.

(ii) The convergence of the $A_{ji}^{(f)}$ towards $a_{ji}^{(f)} x^\alpha$ improves for smaller values of α. This

55

behaviour just reflects the fact that $A_{ji}^{(f)}$ contains, in addition to this leading term, less singular terms proportional to $\ln(x)$. In general, these lower $|A_{ji}^{(f)}|$. If $t(x)$ is less singular that $x^{-1/e}$, the logarithmic terms are larger than the power-like terms for

$$x > x_0(\alpha) = \left(\frac{\omega(\alpha)}{\alpha}\right)^{\frac{1}{\alpha}},$$

where $\omega(\alpha)$ is defined in Appendix A.2. As x_0 decreases very quickly with α ($x_0 \approx 10^{-15}$ for $\alpha = -0.1$), the replacement $A_{ji}^{(f)}(x) \to a_{ji}x^\alpha$, although formally still correct, loses its meaning for values of α close to 0 in any physically relevant region.

(iii) While the $A_{ji}^{(l)}$ resemble the $A_{ji}^{(f)}$ for values of α close to 0, they disagree for smaller α. This feature becomes most striking for the A_{qg} (see Fig. 4.3). The full splitting functions (B.25) predict that a positive gluon polarization in the small-x region will always generate a negative contribution to the sea polarization. In contrast, the leading-pole expanded splitting functions of [68] predict a *positive* sea polarization, if the gluon polarization $\Delta G(x)$ is more singular than $x^{-0.5}$. This behaviour can be inferred from the α dependence of the a_{ji} displayed in Fig. 4.4. The good agreement for higher values of α is due to the fact that all leading contributions in $\ln(x)$ are contained in the $N = 0$ pole and hence are well approximated by the $A_{ji}^{(l)}$. As elaborated above, these contributions remain important for a finite range in $x > x_0 > 0$. The asymptotic predictions of [68] will therefore still approximate the full evolution, provided they are restricted to this finite range.

(iv) The magnitude of A_{gg} is larger by a factor 3 than the magnitude of all the other terms, but A_{gg} is not more singular than any other contribution. Therefore, the small-x estimate of [72] is qualitative at best, and should be expected to yield a less accurate prediction than the corresponding estimate of the unpolarized distributions.

(v) The agreement between leading pole expanded and full splitting functions is better for the A_{gq} and A_{gg} than it is for A_{qq} and A_{qg}. This feature can be understood from

	$N \leq -2$	$N = -1$	$N = 0$
$3/4\, \Delta P_{qq}$	2	1	1
$1/3\, \Delta P_{qg}$	0	2	-1
$3/4\, \Delta P_{gq}$	0	-1	2
$1/3\, \Delta P_{gg}$	2	-2	4

Table 4.2: Residues of the polarized splitting functions in N-moment space. The residues for all negative integers with $N \leq -2$ are identical.

the relative magnitude of the residues in the corresponding splitting functions (Table 4.2): the $N = 0$ residue is dominant only in the P_{gq} and P_{gg} splitting functions, the other two splitting functions contain residues for $N < 0$, which are twice as big as the $N = 0$ residue.

It should be clear from the above that the leading-pole expansion of [68] gives a reliable approximation to the evolution matrix in the small-x region, provided that the initial distributions are significantly less singular than $x^{-1/e}$. For more singular distributions, this approach results in a manifestly different evolution matrix and hence will yield a different small-x behaviour of the polarized parton distributions.

4.4.3 Solution of the DGLAP equations in the small x limit

Provided both polarized singlet quark and gluon densities have power-like boundary conditions in the small-x region,

$$\Delta\Sigma(x, Q_0^2) \sim x^{\alpha_q}, \quad \Delta G(x, Q_0^2) \sim x^{\alpha_G} \qquad \text{with} \; -1 < \alpha_q, \alpha_G < 0,$$

one can find a solution of the DGLAP equations which becomes exact in the limit $x \to 0$ and has the form

$$\Delta q_{val}(x, Q^2) \; = \; R_v(Q^2, Q_0^2)\, x^{\alpha_v},$$

$$\Delta\Sigma(x,Q^2) = R_{qq}(Q^2,Q_0^2)x^{\alpha_q} + R_{qg}(Q^2,Q_0^2)x^{\alpha_G},$$

$$\Delta G(x,Q^2) = R_{gq}(Q^2,Q_0^2)x^{\alpha_q} + R_{gg}(Q^2,Q_0^2)x^{\alpha_G}. \qquad (4.23)$$

This behaviour can be derived by inserting (4.23) as ansatz into (3.7). Keeping only terms proportional to x^{α_v}, x^{α_q} and x^{α_G} on the right-hand side, we obtain the following evolution equations for the R coefficients ($\beta_0 = 11 - 2/3n_f$) :

$$\frac{\partial}{\partial\ln\alpha_s}R_v(Q^2,Q_0^2) = -\frac{2}{\beta_0}a_{qq}(\alpha_v)R_v(Q^2,Q_0^2),$$

$$\frac{\partial}{\partial\ln\alpha_s}\begin{pmatrix} R_{qq} \\ R_{gq} \end{pmatrix}(Q^2,Q_0^2) = -\frac{2}{\beta_0}\begin{pmatrix} a_{qq}(\alpha_q) & a_{qg}(\alpha_q) \\ a_{gq}(\alpha_q) & a_{gg}(\alpha_q) \end{pmatrix}\begin{pmatrix} R_{qq} \\ R_{gq} \end{pmatrix}(Q^2,Q_0^2),$$

$$\frac{\partial}{\partial\ln\alpha_s}\begin{pmatrix} R_{qg} \\ R_{gg} \end{pmatrix}(Q^2,Q_0^2) = -\frac{2}{\beta_0}\begin{pmatrix} a_{qq}(\alpha_G) & a_{qg}(\alpha_G) \\ a_{gq}(\alpha_G) & a_{gg}(\alpha_G) \end{pmatrix}\begin{pmatrix} R_{qg} \\ R_{gg} \end{pmatrix}(Q^2,Q_0^2).$$

As we are interested in the asymptotic solution for the *full* splitting functions, all a_{ji} in the above are $a_{ji}^{(f)}$.

Introducing

$$s = \ln\left(\frac{\ln(Q^2/\Lambda^2)}{\ln(Q_0^2/\Lambda^2)}\right),$$

$$\omega_{\pm}(\alpha) = \frac{1}{2}\left(a_{qq}(\alpha) + a_{gg}(\alpha) \pm \sqrt{(a_{qq}(\alpha) - a_{gg}(\alpha))^2 + 4a_{gq}(\alpha)a_{qg}(\alpha)}\right), \qquad (4.24)$$

the general solution of these equations reads

$$R_v(Q^2,Q_0^2) = N_v \exp\left\{\frac{2}{\beta_0}a_{qq}(\alpha_v)s\right\},$$

$$R_{qq}(Q^2,Q_0^2) = R_{qq+}(Q_0^2)\exp\left\{\frac{2}{\beta_0}\omega_+(\alpha_q)s\right\} + R_{qq-}(Q_0^2)\exp\left\{\frac{2}{\beta_0}\omega_-(\alpha_q)s\right\},$$

$$R_{gq}(Q^2,Q_0^2) = R_{gq+}(Q_0^2)\exp\left\{\frac{2}{\beta_0}\omega_+(\alpha_q)s\right\} + R_{gq-}(Q_0^2)\exp\left\{\frac{2}{\beta_0}\omega_-(\alpha_q)s\right\},$$

$$R_{qg}(Q^2,Q_0^2) = R_{qg+}(Q_0^2)\exp\left\{\frac{2}{\beta_0}\omega_+(\alpha_G)s\right\} + R_{qg-}(Q_0^2)\exp\left\{\frac{2}{\beta_0}\omega_-(\alpha_G)s\right\},$$

$$R_{gg}(Q^2,Q_0^2) = R_{gg+}(Q_0^2)\exp\left\{\frac{2}{\beta_0}\omega_+(\alpha_G)s\right\} + R_{gg-}(Q_0^2)\exp\left\{\frac{2}{\beta_0}\omega_-(\alpha_G)s\right\} \qquad (4.25)$$

where the $R_{ji\pm}(Q_0^2)$ are determined by the boundary conditions at Q_0^2. As we assume that the initial distributions for the quark singlet and the gluon have the form

$$\Delta\Sigma(x, Q_0^2) = N_q\, x^{\alpha_q}, \quad \Delta G(x, Q_0^2) = N_G\, x^{\alpha_G}, \tag{4.26}$$

these constants are determined to be

$$
\begin{aligned}
R_{qq+}(Q_0^2) &= \frac{\omega_+(\alpha_q) - a_{gg}(\alpha_q)}{\omega_+(\alpha_q) - \omega_-(\alpha_q)} N_q, & R_{qq-}(Q_0^2) &= -\frac{\omega_-(\alpha_q) - a_{gg}(\alpha_q)}{\omega_+(\alpha_q) - \omega_-(\alpha_q)} N_q, \\
R_{gq+}(Q_0^2) &= \frac{a_{gg}(\alpha_q)}{\omega_+(\alpha_q) - \omega_-(\alpha_q)} N_q, & R_{gq-}(Q_0^2) &= -\frac{a_{gg}(\alpha_q)}{\omega_+(\alpha_q) - \omega_-(\alpha_q)} N_q, \\
R_{qg+}(Q_0^2) &= \frac{a_{qg}(\alpha_G)}{\omega_+(\alpha_G) - \omega_-(\alpha_G)} N_g, & R_{qg-}(Q_0^2) &= -\frac{a_{qg}(\alpha_G)}{\omega_+(\alpha_G) - \omega_-(\alpha_G)} N_g, \\
R_{gg+}(Q_0^2) &= \frac{\omega_+(\alpha_G) - a_{qq}(\alpha_G)}{\omega_+(\alpha_G) - \omega_-(\alpha_G)} N_g, & R_{gg-}(Q_0^2) &= -\frac{\omega_-(\alpha_G) - a_{qq}(\alpha_G)}{\omega_+(\alpha_G) - \omega_-(\alpha_G)} N_g.
\end{aligned}
\tag{4.27}
$$

Insertion of these boundary conditions into (4.25) finally yields (4.23).

The bounds on α

$$-1 < \alpha_q, \alpha_G < 0$$

cover the whole theoretically allowed range: as the first moments of the distributions have to be finite, we find $\alpha > -1$. Furthermore, inspection of the singularity structure of the evolution equations shows that any initial distribution, which is finite in the small-x region, will develop a logarithmic divergence due to the $N = 0$ singularity of the splitting functions. The case of finite or logarithmic boundary conditions can be treated correctly with the leading-pole approximation – its asymptotics are discussed in [68]. In an earlier analysis [65] of the experimental data on polarized structure functions we have found $\alpha_q = \alpha_v \simeq -0.55$. The experimental data used in this analysis were insufficient to determine α_G, and therefore it was fixed to be 0. The more recent study presented in the following Chapter yields $\alpha_v \simeq -0.4$, $\alpha_q = \alpha_G \simeq -0.5$.

As we have neglected all contributions of order $\ln(x)$ in the above solution, we expect it to be reliable only for $x < x_0(\max(\alpha_q, \alpha_G))$. In order to compare this approach with the leading pole expansion of [68] and the numerical solution of (3.7) with the full splitting

functions, we have evaluated the distributions for $Q_0^2 = 4$ GeV^2 and $Q^2 = 100$ GeV^2, using $n_f = 3$, $\Lambda^{QCD} = 200$ MeV and the following initial distributions:

$$\Delta\Sigma(x, Q_0^2) = N_q x^{\alpha_q}(1-x)^\beta$$

$$\Delta G(x, Q_0^2) = N_G x^{\alpha_G}(1-x)^\beta \qquad (4.28)$$

$$\Delta q_{val}(x, Q_0^2) = N_v x^{\alpha_v}(1-x)^\beta.$$

To illustrate the validity of the various approximations, we choose the following parameter values: $\alpha_q, \alpha_G, \alpha_v = -0.6, -0.25$, $\beta = 4, 9$, and for simplicity we take $N_q = N_g = N_v = 1$.

Figures 4.5.a-c show examples of the behaviour of the gluon, singlet quark and valence quark distributions respectively, at small x and $Q^2 = 4$, 100 GeV^2. The initial distributions $x^\alpha(1-x)^4$ are indicated as solid lines.

Starting with the gluon distribution (Fig. 4.5.a), we find that for $x < 10^{-2}$, the leading-pole approximation to the splitting functions (dotted lines) gives excellent agreement with the full evolution (dashed line), especially for values of α_q, α_G close to 0. This is consistent with the agreement between the corresponding A_{gg} functions shown in Fig. 4.3 and can be understood from the $N = 0$ dominance in the ΔP_{gq} and ΔP_{gg} splitting functions. In contrast, the x^α approximation (short-dashed line) significantly overestimates the evolution in the x range shown, especially for α_q, α_G close to 0. Convergence of this approach can only be observed at even smaller values of x. Note, however, the sensitivity to the large-x behaviour. While both the dotted and the dashed lines are computed with $\beta = 4$, the dot-dashed curve corresponds to full splitting function evolution for $\beta = 9$, i.e. a softer large-x distribution. Evidently there is a significant sensitivity to the behaviour at large x even for x values as small as $O(10^{-3})$. This casts doubt on the idea of using data on the evolution of the small-x structure functions alone to determine the gluon distribution.

For the singlet quark distribution (Fig. 4.5.b) the situation is rather different. Here the leading-pole approximation *overestimates* the evolution at small x. This is readily understood from the behaviour of the corresponding A_{qq} and A_{qg} functions in Fig. 4.3, both of which are systematically more positive for the leading-pole splitting functions. In fact we see that for $\alpha_q = -0.25$ and $\alpha_G = -0.6$, the full evolution gives a negative singlet

60
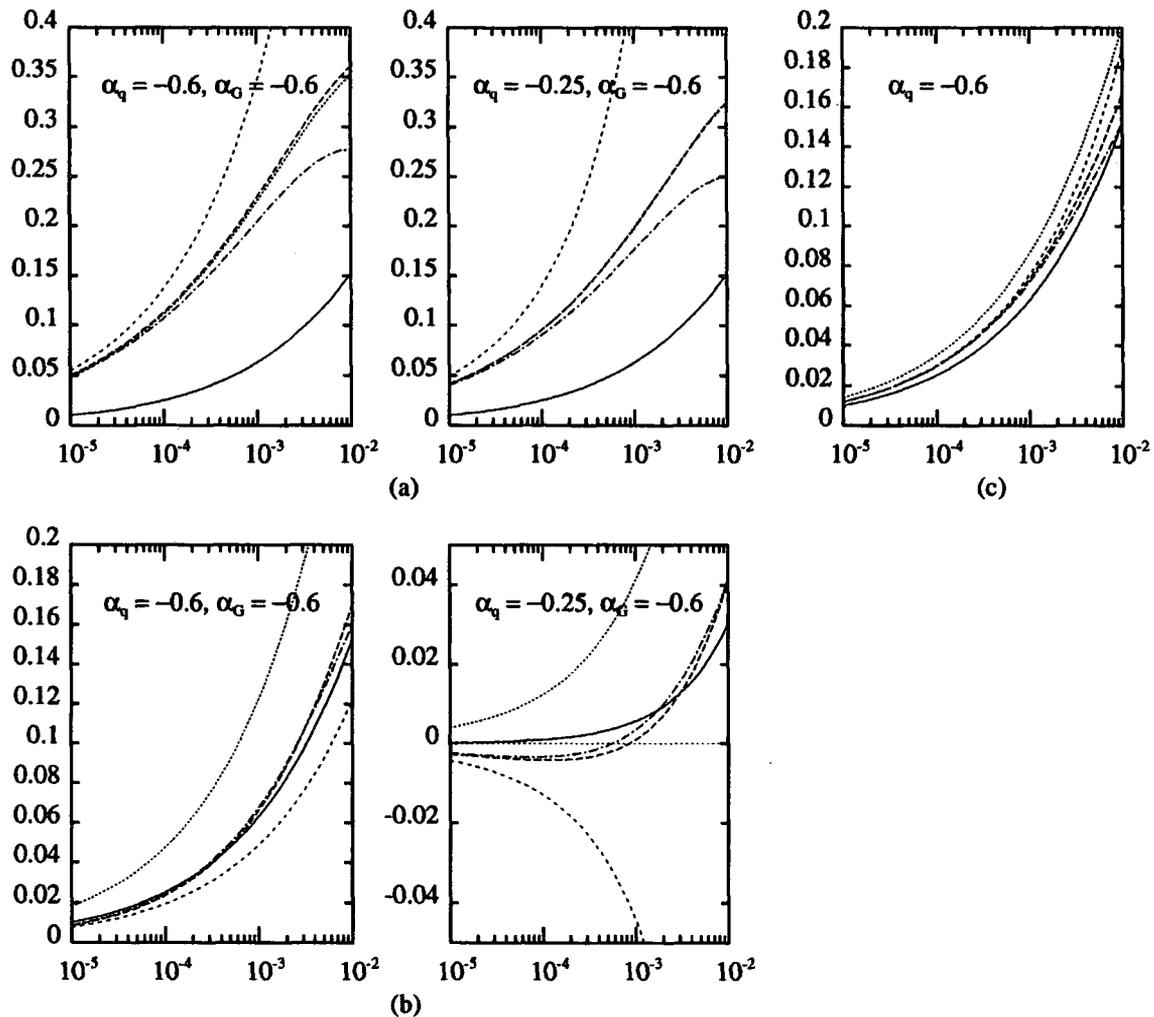
Figure 4.5: Examples of the evolution of test distributions for gluons $(x\Delta G(x, Q^2))$,(a), singlet quarks $(x\Delta\Sigma(x, Q^2))$,(b) and valence quarks $(x\Delta q_{val}(x, Q^2))$,(c) as described in the text. Solid line: starting distribution at 4 GeV^2, long-dashed and dot-dashed line: evolved distributions at 100 GeV^2 for different large-x behaviour at Q_0^2, short dashed line: result of x^α approximation, dotted line: result of leading-pole approximation.

distribution at small x, whereas the leading pole splitting functions give a positive distribution. Notice also that the evolution is less sensitive to the large-x behaviour (compare the dashed and dot-dashed curves which correspond to $\beta = 4, 9$ respectively) than for the

61

gluon distribution. For $\alpha_q = \alpha_G = -0.6$, the x^α approximation is quite reasonable, and certainly better than the leading-pole approximation. However the opposite is true when both α_q, α_G are close to 0.

Finally, Fig. 4.5.c compares the valence quark evolution in the various approximations. This depends only on ΔP_{qq}, and so the behaviour here is a direct reflection of the corresponding A_{qq} shown in Fig. 4.3. In particular, for $\alpha_q = -0.6$ the x^α approximation is very good, while the leading-pole approximation overestimates the evolution at all x values shown. For less singular small-x behaviour ($\alpha_q = -0.25$), however, both approximations reproduce the full evolution, the leading-pole approximation showing slightly better convergence for $x > O(10^{-4})$.

In practice, the normalizations of the singlet quark and gluon distribution, N_q and N_G, will not be the same. As the evolution of the gluon density is dominated by the gluon-to-gluon splitting, it will be almost unaffected by changes of N_q. Only if N_q is one or more orders of magnitude larger than N_G, will the impact of quark-to-gluon splitting become visible. More drastic effects of a change in the relative normalization can be expected for the quark singlet distribution, as contributions from quark-to-quark and gluon-to-quark splitting have the same magnitude but opposite signs (cf. Fig. 4.4). Therefore, a relative increase of N_G yields a faster evolution of the quark distribution to negative values.

The convergence properties of the different analytic approaches are almost unaffected by changes in the normalization. Only for $N_G \gg N_q$ do we find that convergence of the x^α approximation to the singlet distribution sets in for smaller values of x. This simply reflects an increased impact of the gluon-to-gluon splitting.

4.4.4 Conclusions

In this section we have studied the feasibility of two different analytic approaches to the evolution of polarized parton densities at small x, finding that none of these approaches is able to give reliable predictions for the whole theoretically allowed range of boundary conditions in the small-x region. In the leading-pole expansion [68, 75], the full splitting

functions ΔP_{ji} are replaced by the leading terms of their Laurent series around $N = 0$. As this approach correctly reproduces all terms proportional to $\ln x$ generated in the evolution, it is found to be in good agreement with the full evolution if the initial quark and gluon distributions are less singular than $x^{-1/e}$. For more singular boundary conditions, only the gluon distribution is reproduced correctly, in particular the quark distribution is overestimated. Keeping only terms with power-like singularities in the evolution equation, we were able to derive an exact solution of this equation in the limit $x \to 0$. As we have neglected all logarithmic terms in this approach, its convergence is best for boundary conditions of quark and gluon distributions more singular than $x^{-1/e}$. For less singular boundary conditions, this approach still converges towards the full solution, but its predictions are far away from the full solution for any realistic experimental value of x.

We have also shown that the evolution of the polarized gluon distribution is sensitive to the shape of this distribution in the large-x region. This observation raises doubts on the possibility of determining the gluon polarization from the evolution of g_1 in the small-x region. It furthermore demonstrates the need for complementary measurements of $\Delta G(x)$, which will be discussed in Chapter 6.

We have seen that the effects of the evolution on the quark distributions in the small-x region are rather small, as the quark-to-quark and the gluon-to-quark splitting contribute with opposite signs. The gluon distribution is indeed rising with increasing Q^2, but only contributes to g_1 at order $\alpha_s(Q^2)$. Bearing in mind that $\Delta G(x)$ contributes with a negative coefficient function to g_1, one expects that g_1 will become negative at small x for asymptotic values of Q^2. This behaviour is due to the gluonic contribution and the negative sea polarization generated from $g \to q\bar{q}$ splitting.

In general, the effects of the evolution on the polarized parton densities will be more moderate than the effects on the unpolarized densities. The assumption of approximate scaling for $g_1(x)/F_1(x)$ in the small-x region is therefore rather doubtful. It seems more realistic to assume approximate scaling for $g_1(x)$ at small x, due to the partial cancellation of quark and gluon evolution as explained above.

Chapter 5

Polarized parton distributions

It was already outlined in Chapter 3 that perturbative QCD *only* predicts the change of parton distributions with increasing Q^2 without determining these distributions themselves. These are *intrinsic* features of the nucleon, which are controlled by the non-perturbative dynamics of QCD at scales below the proton mass. They cannot be computed with present techniques.

In this chapter, we attempt to extract the polarized parton distributions from a global fit to the presently available data on the polarized proton structure. These data are however of much lower precision than in the unpolarized case. The fit needs therefore to be constrained by additional assumptions and approximate symmetries, as motivated in the previous chapter. The distributions obtained will be less well determined than their unpolarized counterparts.

5.1   A global fit to polarized structure function data

We adopt a similar approach to the global analysis of unpolarized parton distributions in the nucleon [41] by parametrizing the polarized distributions at the starting scale in the form:

$$x\Delta u_v(x, Q_0^2) = \eta_u A_u x^{a_u}(1-x)^{b_u}(1 + \gamma_u x + \rho_u x^{1/2})$$

$$x\Delta d_v(x,Q_0^2) = \eta_d A_d x^{a_d}(1-x)^{b_d}(1+\gamma_d x + \rho_d x^{1/2})$$

$$x\Delta\bar{q}(x,Q_0^2) = \eta_{\bar{q}} A_{\bar{q}} x^{a_q}(1-x)^{b_q}(1+\gamma_{\bar{q}} x + \rho_{\bar{q}} x^{1/2})$$

$$x\Delta G(x,Q_0^2) = \eta_G A_G x^{a_G}(1-x)^{b_G}(1+\gamma_G x + \rho_G x^{1/2}), \tag{5.1}$$

where we take $Q_0^2 = 4$ GeV^2. The normalization factors are

$$A_f^{-1}(f=q,G) = \left(1 + \gamma_f \frac{a_f}{a_f + b_f + 1}\right)\frac{\Gamma(a_f)\Gamma(b_f+1)}{\Gamma(a_f+b_f+1)} + \rho_f \frac{\Gamma(a_f+0.5)\Gamma(b_f+1)}{\Gamma(a_f+b_f+1.5)}$$

which ensures that the first moments of the distributions, $\int_0^1 dx \Delta f(x,Q_0^2)$, are given by η_f.

Various experimental measurements of unpolarized lepton($= e, \mu, \nu$)–nucleon and unpolarized Drell–Yan cross sections yield a reasonably precise flavour decomposition of the light quark (u,d,s) sea. Such a decomposition is not yet possible for the polarization of the light quark sea, as measurements of the structure function g_1 are only sensitive to the charge weighted sum of all quark flavours, not to the individual distributions. We therefore assume a SU(3)–symmetric antiquark polarization $\Delta\bar{q}(x,Q_0^2) = \Delta\bar{u}(x,Q_0^2) = \Delta\bar{d}(x,Q_0^2) = \Delta\bar{s}(x,Q_0^2)$. This *ad-hoc* assumption is only justified at the present level of experimental knowledge, and is furthermore immediately broken by next-to-leading order evolution [76].

As outlined in the previous chapter, one can infer the first moments of the polarized quark distributions from the measured values of the Ellis–Jaffe sum rule. Imposing SU(3)–symmetry at Q_0^2, this sum rule reads

$$\Gamma_1^{p,n}(Q_0^2) = \left(1 - \frac{\alpha_s(Q_0^2)}{\pi}\right)\left(\pm\frac{1}{12}a_3 + \frac{1}{36}a_8 + \frac{1}{9}a_0(Q_0^2)\right) \tag{5.2}$$

with[1]

$$a_3 = \eta_u(Q_0^2) - \eta_d(Q_0^2) = F + D,$$

$$a_8 = \eta_u(Q_0^2) + \eta_d(Q_0^2) = 3F - D,$$

$$a_0(Q_0^2) = \eta_u(Q_0^2) + \eta_d(Q_0^2) + 6\eta_{\bar{q}}(Q_0^2).$$

---

[1] Recall that the first moments of the valence quark polarizations are not conserved in next-to-leading order (B.33). Nevertheless, the scaling violations are only at the per-mille level for realistic values of Q^2.

	LO	NLO
η_u	0.823	0.918
η_d	−0.303	−0.339
η_G	1.9	
$\eta_{\bar{q}}$	−0.0495	−0.060
b_u	3.73	3.96
b_d	4.73	4.96

Table 5.1: Fixed parameters in the LO and NLO($\overline{\text{MS}}$) polarized parton distribution fits.

	LO	NLO (3 GeV^2)	NLO (10 GeV^2)
$\Gamma_1^p - \Gamma_1^n$	0.188	0.191	0.195
Γ_1^p	0.133	0.132	0.135
Γ_1^n	−0.055	−0.059	−0.060
Γ_1^d	0.039	0.037	0.037

Table 5.2: Values of the Bjorken and Ellis–Jaffe sum rules.

In this approach, the first moments of the valence quark polarizations are obtained from the nonsinglet axial-vector current matrix elements [59], while the first moment of the sea quark distribution is inferred from the measured value of Γ_1. For the leading-order (LO) distributions, we correct the normalization of η_u and η_d by the $\mathcal{O}(\alpha_s)$-coefficient function in (5.2) [65]. The first moments obtained by this procedure are listed in Table 5.1. The resulting values for the Bjorken and Ellis–Jaffe sum rules at LO and NLO are listed in Table 5.2. Note that the Ellis–Jaffe sum rule is a (Q^2-independent) constant at leading order in perturbation theory, as the leading-order coefficient functions are only expanded up to $\mathcal{O}(\alpha_s^0)$ and scaling violations in $\eta_{\bar{q}}(Q^2)$ arise only from the splitting functions at next-to-leading order (cf. Section 4.2).

The polarized gluon distribution enters $g_1(x, Q^2)$ at next-to-leading order. It is only

very weakly constrained so far, as no experimental data are available on gluon-initiated processes such as direct-γ or heavy meson production. The polarized gluon distribution $\Delta G(x, Q^2)$ is therefore not well-determined by a fit to the g_1 data alone, and so additional theoretical constraints have to be applied. It was demonstrated in the last chapter that the small-x behaviour of the gluon and sea quark distributions are closely related [77], which justifies the assumption $a_G = a_{\bar{q}}$ in (5.1). In the region $x > 0.1$, structure functions and their evolution are dominated by valence quark contributions, and the impact of the gluon is completely negligible. We therefore explore various possibilities for the form of $\Delta G(x, Q^2)$ at large x: hard (A) and soft (B) distributions with the spin aligned with that of the parent hadron, and a distribution (C) with the spin anti-aligned. We show in the following that all three choices give equally good descriptions of the structure function data. They will be relatively easy to discriminate, once data on polarized gluon-initiated processes are available. The three possible scenarios for the behaviour of $\Delta G(x, Q_0^2)$ can be parametrized as follows:

$$\text{Gluon A}: \quad \gamma_G = 0, \quad \rho_G = 0,$$

$$\text{Gluon B}: \quad \gamma_G = 1, \quad \rho_G = -2,$$

$$\text{Gluon C}: \quad \gamma_G = 0, \quad \rho_G = -3.$$

The normalization η_G of the gluon distribution can only be determined consistently from the experimental data in a next-to-leading order analysis, where it still has a large error. At leading order, we can estimate η_G by attributing *all* the violation of the Ellis–Jaffe sum rule to a large gluon polarization and vanishing sea quark polarization. In this way we obtain $\eta_G = 1.9$, only slightly different from the value 1.97 obtained in our previous analysis [65]. Note, however, that at leading order the apportioning of the singlet contribution to Γ_1 between gluons and sea quarks is completely arbitrary [34]. In fact we shall see below that a consistent NLO treatment gives a value of η_G somewhat less than our estimated leading order value, and similar to the range of values found in [63].

If parton distributions are interpreted in the probabilistic picture of the naïve parton model, the magnitude of the polarized distributions cannot exceed the unpolarized distri-

67

butions, in order to guarantee positive probabilities for the individual polarization states, i.e.

$$|\Delta f(x)| < f(x), \qquad (f = q, G). \tag{5.3}$$

This is in fact only a rigid constraint at leading order, since parton distributions at higher orders are just scheme-dependent renormalization constants and not strict probability densities. The fundamental constraint at any order in perturbation theory is the positivity of physical cross sections for all possible helicity configurations. This constraint does not necessarily imply the positivity of the distributions.

Positivity of the polarized distributions is achieved by constraining the parameters of the starting distributions at Q_0^2 such that

$$|\Delta f(x, Q_0^2)| < f(x, Q_0^2), \qquad (f = q, G).$$

Perturbative evolution preserves the positivity of the individual helicity distributions, hence (5.3) is fulfilled at any Q^2.

In our leading-order analysis, we use the unpolarized distributions from [44] for reference. At $Q_0^2 = 4$ GeV^2 these are

$$xu_v(x, Q_0^2) = 3.221\, x^{0.564}(1 - x)^{3.726}(1 - 0.6889x^{0.200} + 2.254x + 1.261x^{3/2}),$$

$$xd_v(x, Q_0^2) = 0.507\, x^{0.376}(1 - x)^{4.476}(1 + 1.615x^{0.553} + 3.651x + 1.299x^{3/2}),$$

$$x(\bar{u} + \bar{d})(x, Q_0^2) = \left[x^{0.158}(0.738 - 0.981x + 1.063x^2)(-\ln x)^{0.037} + \right.$$
$$\left. 0.00285 \exp\left(\sqrt{-4.010\ln x}\right)\right](1 - x)^{6.356},$$

$$xs(x, Q_0^2) = 0.0034(-\ln x)^{-1.15}(1 - 2.392x^{1/2} + 7.094x)(1 - x)^{6.166}$$
$$\exp\left(\sqrt{-6.719\ln x}\right),$$

$$xG(x, Q_0^2) = \left[x^{0.731}(5.110 - 1.204x - 1.911x^2)(-\ln x)^{-0.4718} + \right.$$
$$\left. 0.0527 \exp\left(\sqrt{-4.584\ln x}\right)\right](1 - x)^{5.566}. \tag{5.4}$$

The reference unpolarized distributions at next-to-leading order are the A$'$ set of [41],

which are parametrized at $Q_0^2 = 4 \text{ GeV}^2$ as

$$xu_v(x, Q_0^2) = 2.26 \, x^{0.559} \, (1-x)^{3.96} \, (1 - 0.54x^{1/2} + 4.65x),$$

$$xd_v(x, Q_0^2) = 0.279 \, x^{0.335} \, (1-x)^{4.46} \, (1 + 6.80x^{1/2} + 1.93x),$$

$$x\text{Sea}(x, Q_0^2) = 0.956 \, x^{-0.17} \, (1-x)^{9.63} \, (1 - 2.55x^{1/2} + 11.2x),$$

$$xG(x, Q_0^2) = 1.94 \, x^{-0.17} \, (1-x)^{5.33} \, (1 - 1.90x^{1/2} + 4.07x). \tag{5.5}$$

Note that the choice of unpolarized distributions is not crucial for the present analysis. All the widely available leading and next-to-leading order distributions provide very good fits to the unpolarized structure function data, and the small differences between them are much smaller than the precision with which the polarized distributions are currently determined. The flavour decomposition of the unpolarized sea quark distributions is also unimportant for our present analysis and will therefore be disregarded. The starting sea quark distribution of [41] contains a very small charm quark contribution which can safely be ignored in the present analysis. To be consistent with the evolution of the unpolarized distributions, we take

$$\Lambda_{\text{LO}}^{n_f=4} = 200 \text{ MeV } [44], \qquad \Lambda_{\text{NLO}}^{n_f=4} = 231 \text{ MeV } [41].$$

These correspond to $\alpha_s(M_Z^2) = 0.123$ (LO) and $\alpha_s(M_Z^2) = 0.112$ (NLO).

The parameters most affected by the positivity constraints are the large-x exponents b_f. For the valence quarks, we fix $b_u = b_u(\text{unpol.})$ and $b_d = b_u(\text{unpol.}) + 1$, motivated by counting rule estimates [66]. The parameters b_G and $b_{\bar{q}}$ are constrained to be at least as large as their unpolarized counterparts in the fit. This constraint has however minimal impact. We find that only the $\Delta d_v(x)$ distribution tends to saturate positivity, requiring the combination $\gamma_d + \rho_d$ to be limited in the fit.

The data currently available on g_1 are not able to test the various theoretical model predictions for the small-x behaviour of the polarized parton distributions. These are however expected to apply at much lower values of x (cf. Section 4.4). The parameters a_f are therefore only effective exponents valid over some finite interval in x. It therefore makes no sense to postulate positivity for $x \to 0$ by constraining the a_f.

The contribution of charmed quarks to $g_1(x, Q^2)$ is negligible at present experimental energies [78, 79] and will not be considered in this analysis. We therefore adopt the evolution procedure of [44] and fix the number of flavours in the splitting functions at $n_f = 3$, while the number of flavours in α_s increases at each mass threshold,

$$m_c = 1.5 \text{ GeV}, \qquad m_b = 4.5 \text{ GeV}, \qquad m_t = 180 \text{ GeV},$$

and $\Lambda(n_f)$ is determined by requiring α_s to be continuous across each threshold.

Rather than measuring $g_1(x, Q^2)$ directly from absolute cross section differences, it is the relative asymmetry

$$A_1(x, Q^2) \simeq \frac{g_1(x, Q^2)}{F_1(x, Q^2)}$$

which is determined experimentally. The structure function $g_1(x, Q^2)$ is then inferred using a particular parametrization of $F_1(x, Q^2)$. Some experimental groups assume Q^2-scaling of $A_1(x, Q^2)$ in their extraction of $g_1(x, Q^2)$. In order to have a consistent set of data, we have instead used the measured values of $A_1(x, Q^2)$ quoted by the experiments and re-evaluated $g_1(x, Q^2)$ from Eq. (4.4), constructing $F_1(x, Q^2)$ (3.11) from the parametrizations of F_2 [80] and R [81] which were used in the most recent measurements.

Applying the constraints outlined above, we have used all available world data on $A_1^p(x, Q^2)$, $A_1^d(x, Q^2)$ and $A_1^p(x, Q^2)$ listed in Table 4.1 to fit [82] the polarized quark and gluon distributions with the parametric forms of (5.1) imposed at $Q_0^2 = 4 \text{ GeV}^2$. About 35% of these data were taken at $Q^2 < Q_0^2$. To have sensible constraints on the distributions, in particular for $x < 0.02$, we include these data-points in the global fit. The distributions in the region $1 \text{ GeV}^2 < Q^2 < Q_0^2$ are obtained by inverting the evolution, which is straightforward in n-moment space (cf. Appendix B.3).

A problem with using low Q^2 data points in the fit is the possible contamination by higher-twist contributions. We have tried to estimate the magnitude of such contributions to g_1 using the parametrization of F_2^{HT} from [83] and assuming $g_1(x, Q^2)^{\text{HT}} \approx g_1(x, Q^2)^{\text{LT}}(1 + C^{\text{HT}}(x)/Q^2)$. The higher-twist contributions estimated in this way are found to be small for all data-points apart from the two lowest x bins of the SMC experiment.
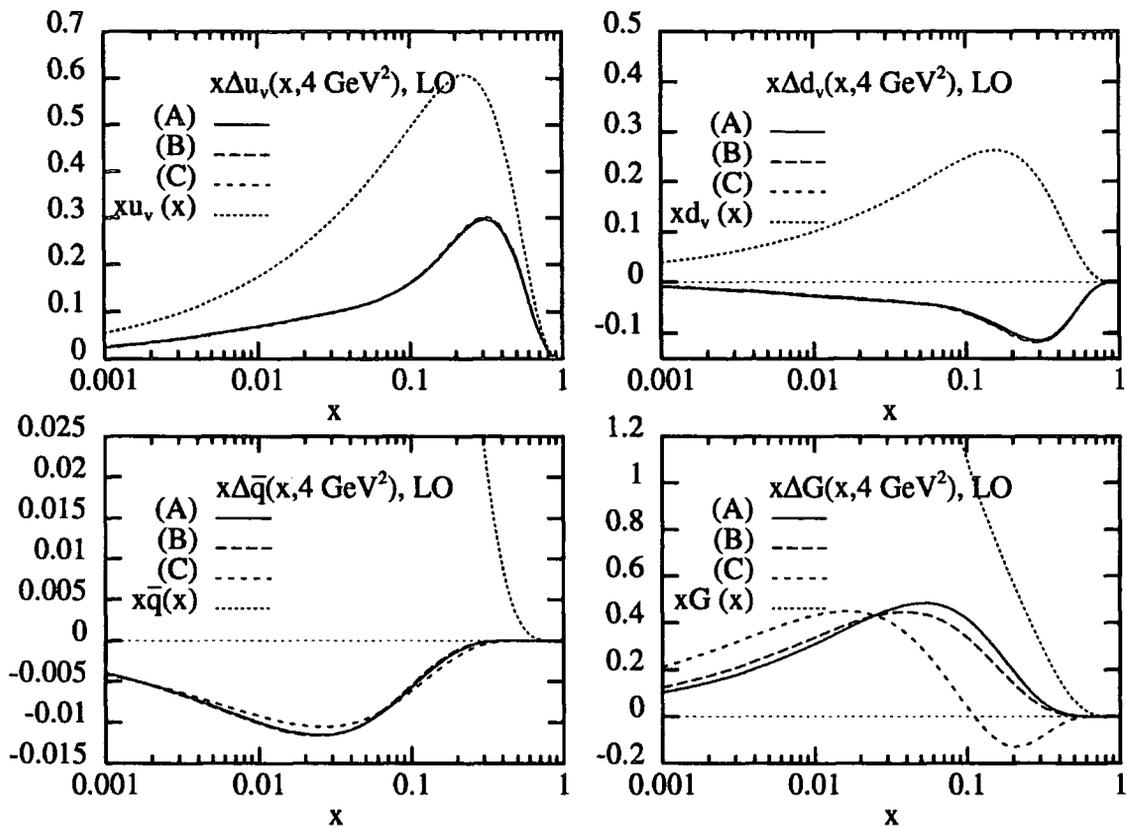
Figure 5.1: Leading order polarized parton distributions as described in the text at $Q_0^2 = 4$ GeV^2 compared to the unpolarized distributions of [44].

The global fit is performed using DGLAP evolution algorithms in N-moment space, as described in Appendix B.3. The distributions and structure functions are then restored by a numerical inversion into x space (Appendix B.4). The results of the global fit using the leading and next-to-leading order ($\overline{MS}$) expressions for the splitting functions and the g_1 coefficient functions are listed in Table 5.3. The resulting distributions at Q_0^2 are shown in Figs. 5.1 (LO) and 5.2 (NLO).

The resulting parameters are not independent of each other. In particular, a_u, a_d and $a_G = a_{\bar{q}}$ are strongly correlated. The a_i of the valence distributions are anticorrelated

71
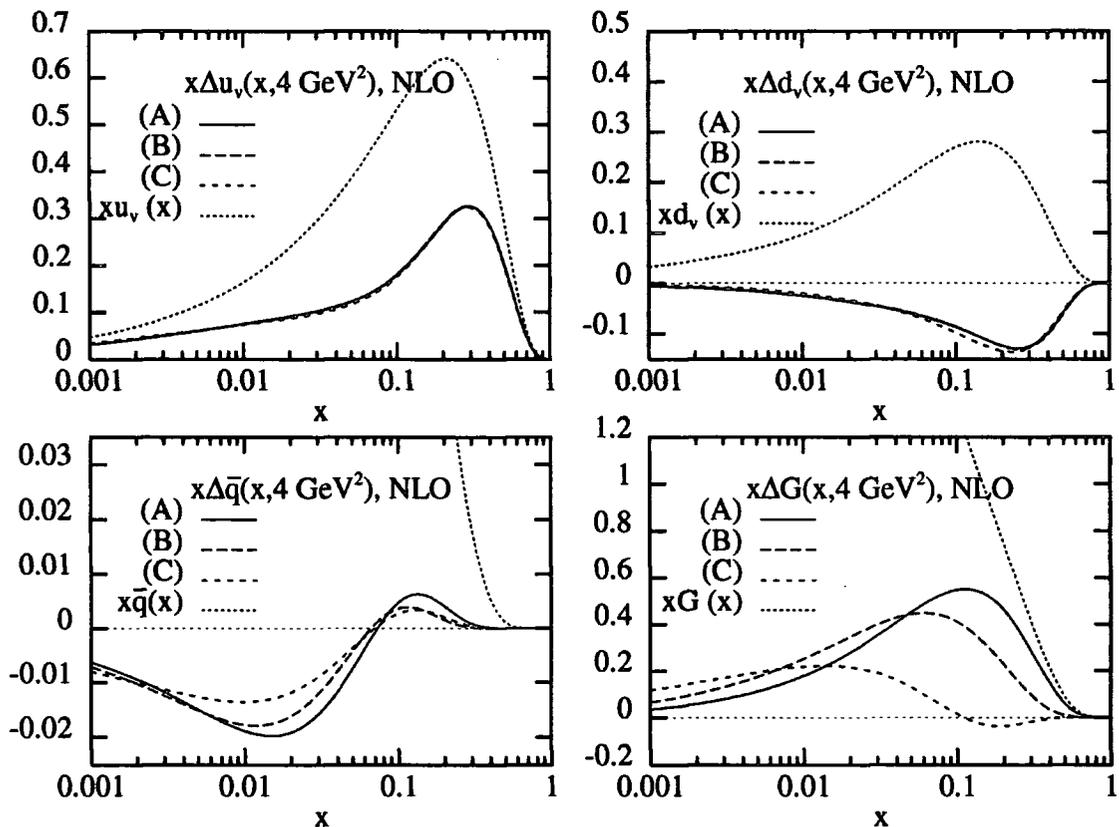
Figure 5.2: Next-to-leading order polarized parton distributions as described in the text at $Q_0^2 = 4$ GeV^2 compared to the unpolarized distributions of [41].

with the corresponding γ_i, reflecting the fact that a_i is only an effective exponent for a finite range in x. The γ_i and ρ_i are also anticorrelated. The χ^2 distribution is very flat around the local minima found by the global fits, especially with respect to the gluon and sea quark parameters.

The three gluon scenarios give fits of almost identical quality, reflecting the small impact of the gluon distribution on $g_1(x, Q^2)$ at large and medium x. The χ^2 obtained in the NLO fits are systematically lower due to the additional degree of freedom given by the normalization of the polarized gluon distribution. All fits give very good descriptions
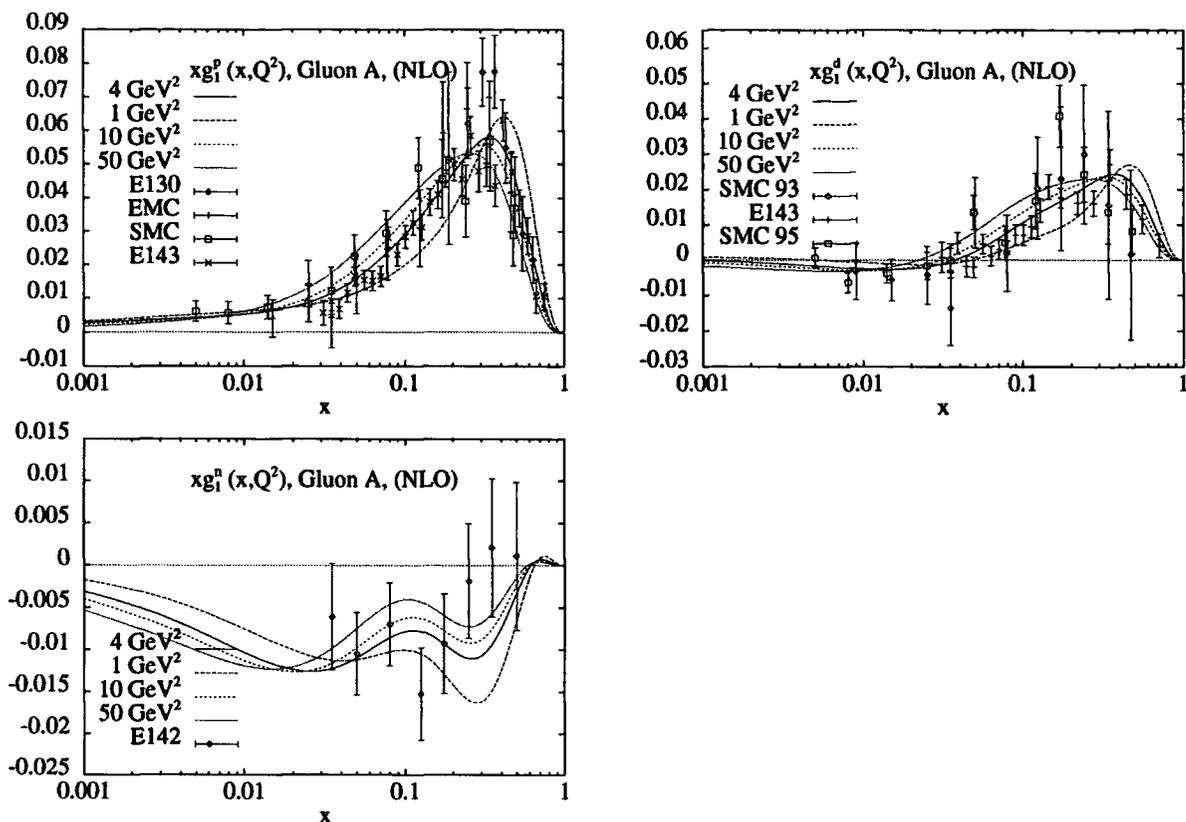
Figure 5.3: Structure function measurements $xg_1(x, Q^2)$ of the proton, deuteron and neutron compared to the next-to-leading order predictions obtained using Gluon A.

for the polarized structure functions $g_1^{p,n,d}(x, Q^2)$. This is illustrated in Fig. 5.3, which shows the NLO description of the various g_1 measurements using Gluon A. The curves correspond to $Q^2 = 1, 4, 10, 50$ GeV^2, reflecting the spread in Q^2 values of the different data sets. There is a systematic decrease in the Q^2 values of the data points from large x to small x.

The contributions of $\Delta u_v(x, Q^2)$ and $\Delta d_v(x, Q^2)$ to the neutron structure function $g_1^n(x, Q^2)$ are almost equal in magnitude but opposite in sign. The neutron structure

73

	A (LO)	B (LO)	C (LO)	A (NLO)	B(NLO)	C (NLO)
a_u	0.578	0.585	0.582	0.512	0.504	0.471
γ_u	9.38	9.31	9.50	11.65	11.98	13.14
ρ_u	−4.26	−4.28	−4.28	−4.60	−4.61	−4.90
a_d	0.666	0.662	0.660	0.780	0.777	0.809
γ_d	10.46	10.91	11.04	7.81	8.18	6.73
ρ_d	−5.10	−5.09	−5.06	−3.48	−3.61	−1.99
η_G				1.71	1.63	1.02
a_G	0.520	0.524	0.456	0.724	0.670	0.425
b_G	9.45	6.87	8.72	5.71	5.34	11.05
$b_{\bar{q}}$	15.06	15.96	11.82	14.40	18.06	16.40
$\gamma_{\bar{q}}$	2.30	2.42	2.11	4.63	5.30	−2.67
$\rho_{\bar{q}}$	−2.00	−2.00	−1.95	−4.96	−5.25	−3.08
χ^2	98.3	97.7	100.0	89.7	91.0	93.4

Table 5.3: Fitted parameters in the LO and NLO($\overline{\text{MS}}$) polarized parton distributions at Q_0^2. The χ^2 values are with respect to the 110 data points included in the global fit.

function is therefore much more sensitive to the sea quark polarization than $g_1^p(x, Q^2)$ and $g_1^d(x, Q^2)$. It displays a clear double peak structure, as the sea quarks are dominant in a different x-region than the valence quarks. A precision measurement of $g_1^{\bar{n}}(x, Q^2)$ [84] will therefore be able to provide important new information on the shape of the sea quark polarization.

From a consideration of the size of the errors on the various fitted parameters, it is apparent that the world data on $g_1(x, Q^2)$ really only constrain the polarized valence quark distributions and, to a lesser extent, the overall magnitude of the sea quark polarization. The flavour decomposition of the polarized sea is still completely unknown. Only dedicated experiments, such as the production of Drell–Yan lepton pairs or the flavour-tagging

of final-state hadrons in polarized deep inelastic scattering, will be able to provide further information. Most important of all, the x dependence of the polarized gluon distribution is almost completely undetermined, as its impact on the polarized structure function is less than the present experimental accuracy[2]. The variation between our three gluon sets certainly underestimates the true uncertainty in this particular distribution.

5.2   Comparison with other approaches and outlook

In this chapter, we have performed leading and next-to-leading order QCD fits to the world data on the g_1 polarized structure function measured with proton, neutron and deuteron targets. We obtain sets of polarized parton distributions which can be used for further phenomenological analyses. The experimental precision is highest for the proton and deuteron data. These constrain the shapes of the valence u and d distributions. The sea quark and gluon distributions are still largely undetermined. There is a weak constraint on the overall size of the former, but almost no information at all on the flavour decomposition of the sea. We have presented three qualitatively different gluon distributions, characterized by different behaviours at large x.

A similar analysis of polarized structure functions has been reported recently in [85], using the 'dynamical parton model' approach in which the distributions at small x are generated dynamically from valence-like distributions at a small starting scale $Q_0^2 \sim 0.3\, m_p^2$. Requiring positivity at this low scale yields more severe constraints on the polarized distributions (in particular the polarized gluon distribution) than in our analysis. The authors of [85] suggest two scenarios for the flavour decomposition of the light quark sea. The 'standard' scenario is identical with our approximation of an SU(3) symmetric sea quark polarization at Q_0^2, while the 'valence' scenario assumes the SU(3)$_f$–symmetry in

---

[2]Working in the Adler–Bardeen scheme, the authors of [63] were able to constrain the first moment of the polarized gluon distribution to be $\eta_G = 1.54 \pm 0.74$ at $Q_0^2 = 1\,\mathrm{GeV}^2$, which is consistent with our results (Table 5.3). As in our analysis, the x-dependence of $\Delta G(x, Q^2)$ was found to have only a weak impact on $g_1(x, Q^2)$.
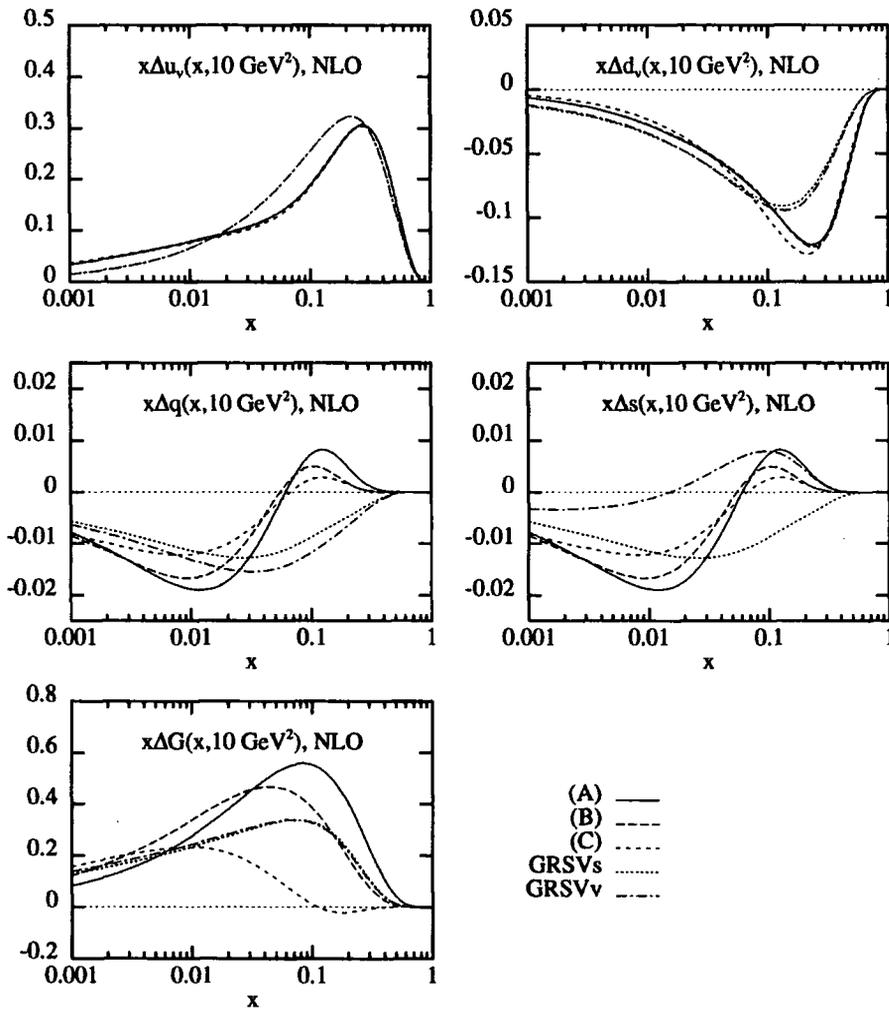
Figure 5.4: Comparison of different polarized parton distributions: Set (A)-(C) obtained in this analysis and Set (s) and (v) from [85].

the Ellis–Jaffe sum rule only to apply to the valence quark contributions – i.e. it breaks, strictly speaking, the $SU(3)_f$ symmetry of the hadronic current by decomposing it into a valence and a sea current. In the 'valence' scenario, all deviations from the naïve expectation of the Ellis–Jaffe sum rule can be attributed to an enhanced polarization of $\bar{u}$ and $\bar{d}$ quarks. A comparison between the NLO distributions of [85] and our results is shown in Fig. 5.4. The valence quark distributions obtained in both analyses are in

relatively good agreement with each other, while the sea quark and gluon distributions show large differences. This again reflects the lack of experimental information on these distributions.

The authors of [63] carry out a comparable analysis in the Adler–Bardeen scheme (cf. Section 4.2), with particular emphasis on a determination of η_G from the structure function data. The resulting distributions do not necessarily respect positivity of the distributions at large x and yield the conceptual problem that asymmetries can exceed unity at large x. Therefore, we refrain from a detailed comparison with our results.

A variety of experiments on polarized nucleons is presently under discussion. In the following chapter, we will examine several observables which could provide more precise information on the polarized gluon and sea quark distributions than the structure functions measured at present. This will illustrate the application of the parton distributions obtained above to other hard processes.

Chapter 6

Measuring polarized parton distributions at future experiments

Up to now, all experimental information on the polarized proton structure comes from the structure function $g_1(x, Q^2)$ of the proton, neutron and deuteron (cf. Table 4.1). It was demonstrated in the previous chapter that these measurements provide sufficient information for a determination of the polarized valence quark distributions $\Delta u_v(x, Q^2)$ and $\Delta d_v(x, Q^2)$, while the polarized sea quark and gluon distributions are only loosely constrained by the structure function data. As $g_1(x, Q^2)$ is dominated by valence quark contributions at presently accessible energies, complementary measurements of other quantities appear to be crucial for a more precise determination of these distributions. This chapter summarizes experimental options presently under construction or discussion and examines the sensitivity of particular observables to polarized parton distributions.

6.1 Future experiments on polarized nucleons

Initiated by the original $g_1(x, Q^2)$ measurement of the EMC collaboration [45] an extensive programme of spin-structure function measurements was started at CERN (SMC), SLAC (E142/E143) and DESY (HERMES). All these experiments have now produced

first results which were the key ingredients in the global parton distribution fit of Chapter 5. The experiments at CERN and DESY are still taking data on various polarized targets while a new generation of experiments at higher beam energies (E154/E155) is presently in operation at SLAC. A variety of spin experiments is planned presently. A short description of the most promising proposals is given below.

RHIC–SPIN

The Relativistic Heavy Ion Collider (RHIC) at Brookhaven will have two longitudinally polarized proton beams at $\sqrt{s} = 200 - 500$ GeV [86]. This collider is presently under construction, first data-taking is expected in the year 2001. Two multi-purpose detectors (STAR and PHENIX) will be installed in the interaction regions; an integrated luminosity of 320 pb^{-1} at $\sqrt{s} = 200$ GeV or 800 pb^{-1} at $\sqrt{s} = 500$ GeV for two years of operation is anticipated.

Inclusive photon and jet production asymmetries will provide a measurement of the polarized gluon distribution, information on the polarized sea quark distributions might be gained from Drell–Yan pair and W-boson production.

COMPASS

Using the muon beam ($E_\mu = 100 - 200$ GeV) and the polarized target of the present SMC experiment with an upgraded detector setup, the COMPASS collaboration [87] plans to study the final states of polarized deep inelastic scattering events. If this experiment is approved, it could start operation in 1999; the expected luminosity is 1.9 fb^{-1} per year.

Apart from an improved measurement of the structure function $g_1(x, Q^2)$, this experiment will yield information on $\Delta G(x, Q^2)$ from the production of charmed mesons.

SLAC programme

In addition to the E154/E155 experiments [88], which are presently measuring polarized structure functions at $E_{beam} = 50$ GeV, several future spin experiments are under

discussion.

The most promising option for a measurement of $\Delta G(x, Q^2)$ is the study of polarized photon–proton collisions using a beam of bremsstrahlung photons at $E_\gamma = 45$ GeV [89].

SPIN @ HERA

A possible option for the future of the HERA collider is the operation of a polarized proton beam. This would provide the unique opportunity of a study of polarized ep collisions at $\sqrt{s} \simeq 300$ GeV [90]. Studies on the machine aspects of this project are presently being carried out. If these yield positive results and the project is approved, it could be realized in the middle of the next decade. Presently, HERA provides a luminosity of 15 pb^{-1}/year, which could be increased by a factor 4 over the next few years.

The physics prospects of this project have been studied in a working group of the "Future physics at HERA"–workshop [91], yielding several possible measurements which appear to be unique at HERA. The prospects for a measurement of $g_1(x, Q^2)$ will be discussed below.

HERA–$\vec{\text{N}}$

Operating the present HERMES spectrometer in the HERA proton beam (HERA-$\vec{\text{N}}$, [92]) offers the possibility to study singly polarized (unpolarized beam on polarized target) hadron–hadron collisions at $\sqrt{s} = 40$ GeV. Such an experiment is under discussion and could start operation after the end of the HERMES programme in 1999. An integrated luminosity of 240 pb^{-1} for three years of data-taking is anticipated.

As single spin asymmetries vanish in the perturbative domain of QCD, this experiment would need additional information on final state polarizations in order to construct a double spin asymmetry sensitive to polarized parton distributions. An example of such an asymmetry is discussed in detail in section 6.6.

If HERA is operated with a polarized proton beam, this experiment could study asymmetries in polarized proton–nucleon collisions at energies well below RHIC-SPIN,

offering in particular better prospects for the measurement of asymmetries in the Drell–Yan process, which will be studied in Section 6.3

6.2 Precision measurements of the polarized structure functions

The derivative of $F_2(x, Q^2)$ with respect to Q^2 has been used to measure the unpolarized gluon distribution in fixed target experiments [93] ($0.008 < x < 0.5$) and at HERA [94] ($2 \cdot 10^{-4} < x < 3 \cdot 10^{-2}$). The method is particularly powerful at small x, where the gluon distribution dominates the Q^2 evolution, $\partial F_2(x)/\partial \ln Q^2 \sim P_{qG}(y) \otimes G(x/y)$. In the same way, we can use our three sets of distributions A, B and C to explore the sensitivity of the polarized structure function evolution to $\Delta G(x, Q^2)$.

6.2.1 Fixed target experiments

The kinematic range of fixed target experiments is limited, as the available lepton–proton centre-of-mass energy only grows like the square root of the beam energy. A substantial increase above the present energies (cf. Table 4.1) cannot be expected.

Fig. 6.1 shows predictions for the asymmetry $A_1(x, Q^2)$ as a function of Q^2 in the kinematic range representative of current fixed target experiments. The asymmetry is obtained from Eq. (4.4) with g_1 calculated using the polarized distributions presented in the previous chapter and F_1 calculated using the NLO unpolarized MRS(A$'$) distributions of [41]. The latter are extrapolated to lower values of Q^2, which reproduces the full backwards evolution to within a few per cent.

At large x, there is no sensitivity to $\Delta G(x, Q^2)$ – the evolution is completely dominated by the quark contribution. At small x, on the other hand, we see some dependence on the gluon. In this region $\Delta P_{qG}(y) \otimes \Delta G(x/y) < 0$ (cf. Section 4.3.2), and so the derivative $\partial A_1/\partial \ln Q^2$ is more negative for the sets that have a larger gluon polarization above the x value considered. In particular, we see that at $x \sim 0.01$ the proton asymmetry is almost Q^2
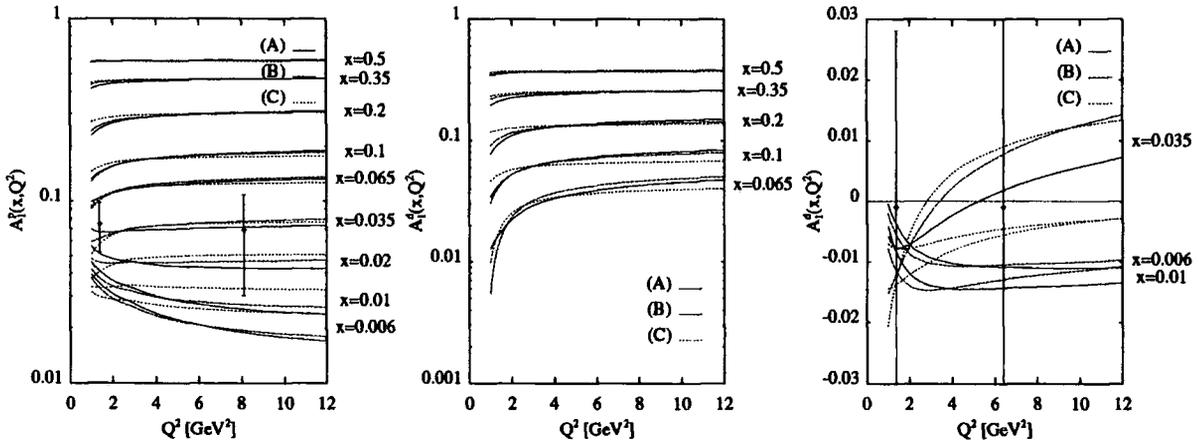
Figure 6.1: Q^2 dependence of $A_1^{p,d}(x, Q^2)$ in next-to-leading order using the Gluons A, B and C. To illustrate the sensitivity of current experiments, we show the $x = 0.035$ data-points from the recent SMC and E143 measurements.

independent for Set C, but decreases with increasing Q^2 for Sets A and B. Unfortunately, the sensitivity of the present experiments is much worse than the differences between the various sets. To illustrate this, we have included two data-points at $x = 0.035$ from the recent SMC and E143 measurements. For the deuteron, the quark contribution to the structure function is smaller, and so the dependence on $\Delta G(x, Q^2)$ at small x is somewhat enhanced. Considering the large errors on the present data, it seems doubtful that a measurement of the polarized gluon distribution from the Q^2 variation of $A_1(x, Q^2)$ is feasible for values of Q^2 where perturbative expressions can be safely applied. The SLAC E154/E155 experiments will clearly improve this measurement, a further decrease of the statistical errors may be achieved by combining several bins in x. Nevertheless, it still has to be kept in mind that a determination of $\Delta G(x, Q^2)$ from the Q^2 dependence of $A_1(x, Q^2)$ can never reach the quality of the corresponding unpolarized measurement, as the gluonic contribution is not as dominant in the evolution of polarized parton distributions as it is in the unpolarized evolution (cf. Section 4.4).

82

6.2.2 HERA

In the foreseeable future, the HERA collider may be able to accelerate polarized protons [90]. This would offer the unique opportunity of measuring the polarized structure function $g_1^p(x, Q^2)$ far beyond the Q^2 range of present fixed target experiments. In order to judge the quality of the new information gained from such a measurement, an order-of-magnitude estimate of the statistical errors is crucial. The structure function $g_1^p(x, Q^2)$ is extracted from a measurement of the asymmetry (4.4). Under realistic experimental conditions, the electron and proton beam will only be partially polarized, yielding the experimentally observable asymmetry

$$A_\parallel(x, Q^2) = \lambda_e \lambda_p \ D \ \frac{g_1^p(x, Q^2)}{F_1^p(x, Q^2)},$$

where λ_e (λ_p) denote the polarizations of the electron (proton) beam. The statistical error on $x g_1(x, Q^2)$ is therefore:

$$\begin{aligned}
\delta[x g_1^p(x, Q^2)] \ = \ & \frac{1}{2\lambda_e \lambda_p} \frac{1 + (1-y)^2}{1 - (1-y)^2} \left[2x F_1^p(x, Q^2) + \frac{2(1-y)}{1 + (1-y)^2} F_L^p(x, Q^2) \right] \\
& \times \ \left(\mathcal{L}_{int} \int \frac{d^2\sigma^{(\text{unpol.})}}{dx dQ^2} dx dQ^2 \right)^{-1/2} \sqrt{1 - A_\parallel(x, Q^2)},
\end{aligned} \qquad (6.1)$$

where the unpolarized differential cross section is integrated over the bin used in the experimental measurement.

To study the accuracy of a measurement of $g_1^p(x, Q^2)$ in the collider mode of HERA, we have evaluated the above expression using the unpolarized parton distribution set MRS(A$'$) from [41] with the next-to-leading order polarized parton distribution set A described in Chapter 5. We apply the following cuts to the HERA phase space [95]: $0.1 < y < 0.95$, $Q^2 > 1$ GeV^2, $\Theta_{e'} < 176°$ and $E_{e'} > 5$ GeV, and consider two scenarios for the beam energies:

$$(a) \ : \ \sqrt{s} = 300 \text{ GeV} \quad \text{with} \quad E_e = 27.44 \text{ GeV}, \ E_p = 820 \text{ GeV},$$

$$(b) \ : \ \sqrt{s} = 150 \text{ GeV} \quad \text{with} \quad E_e = 18.75 \text{ GeV}, \ E_p = 300 \text{ GeV}.$$
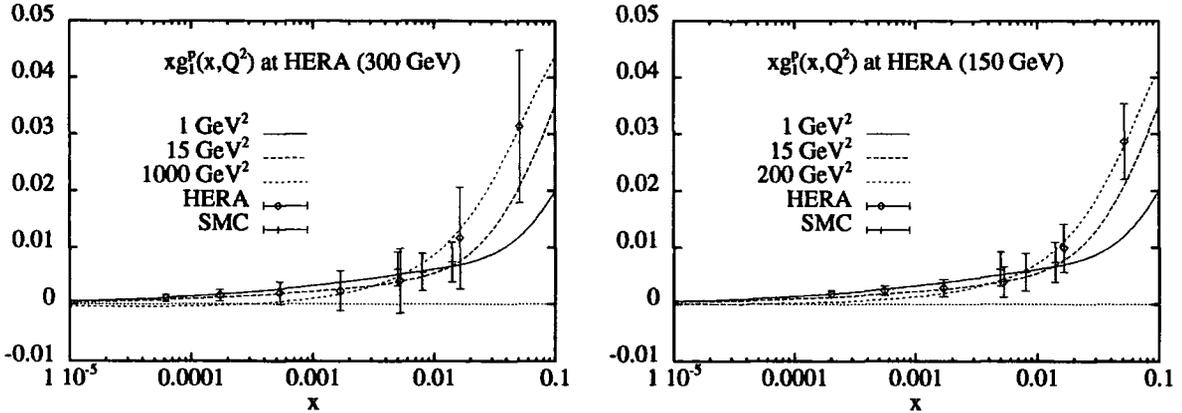
Figure 6.2: Expected errors for a measurement of $g_1^p(x, Q^2)$ at the HERA collider with $s^{1/2} = 300$ GeV and $s^{1/2} = 150$ GeV.

The expected errors for an integrated luminosity of 60 pb^{-1} at $\lambda_e = \lambda_p = 0.8$ in these two scenarios are shown in Fig. 6.2. We take two bins per decade in x and only one bin in Q^2. These results are consistent with the leading-order estimates of [96], bearing in mind the different cuts applied. In particular, we estimate smaller errors in the small-x region, as we apply no cuts on the hadronic final state.

The average Q^2 values probed at HERA range from 2 GeV^2 ($x \approx 6 \cdot 10^{-5}$) to 1060 GeV^2 ($x \approx 0.05$) for $\sqrt{s} = 300$ GeV and from 1.7 GeV^2 ($x \approx 2 \cdot 10^{-4}$) to 270 GeV^2 ($x \approx 0.05$) for $\sqrt{s} = 150$ GeV. For reference, we also show in Fig. 6.2 a parametrization of $g_1^p(x, Q^2)$ obtained from the NLO set A. To illustrate the impact of a measurement at HERA, we include the three lowest data-points reported by the SMC experiment [47], corresponding to Q^2 values around 1.5 GeV^2. It is apparent that a measurement at lower beam energies will yield data of higher statistical quality. In contrast, the higher beam energies yield a measurement at smaller x.

A measurement of $g_1^p(x, Q^2)$ at the HERA collider will evidently not provide a large number of precision data on the x and Q^2 dependencies of this structure function. Hence,

it will not provide sufficient information for an indirect determination of the polarized gluon density[1]. The important physics result of such a measurement is the determination of the small-x behaviour of $g_1^p(x, Q^2)$, for which various, significantly different predictions exist [71, 72, 73]. It is important to stress that a measurement of $g_1^p(x, Q^2)$ at small x will reduce the experimental uncertainty on the Ellis–Jaffe sum rule. The impact of the small x region can be easily seen in Fig. 6.2, as the Ellis–Jaffe sum rule is proportional to the area enclosed by $xg_1^p(x, Q^2)$ and the x axis.

A final remarkable point on the measurability of $g_1^p(x, Q^2)$ at HERA is the impact of the minimum cut on y on the statistical error. As the photon depolarizes for small y, a small cut on y (such as $y > 0.01$) diminishes the average polarization in the bin, even though more data are included. We find that a minimal cut on y between 0.1 and 0.2 yields the optimal accuracy of the measurement.

6.3 Hadroproduction of Drell–Yan pairs

Structure functions measured in deep inelastic lepton–nucleon scattering probe a particular combination of quark distributions in the nucleon. The mere knowledge of these structure functions is therefore insufficient for a distinction between valence and sea quarks and for a further decomposition of the light quark sea into different flavours. These are only possible if additional information from other experimental observables is taken into account.

Fits of unpolarized parton distributions (e.g. [41]) obtain this information from two sources. The weak structure functions measured in neutrino–nucleon scattering probe different combinations of parton distributions than their electromagnetic counterparts. The inclusion of these structure functions in a global fit can therefore constrain the flavour structure of the unpolarized sea. A direct probe of the antiquark distributions in the nucleon is given by the production of lepton pairs in hadron–hadron collisions [28], the

---

[1]Recall that a determination of $\Delta G(x, Q^2)$ requires a precise measurement of the *slope* of g_1 as a function of Q^2.

85

Drell–Yan process. It is in fact the inclusion of data from *both* processes in the global fits which allows a precise determination of the distribution of antiquarks and its flavour decomposition.

The recent fits of polarized parton distributions described in Chapter 5 have to rely entirely on the available data on the polarized structure function $g_1^{p,d,n}(x,Q^2)$. The distinction between valence and sea quark contributions to this structure function is possible to a certain extent if additional information from sum rules is taken into account. The flavour structure of the polarized sea is however completely unknown at present. It seems rather doubtful whether more precise measurements of this structure function will be able to provide more information on these two issues.

Polarized neutrino–nucleon scattering experiments will not be feasible in the foreseeable future, a measurement of polarized weak structure functions may however be possible from charged current interactions at HERA [97] if polarization in the collider mode can be achieved.

An experimental study of the polarized Drell–Yan cross section would be possible with the HERA-$\vec{\text{N}}$ experiment, operated with a polarized proton beam onto a polarized nucleon target. We will examine the prospects of such a measurement in this section.

6.3.1   The polarized Drell–Yan process

The production of lepton pairs in hadronic collisions was already introduced as a test of the parton model in Section 2.5. It can be understood as annihilation of a quark–antiquark pair to a virtual photon, which decays into a lepton pair of invariant mass M^2. The polarized and unpolarized cross sections for this process are conventionally defined to be [98]

$$
d\Delta\sigma \equiv \frac{1}{2}\left(d\sigma^{++} - d\sigma^{+-}\right), \qquad d\sigma \equiv \frac{1}{2}\left(d\sigma^{++} + d\sigma^{+-}\right),
$$

where $(++)$ and $(+-)$ denote the configurations of aligned and antialigned hadron spins. In the QCD corrected parton model, these hadronic cross sections can be expressed as a
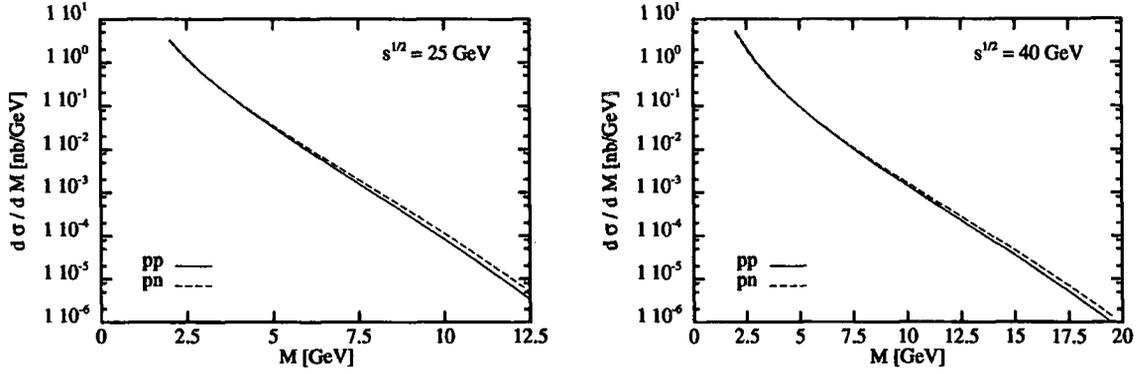
Figure 6.3: Unpolarized Drell–Yan cross section in proton–proton and proton–neutron collisions.

convolution of parton level coefficient functions with the appropriate parton distributions:

$$\frac{d[\Delta]\sigma}{dM^2} = \frac{4\pi\alpha}{9sM^2} \int_0^1 dx_1 dx_2 dz \delta(x_1 x_2 z - \tau) \sum_q e_q^2$$

$$\left\{ \left\{ [\Delta]q_1(x_1, \mu_F^2) [\Delta]\bar{q}_2(x_2, \mu_F^2) + (1 \leftrightarrow 2) \right\} \left([-]\delta(1-z) + \frac{\alpha_s(\mu_F^2)}{2\pi}[\Delta]c_q^{DY}(z) \right) \right.$$

$$\left. + \left\{ \left([\Delta]q_1(x_1, \mu_F^2) + [\Delta]\bar{q}_1(x_1, \mu_F^2) \right) [\Delta]G_2(x_2, \mu_F^2) + (1 \leftrightarrow 2) \right\} \frac{\alpha_s(\mu_F^2)}{2\pi}[\Delta]c_G^{DY}(z) \right\},$$

$$(6.2)$$

where μ_F^2 indicates the mass factorization scale and $\tau = M^2/s$ is the Drell–Yan scaling variable.

The next-to-leading order corrections to the unpolarized coefficient functions have been calculated in [153] and are listed in (8.6). The polarized corrections are given in [98, 100], they read in the $\overline{\text{MS}}$-scheme:

$$\Delta c_q^{DY}(z) = -C_F \left[8 \left(\frac{\ln(1-z)}{1-z} \right)_+ - 2\frac{1+z^2}{1-z} \ln z - 4(1+z)\ln(1-z) \right.$$

$$\left. + \delta(1-z)(-8 + 4\zeta_2) + 2\ln\frac{M^2}{\mu_F^2} \left\{ \left(\frac{2}{1-z} \right)_+ - 1 - z + \frac{3}{2}\delta(1-z) \right\} \right],$$

$$\Delta c_G^{DY}(z) = -T_F \left[(2z-1)\ln\frac{(1-z)^2}{z} + \frac{5}{2} - z - \frac{3}{2}z^2 + \ln\frac{M^2}{\mu_F^2} \{(2z-1)\} \right]. \quad (6.3)$$

87
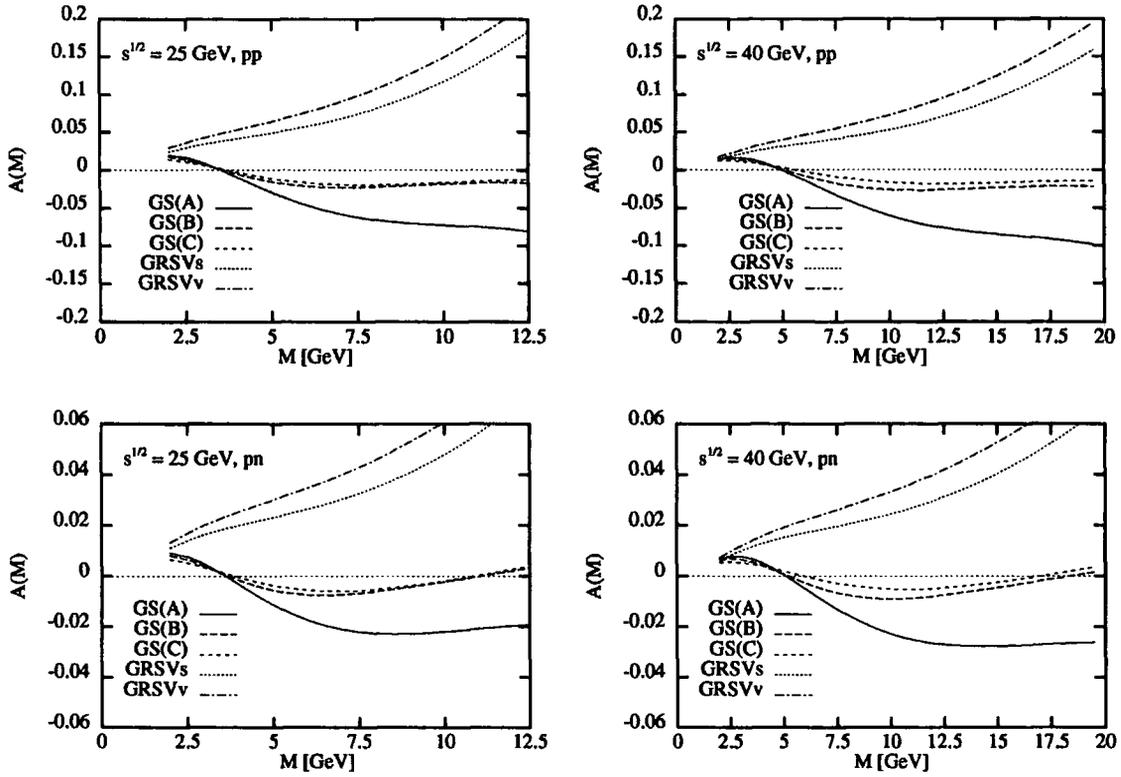
Figure 6.4: Expected asymmetries in the polarized Drell–Yan process.

It turns out that inclusion of these corrections is crucial at fixed target energies, as they contribute about 30% of the total cross section. A fully consistent study of the Drell–Yan process at next-to-leading order was up to now only possible in the unpolarized case, as the polarized parton distributions could only be determined to leading accuracy. With the recently calculated polarized two-loop splitting functions [35], the polarized distributions can now be determined to next-to-leading order from fits to structure function data [69, 85].

Using these distributions in combination with the unpolarized distributions (set A') from [41], we have calculated the total Drell–Yan cross section $d\sigma/dM$ and the expected

asymmetry

$$A(M) \equiv \frac{\mathrm{d}\Delta\sigma/\mathrm{d}M}{\mathrm{d}\sigma/\mathrm{d}M}$$

for proton and (idealized) neutron targets at centre-of-mass energies $\sqrt{s} = 40$ GeV (HERA-$\vec{\mathrm{N}}$) and $\sqrt{s} = 25$ GeV. The latter could be achieved by operating HERA-$\vec{\mathrm{N}}$ with a proton beam energy of about 330 GeV. Figure 6.3 shows the unpolarized Drell–Yan production cross section as a function of the invariant mass of the lepton pair. It has to be noted that invariant masses $M \leq 4$ GeV and 9 GeV $\leq M \leq 11$ GeV must be excluded from an experimental measurement, as lepton pair production in these mass regions is dominated by the decay of quarkonium resonances. An experiment with $\sqrt{s} = 25$ GeV will clearly be restricted to the invariant mass range 4 GeV $< M < 9$ GeV; depending on the available luminosity, a measurement for $M > 11$ GeV could be possible at $\sqrt{s} = 40$ GeV.

The Drell–Yan cross section at HERA-$\vec{\mathrm{N}}$ ($\sqrt{s} = 40$ GeV) is about two orders of magnitude bigger than at RHIC–SPIN ($\sqrt{s} = 200$ GeV) if evaluated at fixed τ.

Figure 6.4 shows the asymmetries obtained with the polarized NLO parton distributions of [69] (GS(A,B,C)) and [85] (GRSVs,v). The spread in these predictions reflects the present lack of knowledge on the behaviour of polarized parton distributions in the region $x > 0.1$. A sizable asymmetry of more than $\pm 10\%$ can be expected in proton–proton collisions, the asymmetry in proton–neutron collisions is considerably smaller.

We have checked the perturbative stability of these results by variation of the mass factorization scale. It turns out that the absolute value of the asymmetry is decreased (increased) by a maximum of 1.5% if we take $\mu_F = 2M$ ($\mu_F = M/2$). This variation is significantly smaller than the difference between the different parton distribution functions.

6.3.2   Conclusions and Outlook

A measurement of the polarized Drell–Yan cross section in the double polarized mode of HERA-$\vec{\mathrm{N}}$ appears feasible, provided an integrated luminosity of 100 pb^{-1} or more can be

achieved. Such a measurement would provide important information on the polarization of the light quark sea at large x, a region which cannot be probed with measurements of polarized weak structure functions. Such a measurement would be unique to HERA-$\vec{N}$, as the polarized Drell–Yan process cannot be studied at the RHIC. Furthermore, HERA-$\vec{N}$ could measure Drell–Yan asymmetries off different targets, which might be used to infer the flavour structure of the polarized sea. Such a measurement would however require much higher luminosity due to the low asymmetries on the (idealized) neutron target.

So far, we have only examined the invariant mass distribution of the Drell–Yan pairs, which is already able to discriminate different parametrizations for the polarized sea quark distributions. Even more information can be gained from more differential distributions (e.g. in the lepton pair rapidity y), which could be obtained with higher luminosity.

6.4 Photoproduction of open charm

The parton model as described in Chapter 3 assumes that the proton mainly consists of light (u, d, s) quarks and gluons. As the photon in the deep inelastic scattering only couples to the charged quarks, the proton structure functions are dominated by the light quark contributions. If the final state of a deep inelastic scattering event contains heavy (c, b) quarks, it seems very likely that these have been produced by photon–gluon fusion in the particular event[2]. Assuming the photon–gluon fusion mechanism, the parton level cross section has been calculated [101], including full helicity dependence [78]. The process is dominated by the photoproduction $(Q^2 \simeq 0)$ region. Therefore, it is a reasonable approximation to consider only real photon–proton interactions with a beam of

---

[2]Alternatively (see e.g. [42]), one could choose to work with an intrinsic heavy quark distribution in the nucleon. This distribution is – apart from a marginal contribution at low scales – generated due to $g \to Q\bar{Q}$-splitting in the evolution process. The impact of the gluon distribution on the physical observable is qualitatively similar, the approaches only differ close to the production threshold.

bremsstrahlung photons[3]. The parton level cross sections then read:

$$\sigma(\hat{s}) = e_q^2 \frac{2\pi\alpha\alpha_s(\hat{s})}{\hat{s}} \left(-\beta(2-\beta^2) + \frac{1}{2}(3-\beta^4)\ln\frac{1+\beta}{1-\beta} \right),$$

$$\Delta\sigma(\hat{s}) = e_q^2 \frac{2\pi\alpha\alpha_s(\hat{s})}{\hat{s}} \left(3\beta - \ln\frac{1+\beta}{1-\beta} \right), \tag{6.4}$$

where $\hat{s}$ is the invariant mass squared at the parton-level and $\beta = \sqrt{1-4m_q^2/\hat{s}}$ is the velocity of the heavy quark. The bremsstrahlung spectrum of real photons emitted off a lepton beam is

$$f_{\gamma/l} = \frac{\alpha}{2\pi} \frac{1+(1-y)^2}{y} \ln\frac{E_l^2}{m_l^2}, \tag{6.5}$$

with $y = E_\gamma/E_l$. Depending on the photon energy, only a certain fraction

$$\frac{\Delta f_{\gamma/l}(y)}{f_{\gamma/l}(y)} = \frac{1-(1-y)^2}{1+(1-y)^2} \tag{6.6}$$

of the lepton polarization is transferred to the photon.

Photoproduction of charm quarks has been used by the EMC collaboration to determine the unpolarized gluon distribution [102], yielding consistency with other determinations. Furthermore, various phenomenological studies [64, 79] have demonstrated the sensitivity of this process to the polarized gluon distribution. In the following we investigate the prospects of such a measurement with the proposed COMPASS experiment described above.

The allowed kinematic range for $\hat{s}$ is determined by the heavy quark production threshold and the maximum available energy

$$4m_q^2 < \hat{s} < s = 2yE_lM_p.$$

At fixed photon energy, one can then define an observable asymmetry

$$A(y) = \frac{\Delta f_{\gamma l}(y)}{f_{\gamma l}(y)} \frac{\int d\hat{s}\, \Delta\sigma(\hat{s})\, \Delta G(\hat{s}/s, \hat{s})}{\int d\hat{s}\, \sigma(\hat{s})\, G(\hat{s}/s, \hat{s})}. \tag{6.7}$$

---

[3]Although perturbative approaches fail to describe structure functions at $Q^2 \simeq 0$, this treatment is justified for the production of heavy quarks, as the quark mass provides a natural hard scale.
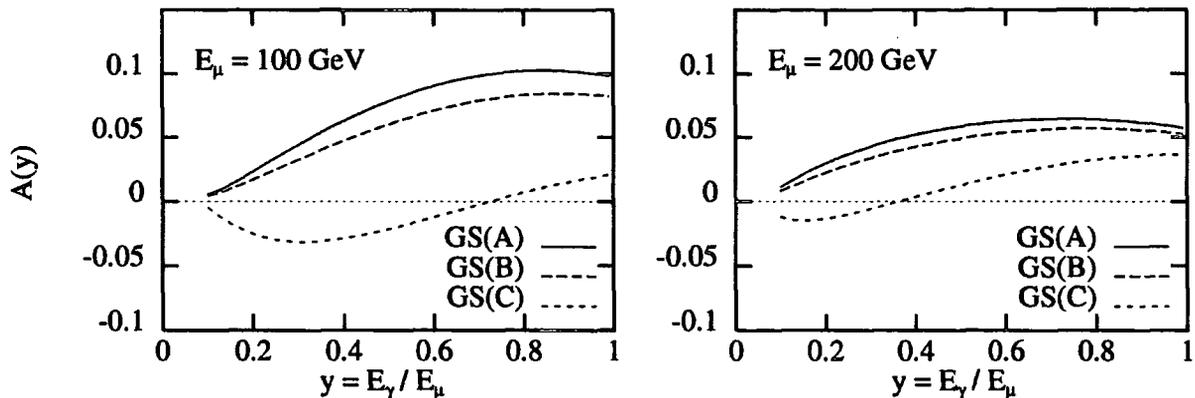
Figure 6.5: Open charm photoproduction asymmetry.

Fig. 6.5 shows this asymmetry evaluated for $E_\mu = 100$ GeV and $E_\mu = 200$ GeV, using the leading order polarized gluon distributions A-C in combination with the unpolarized GRV94 [44] gluon distributions. Given the anticipated luminosity, this asymmetry should be measurable to an accuracy of 3% for a single bin $0.35 < y < 0.85$ [87]. It is apparent that the measurement will yield a better discrimination of the different gluon distributions if carried out at lower beam energies. At low energies, the polarized gluon distribution is probed at larger values of x, where $\Delta G(x)/G(x)$ is larger. Hence a clear distinction between Gluon A and C is possible, and the sign of the polarized gluon distribution at large x can be measured.

6.5 Photoproduction of J/ψ mesons

The J/ψ meson is the lightest $(c\bar{c})$ bound state. Its discovery [103] provided first evidence for the existence of charmed quarks. It decays with a branching ratio of about 12% into lepton–antilepton pairs [58] and can therefore be detected relatively easily as a peak in the final state lepton–antilepton invariant mass distribution of a particular experiment.

Inelastic J/ψ production from a nucleon target directly probes the gluon distribution

via the photon–gluon fusion subprocess $\gamma^* + g \to (c\bar{c}) + g$, which can be described in the colour-singlet model of [104]. This model assumes that both quarks forming the J/ψ have exactly half its velocity and form a colour singlet. The transition amplitude from the quark pair to the meson state is then inferred from the magnitude of the J/ψ wavefunction at the origin. This model successfully describes the production of J/ψ mesons in lepton-hadron collisions [105, 106], provided the theory prediction is scaled with a K-factor accounting for higher order corrections. This K-factor is of order 4 and almost independent of the kinematical variables. The next-to-leading order calculation of J/ψ photoproduction [107] is in better agreement with the experimental data, but still needs to be scaled by a (smaller) K-factor at fixed target energies.

Depending on the virtuality of the photon, one can distinguish two different classes of events: photoproduction ($Q^2 \approx 0$) and leptoproduction ($Q^2 \gg 0$). The EMC [105] and NMC experiments [106] have obtained measurements of the *unpolarized* leading-order gluon distribution in the range $x \sim 0.05 - 0.25$ from the photoproduction process. The results agree well – after K factor correction – with gluon distributions extracted from other processes, for example large-p_T direct photon production. The corresponding cross section for *polarized* J/ψ leptoproduction has been calculated in [108].

Taking the photoproduction limit $Q^2 \to 0$, one obtains

$$\frac{d\sigma_{\lambda h}^{\gamma N}(E_\gamma)}{dp_T^2 dz} = \frac{2\pi}{\alpha} \cdot \eta G_\lambda(\eta, M_{J/\psi}^2) \cdot \frac{8\alpha_s^2 M_{J/\psi} \Gamma_{J/\psi \to e^+ e^-}}{3} \cdot \frac{z(1-z)}{[M_{J/\psi}^2(1-z) + p_T^2]^2}$$
$$\times [A(z) + h\lambda C(z)] \cdot \mathcal{F}(p_T^2, z), \tag{6.8}$$

with

$$\mathcal{F}(p_T^2, z) = \frac{z^2(1-z)^2}{(p_T^2 + (1-z)^2 M_{J/\psi}^2)^2} \frac{1}{(p_T^2 + M_{J/\psi}^2)^2},$$

$$A(z) = \frac{M_{J/\psi}^2}{2} \left(z^2(M_{J/\psi}^2 - zs_{\gamma N})^2 + (1-z)^2(M_{J/\psi}^2 + \right.$$
$$\left. (1-z)s_{\gamma N})^2 + (s_{\gamma N} - M_{J/\psi}^2)^2 \right),$$

$$C(z) = (1-z)(M_{J/\psi}^2 - zs_{\gamma N})(zM_{J/\psi}^2(M_{J/\psi}^2 - zs_{\gamma N}) + (z-2)M_{J/\psi}^2 s_{\gamma N}),$$

$$s_{\gamma N} \;=\; 2 M_N E_\gamma,$$

$$\eta \;=\; \frac{p_T^2 + (1-z) M_{J/\psi}^2}{z(1-z)s_{\gamma N}},$$

$$z \;=\; \frac{E_{J/\psi}}{E_\gamma},$$

$$\lambda \;=\; \text{gluon helicity},$$

$$h \;=\; \text{lepton helicity}.$$

The polarized (unpolarized) cross sections are obtained by taking the difference (sum) over the helicity states. The polarized cross section is then proportional to $\Delta G(\eta) = G_+(\eta) - G_-(\eta)$ and depends only on $C(z)$, while the unpolarized cross section is proportional to $G(\eta) = G_+(\eta) + G_-(\eta)$ and depends only on $A(z)$. Taking the cross sections integrated over one of the variables, one can define two physics asymmetries:

$$\mathcal{A}(z) \;=\; \frac{d\Delta\sigma^{\gamma N}(E_\gamma)}{dz} \bigg/ \frac{d\sigma^{\gamma N}(E_\gamma)}{dz}, \tag{6.9}$$

$$\mathcal{A}(p_T^2) \;=\; \frac{d\Delta\sigma^{\gamma N}(E_\gamma)}{dp_T^2} \bigg/ \frac{d\sigma^{\gamma N}(E_\gamma)}{dp_T^2}. \tag{6.10}$$

Such an asymmetry could be studied in a dedicated experiment with a 45 GeV photon beam at SLAC [89] or using the spectrum of bremsstrahlung photons ($\bar{E}_\gamma \sim 25$ GeV) at HERMES. Both these experiments work at lower photon energies than [105, 106], a discrimination between elastic $z = 1$ and inelastic $z < 1$ photoproduction of J/ψ mesons will therefore be more difficult, if not impossible. The expected cross sections for $p_T^2 > p_{T\min}^2 = 0.1$ GeV^2 and $z = 0.9$ (cuts like in [105, 106]) are shown in Fig. 6.6. The cut on p_T^2 is required to guarantee the applicability of the colour singlet model, which assumes the colour neutrality of the $(c\bar{c})$-pair to be obtained by the emission of a single, hard gluon. The bulk of J/ψ mesons produced will be rejected by this cut.

As illustrated in Fig. 6.7, significantly different asymmetries are expected for the three gluon distributions A, B and C. These predictions are obtained for the asymmetries $\mathcal{A}(z)$ and $\mathcal{A}(p_T^2)$, calculated for $E_\gamma = 45$ GeV using the three leading order distributions in

94
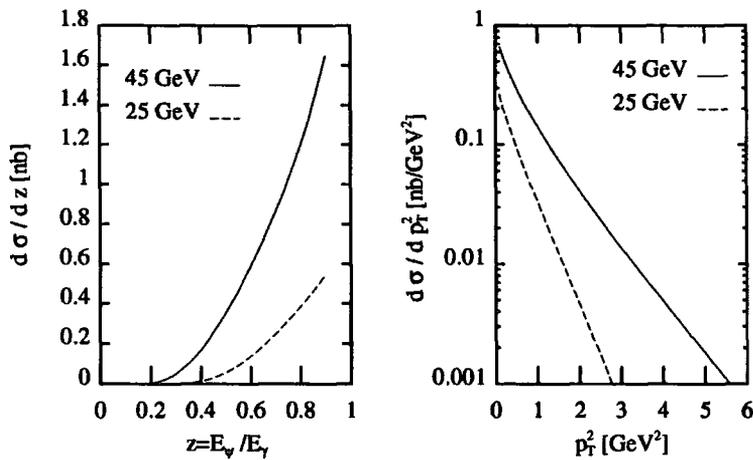
Figure 6.6: Cross section for photoproduction of J/ψ mesons.
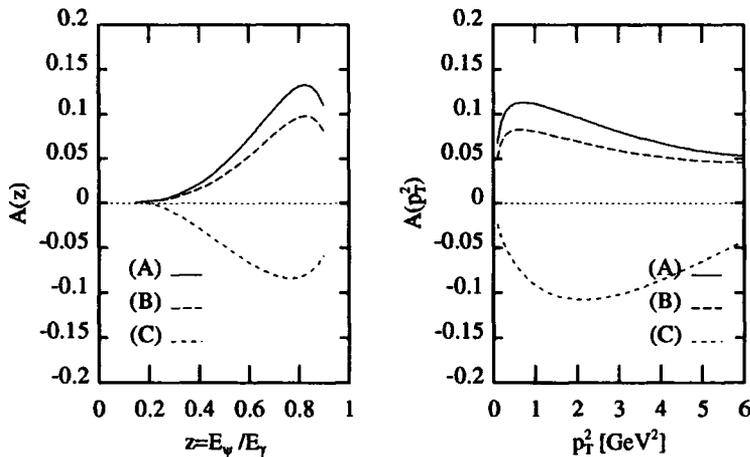
Figure 6.7: Expected asymmetry for J/ψ photoproduction at $E_\gamma = 45$ GeV.

combination with the unpolarized leading order gluon distributions of [44]. The asymmetries at $E_\gamma = 25$ GeV are identical in shape but only half in magnitude. It should be noted that these asymmetries assume 100% photon polarization. Depending on the fraction of photon and lepton energy, the photon only carries a certain percentage of the lepton polarization (cf. eq. (6.6)).

Note that small z corresponds to large η and vice versa. It is furthermore noted that

the ordering of the predictions obtained with different gluon sets simply reflects the ordering of the different gluon distributions in the region $\eta \gtrsim 0.1$. Due to the relatively large asymmetry of up to 15%, such a measurement could provide first information on the leading order polarized gluon distribution at $Q^2 \approx M_{J/\psi}^2$. The x-range in which the distribution is probed depends on the acceptance cuts used in the experimental measurement. A dedicated simulation for the HERMES experiment [109] has shown that a range $0.22 < x < 0.5$ would be accessible there.

It should be noted that the cross section for J/ψ production is about two orders of magnitude lower than the cross section for open charm production. The experimental advantage of studying J/ψ production is the clear decay signature in the leptonic channel, which makes a precise reconstruction of the kinematics possible.

6.6 Hadroproduction of J/ψ pairs

All asymmetries considered so far in this section required the polarization of *both* initial state particles. Present accelerators can provide polarized electron and muon beams at high energies and satisfactory intensities. These are then scattered off fixed polarized nucleon targets. In contrast, polarized proton beams are presently only available as secondary beams from Λ-decay and have hence a low luminosity and a wide energy spread. The acceleration of polarized proton beams and their storage still remains a challenging task.

Therefore it is worth considering whether one can determine the polarized gluon distribution $\Delta G(x, Q^2)$ from collisions of an unpolarized proton beam with a polarized proton target. As outlined above, such a configuration would be possible at the HERA-$\vec{N}$ experiment.

Parity invariance of QCD implies vanishing of all single spin asymmetries in the perturbative region. Therefore, information on the spin state of at least one particle in the final state is required for the construction of a measurable asymmetry. Several observables [92], such as jet handedness or χ'-polarization have been suggested in the literature.

Unfortunately, all these channels suffer from low luminosities and poor analysing power (correlation between parton and hadron helicity). In this section, we examine another process, which might allow the construction of an asymmetry containing one initial and one final spin state: the production of J/ψ pairs in proton–proton collisions.

6.6.1 Theoretical framework

The colour singlet model introduced in the previous section can be extended to the production of J/ψ pairs in hadron–hadron collisions: the dominant subprocess is gluon–gluon fusion to two $(c\bar{c})$ pairs. The condition of non-zero transverse momentum again has to be applied to justify a perturbative treatment. This model yields the parton level cross section [110]

$$\frac{\mathrm{d}\hat{\sigma}(a + b \to J/\psi J/\psi)}{\mathrm{d}\cos\Theta^*} = \frac{\pi^3\alpha_s^4(1 - M_{J/\psi}^2/\hat{s})^{1/2}}{72\hat{s}}\frac{|\Psi(0)|^4}{M_{J/\psi}^2}\frac{1}{64}|\mathcal{M}|^2 \qquad (a+b = q+\bar{q} \text{ or } g+g).$$
(6.11)

The helicity averaged matrix element $\mathcal{M}$ was first calculated in [110], and its full helicity dependence was derived in [111]. The explicit formulae are too lengthy to be included in this chapter.[4].

To relate this parton level cross section to a measurable observable at the hadronic level, it has to be convoluted with the corresponding parton distributions

$$\mathrm{d}\sigma(p + p \to J/\psi J/\psi) = \sum_{a,b}\int \mathrm{d}x_1\mathrm{d}x_2 f_{a/p}(x_1)f_{b/p}(x_2)\mathrm{d}\hat{\sigma}(a + b \to J/\psi J/\psi).$$
(6.12)

The above expression is dominated by the $(g+g)$ subprocess, whose contribution is about five times as big as the one from $(q + \bar{q})$ at HERA-$\vec{\text{N}}$ energies. In what follows, we will restrict ourselves to a study of the gluonic contribution.

To estimate the expected cross section at $\sqrt{s} = 40$ GeV, we have evaluated the above expression for the leading order parton distributions given in [112] (DO1.1) and [44] (GRV94). The resulting p_T^2 distributions are shown in Fig. 6.8. We use $\Lambda_{QCD}^{(4)} = 200$ MeV and $|\Psi(0)|^2 = 0.043$ GeV^3, obtained from the leptonic width of the J/ψ [58].

---

[4]We would like to thank Sergey Baranov for providing the FORTRAN-code for $\mathcal{M}$
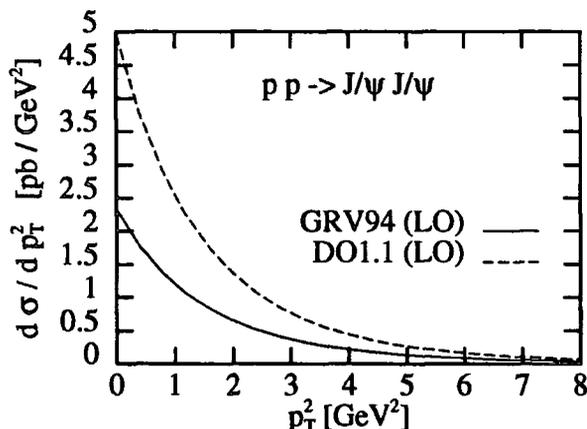
Figure 6.8: Cross section for production of J/ψ pairs at HERA-$\vec{\mathrm{N}}$

	σ^{tot}	$\sigma(p_T^2 > 1\,\mathrm{GeV}^2)$
DO1.1	10.3 pb	6.5 pb
GRV94	4.9 pb	3.0 pb

Table 6.1: Total cross sections for $pp \to J/\psi J/\psi$ evaluated for the parton distributions of [112] and [44].

The large discrepancy between both predictions reflects mainly the uncertainty in the unpolarized gluon distribution $G(x)$ in the high-x region. For consistency with the polarized distributions considered in the remainder of this section, we will work with $G(x)$ from [44]. For the proposed luminosity of HERA-$\vec{\mathrm{N}}$, one can expect 1200 J/ψ pairs to be produced.

It should be recalled that the colour singlet model assumes the colour neutrality of the $(c\bar{c})$-pair to be obtained by a single, hard gluon exchange. This condition is only satisfied for sufficiently large transverse momentum of the final state particles. In the forward region ($p_T^2 \lesssim 0.5\,\mathrm{GeV}^2$), the same neutral state can be obtained by the multiple exchange of soft gluons. Hence the colour singlet model tends to underestimate the cross section in this region.

98

6.6.2 Reconstruction of the J/ψ

The total cross section for proton-proton collisions at $\sqrt{s} = 40$ GeV is $\sigma^{tot}(pp) = 41$ mb [58], ten orders of magnitude bigger than the cross section for the production of J/ψ pairs. In order to identify these events in the background of mulithadron production, a clear decay signature of at least one of the J/ψ mesons is needed. Only the leptonic decay $J/\psi \to \gamma^* \to l^+l^-$ can provide such a clear signature, as the pair of oppositely charged leptons can easily be distinguished from the hadronic background. The branching ratio [58]

$$Br(J/\psi \to \gamma^* \to l^+l^-) = 12\%$$

of this decay channel therefore reduces the number of visible events.

HERA-$\vec{\mathrm{N}}$ will (at least for the first years of running) only have a polarized target, with an unpolarized beam. Information on the initial state polarization will therefore have to be extracted from the final state. In the case of J/ψ pair production, at least the helicity of one of the J/ψ's has to be measured. As the J/ψ is a massive spin-1 vector meson, it has three possible helicity states: $-1, 0, +1$. The 0 and ± 1 states correspond to different partial waves, and can therefore be easily distinguished from the energy spectra of the decay products. Unfortunately, no information on the initial state polarization can be gained from the 0 state, as the corresponding differential cross section is symmetric under the change of one initial state helicity. We will discuss the possible decay channels of the J/ψ with a view to distinguishing the $+1$ and -1 helicity states:

(i) **weak decays:** Parity violating weak decay modes could provide a clear separation between these two states. As the J/ψ does not have any known weak decay modes, this possibility is ruled out.

(ii) **leptonic decays:** Parity invariance of the electromagnetic interaction relates the decay cross sections of both helicity states. As the lepton helicities cannot be measured, both states are indistinguishable.

(iii) **decays to scalar mesons:** The distribution of the final state particles in these

99

decays is given by the $l = 1, m = \pm 1$ partial waves. As the partial waves for $m = -1$ and $m = 1$ are identical for vector particles, this decay channel cannot distinguish between these states.

(iv) **radiative decays:** If the J/ψ decays into a real photon and scalar mesons (e.g. $J/\psi \rightarrow \eta_c \gamma$), the helicity of the J/ψ could be reconstructed from the measured helicity of the photon[5]. This decay channel contributes with a branching ratio of about 4% [58]. Provided a helicity measurement on the photon, this is the only channel in which the helicity of the J/ψ can be measured.

From the above considerations, it becomes clear that a J/ψ pair produced in single polarized proton-proton collisions can only be used for an asymmetry measurement for the specific final state configuration in which one J/ψ decays leptonically while the other decays into a photon accompanied by scalar mesons. The probability of this configuration is

$$P = 2 \times \left(Br(J/\psi \rightarrow l^+ l^-)\right) \times \left(Br(J/\psi \rightarrow \gamma + \text{scalars})\right) \simeq 1\%.$$

Therefore, only twelve of the expected 1200 events can provide an asymmetry measurement under ideal experimental conditions at HERA-$\vec{\text{N}}$. It should therefore be already clear at this point that such a measurement will fail to provide information on $\Delta G(x)$. Regardless of this negative result, we will provide an estimate of the asymmetries one could expect at HERA-$\vec{\text{N}}$.

6.6.3 Expected asymmetries

Under ideal experimental conditions at HERA-$\vec{\text{N}}$, the spin of the target proton and the helicity of one of the two J/ψ mesons can be measured in a rather small fraction of the events. Using this information, we can construct the following asymmetry

$$A = \frac{d\sigma(p^+ J/\psi^+) + d\sigma(p^- J/\psi^-) - d\sigma(p^- J/\psi^+) - d\sigma(p^+ J/\psi^-)}{d\sigma(p^+ J/\psi^\pm) + d\sigma(p^- J/\psi^\pm)}.$$

---

[5]Even though such a measurement could be possible in principle, it seems rather doubtful that it could be carried out with the HERA-$\vec{\text{N}}$ apparatus.
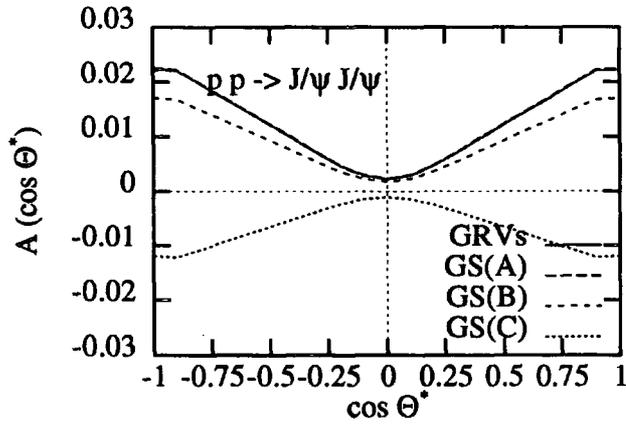
Figure 6.9: Expected asymmetry in the single polarized mode of HERA-$\vec{N}$.
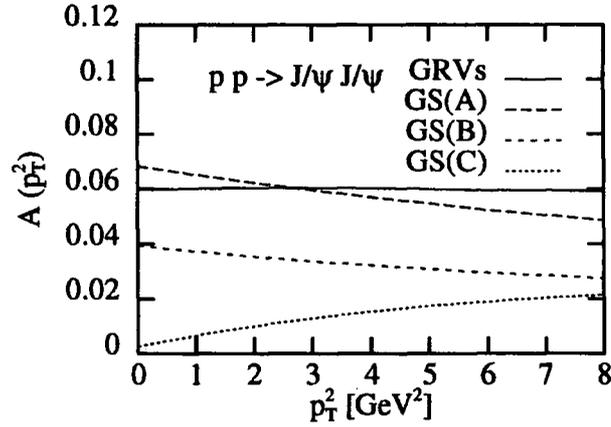
Figure 6.10: Expected asymmetry in the double polarized mode of HERA-$\vec{N}$.

This asymmetry can be related to the parton level cross sections, keeping in mind that the helicity state of the second J/ψ is summed over. For convenience, we use the following shorthand notation for the parton level matrix elements of particular helicity combinations:

$$[h(g, \text{beam})\ h(g, \text{target})\ h(J/\psi_1)\ h(J/\psi_2)] \equiv$$

$$d\hat{\sigma}(g(h(\text{beam})) + g(h(\text{target})) \rightarrow J/\psi(h_1)J/\psi(h_2)). \tag{6.13}$$

101

Omitting terms related by parity invariance, the asymmetry is

$$A = \frac{\int dx_1 dx_2 G(x_1, Q^2) \Delta G(x_2, Q^2) \{2[\Sigma \Delta + +] + [\Sigma \Delta 0+] + [\Sigma \Delta + 0]\}}{\int dx_1 dx_2 G(x_1, Q^2) G(x_2, Q^2)[\Sigma \Sigma \pm \pm]}, \qquad (6.14)$$

where Σ (Δ) denotes the sum (difference) of the possible helicity states.

The scale of the parton distributions in the above expression and the scale of $\alpha_s(Q^2)$ in the matrix elements is taken to be $Q^2 = (M_{J/\psi})^2$. We have evaluated the above asymmetry as a function of the angle between the J/ψ pair and the proton beam direction in the parton-parton centre-of-mass system (which can be reconstructed from the final state). The unpolarized $G(x, Q^2)$ is taken from [44]. In Fig 6.9, we compare the predictions obtained with the parametrizations of $\Delta G(x, Q^2)$ from [113] (standard scenario) and [69] (Gluon A-C). Although the asymmetries obtained with these parametrizations are significantly different from each other, $A(\cos \Theta^*)$ never exceeds 3%. The asymmetry becomes maximal if the J/ψ pair is produced at very small angles with respect to the proton beam, i.e. at low transverse momenta.

Keeping in mind the low number of reconstructable events, this small asymmetry turns out to be unmeasurable in the single polarized mode of HERA-$\vec{N}$. The situation would be different for a double polarized measurement (i.e. with a polarized HERA proton beam): in this case, the reconstruction of helicities in the final state is no longer necessary for an asymmetry measurement. Therefore, one can expect about 270 J/ψ pairs with at least one lepton pair decay. The asymmetry can be defined in the standard way

$$A = \frac{d\sigma(p^+ p^+) + d\sigma(p^- p^-) - d\sigma(p^+ p^-) - d\sigma(p^- p^+)}{d\sigma(pp)}.$$

In terms of the parton densities this asymmetry reads

$$A = \frac{\int dx_1 dx_2 \Delta G(x_1, Q^2) \Delta G(x_2, Q^2)[+\Delta \Sigma \Sigma] - [-\Delta \Sigma \Sigma]}{\int dx_1 dx_2 G(x_1, Q^2) G(x_2, Q^2)[\Sigma \Sigma \Sigma \Sigma]}. \qquad (6.15)$$

Fig. 6.10 shows this asymmetry as a function of p_T^2 for the different parametrizations of $\Delta G(x, Q^2)$ mentioned above. Depending on the parametrization, the asymmetry could be as large as 7% and depends only weakly on p_T^2. If HERA-$\vec{N}$ would have a polarized HERA proton beam available, this measurement could give some indications on $\Delta G(x, Q^2)$ for $x \approx 0.3$.

102

6.7 Prospects and outlook

In this section we have discussed several experimental observables which could probe the polarized gluon and sea quark distributions. We have found that an indirect determination of the polarized gluon distribution from the evolution of the cross section asymmetry $A_1(x, Q^2)$ seems to be hardly feasible both at fixed target experiments and at HERA with polarized beams.

The production of Drell–Yan pairs in polarized proton–proton collisions can put severe constraints on the shape of the polarized sea quark distribution at $x > 0.1$. Due to the decrease of the cross section with energy, a fixed target experiment would be favourable.

It was found that the production of charmed quarks in lepton–proton collisions induced by quasi–real photons could be a sensitive probe on the polarized gluon distribution. We have studied the production of charmed mesons (open charm) and of the lightest $(c\bar{c})$ bound state, both turn out to provide promising experimental observables. Finally, we have studied a rather exotic channel in singly polarized proton–proton collisions, which yielded a negative result like most other singly polarized observables.

The RHIC-SPIN collider will provide first information on the polarized gluon distribution at the beginning of the next decade. If the COMPASS experiment is approved, it will yield a complementary measurement at the same time. Provided all technical problems can be overcome, the HERA collider might be operated with a polarized proton beam in about ten years from now. This would open a new kinematic region for the measurement of the polarized structure function and provide a facility for polarized proton–nucleon collisions at fixed target energies.

Chapter 7

Hard diffraction at HERA

The electron–proton collider HERA allows detailed studies of the final state of deep inelastic scattering events, which are not possible at fixed target experiments. It is in particular possible in the hadronic final state, to distinguish between fragments of the struck parton (current jet) and fragments of the remnant proton (remnant jet). While the former are found in direction of the virtual photon, the latter are moving in the direction of the proton beam.

The struck parton (quark or gluon) and the proton remnant both carry colour charge, whereas the final state contains only colour-neutral hadrons. The hadronization of current and remnant jets is not completely independent, a few hadrons are emitted in the rapidity interval between these jets.

Soon after the start of the experimental programme at HERA, the ZEUS collaboration reported [114] that a significant fraction of DIS events at small x showed a different event topology: no remnant jet was observed and no hadronic activity was found in the rapidity region between the current jet and the proton beam direction (Fig. 7.1). This observation was confirmed by the H1 experiment shortly afterwards [115].

The lack of any hadronic activity around the proton beam direction and the mismatch between the initial-state and observed final-state energy requires the proton (deflected only by a small angle and therefore outside the rapidity coverage of the detectors) to be
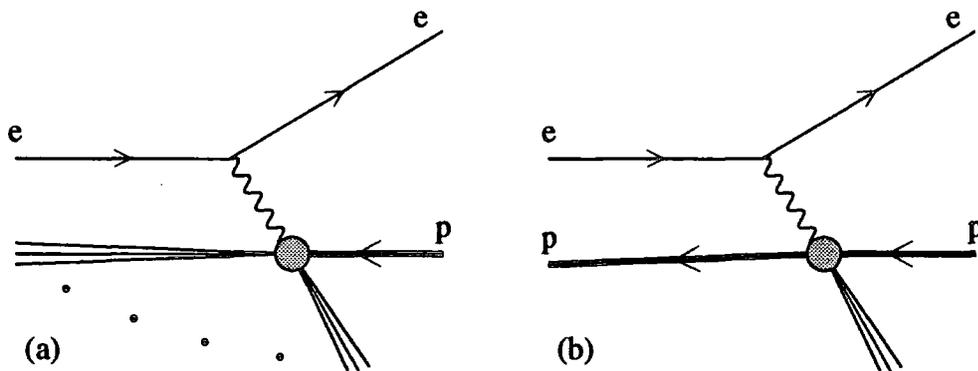
Figure 7.1: Event topology of deep inelastic scattering (a) and diffractive deep inelastic scattering (b) at HERA.

in the final state, still carrying a large fraction of its initial momentum. These events with a remnant proton in the final state are classified as diffractive deep inelastic scattering (DS) events.

The physical origin of this phenomenon is not understood at present. A possible explanation is given by the pomeron model, which was originally introduced in [116] to explain the high energy behaviour of *elastic* hadron–hadron cross sections.

In this chapter we will study the application of the pomeron model to diffractive deep inelastic scattering at HERA. An introduction to the phenomenology of this process and its interpretation in terms of the pomeron model is given in Section 7.1. As the remnant proton in DS cannot be detected, a complete reconstruction of the event kinematics is not possible. We examine the reliability of the kinematical approximations made at HERA in Section 7.2 and show in Section 7.3 that the pomeron model predicts a kinematical correlation between outgoing electron and remnant proton. If the pomeron interpretation of DS is correct, one should be able to study the pomeron structure function from this process. A very simple model for the pomeron structure will be presented in Section 7.4. This model allows the study of other observables, such as the charm quark contribution to DS, which can provide a consistency check of the pomeron interpretation. We will

105

determine the parameters of this model from experimental data in Section 7.5. Finally, section 7.6 contains the conclusions of our study. Experimental data on diffractive deep inelastic scattering have improved considerably since the study in this chapter was originally published [117]. We shall briefly comment on these new results in the conclusions of this chapter.

7.1 Phenomenology of hard diffraction at HERA

Measurements at HERA have indicated that a significant fraction of deep inelastic electron–proton scattering events have a final state with a large rapidity gap between the proton beam direction and the observed final state particles [114, 115]. The cross section for this diffractive deep inelastic scattering can be written in a form similar to the cross section for deep inelastic scattering (3.12), it reads

$$\frac{\mathrm{d}\sigma^{DS}}{\mathrm{d}\alpha_p \mathrm{d}t \mathrm{d}x \mathrm{d}Q^2} = \frac{4\pi\alpha^2}{xQ^4} \left\{ 1 - y + \frac{y^2}{2[1 + R^{DS}(x, Q^2, \alpha_p, t)]} \right\} F_2^{DS}(x, Q^2, \alpha_p, t). \quad (7.1)$$

Apart from the DIS variables x and Q^2, we need two more variables to describe the four-momentum of the outgoing proton: the proton loses a fraction α_p of its initial longitudinal momentum, its deflection is described by the invariant momentum transfer t between the incoming and outgoing proton.

The presence of a large rapidity gap between the proton beam direction and the current jet suggests that the diffractive events are caused by a deep inelastic scattering off an uncharged and colourless object, which was emitted from the proton beforehand, Fig. 7.3. We shall show below that the experimental data give strong indications that this object is the pomeron, which was postulated to explain the high energy behaviour of hadronic cross sections. To motivate this interpretation, we briefly review some features of the theory of elastic hadron interactions (Regge theory) in this section. The Regge theory interpretation of hadron–hadron scattering yields the existence of the pomeron and determines some of its properties.

106

7.1.1 A brief excursion into Regge theory

Elastic hadron–hadron dynamics at high energies and low momentum transfers are not calculable in perturbative QCD. A theoretical description of these dynamics is however possible in the framework of Regge theory [118, 119][1].

Quantum field theories like QED or QCD have matter fields and gauge fields as fundamental degrees of freedom, scattering amplitudes are calculable from first principles. Regge theory does not provide a method to *calculate* scattering amplitudes, but to *relate* amplitudes for different processes using fundamental symmetry and analyticity properties. In addition to the 'classical' symmetries such as isospin or crossing, Regge theory introduces the analyticity in the angular momentum variable l. We illustrate this using the example of an arbitrary $2 \rightarrow 2$ scattering amplitude $A(s,t)$. Keeping in mind, that the variable s can be reexpressed by the centre-of-mass scattering angle $z_t \equiv \cos\Theta|_t$ at fixed t, this amplitude can be written

$$A(s,t) = 16\pi \sum_{l=0}^{\infty}(2l+1)A_l(t)P_l(z_t), \tag{7.2}$$

where P_l is the l-th Legendre polynomial. The above expression is called *partial wave expansion* of the scattering amplitude. Its coefficients can be obtained from

$$A_l(t) = \frac{1}{16\pi}\frac{1}{2}\int_{-1}^{1}\mathrm{d}z_t P_l(z_t)A\left(s(z_t,t),t\right). \tag{7.3}$$

The analytical continuation of the Legendre polynomials is given by the hypergeometric function [70]

$$P_l(z) = {}_2F_1(-l, l+1; 1; (1-z)/2),$$

which is an alternating finite series for integer values of l. Like for the partial sums encountered in Appendix A.4, one finds that the sums with odd l are on a different branch in the complex l plane than those with even l. The analytical continuation for odd and even l will therefore be different. Hence we have to consider amplitudes of odd

---

[1]We will outline the basic features of Regge theory in this section. The discussion follows closely the book of Collins [119], where more details can be found.

(A_l^-) and even (A_l^+) signature, which can be expressed similar to (7.2)

$$A^S(s,t) = 16\pi \sum_{l=0}^{\infty} (2l+1)A_l^S(t)P_l(z_t).$$ (7.4)

The fundamental assumption of Regge theory is that the partial wave amplitude $A_l^S(t)$ has only isolated poles in $\alpha(t)$ in the complex l plane. If this is true, and $A_l^S(t)$ is moreover free of branch cuts in the right half plane $\text{Re}(l) > 0$, the partial wave expansion (7.4) can be written as a contour integral in the complex l-plane [119]:

$$\begin{aligned}
A^S(s,t) &= -\frac{16\pi}{2i} \int_{-0.5-i\infty}^{-0.5+i\infty} (2l+1)A_l^S(t)\frac{P_l(-z_t)}{\sin \pi l}\mathrm{d}l \\
&\quad -16\pi^2(2\alpha(t)+1)\beta(t)\frac{P_{\alpha(t)}(-z_t)}{\sin \pi\alpha(t)}.
\end{aligned}$$ (7.5)

For simplicity it is assumed, that A_l^S has only a single pole $\alpha(t)$, which is in the right half plane. The behaviour at $s \to \infty$ can be studied from the limit $z_t \to \infty$. One finds that the first term in (7.5) is suppressed like $s^{-0.5}$, while the second term behaves like $s^{\alpha(t)}$, i.e. it dominates the high energy behaviour of the scattering amplitude. This term is called *Regge pole*. The function $\alpha(t)$ is called *Regge trajectory*. In calculating the contribution of a Regge pole to the physical trajectory $A(s,t)$, which contains partial waves of odd and even signature, one has to take into account that the corresponding trajectory has a definite signature. Even trajectories should only yield poles in the amplitude for even l, odd trajectories only for odd l. The physical amplitude therefore reads

$$A(s,t) = -16\pi^2(2\alpha(t)+1)\beta(t)\left(1 + \mathcal{S}e^{-i\pi\alpha(t)}\right)\frac{P_{\alpha(t)}(-z_t)}{\sin \pi\alpha(t)}.$$ (7.6)

Inspection of the above amplitude yields that $A(s,t)$ develops a resonance pole if $\alpha(t)$ coincides with a positive (odd or even) integer. If this occurs for a positive argument $t = t_R$, it can be interpreted as a particle resonance of spin $\alpha(t_R)$ and mass $\sqrt{t_R}$. Classifying light hadrons of identical quantum numbers and increasing spin onto Regge trajectories, one finds that $\alpha(t)$ can be put into the simple form

$$\alpha(t) = \alpha_0 + \alpha' t.$$

108
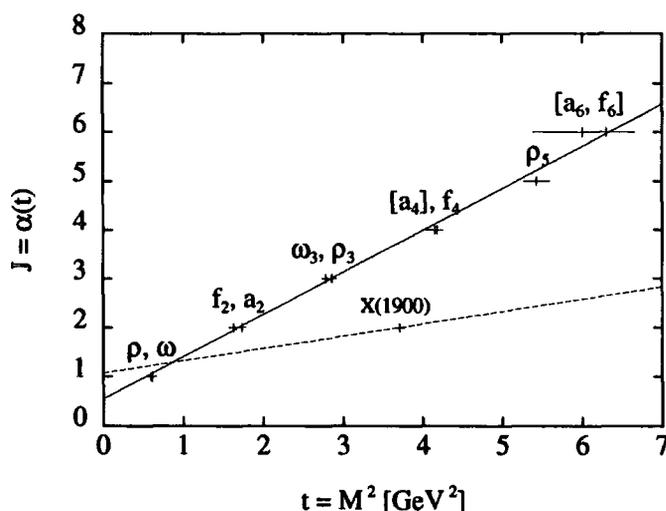
Figure 7.2: An example of a particle trajectory (solid line) and the pomeron trajectory (dashed line). The particle trajectory shown is the quadruple degenerate (ρ, ω, a_2, f_2)-trajectory. The masses of the particles on this trajectory are taken from [58], the particles in square brackets have only been observed indirectly. A recently observed $X(1900)$ state [120] is the first particle candidate on the pomeron trajectory. The parameterizations for both trajectories are taken from the fit of [121].

The crossed amplitude with negative t can be understood as simultaneous exchange of all particles on the particular trajectory. The differential cross section for the exchange of a Regge trajectory in $2 \rightarrow 2$ scattering in the limit $s \rightarrow \infty$ can be written

$$\frac{d\sigma}{dt} = F(t) \left(\frac{s}{s_0}\right)^{2\alpha(t)-2}, \tag{7.7}$$

where $F(t)$ is a function of t only, s_0 is an arbitrary scale factor. The optical theorem yields moreover the total $2 \rightarrow X$ cross section due to Regge trajectory exchange to be

$$\sigma^{tot} \sim \left(\frac{s}{s_0}\right)^{\alpha(0)-1}. \tag{7.8}$$

While many elastic hadron–hadron scattering processes can be described as due to the exchange of particle trajectories, it turns out that experimental data on certain elastic scattering processes and on total hadron–hadron cross sections at large s cannot be

explained by the exchange of known particle trajectories. While the most singular Regge trajectories have $\alpha(0) \approx 0.5$, the total proton–proton cross section appears to be constant – even slightly rising – at large s. This indicates the presence of a trajectory with $\alpha(0) \approx 1$ – the *pomeron trajectory* [116]. An example of a particle trajectory and the pomeron trajectory are displayed in Fig. 7.2.

So far, no particle on the pomeron trajectory has been observed experimentally, there is however some experimental evidence [120] for a spin–2 resonance state on this trajectory (cf. Figure 7.2). The properties of the pomeron trajectory, in particular the pomeron coupling to hadrons, can therefore not be studied from pomeron production and decay, they have to be *modeled* on the basis of cross section data. A successful description of hadronic scattering data can be obtained in the pomeron model of Donnachie and Landshoff [122]. This model assumes, that the pomeron couples to the total number of constituent quarks in a hadron with a coupling strength b. The pomeron–proton vertex is very similar to the photon–proton vertex of (1.3), with two minor modifications: (a) the anomalous magnetic form factor $F_2(t)$ vanishes, as the pomeron is an isoscalar; (b) an overall factor of i yields the positive C-parity of the pomeron. The contribution of pomeron exchange to the elastic proton–proton cross section reads in this model

$$\frac{\mathrm{d}\sigma}{\mathrm{d}t} = \frac{[3bF_1(t)]^4}{4\pi} \left(\frac{s}{s_0}\right)^{2\alpha(t)-2} . \tag{7.9}$$

The pomeron coupling strength to quarks $b \approx 1.8$ GeV^{-1} and the pomeron trajectory

$$\alpha(t) = 1 + \epsilon + \alpha' t \quad \text{with} \quad \epsilon = 0.086, \quad \alpha' = 0.25 \text{ GeV}^{-2} \tag{7.10}$$

are tuned to explain a wide range of experimental results in pp, $p\bar{p}$, and πp scattering [121]. The vertex form factor $F_1(t)$ is identical to the photon–proton form factor of (1.7).

7.1.2 The pomeron interpretation of diffractive deep inelastic scattering

From the kinematical distribution of the diffractive deep inelastic scattering events at HERA, it seems most likely that this process is mediated by the pomeron. The deep
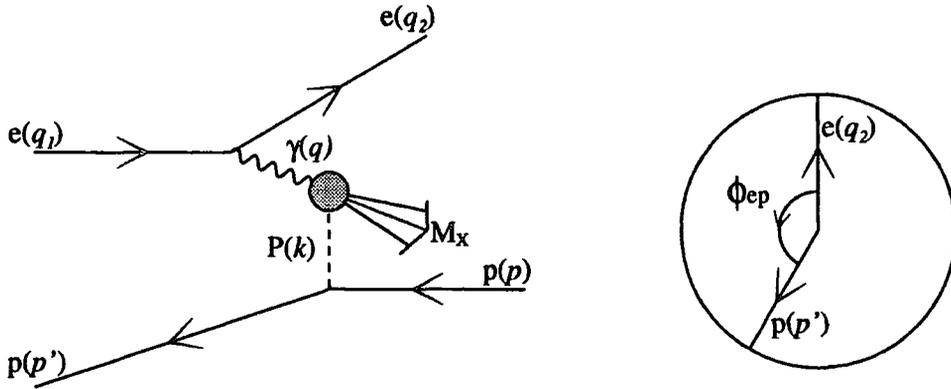
Figure 7.3: Kinematics of deep inelastic electron-pomeron scattering

inelastic scattering in this process (Fig. 7.3) therefore probes the structure function of the pomeron. The idea that the pomeron has partonic constituents was first proposed by Ingelman and Schlein [123], and given strong support by the hadron collider experiments of the UA8 collaboration [124, 125].

If this interpretation is correct, then one would expect that the diffractive cross section (7.1) could be factorized into a part corresponding to the emission of an uncharged, colourless pomeron from the proton and another part corresponding to a hard scattering off the partonic constituents of the pomeron:

$$\frac{d\sigma^{DS}}{d\alpha_p dt dz dQ^2} = \left[\frac{4\pi\alpha^2}{zQ^4} \left\{ 1 - y_P + \frac{y_P^2}{2[1 + R^P(z, Q^2, t)]} \right\} F_2^P(z, Q^2, t) \right] f(\alpha_p, t), \quad (7.11)$$

where $z = z(x, Q^2, \alpha_p, t)$ is the fraction of pomeron momentum carried by the struck parton and

$$y_P = \frac{yx}{\alpha_p z} \quad (7.12)$$

is the virtual photon energy 'seen' by the pomeron. $F_2^P(z, Q^2, t)$ denotes the DIS structure function of the pomeron, $f(\alpha_p, t)$ represents the probability that a proton emits a pomeron with momentum fraction α_p and t-channel invariant momentum transfer t.

A common but only approximately correct way of parametrizing this factorization property is to write the diffractive structure function as the product of an emission factor

111

and the deep inelastic structure function of the pomeron [126, 127]:

$$F_2^{DS}(x, Q^2, \alpha_p, t) = F_2^P(z, Q^2, t)\, f(\alpha_p, t).$$ (7.13)

However R^{DS} and R^P functions cannot be related in such a simple manner. We will discuss various tests of the factorizability of the cross section and investigate the applicability of the factorization at the level of structure functions (7.13) later.

If the object struck by the virtual photon in diffractive deep inelastic scattering is indeed the same pomeron which controls the high energy behaviour of hadronic scattering amplitudes, then its basic properties and in particular its coupling to the proton are already known. For example, Donnachie and Landshoff give a simple form for $f(\alpha_p, t)$ [126] which they derive from their model for the pomeron–proton coupling discussed in the previous subsection:

$$f(\alpha_p, t) = \frac{9b^2}{4\pi^2}\, [F_1(t)]^2\, \alpha_p^{1-2\alpha(t)}.$$ (7.14)

Other similar forms[2] for f have been proposed in the literature, see for example [123], but the differences are not crucial to the present discussion.

The above picture has recently been given strong support by a detailed analysis of diffractive deep inelastic scattering events by the H1 collaboration at HERA [130]. Their principle conclusions are:

(i) The Q^2 dependence of F_2^{DS} is consistent with scattering off point-like objects.

(ii) The factorization of the diffractive structure function into pieces which depend separately on z and α_p, cf. (7.13), is observed.

(iii) The α_p dependence of f is consistent with that predicted by Donnachie and Landshoff, i.e. $\sim \alpha_p^{1-2\alpha(0)}$.

---

[2]There have been several recent attempts to derive a perturbative formulation of the pomeron. These approaches [128], all based on the BFKL equation [129], will not be discussed in the present context, as there is insufficient conclusive evidence at present for the applicability of the BFKL equation in the kinematic range covered at HERA. In the following discussion, we will always assume $f(\alpha_p, t)$ (as for any other hadron–hadron interaction at low invariant momentum transfer) to represent a non-perturbative coupling of pomerons to the proton, which can be determined from the experimental data.

(iv) The pomeron structure function F_2^P is 'hard', i.e. the point-like constituents carry a significant fraction of the pomeron's momentum on average.

Not yet determined experimentally are:

(i) The 'nature' of these hard constituents (i.e. whether the pomeron predominantly consists of quarks or of gluons).

(ii) The kinematical distribution of the remnant protons.

If diffractive deep inelastic scattering is interpreted as deep inelastic scattering off a pomeron target, it is possible to make definite predictions for these undetermined observables. These can serve as experimental test of this interpretation, once a more precise measurement is possible. The 'nature' of the pomeron constituents can be determined from an analysis of its structure function if interpreted in the parton model. The kinematical distribution of the remnant protons can be calculated from the known emission factor $f(\alpha_p, t)$. We will address both issues below.

7.2 Kinematics of electron-pomeron deep inelastic scattering

7.2.1 Reconstruction of the kinematical invariants

To reconstruct all kinematical parameters in the diffractive deep inelastic scattering cross section (7.11), it is sufficient to measure the momenta of the outgoing electron (q_2) and the remnant proton (p'). It is convenient to parametrize these momenta in a Sudakov decomposition using two light-like vectors directed along the beam and a space-like transverse vector. Since we are ignoring the electron mass we can use the incoming electron momentum q_1 for one of the light-like vectors. For the other, we define

$$\bar{p} = p - \frac{M^2}{s - M^2} q_1 \, ,$$

113

where $s = (p + q_1)^2$, $p^2 = M^2$ and, by construction, $\bar{p}^2 = 0$. Hence we can write

$$
\begin{aligned}
q_2 &= A\bar{p} + Bq_1 + \vec{q_T}\ , \\
p' &= C\bar{p} + Dq_1 + \vec{k_T}\ ,
\end{aligned}
\tag{7.15}
$$

which implies

$$
\begin{aligned}
q &= -A\bar{p} + (1 - B)q_1 - \vec{q_T}\ , \\
k &= (1 - C)\bar{p} + \left(\frac{M^2}{s - M^2} - D \right) q_1 - \vec{k_T}\ .
\end{aligned}
$$

The eight degrees of freedom in (7.15) are reduced to five by requiring that $q_2^2 = 0$, $p'^2 = M^2$ and disregarding an overall azimuthal angle. The next step is to relate the remaining degrees of freedom to more familiar deep inelastic and diffractive variables. The electron is described by the usual two DIS variables x and Q^2, and three additional parameters define the proton:

$$
\begin{aligned}
\alpha_p &= \text{fraction of longitudinal momentum transferred to the pomeron,} \\
t &= t\text{-channel invariant momentum transfer to the pomeron,} \\
\phi_{ep} &= \text{angle between the outgoing electron and outgoing proton} \\
&\quad\ \text{in the plane transverse to the beam direction.}
\end{aligned}
$$

In terms of Lorentz invariants,

$$
Q^2 = -q^2, \quad x = \frac{Q^2}{2p \cdot q}, \quad t = k^2, \quad \alpha_p = \frac{k \cdot q_1}{p \cdot q_1}.
\tag{7.16}
$$

Some straightforward algebra then gives the photon and pomeron momenta:

$$
\begin{aligned}
q &= \left(\frac{Q^2}{s - M^2} \right) \left[-\bar{p} + \left(\frac{1}{x} + \frac{M^2}{s - M^2} \right) q_1 \right] - \vec{q_T}\ , \\
k &= \alpha_p \bar{p} + \frac{t - \alpha_p M^2}{s - M^2} q_1 - \vec{k_T}\ ,
\end{aligned}
\tag{7.17}
$$

114

where

$$q_T^2 = Q^2 \left(1 - \frac{Q^2}{x(s-M^2)} - \frac{M^2 Q^2}{(s-M^2)^2} \right) ,$$

$$k_T^2 = -t(1-\alpha_p) - \alpha_p^2 M^2 ,$$

$$\cos \phi_{ep} = \frac{\vec{q_T} \cdot \vec{k_T}}{\sqrt{q_T^2 k_T^2}} .$$

As already mentioned, neither α_p, t or ϕ_{ep} are directly measured. An additional constraint on the kinematical variables can however be obtained by measuring the mass of the final state in the $\gamma^*(q)P(k) \to X$ hard scattering, $M_X^2 = (q+k)^2$. In analogy with the usual Bjorken x variable (7.16) we introduce

$$z \equiv \frac{Q^2}{2q \cdot k} = \frac{Q^2}{M_X^2 + Q^2 - t}. \tag{7.18}$$

Substituting the expressions for q and k from (7.17) then yields a relation between z and the other kinematical variables:

$$\frac{1}{z} = \frac{\alpha_p}{x} + \frac{2\alpha_p M^2 - t}{s - M^2}$$

$$- \frac{2\cos\phi_{ep}}{Q} \left[\left\{ -t(1-\alpha_p) - \alpha_p^2 M^2 \right\} \left\{ 1 - \frac{Q^2}{x(s-M^2)} - \frac{M^2 Q^2}{(s-M^2)^2} \right\} \right]^{\frac{1}{2}} \tag{7.19}$$

From (7.14) we see that the DS cross section is expected to be heavily suppressed for large values of $|t|$. This is consistent with the fact that no final-state protons are observed outside the beam pipe. It is therefore a reasonable first approximation to set $t = 0$ in the kinematical relations above. With the substitution $t = M^2 = 0$, (7.19) becomes

$$\frac{1}{z} = \frac{\alpha_p}{x} \quad \Rightarrow \quad \alpha_p = \frac{x}{z}. \tag{7.20}$$

Hence, the momentum fraction of the quark in the proton (x) is simply the product of the momentum fraction of the quark in the pomeron (z) and the momentum fraction of the pomeron in the proton (α_p). Note that in this approximation

$$z = Q^2/(Q^2 + M_X^2). \tag{7.21}$$

In this way, the parameter α_p is easily determined from measured quantities.

It is important to stress, however, that the corrections to (7.20) are not obviously negligible. In particular, we note that the terms of order $\sqrt{-t}/Q$ and M/Q may not be small. Corrections to (7.21) start at order $t/(M_X^2 + Q^2)$ and will therefore be ignored in the following. In practice, diffractive events are identified by the presence of a large rapidity gap. This requires the pomeron to be slowly moving in the laboratory frame, and consequently $\alpha_p \ll 1$. In this limit, including the most important subleading corrections gives

$$\alpha_p = \frac{x}{z} \left[1 + 2\sqrt{1 - \frac{Q^2}{xs}} \, \frac{z\sqrt{-t}}{Q} \, \cos \phi_{ep} \right]. \tag{7.22}$$

This result shows that the distribution in the angle ϕ_{ep} will not be uniform in general. For any non-zero t, and at fixed z, x and Q^2, α_p varies with ϕ_{ep}. Since the diffractive structure function (7.13,7.14) is a steeply falling function in α_p the impact of a variation of ϕ_{ep} can be quite large. This effect will be studied in greater detail below, and in particular the implications for angular correlations between the outgoing electron and the remnant proton will be elaborated in Section 7.3.

7.2.2 Estimates for the systematic uncertainties at HERA

The dependence of α_p on the presently unmeasurable angle ϕ_{ep} gives rise to a systematic uncertainty on reconstructing the variables y_P and α_p which appear in (7.11). In this section we attempt to quantify these uncertainties in order to test the validity of the approximations–

$$\alpha_p \approx \frac{x}{z}, \qquad y_P \approx y \tag{7.23}$$

used to extract $F_2^P(z, Q^2)$ from the HERA data [130][3]. We will also test the factorizability of the diffractive structure function (7.13).

For any parametrization of $f(\alpha_p, t)$ which has a similar α_p dependence to (7.14), one obtains a diffractive cross section which decreases steeply with α_p. This decrease

---

[3]We use $\sqrt{s} = 296$ GeV for all following numerical evaluations.

is quantified by the *pomeron intercept* $2\alpha(0) - 1$ in (7.14), which is equal to 1.17 for the Donnachie–Landshoff model.

Due to this non-linear decrease, the correction (7.22) will *not* average out over all angles ϕ_{ep}, it will rather accumulate to give a non-zero average deviation from (7.23). The relative deviation of α_p from x/z is given by

$$\frac{\alpha_p - x/z}{x/z} = 2\sqrt{1 - \frac{Q^2}{xs} \frac{z\sqrt{-t}}{Q}} \cos\phi_{ep},$$

while the relative deviation of y_P from y has a similar form:

$$\frac{y_P - y}{y} = \frac{x}{z\alpha_p} - 1 \simeq -2\sqrt{1 - \frac{Q^2}{xs} \frac{z\sqrt{-t}}{Q}} \cos\phi_{ep} = -\frac{\alpha_p - x/z}{x/z}.$$

Since ϕ_{ep} and t are not directly measured, we define the expectation value of the deviation to be the weighted average over all angles and values[4] of t:

$$\left\langle \frac{\alpha_p - x/z}{x/z} \right\rangle (x, z, Q^2) = \frac{\int_{-\infty}^{0} dt \int_{0}^{2\pi} d\phi_{ep} \left(\frac{\alpha_p - x/z}{x/z} \right) f(\alpha_p, t)}{\int_{-\infty}^{0} dt \int_{0}^{2\pi} d\phi_{ep} f(\alpha_p, t)},$$

$$\left\langle \frac{y_P - y}{y} \right\rangle (x, z, Q^2) = -\left\langle \frac{\alpha_p - x/z}{x/z} \right\rangle (x, z, Q^2),$$

which becomes, for any $f(\alpha_p, t)$ with a similar form to (7.14),

$$\left\langle \frac{\alpha_p - x/z}{x/z} \right\rangle (x, z, Q^2) = 2\left(1 - \frac{Q^2}{xs}\right) \frac{z^2}{Q^2} \frac{\int_{-\infty}^{0} dt\,(-t)(1 - 2\alpha(t))f\left(\frac{x}{z}, t\right)}{\int_{-\infty}^{0} dt\, f\left(\frac{x}{z}, t\right)}. \qquad (7.24)$$

Figure 7.4.a shows this systematic deviation for the DL parametrization of $f(\alpha_p, t)$ (7.14). We see that there is a small ($<5\%$) negative correction to the approximation (7.23) for α_p and the same, but positive, correction for y_P. This effect can be understood intuitively as follows. The form of $f(\alpha_p, t)$ favours low values of α_p and therefore values of $90° \leq \phi_{ep} \leq 270°$, i.e. $\cos\phi_{ep} \leq 0$. In this region, the pomeron moves towards the virtual

---

[4]We assume here that F_2^P is independent of t, i.e. that $f(\alpha_p, t)$ in (7.11) takes account of the full t-dependence.
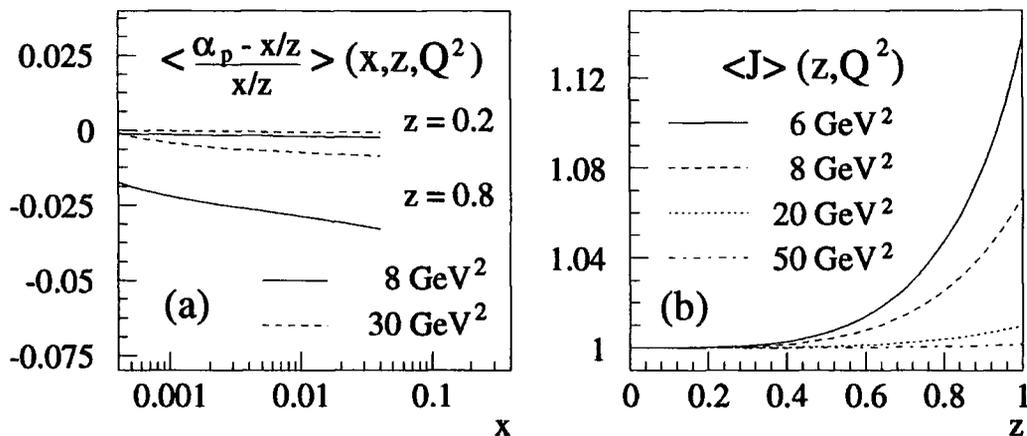
Figure 7.4: Systematic deviations after averaging over t and ϕ_{ep}, using the DL-parametrization for $f(\alpha_p, t)$ (7.14): (a) systematic relative deviation between α_p and its approximation x/z as a function of x. The upper lines correspond to $z = 0.2$, the lower ones to $z = 0.8$. y_P and y show the same systematic deviations with the opposite sign; (b) magnitude of the Jacobian factor defined in (7.28).

photon, thus increasing the virtual photon energy y_P 'seen' by the pomeron. Note that this effect decreases with increasing Q^2 and so will vanish in the asymptotic scaling limit. Furthermore, the deviation is proportional to the intercept $2\alpha(0) - 1$. As phenomenological studies of the BFKL equation predict larger intercepts [128] than the model of Donnachie–Landshoff, one should expect corrections of up to 8% in BFKL motivated approaches.

In order to examine the factorizability of the diffractive structure function (7.13), we return to (7.1) in its fully differential form:

$$\frac{d\sigma^{DS}}{d\alpha_p dt dx dz dQ^2} = \frac{4\pi\alpha^2}{xQ^4} \left\{ \frac{1 + (1-y)^2}{2} F_2^{DS}(x, Q^2, \alpha_p, t) \right.$$

$$\left. - \frac{y^2}{2} F_L^{DS}(x, Q^2, \alpha_p, t) \right\} \int_0^{2\pi} \frac{d\phi_{ep}}{2\pi} \delta(z - z(x, Q^2, \alpha_p, t)), \quad (7.25)$$

where we have made the replacement

$$R(x, Q^2, \alpha_p, t) = \frac{F_L(x, Q^2, \alpha_p, t)}{F_2(x, Q^2, \alpha_p, t) - F_L(x, Q^2, \alpha_p, t)}. \quad (7.26)$$

118

Assuming that the factorization (7.13) of the structure functions F_2 and F_L gives a valid approximation for the factorizability of the cross section, this can be expressed as

$$\frac{d\sigma^{DS}}{d\alpha_p dt dx dz dQ^2} = \frac{4\pi\alpha^2}{xQ^4}\left\{\frac{1+(1-y)^2}{2} F_2^P(z,Q^2,t)\right.$$
$$\left.-\frac{y^2}{2} F_L^P(z,Q^2,t)\right\}f(\alpha_p,t)\int_0^{2\pi}\frac{d\phi_{ep}}{2\pi}\delta(z-z(x,Q^2,\alpha_p,t)).$$

After a simple integration over ϕ and x, restricted to the kinematically allowed values of the latter for fixed α_p and z, we finally obtain an expression for the differential cross section similar to (7.11):

$$\frac{d\sigma^{DS}}{d\alpha_p dt dz dQ^2} = \frac{4\pi\alpha^2}{zQ^4}\left(1+\frac{4tz^2}{Q^2}\right)^{-\frac{1}{2}}\left\{1-y+\frac{y^2}{2[1+R^P(z,Q^2,t)]}\right\} F_2^P(z,Q^2,t)f(\alpha_p,t).$$
$$(7.27)$$

Assuming F_2^P and F_L^P to be independent of t, we can estimate of the magnitude of the Jacobian factor,

$$\langle J\rangle(z,Q^2,\alpha_p) \equiv \left\langle\left(1+\frac{4tz^2}{Q^2}\right)^{-\frac{1}{2}}\right\rangle(z,Q^2,\alpha_p) = \frac{\int_{-Q^2/4z^2}^0 dt\,\left(1+\frac{4tz^2}{Q^2}\right)^{-\frac{1}{2}}f(\alpha_p,t)}{\int_{-\infty}^0 dt\,f(\alpha_p,t)},$$
$$(7.28)$$

which is shown in Fig. 7.4.b as a function of z and Q^2.[5] We see that this Jacobian factor differs by less than 5% from unity for the whole kinematical range experimentally accessible at HERA. Together with the systematic difference between y_P and y, which is of about the same order, we find that the cross sections defined by (7.11) and (7.27) agree within a maximum deviation of 10%, which is attained only in the large-z region. For values of $z < 0.4$ the agreement is already better than 5%. Furthermore, both expressions become equal in the scaling limit $Q^2 \to \infty$. As the experimental errors on the diffractive structure function are still well above these corrections [130], and uncertainties arising from the R-factor are twice as big as these corrections, it seems appropriate at this time

---

[5]The α_p dependence turns out to be negligible.

119

to factorize the diffractive structure function into a pomeron emission factor and a deep inelastic structure function of the pomeron, (7.13).

When, in the future, the data improve and the full pomeron kinematics can be reconstructed, it should be kept in mind that the factorization (7.13) of the diffractive structure function is only an approximation to the factorization of the diffractive cross section (7.11).

A final point concerns the measured intercept of the pomeron trajectory. As a measurement of t is not possible at present, only an 'average' coupling of the pomeron to the proton can be determined:

$$f(\alpha_p) = \int_{-\infty}^{0} dt\, f(\alpha, t) \sim \alpha_p^{-n(\text{eff})}. \tag{7.29}$$

Using the DL-parametrization (7.14) for $f(\alpha_p)$, one finds $n(\text{eff}) \simeq 1.09 \pm 0.02$. The error here represents the spread in $n(\text{eff})$ values as α_p varies over the range $10^{-4} < \alpha_p < 10^{-2}$. If α_p is approximated by x/z, the effective power increases slightly to $n(\text{eff}) \simeq 1.11 \pm 0.03$, which is a non-negligible shift. Both these values are significantly lower than the 'naïve' approximation $n(\text{eff}) \approx 1 - 2\alpha(0) = 1.17$, and therefore this effect should be taken into account in comparing the measured intercept with model predictions.

In summary, we have shown in this section that effects arising from an incomplete reconstruction of the pomeron kinematics at HERA give systematic corrections of only a few percent to α_p, y_P and the measured intercept of the pomeron trajectory. Furthermore we have demonstrated that the factorization of the diffractive structure function gives a correct approximation of the factorization of the diffractive cross section up to a relatively minor error, which vanishes in the large Q^2 scaling limit.

7.3 Final-state electron-proton correlations

It should be clear from the above discussion that identification of the scattered proton and measurement of its four momentum p' will provide a crucial test of the pomeron picture. In principle, this would allow a direct measurement of the parameters α_p and t

and hence of the pomeron emission factor f. However in practice it will be difficult to make a precision measurement of the proton energy, which would be needed to obtain sufficient experimental resolution on α_p and hence a precise determination of t. In the short term, it therefore seems more promising to test the t-dependence of f by using the angular correlation between the transverse momenta of the outgoing electron and proton, Fig. 7.3.

As discussed in the previous section, the α_p dependence of any Regge-motivated $f(\alpha_p, t)$ favours low values of α_p, and therefore final state configurations in which the scattered electron and proton are approximately back-to-back. This correlation will be enhanced with increasing transverse momentum of the pomeron. Thus the distribution of events in the relative azimuthal angle ϕ_{ep} is a measure of the average size of t involved in the process. The ϕ_{ep} dependence of the diffractive cross section can be parametrized in the form of a distribution function:

$$\frac{dN}{d\phi_{ep}}(x, z, Q^2, \phi_{ep}) = \frac{\int_{t_{min}}^{0} dt\, f\left(\frac{x}{z} + 2x\sqrt{1 - \frac{Q^2}{xs}}\frac{\sqrt{-t}}{Q}\cos\phi_{ep}, t\right)}{\int_{-\infty}^{0} dt\, f\left(\frac{x}{z}, t\right)}, \qquad (7.30)$$

where the lower limit on t arises from the physical range of the fractional proton momentum carried by the pomeron $0 \le \alpha_p \le 1$:[6]

$$t_{min} = \begin{cases} -\dfrac{Q^2}{4z^2(1 - Q^2/xs)\cos^2\phi_{ep}} & : \quad 90° \le \phi_{ep} \le 270° \\[4mm] -\dfrac{Q^2}{4(1 - Q^2/xs)\cos^2\phi_{ep}}\left(\dfrac{1}{x} - \dfrac{1}{z}\right)^2 & : \quad \phi_{ep} < 90°, \phi_{ep} > 270°. \end{cases}$$

In practice, these bounds on t have minimal impact on the $dN/d\phi_{ep}$ distribution, since one expects f to be strongly suppressed for $|t|$ values larger than a 'typical' hadronic scale of $\mathcal{O}(1\,\text{GeV}^2)$.

Figure 7.5 shows the predicted correlation between the outgoing electron and the remnant proton as a function of x, z and Q^2. In fact it turns out that this function is

---

[6]This constraint is not to be confused with the more restrictive experimental cuts on the quantity x/z, since x and z are fixed in this distribution.
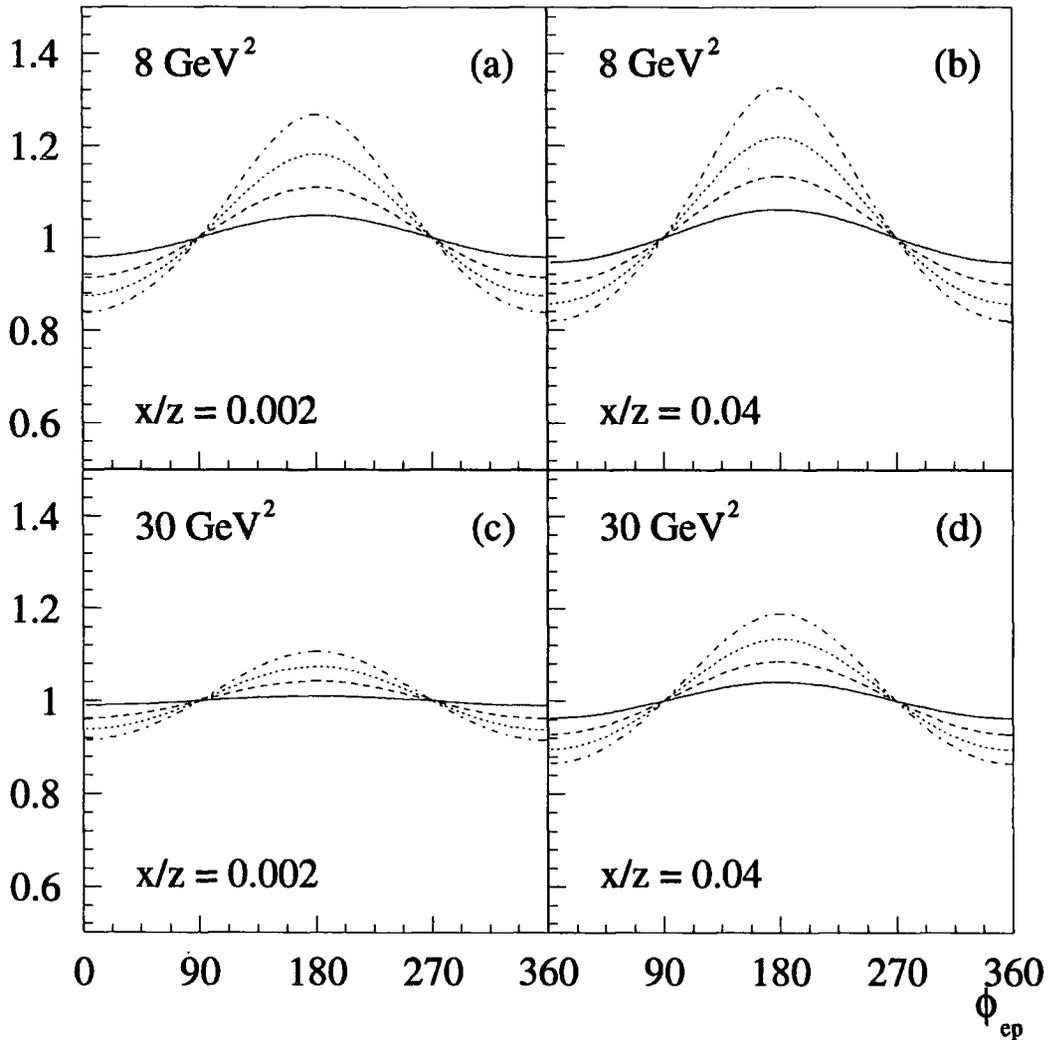
Figure 7.5: $\mathrm{d}N/\mathrm{d}\phi_{ep}(x, z, Q^2, \phi_{ep})$ distribution for fixed values of x/z and Q^2, at $z = 0.2$ (solid lines), $z = 0.4$ (dashed lines), $z = 0.6$ (dotted lines), and $z = 0.8$ (dot-dashed lines).

almost independent of the ratio x/z, the naïve expectation for α_p. As expected from (7.30), the maximum asymmetry between the same-side and opposite-side hemispheres is obtained for low values of Q^2 and high values of z. Note that the asymmetry reaches a magnitude of up to 30% for realistic HERA kinematics ($Q^2 = 8\,\mathrm{GeV}^2, z = 0.6$), and hence

should be distinguishable from statistical fluctuations.

As we have discussed in detail in the previous section, the discrepancy between factorization at the level of diffractive structure functions and diffractive cross sections is of order $-t/Q^2$, which is subleading to the $\sqrt{-t}/Q$ dependence in (7.30). It is therefore appropriate to use the angular distribution $dN/d\phi_{ep}$ in connection with the factorized structure function (7.13). Assuming the structure functions F_L^P and F_2^P to be independent of t, this yields the following result for the diffractive cross section:

$$\frac{d\sigma^{DS}}{dx\,dz\,dQ^2\,d\phi_{ep}} = \frac{4\pi\alpha^2}{zQ^4}\left\{1 - y + \frac{y^2}{2[1 + R^P(z,Q^2)]}\right\} F_2^P(z,Q^2)\frac{1}{2\pi}\frac{dN}{d\phi_{ep}}(x,z,Q^2,\phi_{ep}).$$

$$(7.31)$$

The error implicit in this expression due to the neglect of the Jacobian factor discussed in the previous section affects the normalization of $dN/d\phi_{ep}$, and leads to

$$\int_0^{2\pi} d\phi_{ep}\,\frac{dN}{d\phi_{ep}}(x,z,Q^2,\phi_{ep}) > 2\pi.$$

However this deviation is less than 5% for the kinematical range at HERA, since it only reparametrizes the Jacobian factor (7.28), which is small compared to the angular asymmetry of up to 30%.

Eq. (7.31) can be used to extract the $dN/d\phi_{ep}$ distribution from the HERA data, since it only requires information on the coordinates of the remnant proton, and not on its momentum. This distribution can provide a crucial test of the applicability of DL-like parametrizations of $f(\alpha_p, t)$. Furthermore, any t-dependence of F_2^P would result in deviations from the predicted z-dependence of $dN/d\phi_{ep}$. In particular, a significant t-dependent contribution to F_2^P would map the z-dependence of F_2^P onto the z-dependence of $dN/d\phi_{ep}$.

In summary, we have derived a kinematical correlation between the transverse momenta of the outgoing electron and proton momenta in DS. Assuming the pomeron emission factor of (7.14), we find an asymmetry of up to 30% between aligned and anti-aligned configurations. This asymmetry can serve as a first test of the pomeron interpretation of diffractive deep inelastic scattering.

7.4 Predictions for $\mathbf{F}_2^P$ and $\mathbf{F}_2^{DS}$

7.4.1 Models for the partonic content of the pomeron

The type and distribution of the parton constituents of the pomeron has been the topic of some debate [131]. On one hand, it seems natural to assume that the pomeron is predominantly 'gluonic' [132]. On the other hand, the pomeron has to couple to quarks at some level. In fact Donnachie and Landshoff have presented [126] a prediction for the quark distribution in a pomeron

$$zq^P(z) \approx \tfrac{1}{3}C\pi z(1 - z), \qquad (7.32)$$

with $C \approx 0.17$. This result is obtained from calculating the box diagram for $\gamma^* P \to q\bar{q}$, in the same way as the photon structure function is calculated in the parton model from the box diagram for $\gamma^*\gamma \to q\bar{q}$. A crucial difference for the above pomeron calculation is the softening of the pomeron–quark vertex by a form factor which suppresses large virtualities. This leads to the *scaling* behaviour (7.32) in the $Q^2 \to \infty$ limit, in contrast to the asymptotic growth $q^\gamma(x, Q^2) \sim a(x)\ln(Q^2/\Lambda^2)$ obtained for the quark distributions in the photon[7].

The absence of point-like pomeron–quark couplings in the above model, which gives rise to asymptotic Bjorken scaling for the pomeron structure function, suggests that the partonic content of the pomeron is on a similar footing to that of any other hadron, with the quark and gluon distributions in the pomeron obeying the DGLAP evolution equations (3.7). There is, however, a crucial difference between the pomeron and other hadrons. The second moments of quark singlet and gluon distributions of on-shell hadrons have to add up to unity due to momentum conservation (4.5). This condition is not true for the pomeron, as it cannot be regarded as on-shell or quasi on-shell particle.

The sum of quark and gluon momenta in the pomeron can therefore be an arbitrary number, which can only be determined from experimental data. This normalization factor

---

[7]Alternative scenarios *with* a point-like quark–pomeron coupling have been discussed in the literature [117, 133].

$\mathcal{N}$ is however preserved by perturbative evolution.

The first evidence for partons in the pomeron was given by the discovery of jets at large transverse momenta in diffractive proton–antiproton collisions [124]. This measurement has indicated that the parton distributions in the pomeron are *hard*, i.e. individual partons carry a significant fraction of the pomeron's momentum on average, as in (7.32) for example. From this data, it was however not possible to determine, whether the pomeron consists of quarks or gluons.

To enable further studies of possible observables, we would like to propose a very simple, physically motivated model for the pomeron's parton structure. It basic features are outlined below. Two free parameters of the model are adjusted to the recent data on the diffractive structure function published by the H1 collaboration [130].

As the pomeron carries the quantum numbers of the vacuum, its quark and antiquark distributions have to be identical. Therefore, one has to consider only two parton distributions in the pomeron, the quark singlet $\Sigma^P = \sum_i (q_i^P + \bar{q}_i^P)$ and the gluon. These are assumed to have the following, valence-like shapes at $Q_0^2 = 2$ GeV^2:

$$z\Sigma^P(z, Q_0^2) = f_q(Q_0^2)\, 6z(1 - z), \quad zg^P(z, Q_0^2) = f_g(Q_0^2)\, 6z(1 - z), \qquad (7.33)$$

where f_q and f_g are the fractions of pomeron momentum carried by quarks and gluons. The DGLAP evolution equations (3.7) determine the change of these momentum fractions with increasing Q^2. In fact, leading-order perturbative QCD predicts that the asymptotic $(Q^2 \to \infty)$ momentum fractions are, regardless of the type of hadron,

$$f_q \to \frac{3n_f}{16 + 3n_f}, \quad f_g \to \frac{16}{16 + 3n_f}.$$

This model is motivated by the dynamical parton model [134] for the parton distributions in the proton, which assumes valence-like shapes for quarks *and* gluons [135] at some low scale $(Q^2 < 1$ GeV$^2)$.

In the evolution of these parton distributions we always define the quark singlet to be the sum of only three light quark flavours (u, d, s). Contributions of heavy quarks to F_2^P, of which we will only consider the dominant charm quark contribution, are incorporated

125

by projecting the massive contribution from the $\gamma^* g \to c\bar{c}$ fusion process onto F_2^P (cf. Section 3.1). The number of active flavours in the evolution is fixed to $n_f = 3$, as explained in Appendix B.3.1.

Assuming that SU(3) flavour symmetry is already established at Q_0^2, the contribution of the light quarks flavours to F_2^P is just the singlet distribution times a charge factor:

$$F_2^{P(u,d,s)}(z, Q^2) = \frac{2}{9} z \Sigma^P(z, Q^2). \tag{7.34}$$

The massive charm contribution arising from photon-gluon fusion takes the form

$$F_2^{P(c)}(z, Q^2, m_c^2) = 2z q_c^2 \frac{\alpha_s(\mu_c^2)}{2\pi} \int_{az}^1 \frac{dy}{y} \, C\left(\frac{z}{y}, \frac{m_c^2}{Q^2}\right) g^P(y, \mu_c^2), \tag{7.35}$$

with the kinematical bound $a = 1 + 4m_c^2/Q^2$ and the LO coefficient function

$$
\begin{aligned}
C(\zeta, r) &= \frac{1}{2}[\zeta^2 + (1 - \zeta)^2 + 4\zeta(1 - 3\zeta)r - 8\zeta^2 r^2] \ln\frac{1 + \beta}{1 - \beta} \\
&\quad + \frac{\beta}{2}[-1 + 8\zeta(1 - \zeta) - 4\zeta(1 - \zeta)r],
\end{aligned}
$$

where

$$\beta^2 = 1 - \frac{4r\zeta}{1 - \zeta}.$$

It has been shown in [136] that a mass factorization scale of $\mu_c^2 = 4m_c^2$ for the gluon distribution in (7.35) is the most appropriate choice with regard to the perturbative stability of the expression. We will use $m_c = 1.5$ GeV in our numerical evaluations presented below. The complete prediction for F_2^P is the sum of light and heavy quark contributions; it reads

$$F_2^P(z, Q^2) = \frac{2}{9} z \Sigma^P(z, Q^2) + F_2^{P(c)}(z, Q^2, m_c^2). \tag{7.36}$$

The above treatment of the charm contribution takes proper account of the threshold behaviour which, as we will see in Section 7.5, makes a significant contribution to the Q^2 dependence of the structure function.

Finally, to take into account the ambiguity in the pomeron momentum sum rule discussed above, we multiply the structure function (7.36) by an overall normalization factor

126

$\mathcal{N}$,

$$F_2^P(z, Q^2) \longrightarrow \mathcal{N} F_2^P(z, Q^2). \tag{7.37}$$

We shall see below that $\mathcal{N} \approx 2$ gives a good representation of the H1 data.

7.4.2 Q^2 evolution of F_2^{DS}

The assumption that F_2^{DS} is factorizable into an emission and a DIS part (7.13) implies that the Q^2 dependence of F_2^{DS} arises entirely from F_2^P. Assuming the parton interpretation of F_2^P to be valid, then this Q^2 dependence is given by the standard DGLAP evolution equations (3.7) of perturbative QCD, as we will prove in this subsection. The observation of such a Q^2 dependence is an important test of the parton interpretation of the pomeron and of the factorizability of diffractive scattering cross sections.

For F_2^{DS} we must fold the results with the pomeron flux factor f. In particular we can define 'diffractive' parton distributions in the proton by

$$\begin{pmatrix} \Sigma^{DS}(x, Q^2, t) \\ g^{DS}(x, Q^2, t) \end{pmatrix} = \int_0^1 dz d\alpha_p \begin{pmatrix} \Sigma^P(z, Q^2, t) \\ g^P(z, Q^2, t) \end{pmatrix} f(\alpha_P, t) \delta(z - x/\alpha_p), \tag{7.38}$$

where we have used (7.19), dropping the small corrections due to finite t and M^2 effects. Taking $\partial/\partial \ln Q^2$ of both sides, and using the fact that the pomeron parton distributions Σ^P, g^P satisfy the DGLAP equation, gives

$$\frac{\partial}{\partial \ln Q^2} \begin{pmatrix} \Sigma^{DS}(x, Q^2, t) \\ g^{DS}(x, Q^2, t) \end{pmatrix} = \frac{\alpha_s(Q^2)}{2\pi} \int_0^1 dy' d\eta dz d\alpha_p \, [\mathcal{P}(\eta)] \begin{pmatrix} \Sigma^P(y', Q^2, t) \\ g^P(y', Q^2, t) \end{pmatrix}$$
$$\times f(\alpha_P, t) \, \delta(z - x/\alpha_p) \, \delta(z - \eta y'),$$

where $[\mathcal{P}(\eta)]$ is the 2×2 matrix of splitting functions (B.24). Introducing $1 = \int dy \delta(y - y'\alpha_p)$ and integrating over y' and z gives

$$\frac{\partial}{\partial \ln Q^2} \begin{pmatrix} \Sigma^{DS}(x, Q^2, t) \\ g^{DS}(x, Q^2, t) \end{pmatrix} = \frac{\alpha_s(Q^2)}{2\pi} \int_x^1 \frac{dy}{y} \, [\mathcal{P}(x/y)] \begin{pmatrix} \Sigma^{DS}(y, Q^2, t) \\ g^{DS}(y, Q^2, t) \end{pmatrix},$$

which is the usual DGLAP equation, but now for the diffractive parton distributions.

Therefore, one should find experimentally that the Q^2 dependence of both $F_2^{DS}(x, Q^2, t)$ and $F_2^P(z, Q^2, t)$ is consistent with perturbative QCD while the corresponding parton distributions are related by (7.38).

It is worth stressing that the Q^2 dependences of the proton structure function F_2 and F_2^{DS} *at the same Bjorken x value* are completely unrelated. In particular, F_2 rises rapidly with increasing Q^2 at small x as more and more slowly-moving partons are generated by the branching process. This rise is observed [137] to be proportional to $\ln Q^2$ at fixed x, which is consistent with recent parametrizations [41, 43, 44] of the parton densities in the proton. In contrast, the quarks in the pomeron are sampled at z values much larger than x, where the distributions evolve more slowly. One should therefore find that the fraction of diffractive events in deep inelastic scattering at fixed x (corresponding to $F_2^{DS}(x)/F_2(x)$) is *decreasing* approximately like $1/\ln Q^2$.

7.5   Comparison with data

When the study presented in this chapter was carried out originally [117], only the H1 collaboration had measured [130] the diffractive structure function. A similar measurement from the ZEUS collaboration appeared some months later [138]. We will therefore focus on the results from H1 in this section. The description of the pomeron structure function obtained in our analysis is however consistent with the ZEUS measurement, as we will show at the end of this section.

Based on a sample of events without hadronic activity around the proton beam direction, the H1 collaboration has measured [130] the diffractive structure function $F_2^{D(3)}$

$$\frac{d\sigma^{DS}}{dx dQ^2 dx_P} = \frac{4\pi\alpha^2}{xQ^4} \frac{1 + (1-y)^2}{2} F_2^{D(3)}(\beta, Q^2, x_P)$$

as a function of the three kinematic variables, $\{\beta, Q^2, x_P\}$ where

$$\beta = \frac{Q^2}{M_X^2 + Q^2} \approx z,$$

$$x_P = \frac{x}{\beta} \approx \alpha_P,$$

with the approximations becoming exact when $t = M^2 = 0$. The variables α_P, t and ϕ_{ep} are not measured directly. It is estimated that $|t| \lesssim 7$ GeV^2 [130], while ϕ_{ep} is unconstrained.

A prediction for the measured diffractive structure function $F_2^{D(3)}$ from our model can be obtained by inserting (7.13) into (7.1) and integrating over α_p, t and ϕ_{ep}

$$F_2^{D(3)}(\beta, Q^2, x_P) = \int_0^1 \mathrm{d}\alpha_p \int_{t_{\min}}^{t_{\max}} \mathrm{d}t \int_0^{2\pi} \frac{\mathrm{d}\phi_{ep}}{2\pi} \, \delta\left(x_P - \frac{x}{z} - \frac{xt}{Q^2}\right) \, f(\alpha_p, t) \, F_2^P(z, Q^2, t),$$

with z given in terms of the other variables by (7.19). Ignoring the t dependence everywhere except in f, and setting the proton mass to zero, we obtain the simple factorising approximation

$$F_2^{D(3)}(\beta, Q^2, x_P) \approx \left[\int_{t_{\min}}^{t_{\max}} \mathrm{d}t \, f(x_P, t)\right] \, F_2^P(\beta, Q^2),$$

which implies that the dependence of the structure function on x_P should be universal, i.e. independent of β and Q^2. Furthermore, if we substitute for f using (7.14) we find

$$F_2^{D(3)}(\beta, Q^2, x_P) \approx K \, x_P^{-n} \, F_2^P(\beta, Q^2).$$

Precisely this behaviour has recently been observed by the H1 collaboration [130]. In fact their measured 'universal' power n of x_P is $n = 1.19 \pm 0.06(stat.) \pm 0.07(sys.)$, which is in excellent agreement with our prediction of 1.11 ± 0.03 (Section 7.2.2) based on a correct treatment of kinematics and using the pomeron emission factor of Donnachie and Landshoff [126].

The H1 collaboration have also attempted to measure the pomeron structure function directly, by defining an x_P-integrated diffractive structure function

$$\tilde{F}_2^D(\beta, Q^2) = \int_{0.0003}^{0.05} \mathrm{d}x_P \, F_2^{D(3)}(\beta, Q^2, x_P), \tag{7.39}$$

where the range of integration is chosen to span the entire x_P measurement range. According to the simple factorization hypothesis, the diffractive structure function is proportional to the pomeron structure function:

$$\tilde{F}_2^D(\beta, Q^2) \approx A \, F_2^P(\beta, Q^2), \tag{7.40}$$

with

$$A(\text{H1}) = \int_{0.0003}^{0.05} d\alpha_p \int_{t_{\text{min}}}^{t_{\text{max}}} dt \, f(\alpha_p, t) \approx 1.5. \tag{7.41}$$

The numerical value in (7.41) corresponds to the Donnachie–Landshoff form (7.14) for f. In what follows we will use (7.40) with $A = 1.5$ to convert the measured structure function [130] into the pomeron structure function. The measurement of ZEUS [138] covers only a smaller x_P range ($0.00063 < x_P < 0.01$). One therefore obtains:

$$A(\text{ZEUS}) = \int_{0.00065}^{0.01} d\alpha_p \int_{t_{\text{min}}}^{t_{\text{max}}} dt \, f(\alpha_p, t) \approx 0.8.$$

In [130], data on $\tilde{F}_2^P(\beta, Q^2)$ are presented in four Q^2 bins, $Q^2 = 8.5$, 12, 25, 50 GeV^2. In the first of these, the charm contribution should be relatively small, and hence $\tilde{F}_2^P(\beta, Q^2)$ can be directly compared with the predictions of our simple model for the light quark distributions derived in the previous section. It furthermore allows us to tune the parameters of this model.

In particular, the first moment of $\tilde{F}_2^D$, which is related to the the momentum fraction carried by quarks in the pomeron, reads

$$A^{-1} \int_0^1 d\beta \, \tilde{F}_2^D(\beta, Q^2) \approx \int_0^1 d\beta \, F_2^P(\beta, Q^2) \approx \frac{2}{9} \mathcal{N} \int_0^1 dz \, z\Sigma^P(z, Q^2) = \frac{2}{9} \mathcal{N} f_q(Q^2). \tag{7.42}$$

The parameters $\mathcal{N}$ and $f_q(Q_0^2)$ are strongly correlated — their product is essentially determined by the first moment of $\tilde{F}_2^D$ in the lowest Q^2 bin. We find the best agreement with the data for $\mathcal{N} = 2$ and the following momentum fractions of quarks and gluons at Q_0^2:

$$f_q(Q_0^2) = 0.17, \quad f_g(Q_0^2) = 0.83. \tag{7.43}$$

Fig. 7.6 shows the values of f_q extracted from the H1 data [130] in this way[8] at the four Q^2 values. Note that in the measured Q^2 range, the momentum fractions are predicted to vary only slightly with Q^2. The apparent rise in the data has a simple interpretation as the onset of the charm contribution, as predicted by (7.36).

---

[8]The β-integrated structure function in (7.42) is estimated by assuming that the structure function is independent of β at each Q^2 value. This is a very crude procedure, and we have no way of estimating the errors on the integral obtained by this method. Our comparison is therefore only qualitative at best.
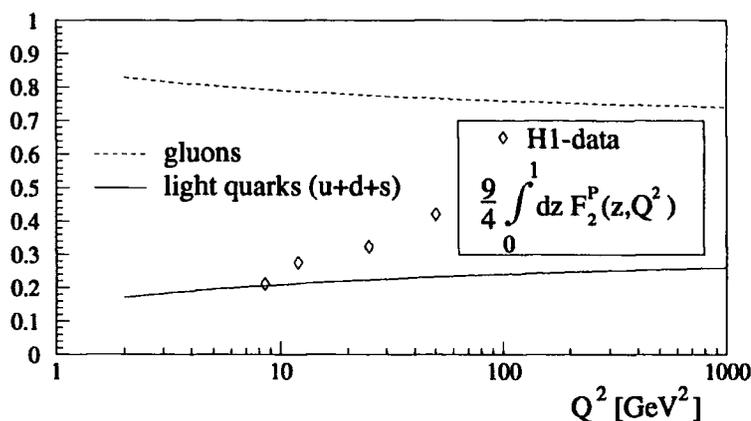
Figure 7.6: Fractions of total pomeron momentum carried by light quarks and gluons as predicted by leading-order DGLAP evolution for three light flavours. The H1 data-points shown in comparison are the values for the momentum fraction carried by the sum of all light quarks under the naïve assumption of a negligible direct charm contribution to F_2^P. The data are furthermore divided by a normalization of $\mathcal{N} = 2$, as discussed in the text.

In Fig. 7.7 the predictions of this model for the pomeron structure function are compared with the data from H1 and ZEUS, as defined by (7.40). The solid curves show the full prediction including the charm contribution, and the dotted curves are the contributions from the three light quarks only. We note that

(i) the variation of the dotted curves with Q^2 shows that the scaling violations predicted by the QCD evolution equations are rather weak in this kinematic range;

(ii) the charm contribution grows rapidly above threshold (in fact, this growth is evidently responsible for the bulk of the predicted Q^2 dependence), and constitutes a significant fraction of the structure function at high Q^2 and low z;

(iii) as Q^2 is increased to higher values, the pomeron structure function is expected to rise rapidly at low z and to decrease slowly at high z.
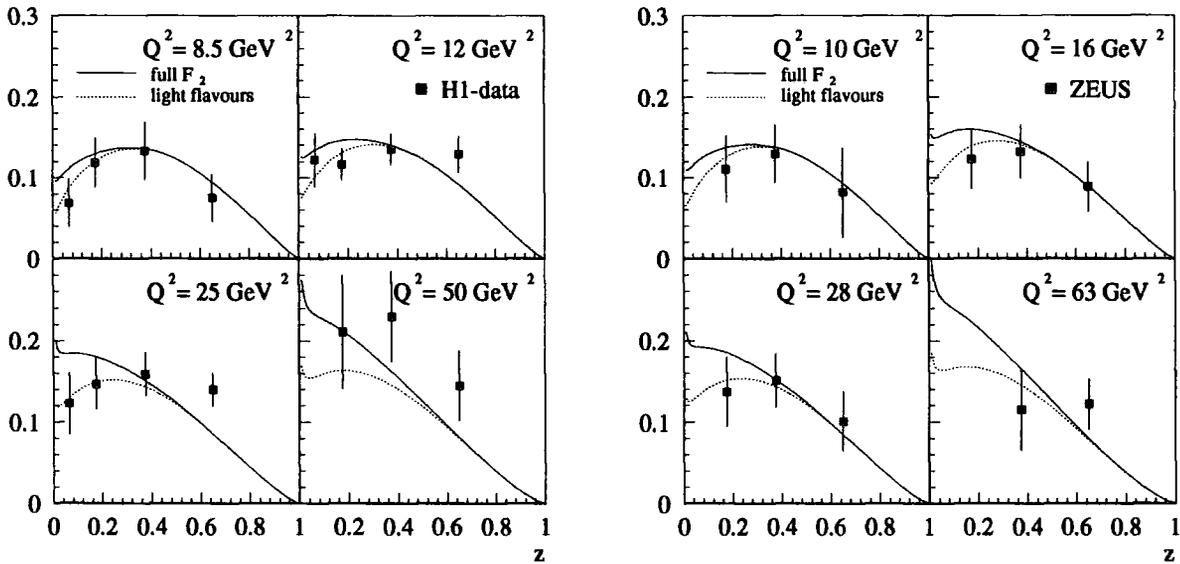
131

Figure 7.7: The deep inelastic structure function of the pomeron $F_2^P(z,Q^2)$. The H1 data are obtained from values for the diffractive structure function in terms of these variables [130], divided by a pomeron emission factor of 1.5 (derived from the model of Donnachie and Landshoff). This factor is 0.8 for the ZEUS data [138]. The theoretical predictions are scaled by a factor $\mathcal{N} = 2$, as discussed in the text.

Finally, in Fig. 7.8 we show the gluon and singlet (light) quark distributions in the pomeron, as predicted in this model. Since we are assuming exact SU(3) flavour symmetry, the individual quark or antiquark distributions are simply $q^P = \frac{1}{6}\Sigma^P$. Note that as Q^2 increases, both the quark and gluon distributions evolve slowly to small z, as expected. The emergence of a small-z 'sea' of $q\bar{q}$ pairs can be seen at high Q^2.

7.6 Conclusions and Outlook

The idea that the pomeron has a partonic structure [123] has been given strong support by the recent measurements of the diffractive structure function at HERA. In this chapter
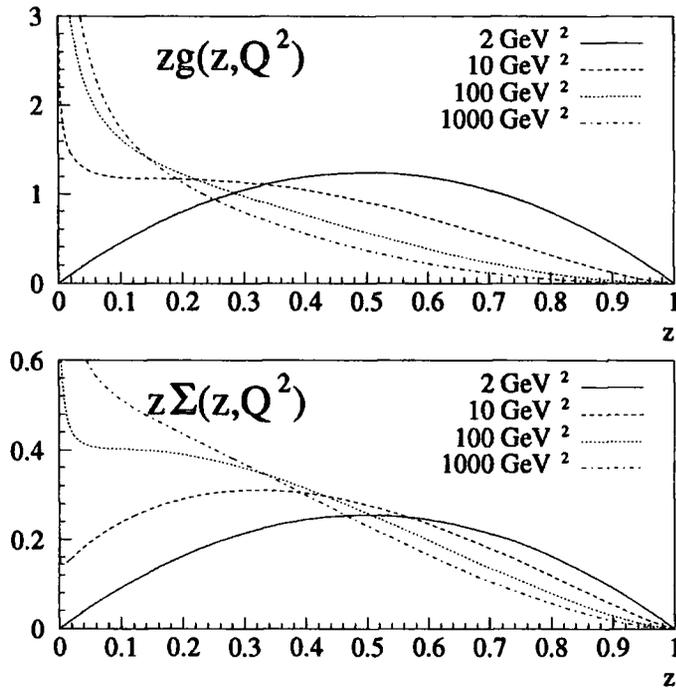
Figure 7.8: Parton distributions in the pomeron, assuming a valence-like structure at $Q_0^2 = 2$ GeV^2. The relative normalizations are chosen such that gluons carry 83% and light quarks carry 17% of the pomeron's momentum at Q_0^2.

we have presented a detailed study of deep inelastic electron-pomeron scattering. We first derived the complete set of kinematic variables for the deep inelastic diffractive cross section. We showed that when expressed in terms of appropriate variables this cross section is expected to factorize into a pomeron structure function multiplied by a pomeron emission factor, the latter being obtainable from hadron–hadron cross sections. At present the variables which define the pomeron momentum are not directly measured, although they can be inferred from the observed hadronic final state. However, in terms of the measured variables the factorization is only approximate. In Section 7.2 we quantified the corresponding systematic error, and showed that it was below the present level of experimental precision.

133

When the remnant protons are eventually detected at HERA, it should be possible to measure their scattering angle ϕ_{ep} relative to the electron in the transverse plane. If the electron–pomeron scattering picture is correct, this distribution is predicted to be non-uniform, with a preference for back-to-back scattering. We presented quantitative predictions for this angular distribution in Section 7.3, using the Donnachie-Landshoff parametrization for the pomeron emission factor.

Finally, we presented a simple phenomenological model for the pomeron structure function in Section 7.4. This model is based on the idea that at a low Q^2 scale, the pomeron consists predominantly of valence-like gluons, with a small admixture of valence-like quarks. At higher Q^2-scales the distributions are determined by standard DGLAP perturbative evolution. Our starting quark distributions are identical in shape, and similar in size, to those calculated by Donnachie and Landshoff. In this model it is necessary to rescale the pomeron momentum sum (by a factor of approximately 2 in the case of the emission factor of [121]) to account for the normalization of the H1 data, whereupon good agreement is obtained with the measured z and Q^2 dependence of the pomeron structure function. The light (u, d, s) quarks carry about 17–25% of the pomeron's momentum in the range of Q^2 currently measured by H1.

The experimentally measured (z, Q^2) range of the pomeron structure function includes the charm quark threshold region. This requires special treatment, since the charm contribution to F_2^P is expected to be significant above threshold. We have calculated this effect using the photon–gluon fusion process, which takes the threshold kinematics correctly into account. We have found that the charm contribution to F_2^P is indeed sizable, especially at high Q^2 and low z. The rapid increase of the charm contribution with increasing Q^2 appears to account for the bulk of the observed Q^2 dependence.

Our results on the quark and gluon content of the pomeron have many implications. As already mentioned, we expect that a significant fraction of hard diffractive scattering events will contain charm, and our distributions provide a way of quantifying this. The overall magnitude of the gluon distribution compared to the quark distribution also predicts a large value for the pomeron's R-factor. In particular, we expect $R^P \sim O(1)$,

134

in contrast to $R \sim O(\alpha_s) \ll 1$ for the proton, which results in a similar magnitude of R^{DS}. However, a consistent estimate of this would require a full next-to-leading order perturbative calculation, which is beyond the scope of the present study.

In summary, we have shown that a simple quark and gluon parton model of the pomeron, combined with a pomeron emission factor extracted from the high energy behaviour of elastic hadron–hadron scattering cross sections, gives an excellent description of the H1 data. There are many ways in which this simple picture can be tested, both at HERA and elsewhere. In the short term, the measurement of the ϕ_{ep} correlation, the Q^2 dependence of the pomeron structure function and the diffractive structure function and the identification of the predicted large charm contribution to the diffractive structure function appear to offer the best possibilities.

7.6.1   Hard diffraction in the light of new HERA data

Both HERA collaborations [139, 140] have very recently presented new, improved measurements of the diffractive structure function. These measurements appear to be in significant disagreement. The selection criteria for diffractive events are however different at H1 and ZEUS, and the pomeron model as presented in this chapter appears to be only applicable to the H1 measurement, which defines diffractive scattering by an observed rapidity gap around the proton beam direction.

The new H1 measurement covers a largely extended kinematical range compared to [130]. It shows, that the simple factorization of the diffractive structure function (7.13) is broken for large values of α_p. This observation can be interpreted [141] as due to the presence of subleading Regge trajectories (vector mesons) at increasing α_p. The dominant contribution to this process is however due to pomeron exchange.

The new data on the diffractive structure function $\tilde{F}_2^D$ allow a more precise determination of the parton distributions in the pomeron. A fit to these data [139] yields a gluon distribution which is even *harder* than in our simple model, the ratio between the pomeron momentum carried by gluons and quarks is found to be 80:20. Using the

135

distributions obtained from a fit to the new data, one can furthermore make predictions for the charm content of the diffractive structure function and for the transverse energy flow in diffractive DIS events. These are found in good agreement with the experimental measurements of these two observables [139].

Chapter 8

A study beyond the Standard Model

With this chapter we will leave the general topic of this thesis, the structure of the proton, for a while to demonstrate an important application of parton distributions: the precision calculation of cross sections in hadron–hadron collisions at high energies.

The present understanding of the physics of elementary particles is described by the Standard Model, whose basic aspects were outlined in Section 2.3. This model has been tested in a great variety of collider experiments over the last twenty–five years, yielding an impressive agreement between theory and experiment. However, during the last two years, some experimental evidence for deviations from the Standard Model has been reported. Motivated by these observations, a multitude of models for new physics beyond the Standard Model has been suggested. A stringent constraint on all these models is given by the large number of experimental observables which are found to be in good agreement with the predictions of the Standard Model: any new physics should only have minor impact on them. It is such a consistency check which we will perform in the following chapter.

We are studying the impact of a new neutral vector boson Z', with a mass of $\mathcal{O}(1 \text{ TeV})$, on the top quark production cross section at the Fermilab Tevatron collider. This cross

section has been measured only very recently, and it agrees within large errors with the prediction of the Standard Model. We motivate the introduction of the Z', discuss its properties and illustrate how a more precise measurement of the top quark cross section can provide a crucial test of the Z' model.

8.1 Motivation

Two experimental observations have received particular attention in recent times, as they appear to deviate from the predictions of the Standard Model. The nature of these observations is very different. The fractions of charm and bottom quarks produced in hadronic decays of the Z-boson are measured within an accuracy of better than 1%, and appear to differ from the Standard Model expectations by a few percent. The other observable, the single jet inclusive cross section in $p\bar{p}$ collisions at the highest energies accessible at present, is only measured with large systematic and statistical uncertainties. Even within these errors, it appears to deviate systematically from the theoretical prediction as the energy of the jet increases. Both observations are *not* reproduced by competing experiments, and they can therefore only be considered as indications for a possible failure of the Standard Model, not as solid evidence. We will briefly discuss the observables.

8.1.1 R_b and R_c at LEP

The collision of electrons and positrons at $\sqrt{s} = M_Z$ at LEP(CERN) and SLC(SLAC) allows a precise study of the decay properties of the Z-boson. By tagging hadrons containing charm or bottom quarks in the final state, a direct measurement of the decay probability into these quark flavours is possible. The ratio between the partial decay width

$$\Gamma(Z \rightarrow q\bar{q}) = \frac{G_F M_Z^3}{2\sqrt{2}\pi} \left[v_q^2 + a_q^2 \right]$$

and the total hadronic width is then indicated by R_q. The ratios R_c and R_b provide a precise measurement of the couplings of charm and bottom quarks to the Z-boson. While

138

the Standard Model predicts

$$R_c = 0.17238, \qquad R_b = 0.21569,$$

a measurement at LEP (average over all four experiments) yields [142]

$$R_c = 0.1543 \pm 0.0074, \qquad R_b = 0.2219 \pm 0.0017.$$

On the contrary, a similar measurement at SLAC [143] is in good agreement with the Standard Model:

$$R_b = 0.2176 \pm 0.0033 \pm 0.0017.$$

8.1.2 Large-E_T jets at CDF

Jet production in hadron–hadron collisions at high energies is mediated by hard parton–parton scattering processes. The kinematical distribution of jets can therefore be calculated by convoluting the parton–parton scattering cross sections with the partonic distributions in the proton. Usually, jet cross sections are expressed as function of the transverse energy E_T and the rapidity η of the jet. For jets produced in the central region of the detector ($\eta \simeq 0$), the transverse energy is approximately $E_T \simeq 1/2\sqrt{x_1 x_2 s}$, where x_1 and x_2 are the longitudinal momentum fractions carried by the incoming partons. The jet cross section at large transverse momenta is therefore determined by the behaviour of parton densities at large x: it is dominated by quark–antiquark scattering, a considerably smaller contribution comes from (anti-)quark–gluon scattering. The quark distributions at large x are accurately determined from lepton–nucleon scattering experiments at lower energies, and so a precise prediction of the single jet inclusive cross section is possible.

The recent measurement of the CDF collaboration [144] seems to indicate, that the jet production cross section for $E_T > 250$ GeV is systematically above the theoretical prediction. It seems rather unlikely that the uncertainty on the parton distributions is responsible for this disagreement: attempts to adjust the quark [145] or gluon [146] distributions yielded results inconsistent with data at lower energies.
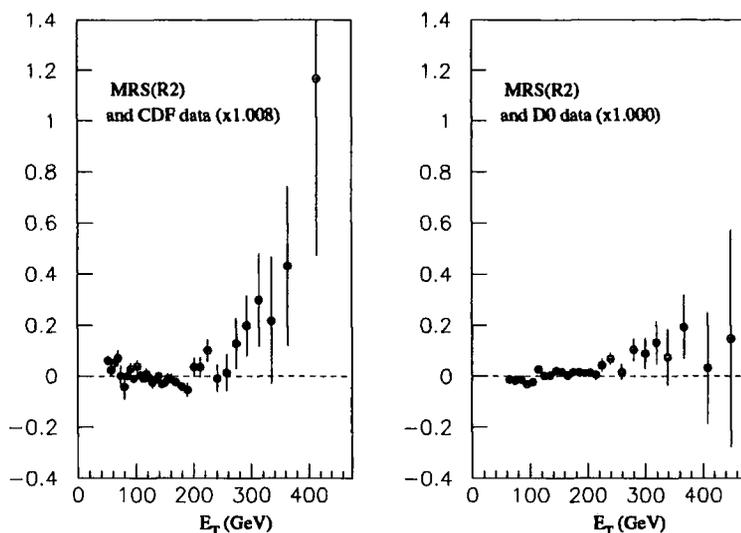
139

Figure 8.1: Single jet inclusive cross section at the Tevatron: (Data–Theory)/Theory. Figure taken from [67], only statistical errors are shown.

A similar measurement of the same observable by the D0 collaboration [147] is on the other hand in good agreement with the Standard Model. Both measurements are compared with the theoretical prediction in Fig. 8.1, which is taken from [67].

8.2 Z' model

Both observations discussed in the above section can not yet be regarded as solid evidence for a failure of the Standard Model. Nevertheless, one might speculate about possible explanations for these anomalies. It has recently been pointed out [148, 149] that both these effects could be explained by introducing a new U(1) gauge boson (Z') of mass $\mathcal{O}(1\ \text{TeV})$ which mixes at the 10^{-3} level with the Z^0 and has similar couplings to quarks. In the remainder of this chapter, we will work with the Z' model suggested in [148], whose basic features are outlined below.

The neutral current sector of the electroweak Lagrangian receives an additional con-

tribution

$$\mathcal{L}_{Z'} = \frac{e}{2\sin\theta_W \cos\theta_W} Z'^\mu \sum_f \bar{\psi}_f \gamma_\mu (v'_f + a'_f \gamma_5)\psi_f \tag{8.1}$$

where the vector and axial couplings of the Z' are parametrized as

$$v'_u = x + y_u , \qquad a'_u = -x + y_u$$

$$v'_d = x + y_d , \qquad a'_d = -x + y_d$$

$$v'_l = v'_\nu = 0 , \qquad a'_l = a'_\nu = 0 ,$$

with $v'_u = v'_c = v'_t$ etc. The couplings to leptons are assumed to be negligible and are hence set to zero. It is furthermore assumed that the mass eigenstates Z^0 and Z' are mixtures of the weak eigenstates Z^0_W and Z'_W:

$$Z^0 = \cos\xi\, Z^0_W + \sin\xi\, Z'_W, \qquad Z' = -\sin\xi Z^0 + \cos\xi\, Z'_W,$$

which modifies the couplings of the physical Z-boson to quarks:

$$v^{eff}_q = \cos\xi\, v_q + \sin\xi\, v'_q, \qquad a^{eff}_q = \cos\xi\, a_q + \sin\xi a'_q.$$

The mixing furthermore affects the mass ratio of W and Z bosons, the ρ-parameter, which is unity at tree level:

$$\rho = \frac{M^2_W}{M^2_{Z^0}\cos^2\theta_W} \rightarrow \rho^{eff} = \rho + \left(\frac{M_{Z'}}{M_{Z^0}}\right)^2 \xi^2,$$

and enters in practically every physical observable in Z-boson decays.

Fixing the mass of the Z' at $M_{Z'} = 1$ TeV, the parameters ξ, x, y_u and y_d can be adjusted to fit the measurements of $R_{b,c}$ while retaining the quality of the Standard Model description of other electroweak observables.

The centre-of-mass energy at the Tevatron is not sufficient to produce a sizable number of on-shell Z'-bosons of the above mass. Effects of the Z' are nevertheless visible in jet production at large E_T, as quark–quark scattering can be mediated by the s- or t-channel exchange of an off-shell Z'. Including the CDF jet data in a combined fit, the authors of [148] obtain

$$\xi = 3.8 \cdot 10^{-3}, \quad x = -1, \quad y_u = 2.2, \quad y_d = 0 , \tag{8.2}$$

141

which we will refer to as 'final fit' in the following. Note that a variation of x between -1.5 and -0.5 and of y_u between 2 and 4 yields values for observables which are still compatible with the experimental data [148].

An important feature of the Z' models of [148, 149] is that the Z' vector and axial couplings to $u-$type quarks turn out to be quite large. In fact the effective $Z'u\bar{u}$ coupling is of the same order as the strong coupling: $(v_u'^2 + a_u'^2)\alpha_W \sim \mathcal{O}(10)\ \alpha_W \sim \alpha_s$, which explains why the Z' contribution to the large E_T jet cross section is comparable to the QCD contribution. Another implication of this is that the top quark production cross section at the Tevatron collider (σ_t) is similarly enhanced, i.e. the model gives rise to an additional 'anomalous' contribution σ_t' from $q\bar{q} \to (Z')^* \to t\bar{t}$ which is the same order as the standard QCD contribution σ_t from $q\bar{q}, gg \to t\bar{t}$. A precise measurement of the top cross section therefore provides an important check on the model. We shall quantify this in what follows, using the same parameters as were determined in [148].

8.3   Hadroproduction of top quark pairs

The top cross section has been studied in the context of a variety of new physics scenarios [150], especially since the original measurement by the CDF collaboration gave a value somewhat higher than the standard QCD prediction [151]. What distinguishes the present study is that we are using a model whose parameters have already been constrained, and therefore our predictions are on a firmer footing.

The production of top-quark pairs at Tevatron energies is predominantly due to quark–antiquark annihilation. The leading-order subprocess cross sections from standard QCD and from the anomalous Z' contribution are:

$$\hat{\sigma}_t(q\bar{q} \to t\bar{t}) = \frac{4\pi\alpha_s^2}{27\hat{s}}\,\beta(3 - \beta^2)\,,$$

$$\hat{\sigma}_t'(q\bar{q} \to Z' \to t\bar{t}) = \frac{(G_F M_Z^2)^2}{6\pi}\ \frac{\hat{s}}{(\hat{s} - M_{Z'}^2)^2 + (\hat{s}\Gamma_{Z'}/M_{Z'})^2}$$

$$\times\ (v_q'^2 + a_q'^2)\ \left[\frac{\beta}{2}(3 - \beta^2)v_t'^2 + \beta^3 a_t'^2\right]\,, \qquad (8.3)$$
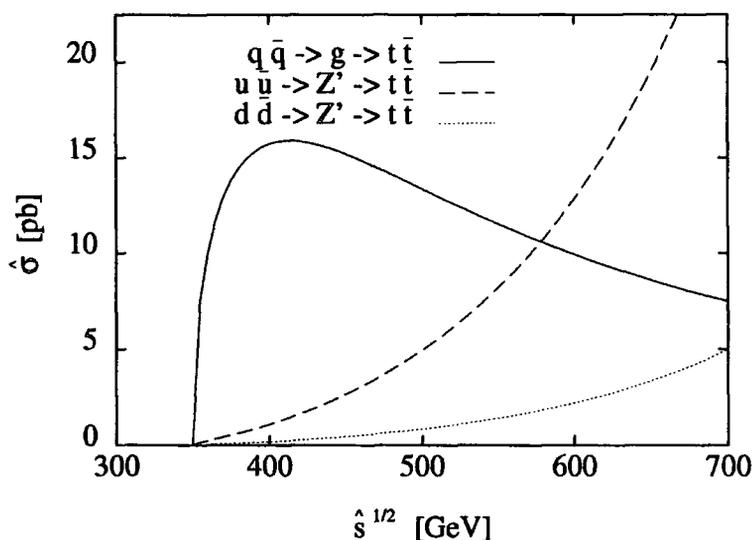
Figure 8.2: Parton-level cross sections for the production of a $t\bar{t}$ pair at leading order. The coupling parameters for the Z' correspond to the 'final fit' of [148].

where $\beta^2 = 1 - 4m_t^2/\hat{s}$ and the Z' width is (for $M_{Z'} \gg m_q$)

$$\Gamma_{Z'} = \frac{G_F M_Z^2}{2\sqrt{2}\pi} 3M_{Z'} \left[v_u'^2 + a_u'^2 + v_d'^2 + a_d'^2 \right] . \qquad (8.4)$$

Figure 8.2 displays these parton-level cross sections as a function of the subprocess centre-of-mass energy for $m_t = 175$ GeV. For the anomalous contribution, it is evident that only $u\bar{u}$ annihilation will yield a sizable contribution to the cross section.

Our calculations of the corresponding $p\bar{p}$ cross sections use the MRS(A$'$) parton distributions [41], with $\alpha_s(M_Z^2) = 0.112$. The factorization and renormalization scales are set equal to m_t. Note that approximately 90% of the QCD cross section comes from the $q\bar{q} \to t\bar{t}$ subprocess. We include also the next-to-leading-order (NLO) perturbative QCD corrections to (8.3). For the standard QCD $q\bar{q}, gg \to t\bar{t}$ cross sections these are taken from [152].

The hadroproduction of a $t\bar{t}$ pair via Z' exchange can be viewed as the production of an off-shell Z'-boson which then decays into a $t\bar{t}$ pair. The NLO corrections to σ_t' can

143

therefore be factored into two contributions, which we discuss in turn below.

8.3.1 Initial state corrections

The Z' behaves – apart from the different values of its vector and axial vector couplings – like the standard model Z-boson. The initial state corrections for the hadronic production of an off-shell Z' are therefore identical to the corrections to the Drell–Yan cross section [153]:

$$
\begin{aligned}
\sigma'_t(s) = & \int_\tau^1 dx_1 \int_{\tau/x_1}^1 dx_2 \int_{\tau/(x_1 x_2)}^1 dz\ \delta(x_1 x_2 z - M^2/s) \\
& \hat{\sigma}'_t(z x_1 x_2 s) \sum_q e_q^2 \left\{ D^{q\bar{q}}(z) \left(q(x_1, \mu_F^2) \bar{q}(x_2, \mu_F^2) + (x_1 \leftrightarrow x_2) \right) \right. \\
& \left. + D^{qg}(z) \left(\left(q(x_1, \mu_F^2) + \bar{q}(x_1, \mu_F^2) \right) g(x_2, \mu_F^2) + (x_1 \leftrightarrow x_2) \right) \right\}
\end{aligned} \quad (8.5)
$$

$$
\begin{aligned}
D^{q\bar{q}}(z) = & \ \delta(1-z) + \frac{\alpha_s(\mu_F^2)}{2\pi} C_F \left[8 \left(\frac{\ln(1-z)}{1-z} \right)_+ - 2 \frac{1+z^2}{1-z} \ln z - 4(1+z) \ln(1-z) \right. \\
& \left. + \delta(1-z)(-8 + 4\zeta_2) + 2 \ln \frac{M^2}{\mu_F^2} \left\{ \left(\frac{2}{1-z} \right)_+ - 1 - z + \frac{3}{2} \delta(1-z) \right\} \right]
\end{aligned}
$$

$$
\begin{aligned}
D^{qg}(z) = & \ \frac{\alpha_s(\mu_F^2)}{2\pi} T_F \left[\left(z^2 + (1-z)^2 \right) \ln \frac{(1-z)^2}{z} + \frac{1}{2} + 3z - \frac{7}{2} z^2 \right. \\
& \left. + \ln \frac{M^2}{\mu_F^2} \left\{ (z^2 + (1-z)^2) \right\} \right]
\end{aligned} \quad (8.6)
$$

with the production threshold $\tau = 4m_t^2/s$ and the invariant mass of the off-shell vector boson $M^2 = z x_1 x_2 s$. The mass factorization scale is chosen to be $\mu_F^2 = m_t^2$; variation of μ_F^2 enables us to estimate the uncertainty of the theoretical prediction. $\hat{\sigma}'_t(\hat{s})$ denotes the cross section for the parton level subprocess $q\bar{q} \to Z' \to t\bar{t}$. Final state radiative corrections will only apply to this quantity.

8.3.2 Final state corrections

The final state corrections for the decay $Z' \to t\bar{t}$ are identical to the corrections for the Z-boson decay into heavy quarks [154]. We can express the parton level cross section

$q\bar{q} \to Z' \to t\bar{t}$ as [155]

$$\hat{\sigma}'_t(\hat{s}) = \frac{(G_F M_Z^2)^2}{6\pi} \frac{\hat{s}}{(\hat{s} - M_{Z'}^2)^2 + (\hat{s}\Gamma_{Z'}/M_{Z'})^2}$$

$$\times (v'^2_q + a'^2_q) \left[\frac{\beta}{2}(3 - \beta^2)v'^2_t \left(1 + \frac{\alpha_s}{\pi}C_F K_V\right) + \beta^3 a'^2_t \left(1 + \frac{\alpha_s}{\pi}C_F K_A\right) \right] \quad (8.7)$$

$$K_V = \frac{1}{\beta}\left[A + \frac{P_V}{1 - \beta^2/3}\ln\frac{1+\beta}{1-\beta} + \frac{Q_V}{1 - \beta^2/3}\right],$$

$$K_A = \frac{1}{\beta}\left[A + \frac{P_A}{\beta^2}\ln\frac{1+\beta}{1-\beta} + \frac{Q_A}{\beta^2}\right],$$

$$A = \left(1 + \beta^2\right)\left[\zeta_2 + \ln\frac{1+\beta}{1-\beta}\ln\frac{1+\beta}{2} + 2\,\mathrm{Li}_2\left(\frac{1-\beta}{1+\beta}\right) + 2\,\mathrm{Li}_2\left(\frac{1+\beta}{2}\right)\right.$$

$$\left. -2\,\mathrm{Li}_2\left(\frac{1-\beta}{2}\right) - 4\,\mathrm{Li}_2(\beta) + \mathrm{Li}_2(\beta^2)\right] + 3\beta\ln\frac{1-\beta^2}{4\beta} - \beta\ln\beta,$$

$$P_V = \frac{33}{24} + \frac{22}{24}\beta^2 - \frac{7}{24}\beta^4, \qquad\qquad Q_V = \frac{5}{4}\beta - \frac{3}{4}\beta^3,$$

$$P_A = \frac{21}{32} + \frac{59}{32}\beta^2 + \frac{19}{32}\beta^4 - \frac{3}{32}\beta^6, \qquad Q_A = -\frac{21}{16}\beta + \frac{30}{16}\beta^3 + \frac{3}{16}\beta^5. \quad (8.8)$$

The vector-corrections K_V in the above formula were originally derived in the QED treatment of the hyper-fine structure of atoms [156], where they cause the splitting between the $^2S_{1/2}$ and $^2P_{1/2}$ levels.

Quantitatively, we observe that each of the above corrections increases the lowest-order cross section by about 15–20%. Using the 'final fit' of (8.2), we find at $\sqrt{s} = 1.8$ TeV and $m_t = 175$ GeV:

$$\sigma'_{\mathrm{LO}} = 1.50\,\mathrm{pb}$$

$$\sigma'_{\mathrm{LO}} \otimes K_{DY} = 1.74\,\mathrm{pb}$$

$$\sigma'_t = \sigma'_{\mathrm{LO}} \otimes K_{DY} \otimes K_{Z' \to t\bar{t}} = 2.00\,\mathrm{pb}, \quad (8.9)$$

to be compared to the Standard Model prediction of $\sigma_t = 4.75$ pb. An estimate of the theoretical uncertainty on these quantities can be obtained by varying the mass factorization
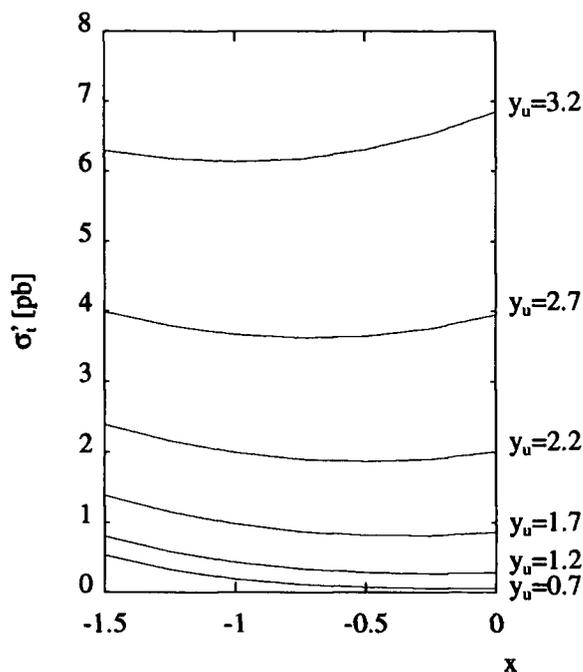
Figure 8.3: Variation of σ_t' with x, y_u.

scale between $m_t/2$ and $2\,m_t$:

$$\sigma_t + \sigma_t' \left(\mu_F = m_t/2\right) \;=\; 5.00 \text{ pb} + 2.09 \text{ pb},$$

$$\sigma_t + \sigma_t' \left(\mu_F = 2\,m_t\right) \;=\; 4.25 \text{ pb} + 1.88 \text{ pb}. \tag{8.10}$$

The NLO σ_t' cross section, for $p\bar{p}$ collisions at $\sqrt{s} = 1.8$ TeV with $m_t = 175$ GeV and MRS(A$'$) partons [41], is shown as a function of the parameters x and y_u in Fig. 8.3. The dependence on the third parameter y_d is very weak. Note that that $y_u < 2$ is disfavoured by the LEP/SLC data [148]. The relative insensitivity to the parameter x evident in the figure can be easily understood, as x enters directly in the $u\bar{u}, d\bar{d} \rightarrow Z'$ production cross sections, see Eq. (8.3). An increase in the production of Z'-bosons is however compensated by a larger amount of Z' decays to d-type quarks. In contrast, an increase in y_u yields only an increase in $u\bar{u} \rightarrow Z'$, and correspondingly in the overall top cross section.
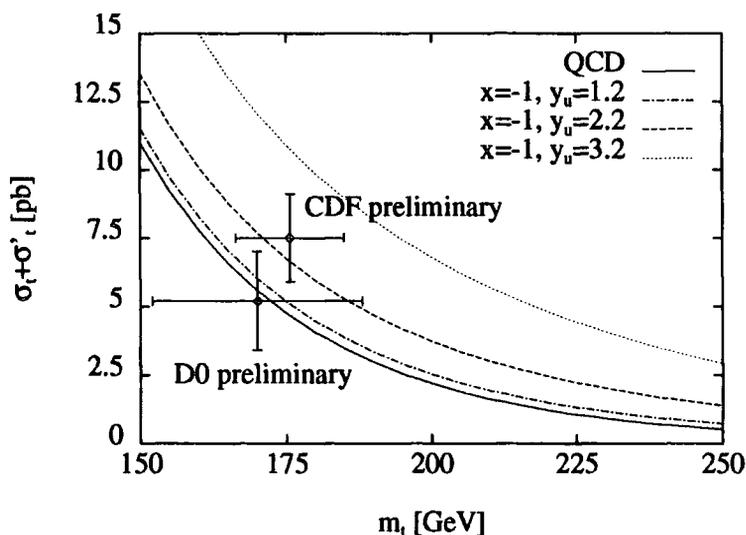
146

Figure 8.4: Predictions for $\sigma_t + \sigma_{t'}$ as a function of m_t, with data points from CDF and D0.

Figure 8.4 shows the total cross section $\sigma_t + \sigma'_t$ as a function of m_t at the Tevatron collider. The solid line is the standard NLO QCD prediction, the dashed line includes Z'-exchange with the 'final fit' (8.2) coupling parameters, and the dot-dashed (dotted) line corresponds to a smaller (larger) value for the coupling parameter y_u. The data points are from CDF [157] and D0 [158]. It is apparent that large values $y_u \simeq 3$ are already ruled out by the CDF and D0 measurements. The 'final fit' estimate (8.2) for the Z' couplings is however still consistent with both experiments. Taking the average of the CDF and D0 results, one finds a top quark cross section slightly above, but consistent with the Standard Model prediction. At the present level of experimental accuracy, the presence of an anomalous contribution can therefore neither be confirmed nor ruled out.

The confirmation of an excess in the measured top cross section must of course take into account the theoretical uncertainty in the Standard Model prediction. There are three major sources of such uncertainty: unknown higher-order perturbative corrections, the value of α_s and parton distributions. A very complete study of this issue has recently
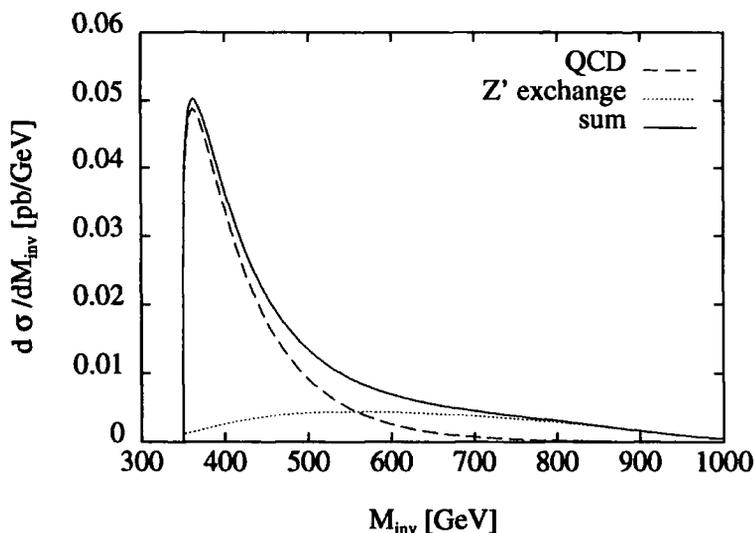
Figure 8.5: Invariant mass distribution of $t\bar{t}$ final states at the Tevatron.

been performed in [159] (see also earlier discussions in [160]). The 'best estimate' of the top cross section (at $\sqrt{s} = 1.8$ TeV) and its error from [159] is

$$\sigma_t = 4.75\,^{+0.73}_{-0.62}\ \text{pb}\ . \tag{8.11}$$

Note that the central value in (8.11) agrees with our result for σ_t given above. More generally, the error is approximately $\pm 15\%$ over the allowed top mass range. The important point to note is that the 'final fit' prediction for σ'_t is about three times larger than the error on the QCD prediction.

Given the uncertainties in the standard QCD prediction and in the data, it is important to investigate other properties of the final state which could help distinguish an anomalous contribution to the cross section. Examples include the angular distributions of the top quarks and their decay products, as emphasized in [161].

Notice in particular that the rapidity distribution of the t quark produced in $q\bar{q} \rightarrow Z' \rightarrow t\bar{t}$ is *not* forward–backward symmetric, in contrast to the standard production mechanism. However the simplest discriminator of the anomalous and standard contributions is the distribution in the invariant mass $M_{\text{inv}} = x_1 x_2 s$ of events containing $t\bar{t}$ pairs, shown

in Fig. 8.5 for $\sqrt{s} = 1.8$ TeV, $m_t = 175$ GeV and the parameters of (8.2). The dashed line denotes the Standard Model prediction, the additional contribution due to the exchange of the 'final fit' Z' is indicated by the dotted line, and the solid line is the sum of these. Just as for the excess in the single jet inclusive distribution [144], the Z' contribution is visible as an enhancement of the measured cross section at large invariant masses. Note that the final-state invariant mass at next-to-leading order can include the contribution from additional gluon emission where appropriate. In practice, the invariant mass distribution of $t\bar{t}$ pairs will also depend on kinematical cuts and the jet definition used in the event reconstruction. A detailed study of these effects is beyond the scope of this thesis.

8.4 Summary and Outlook

In summary, we have shown that the new-physics model proposed in [148] to explain the anomalies in the measurements of $R_{b,c}$ at LEP and the CDF large E_T jet cross section predicts a significant enhancement of the top quark production cross section. The 'final fit' estimate of the increase is about three times larger than the theoretical uncertainty in the standard QCD prediction and yields a substantially different distribution in the final state invariant mass. Given the expected increase in the precision of the experimental measurement, the presence of such an additional non-standard contribution to the cross section should be detectable.

The sensitivity to an anomalous Z' contribution to the $t\bar{t}$ production cross section will be increased further once the Tevatron has been upgraded to operate at $\sqrt{s} = 2$ TeV. The effect is considerably smaller at the LHC, where the predominant top quark production mechanism is gluon–gluon fusion. The expected cross sections at the upgraded Tevatron and the LHC are shown in Fig. 8.6:

$$\sigma_t + \sigma_t' \ (p\bar{p}, \sqrt{s} = \ \ 2 \ \text{TeV}) \ = \ 6.53 \ \text{pb} + 3.33 \ \text{pb}\,,$$

$$\sigma_t + \sigma_t' \ (pp, \sqrt{s} = 10 \ \text{TeV}) \ = \ 357 \ \text{pb} + 61 \ \text{pb}\,,$$

$$\sigma_t + \sigma_t' \ (pp, \sqrt{s} = 14 \ \text{TeV}) \ = \ 768 \ \text{pb} + 115 \ \text{pb}\,.$$
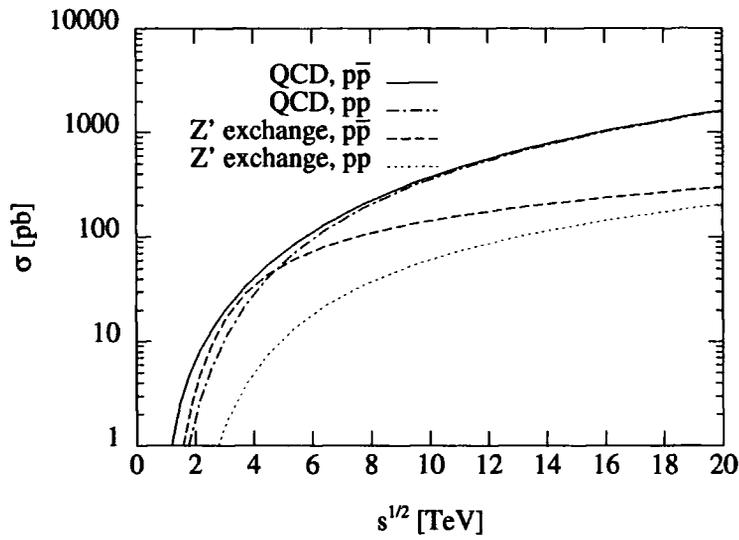
Figure 8.6: Expected top quark cross sections in $p\bar{p}$ and pp collisions as a function of the collider energy.

It has to be stressed that the observation of an anomalous enhancement of the top quark cross section will *not* be sufficient to prove the existence of the Z'-boson. On the contrary, a measurement of this cross section in agreement with the Standard Model would put severe bounds on allowed space of parameters for the Z'. These bounds could be sufficient to contradict the existence of the Z' as postulated in [148].

Chapter 9

Summary and Conclusions

Protons and neutrons, the fundamental constituents of atomic nuclei, display a complicated substructure if looked at closely enough. Several aspects of this substructure have been studied in this thesis.

The form and structure of the proton are described by *form factors* and *structure functions*, which can be measured in electron–proton scattering. We reviewed the phenomenology of elastic and inelastic electron–proton scattering in Chapter 1. While the elastic proton form factors are rapidly decreasing with increasing momentum transfer Q^2, it appears that the inelastic structure functions are only weakly dependent on Q^2. This *scaling behaviour* indicates the existence of point-like constituents, *partons*, inside the proton. An interpretation of the proton structure is given in the *parton model*, which describes the proton structure in terms of distribution functions $f_i(x, Q^2)$ for point-like, non-interacting partons. These determine the probability that a parton of species i carries a momentum fraction x of the total proton momentum if probed at a scale Q^2. We discussed the parton model and its implications in Chapter 2. These partons can be identified with quarks and gluons, which appear to be the fundamental constituents of the proton. The dynamics of quarks and gluons are described by the theory of *Quantum Chromodynamics (QCD)*, Section 2.2. A calculation of parton distribution functions in perturbative QCD is not possible with present methods. However, one can calculate

the *change* of these distributions with increasing Q^2 from first principles. This change is described by the *splitting functions* and *evolution equations* introduced in Chapter 3.

The *spin structure* of the proton in the parton model is described by the *polarized parton distributions* $\Delta f_i(x, Q^2) = f_i^\uparrow(x, Q^2) - f_i^\downarrow(x, Q^2)$, where $f^\uparrow$ ($f^\downarrow$) denotes the distribution for partons with spin aligned (anti-aligned) to the proton spin. Several aspects of these distributions can be determined from sum rules for their first moments and from a study of the QCD predictions in asymptotic kinematical limits. We summarized this information in Chapter 4. We studied in particular the behaviour of the *polarized* parton distributions in the limit $x \to 0$ (Section 4.4), finding a complicated interplay of contributions from quarks and gluons. This is in contrast to the small-x behaviour of the *unpolarized* distributions, which are dominated by evolution of the gluon distribution and consecutive $g \to q\bar{q}$ splitting.

In Chapter 5, we attempted to determine the polarized quark and gluon distributions in the proton from a fit to the experimental data on the polarized structure functions $g_1^{p,d,n}(x, Q^2)$. It turned out that these data, supplemented with additional information from sum rules, constrain the size and shape of the polarized valence quark distributions $\Delta u_v(x, Q^2)$ and $\Delta d_v(x, Q^2)$. The overall magnitude of the polarized sea quark distribution was determined as well. A flavour decomposition of the polarized quark sea and a determination of the polarized gluon distribution $\Delta G(x, Q^2)$ were however not possible on the basis of the polarized structure function data.

Motivated by these uncertainties, we investigated in Chapter 6 how future experiments could measure the polarized sea quark and gluon distributions. It was found that even improved measurements of the polarized structure function will fail to provide sufficient information on these distributions.

A determination of the polarized sea quark distributions in the region $x > 0.1$ seemed to be feasible from the measurement of asymmetries in the Drell–Yan process. It has however to be kept in mind that fixed target measurements of the Drell–Yan cross section usually only cover a restricted rapidity region of the final state phase space. A reliable determination of the polarized sea quark distributions from fixed target Drell–Yan data

will therefore require the knowledge of the QCD corrections to the Drell–Yan cross section as a function of the lepton pair rapidity. This study is presently in progress.

The polarized gluon distribution could be measured from charm production asymmetries in polarized electron–proton scattering. The production of charmed mesons and of the lightest ($c\bar{c}$) bound state both appeared to be promising observables.

Another aspect of the proton structure is the experimental observation of *diffractive deep inelastic scattering* in electron–proton collisions at HERA. We showed in Chapter 7 how this observation can be interpreted as emission of a *pomeron* off the proton, followed by deep inelastic electron–pomeron scattering. We studied implications of this model, finding an angular correlation between the outgoing electron and proton momenta. Furthermore, we suggested a very simple phenomenological model for the partonic structure of the pomeron. In this model, the pomeron is made up of valence-like gluons with a small admixture of valence-like quarks at some low scale Q_0^2. Perturbative evolution then increases the quark content of the pomeron with increasing Q^2. Using this model, we predicted a large fraction of diffractive events with charmed quarks in the final state. The angular correlation and the charm content of diffractive events could both serve as experimental tests of this interpretation. Preliminary measurements of charm production in diffractive deep inelastic scattering appear to be consistent with the pomeron picture.

The most important *application of parton distributions* is the precise prediction of observables in hadron–hadron collisions. Comparison of these predictions with the experimental results can help to confirm or extend our present understanding of particle physics as described by the Standard Model.

We illustrated this for a particular example in Chapter 8. In the recent past, several authors have postulated the existence of a heavy neutral vector boson Z' to explain two experimental observations which appear to deviate from the predictions of the Standard Model. We calculated the effect of the Z' on the top quark production cross section in high energy hadron–hadron collisions. It was found that the Z' contribution yields a sizable enhancement of this observable at presently accessible energies. Recent measurements of the top quark cross section at the Fermilab Tevatron can already put constraints on the

153

coupling of the Z' to quarks, but do not yield conclusive information to verify or falsify the existence of the Z'. Given the anticipated increase in luminosity and collider energy at the Tevatron, the presence or absence of a non-standard contribution due to Z' exchange should be detectable.

In summary, we investigated three different aspects of the internal structure of the proton in this thesis. The first aspect concerned the distribution of the proton spin among its constituents. We estimated the polarized quark and gluon distributions in a global analysis of polarized structure function data. We studied furthermore how the knowledge on the spin-structure of the proton can be improved at future experiments. Secondly, we showed how hard diffraction in electron–proton collisions can be understood to be due to the pomeron, an object predicted from hadronic interaction physics. We suggested various tests for this interpretation. Finally, we demonstrated how the precise knowledge of the proton structure can be used to compute observables in proton–antiproton collisions, extending or confirming the Standard Model picture of particle physics.

Appendix A

Special functions

A.1 The Gamma function $\Gamma(x)$ and its derivatives

The Gamma function is defined as [70]

$$\Gamma(z) = \int_0^\infty t^{z-1} e^{-t} \, dt \qquad \{\text{Re}(z) > 0\}. \tag{A.1}$$

For positive integer arguments, $\Gamma(n)$ can be expressed as factorial

$$\Gamma(n+1) = n!,$$

which yields the recurrence formula

$$\Gamma(z+1) = z\Gamma(z). \tag{A.2}$$

$\Gamma(z)$ can be continued analytically to ($\{\text{Re}(z) \leq 0\} \setminus \{z = -i \mid i \in \mathbb{N}_0\}$) by recursive use of this formula.

The ψ-function is the logarithmic derivative of the Γ-function

$$\psi(z) \equiv \frac{d[\ln \Gamma(z)]}{dz}, \tag{A.3}$$

$$\psi'(z) = \frac{d\psi}{dz}, \tag{A.4}$$

$$\psi''(z) = \frac{d\psi'}{dz}. \tag{A.5}$$

155

These functions reduce to finite sums for positive integer arguments

$$\psi(n) \;=\; -\gamma_E + \sum_{k=1}^{n-1} k^{-1}, \tag{A.6}$$

$$\psi'(n) \;=\; \zeta_2 - \sum_{k=1}^{n-1} k^{-2}, \tag{A.7}$$

$$\psi''(n) \;=\; -2\zeta_3 + 2\sum_{k=1}^{n-1} k^{-3}, \tag{A.8}$$

where $\gamma_E = 0.5772156649\ldots$, $\zeta_2 = \pi^2/6$, $\zeta_3 = 1.2020569031\ldots$. The recurrence formulae

$$\psi^{(i)}(z+1) = \psi^{(i)}(z) + (-1)^i\, i!\, z^{-i-1} \tag{A.9}$$

yield an analytic continuation for $(\{\mathrm{Re}(z) \le 0\} \setminus \{z = -i \mid i \in \mathbb{N}_0\})$.

Numerical implementation

Due to the factorial growth of the Γ-function, a numerical implementation of $\ln\Gamma(x)$ is more appropriate. We have used the following interpolation formula [162] for $\mathrm{Re}(z) > 0$:

$$\ln\Gamma(z) \;=\; \left(z - \frac{1}{2}\right) \ln\left(z + \gamma - \frac{1}{2}\right) - z - \gamma + \frac{1}{2} + \ln\left(\sqrt{2\pi}F(z)\right), \tag{A.10}$$

$$F(z) \;\equiv\; \left[c_0 + \sum_{n=1}^{6} \frac{c_n}{z+n-1}\right],$$

with $\gamma = 5$ and

$$c_{0,\ldots,6} \;=\; (1, 76.18009173, -86.50532033, 24.01409822,$$

$$-1.231739516, 0.00120858003, -0.000005364).$$

For negative arguments, (A.2) is used recursively.

Using (A.10), it is straightforward to obtain interpolations for the ψ function and its derivatives:

$$\psi(z) \;=\; \frac{z - \frac{1}{2}}{z + \gamma - \frac{1}{2}} + \ln\left(z + \gamma - \frac{1}{2}\right) - 1 + \frac{F'}{F},$$

156

$$\psi'(z) = \frac{\gamma}{\left(z + \gamma - \frac{1}{2}\right)^2} + \frac{1}{z + \gamma - \frac{1}{2}} + \frac{F''F - [F']^2}{F^2},$$

$$\psi''(z) = -\frac{2\gamma}{\left(z + \gamma - \frac{1}{2}\right)^3} - \frac{1}{\left(z + \gamma - \frac{1}{2}\right)^2} + \frac{F'''F^2 - 3F''F'F + 2[F']^2}{F^3},$$

where F' etc. denote derivatives of $F(z)$ with respect to z. For negative arguments, the recursion relations (A.9) are applied.

A.2 The Lambert ω-function

The Lambert ω-function [163] is defined by the implicit equation

$$\omega(x)\exp\{\omega(x)\} = x, \qquad\qquad (A.11)$$

which has infinitely many solutions $\omega(x)$ in the complex plane. A principal branch can be defined by requiring analyticity of $\omega(x)$ in $x = 0$. This principal branch is real-valued in the interval $[-1/e; \infty[$ and is displayed in Fig. A.1.
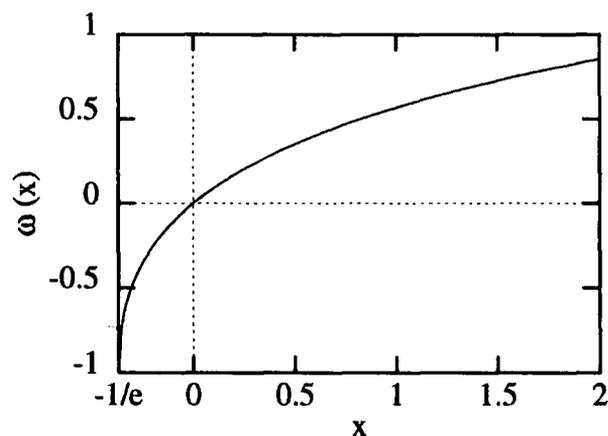

Figure A.1: The principal branch of the Lambert w-function.

The ω-function can be used to solve the equation

$$x^\alpha + \ln x = 0 \qquad\qquad (A.12)$$

157

with respect to x. For $\alpha > -1/e$, this equation has a real solution

$$x = \left(\frac{\omega(\alpha)}{\alpha} \right)^{1/\alpha}, \tag{A.13}$$

which can be used to discriminate regions in x dominated by logarithmic and powerlike terms.

A.3 The dilogarithm $\mathrm{Li}_2(x)$

The dilogarithm is defined by the integral [164]

$$\mathrm{Li}_2(x) = - \int_0^1 \frac{\ln(1 - xy)}{x} \, dx. \tag{A.14}$$

It is real-valued in the interval $] - \infty; 1]$ and can be expressed as a power series

$$\mathrm{Li}_2(x) = \sum_{n=1}^{\infty} \frac{x^n}{n^2}. \tag{A.15}$$

The following formulae relate dilogarithms of different arguments:

$$
\begin{aligned}
\mathrm{Li}_2(1 - x) &= -\mathrm{Li}_2(x) - \ln x \ln(1 - x) + \zeta_2, \\
\mathrm{Li}_2\left(\frac{1}{x} \right) &= -\mathrm{Li}_2(x) - \frac{1}{2} \ln^2(-x) - \zeta_2, \\
\mathrm{Li}_2\left(\frac{1}{1 - x} \right) &= \mathrm{Li}_2(x) + \ln(1 - x) \ln(-x) - \frac{1}{2} \ln^2(1 - x) + \zeta_2, \\
\mathrm{Li}_2\left(-\frac{1 - x}{x} \right) &= \mathrm{Li}_2(x) + \ln x \ln(1 - x) - \frac{1}{2} \ln^2 x - \zeta_2, \\
\mathrm{Li}_2\left(-\frac{x}{1 - x} \right) &= -\mathrm{Li}_2(x) - \frac{1}{2} \ln^2(1 - x).
\end{aligned}
\tag{A.16}
$$

Numerical implementation

The power series expression (A.15) is only slowly convergent. It is therefore not appropriate for an efficient numerical evaluation of the dilogarithm function. Introducing $u \equiv -\ln(1 - x)$, the dilogarithm can be expressed as [164]

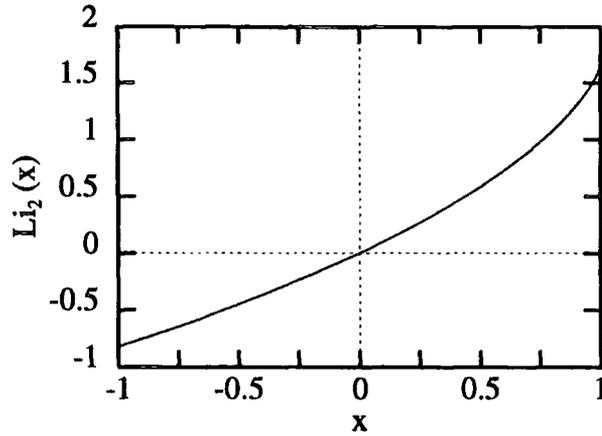$$\mathrm{Li}_2(x) = \int_0^u \frac{t}{e^t - 1} \, dt,$$

158

Figure A.2: The dilogarithm function $\text{Li}_2(x)$.

where the integrand is now the generating function of the Bernoulli numbers [70]. Therefore,

$$\text{Li}_2(x) = \sum_{n=0}^{\infty} B_n \frac{u^{n+1}}{(n+1)!}. \tag{A.17}$$

We have used the above equation truncated to finite order to compute $\text{Li}_2(x)$ if $-0.5 \leq x \leq 0.5$. For arguments outside this range, one of the relations (A.16) can be applied.

A.4 Finite sums

Computation of the moments of DGLAP splitting functions yields the following finite sums (cf. Appendix B.1.1):

$$S_i(n) = \sum_{k=1}^{n} \frac{1}{k^i} \qquad (i = 1, 2, 3) \tag{A.18}$$

$$\tilde{S}_i(n) = \sum_{k=1}^{n} \frac{(-1)^k}{k^i} \qquad (i = 1, 2, 3) \tag{A.19}$$

$$S_{12}(n) + S_{21}(n) = \sum_{k=1}^{n} \left(\frac{1}{k} S_2(k) + \frac{1}{k^2} S_1(k) \right) \tag{A.20}$$

159

$$\tilde{S}_{12}(n) = \sum_{k=1}^{n} \frac{1}{k} \tilde{S}_2(k). \tag{A.21}$$

The inversion of moments into x-space requires continuation of the n-moments into the complex plane. This is straightforward only for

$$S_{12}(n) + S_{21}(n) = S_1(n)S_2(n) + S_3(n),$$

$$S_1(n) = \gamma_E + \psi(n+1),$$

$$S_2(n) = \zeta_2 - \psi'(n+1),$$

$$S_3(n) = \zeta_3 + \frac{1}{2}\psi''(n+1), \tag{A.22}$$

using the definitions (A.6)–(A.8). For the remaining sums, we have to distinguish the cases n even and n odd, which we denote by $\eta = \pm 1$.

We define [165]

$$S_i'(n/2) \equiv 2^{i-1} \sum_{k=1}^{n} \frac{1+(-1)^k}{k^i} \tag{A.23}$$

$$= \frac{1}{2}(1+\eta)\, S_i(n/2) + \frac{1}{2}(1-\eta)\, S_i((n-1)/2)$$

$$\tilde{S}(n) \equiv \sum_{k=1}^{n} \frac{(-1)^k}{k^2} S_1(k). \tag{A.24}$$

In terms of these, the remaining sums read

$$\tilde{S}_i(n) = 2^{1-i} S_i'(n/2) - S_i(n)$$

$$\tilde{S}_{12}(n) = S_1(n)\tilde{S}_2(n) + \tilde{S}_3(n) - \tilde{S}(n). \tag{A.25}$$

The analytic continuation of (A.24) is given by[1] [135]:

$$\tilde{S}(n) = -\frac{5}{8}\zeta_3 + \eta \left(\frac{S_1(n)}{n^2} - \frac{\zeta_2}{2}\left(\psi((n+1)/2) - \psi(n/2)\right) + \int_0^1 x^{n-1} \frac{\mathrm{Li}_2(x)}{1+x}\, \mathrm{d}x \right),$$

---

[1]Please note that this expression is misprinted in the appendices of [85, 135].

160

where the last term can be numerically approximated by replacing the factor $(1 + x)^{-1}$ by its orthogonal expansion with the weight function $(x(1 - x))^{-1/2}$ (shifted Chebyshev of first kind [70]). The integral can then be computed analytically by use of (B.12)[2].

A peculiar feature of the finite sums (A.23) and (A.24) is that their analytic continuations depend on η, i.e. they are different if even and odd moments are considered.

A.5 "+"-functions

Both coefficient and splitting functions develop a singular behaviour as $x \to 1$, which is compensated by a contribution in $x = 1$, such that the convolution integral of these functions with any test function is finite. This behaviour is expressed conveniently by the introduction of a "+"-prescription:

$$\int_0^1 \mathrm{d}x \; [f(x)]_+ \; g(x) \equiv \int_0^1 \mathrm{d}x \; f(x) \; [g(x) - g(1)] \; . \tag{A.26}$$

Only two types of "+"-functions appear in the coefficient and splitting functions up to the next-to-leading order:

$$\left(\frac{1}{1 - x} \right)_+ \quad \text{and} \quad \left(\frac{\ln(1 - x)}{1 - x} \right)_+ \; . \tag{A.27}$$

The convolution integrals with the parton distributions usually take the form

$$\int_x^1 \frac{\mathrm{d}y}{y} \; [f(y)]_+ \; g\left(\frac{x}{y} \right) \; .$$

Using the definition (A.26), we can rewrite the two "+"-functions (A.27) into a form suitable for numerical implementation:

$$\int_x^1 \frac{\mathrm{d}y}{y} \left(\frac{1}{1 - y} \right)_+ g\left(\frac{x}{y} \right) = g(x) \ln \frac{1 - x}{x} + \int_x^1 \frac{\mathrm{d}y}{y} \frac{1}{1 - y} \left[g\left(\frac{x}{y} \right) - g(x) \right] \; ,$$

$$\int_x^1 \frac{\mathrm{d}y}{y} \left(\frac{\ln(1 - y)}{1 - y} \right)_+ g\left(\frac{x}{y} \right) = g(x) \left(\frac{1}{2} \ln^2(1 - x) - \zeta_2 + \mathrm{Li}_2(x) \right)$$

$$+ \int_x^1 \frac{\mathrm{d}y}{y} \frac{\ln(1 - y)}{1 - y} \left[g\left(\frac{x}{y} \right) - g(x) \right] \; . \tag{A.28}$$

---

[2]This expansion applied to the whole integrand [135] converges far more slowly due to the nonanalyticity of $\mathrm{Li}_2(x)$ in $x = 1$.

Appendix B

Evolution of parton densities

This chapter contains the mathematical techniques used in our parton distribution evolution programme, the algorithm applied is outlined. For reference, we give explicit expressions for both polarized and unpolarized splitting functions at leading and next-to-leading order in x and n space.

B.1 Mellin transformations and their inversion

The Mellin transformation $f(n) \equiv \mathcal{M}[f(x)]$ of a function $f(x)$ is defined to be

$$f(n) \equiv \mathcal{M}[f(x)] = \int_0^1 dx\, x^{n-1} f(x). \tag{B.1}$$

This transformation can be inverted in the complex n-plane

$$f(x) = \frac{1}{2\pi i} \int_{a-i\infty}^{a+i\infty} dn\, x^{-n} f(n), \tag{B.2}$$

where a is to be chosen such that all singularities of the function are lying to the left of the integration contour. The following properties of the transformation are relevant in the present context:

$$\mathcal{M}[af(x) + bg(x)] = af(n) + bg(n) \qquad \text{(Linearity)}, \tag{B.3}$$

162

$$\mathcal{M}\left[\frac{\mathrm{d}^k}{\mathrm{d}x^k}f(x)\right] \;=\; (-1)^n\frac{\Gamma(n)}{\Gamma(n-k)}f(n-k) \qquad \text{(Derivative)}, \qquad \text{(B.4)}$$

$$\mathcal{M}\left[\int_x^1 \frac{\mathrm{d}y}{y}f(y)g(x/y)\right] \;=\; f(n)g(n) \qquad\qquad\qquad \text{(Convolution)}. \qquad \text{(B.5)}$$

It is the latter property which makes this transformation useful to reduce the DGLAP integro-differential equations in x space to a set of coupled ordinary differential equations in n space.

B.1.1 Mellin integrals

In the following, we list the integrals required to compute the moments of splitting functions and initial distributions:

$$\int_0^1 x^{n-1}\,\mathrm{d}x \;=\; \frac{1}{n}\,, \qquad\qquad\qquad\qquad\qquad \text{(B.6)}$$

$$\int_0^1 x^{n-1}\ln x\,\mathrm{d}x \;=\; -\frac{1}{n^2}\,, \qquad\qquad\qquad\qquad \text{(B.7)}$$

$$\int_0^1 x^{n-1}\ln^2 x\,\mathrm{d}x \;=\; \frac{2}{n^3}\,, \qquad\qquad\qquad\qquad \text{(B.8)}$$

$$\int_0^1 x^{n-1}\ln(1-x)\,\mathrm{d}x \;=\; -\frac{1}{n}S_1(n)\,, \qquad\qquad\qquad \text{(B.9)}$$

$$\int_0^1 x^{n-1}\ln^2(1-x)\,\mathrm{d}x \;=\; \frac{1}{n}\left[S_2(n) + S_1^2(n)\right]\,, \qquad\qquad \text{(B.10)}$$

$$\int_0^1 x^{n-1}\ln x\ln(1-x)\,\mathrm{d}x \;=\; \frac{1}{n^2}S_1(n) - \frac{1}{n}\left(\zeta_2 - S_2(n)\right)\,, \qquad \text{(B.11)}$$

$$\int_0^1 x^{n-1}\,\mathrm{Li}_2(x)\,\mathrm{d}x \;=\; \frac{1}{n}\zeta_2 - \frac{1}{n^2}S_1(n)\,, \qquad\qquad \text{(B.12)}$$

$$\int_0^1 x^{n-1}\left(\mathrm{Li}_2(-x) + \ln x\ln(1+x)\right)\,\mathrm{d}x \;=\; -\frac{1}{2n}\zeta_2 + \frac{(-1)^n}{n}\left(\frac{1}{2}\zeta_2 + \tilde{S}_2(n)\right)\,, \quad \text{(B.13)}$$

$$\int_0^1 x^{n-1}\frac{1}{1-x}\ln x\,\mathrm{d}x \;=\; S_2(n) - \zeta_2 - \frac{1}{n^2}\,, \qquad\qquad \text{(B.14)}$$

$$\int_0^1 x^{n-1}\frac{1}{1-x}\ln^2 x\,\mathrm{d}x \;=\; 2\left(\zeta_3 + \frac{1}{n} - S_3(n)\right)\,, \qquad\qquad \text{(B.15)}$$

$$\int_0^1 x^{n-1}\frac{1}{1-x}\ln x\ln(1-x)\,\mathrm{d}x \;=\; \zeta_3 - \left(S_{12}(n) + S_{21}(n)\right) + \frac{1}{n^2}S_1(n)$$

163

$$+\frac{1}{n}S_2(n) - \left(\frac{1}{n} - S_1(n)\right)\zeta_2 \,, \qquad (B.16)$$

$$\int_0^1 x^{n-1} \frac{1}{1+x}\,dx = \frac{1}{n} - (-1)^n \left(\ln 2 + \tilde{S}_1(n)\right)\,, \qquad (B.17)$$

$$\int_0^1 x^{n-1} \frac{1}{1+x}\ln x\,dx = -\frac{1}{n^2} + (-1)^n \left(\tilde{S}_2(n) + \frac{1}{2}\zeta_2\right)\,, \qquad (B.18)$$

$$\int_0^1 x^{n-1} \frac{1}{1+x}\ln^2 x\,dx = \frac{2}{n^3} - 2(-1)^n \left(\frac{3}{4}\zeta_3 + \tilde{S}_3(n)\right)\,, \qquad (B.19)$$

$$\int_0^1 x^{n-1} \frac{\mathrm{Li}_2(-x) + \ln x \ln(1+x)}{1+x}\,dx = -\frac{1}{2n}\zeta_2 + (-1)^n \left[\frac{1}{n}\tilde{S}_2(n) - \tilde{S}_{12}(n) - \frac{1}{8}\zeta_3\right.$$
$$\left. +\frac{1}{2}\zeta_2 \left(\ln 2 + \tilde{S}_1(n) - S_1(n) + \frac{1}{n}\right)\right]\,, (B.20)$$

$$\int_0^1 x^{n-1} \left(\frac{1}{1-x}\right)_+ dx = -S_1(n) + \frac{1}{n}\,, \qquad (B.21)$$

$$\int_0^1 x^{n-1} \left(\frac{\ln(1-x)}{1-x}\right)_+ dx = \frac{1}{2}\left(S_1^2(n) + S_2(n)\right) - \frac{1}{n}S_1(n)\,, \qquad (B.22)$$

$$\int_0^1 x^{n-1} x^\alpha (1-x)^\beta\,dx = \frac{\Gamma(n+\alpha)\Gamma(1+\beta)}{\Gamma(n+1+\alpha+\beta)}\,. \qquad (B.23)$$

B.2 Splitting functions

B.2.1 x-space

The evolution of (polarized) parton distributions is governed by the splitting function matrix $(\Delta)P_{ji}(x)$ in the DGLAP evolution equations (3.7). These splitting functions can be expanded in powers of the QCD coupling constant

$$(\Delta)P_{ji}(x,\alpha_s) = \frac{\alpha_s}{2\pi}(\Delta)P_{ji}^{(0)} + \left(\frac{\alpha_s}{2\pi}\right)^2 (\Delta)P_{ji}^{(1)} + \dots$$

and have a naïve interpretation as the probability of a parton i splitting into a parton j while transferring a fraction x of its initial momentum.

The leading order unpolarized and polarized splitting functions are [31]

$$P_{qq}^{(0)} = C_F \left[\left(\frac{2}{1-x}\right)_+ - 1 - x + \frac{3}{2}\delta(1-x)\right]\,,$$

164

$$P_{qg}^{(0)} = 2T_f \left[x^2 + (1-x)^2 \right] ,$$

$$P_{gq}^{(0)} = C_F \frac{1 + (1-x)^2}{x} ,$$

$$P_{gg}^{(0)} = 2C_A \left[\left(\frac{1}{1-x} \right)_+ + \frac{1 - 2x + x^2 - x^3}{x} + \left(\frac{11}{12} - \frac{1}{3} \frac{T_f}{C_A} \right) \delta(1-x) \right] ; \text{(B.24)}$$

$$\Delta P_{qq}^{(0)} = C_F \left[\left(\frac{2}{1-x} \right)_+ - 1 - x + \frac{3}{2} \delta(1-x) \right] ,$$

$$\Delta P_{qg}^{(0)} = 2T_f \left[x^2 - (1-x)^2 \right] ,$$

$$\Delta P_{gq}^{(0)} = C_F \frac{1 - (1-x)^2}{x} ,$$

$$\Delta P_{gg}^{(0)} = 2C_A \left[\left(\frac{1}{1-x} \right)_+ + 1 - 2x + \left(\frac{11}{12} - \frac{1}{3} \frac{T_f}{C_A} \right) \delta(1-x) \right] . \qquad \text{(B.25)}$$

The leading order splitting function $(\Delta)P_{qq}^{(0)}$ governs the evolution of *all* possible non-singlet quark combinations *and* of the quark singlet in the coupled singlet–gluon equations. Beyond the leading order, the evolution of flavour non-singlet (+) combinations $(\Delta)q_i + (\Delta)\bar{q}_i - (\Delta)q_j - (\Delta)\bar{q}_j$ and valence non-singlet (–) combinations $(\Delta)q_i - (\Delta)\bar{q}_i$ is controlled by different splitting functions $(\Delta)P_{qq,+}$ and $(\Delta)P_{qq,-}$; the evolution of the non-singlet quarks is controlled by a third splitting function $(\Delta)P_{qq,S}$. These three splitting functions can be written as

$$(\Delta)P_{qq,\pm} = (\Delta)P_{qq} \pm (\Delta)P_{q\bar{q}} \quad \text{and} \quad (\Delta)P_{qq,S} = (\Delta)P_{qq,+} + (\Delta)P_{qq,PS}. \qquad \text{(B.26)}$$

The next-to-leading order correction terms read [33, 35]:

$$\begin{aligned}
P_{qq}^{(1)} = \quad & C_F^2 \left[-\frac{1+x^2}{1-x} \left(\frac{3}{2} \ln x + 2 \ln x \ln(1-x) \right) - 5 + 5x - \left(\frac{3}{2} + \frac{7}{2}x \right) \ln x \right. \\
& \left. - \frac{1}{2}(1+x) \ln^2 x + \left(\frac{3}{8} - 3\zeta_2 + 6\zeta_3 \right) \delta(1-x) \right] \\
& + C_F C_A \left[\frac{1+x^2}{1-x} \left(\frac{1}{2} \ln^2 x + \frac{11}{6} \ln x \right) + \left(\frac{67}{18} - \zeta_2 \right) \left(\left(\frac{2}{1-x} \right)_+ - 1 - x \right) \right. \\
& \left. + \frac{20}{3}(1-x) + (1+x) \ln x + \left(\frac{17}{24} + \frac{11}{3} \zeta_2 - 3\zeta_3 \right) \delta(1-x) \right]
\end{aligned}$$

$$+C_F T_f \left[-\frac{2}{3} \frac{1+x^2}{1-x} \ln x - \frac{20}{9} \left(\frac{1}{1-x} \right)_+ - \frac{2}{9} + \frac{22}{9} x - \left(\frac{1}{6} + \frac{4}{3} \zeta_2 \right) \delta(1-x) \right],$$

$$P_{q\bar{q}}^{(1)} = \left(C_F^2 - \frac{1}{2} C_F C_A \right) \left[\frac{1+x^2}{1+x} \left(\ln^2 x - 4 \ln x \ln(1+x) - 4\text{Li}_2(-x) - 2\zeta_2 \right) \right.$$

$$\left. + 2(1+x) \ln x + 4(1-x) \right],$$

$$P_{qq,PS}^{(1)} = 2 C_F T_f \left[\frac{20}{9x} - 2 + 6x - \frac{56}{9} x^2 + \left(1 + 5x + \frac{8}{3} x^2 \right) \ln x - (1+x) \ln^2 x \right],$$

$$P_{qg}^{(1)} = C_A T_f \left[\frac{40}{9x} + \frac{182}{9} + \frac{14}{9} x + \left(\frac{136}{3} x - \frac{38}{3} \right) \ln x - 4 \ln(1-x) - (2+8x) \ln^2 x \right.$$

$$+ \left(-\frac{218}{9} + \frac{44}{3} \ln x + 4 \ln(1-x) - \ln^2 x - 2 \ln^2(1-x) + 2 \zeta_2 \right)$$

$$\left(x^2 + (1-x)^2 \right) + \left(\ln^2 x - 4 \ln x \ln(1+x) - 4\text{Li}_2(-x) - 2\zeta_2 \right)$$

$$\left. \left(x^2 + (1+x)^2 \right) \right]$$

$$+ C_F T_f \left[4 - 9x - (1-4x) \ln x - (1-2x) \ln^2 x + 4 \ln(1-x) \right.$$

$$+ (10 + 4 \ln x - 4 \ln(1-x) - 4 \ln x \ln(1-x) + 2 \ln^2 x + 2 \ln^2(1-x)$$

$$\left. - 4 \zeta_2) \left(x^2 + (1-x)^2 \right) \right],$$

$$P_{gg}^{(1)} = C_F^2 \left[-\frac{5}{2} - \frac{7}{2} x + \left(2 + \frac{7}{2} x \right) \ln x - 2x \ln(1-x) - \left(1 - \frac{1}{2} x \right) \ln^2 x \right.$$

$$\left. - \left(3 \ln(1-x) + \ln^2(1-x) \right) \frac{1 + (1-x)^2}{x} \right]$$

$$+ C_F C_A \left[\frac{28}{9} + \frac{65}{18} x + \frac{44}{9} x^2 - \left(12 + 5x + \frac{8}{3} x^2 \right) \ln x + 2x \ln(1-x) \right.$$

$$+ (4+x) \ln^2 x + \left(\frac{1}{2} + \frac{11}{3} \ln(1-x) - 2 \ln x \ln(1-x) + \frac{1}{2} \ln^2 x \right.$$

$$+ \ln^2(1-x) - \zeta_2 \right) \frac{1 + (1-x)^2}{x} - \left(\frac{1}{2} \ln^2 x - 2 \ln x \ln(1+x) \right.$$

$$\left. \left. - 2\text{Li}_2(-x) - \zeta_2 \right) \frac{1 + (1+x)^2}{x} \right],$$

166

$$P_{gg}^{(1)} = C_A^2 \left[\frac{27}{2}(1-x) + \frac{67}{9}\left(x^2 - \frac{1}{x}\right) - \left(\frac{25}{3} - \frac{11}{3}x + \frac{44}{3}x^2\right)\ln x + 4(1+x)\ln^2 x \right.$$

$$- \left(4\ln x\ln(1-x) - \ln^2 x\right)\frac{(x^2-x+1)^2}{x(1-x)} + \left(\frac{8}{3} + 3\zeta_3\right)\delta(1-x)$$

$$+ \left(\frac{67}{9} - 2\zeta_2\right)\left(\left(\frac{1}{1-x}\right)_+ + \frac{1-2x+x^2-x^3}{x}\right)$$

$$\left. - \frac{(x^2+x+1)^2}{x(1+x)}\left(\ln^2 x - 4\ln x\ln(1+x) - 4\mathrm{Li}_2(-x) - 2\zeta_2\right) \right]$$

$$+ C_F T_f \left[\frac{4}{3x} - 16 + 8x + \frac{20}{3}x^2 - (6+10x)\ln x - 2(1+x)\ln^2 x - \delta(1-x)\right]$$

$$+ C_A T_f \left[2 - 2x + \frac{26}{9}\left(x^2 - \frac{1}{x}\right) - \frac{4}{3}(1+x)\ln x \right.$$

$$\left. - \frac{20}{9}\left(\left(\frac{1}{1-x}\right)_+ + \frac{1-2x+x^2-x^3}{x}\right) - \frac{4}{3}\delta(1-x)\right] ; \qquad \text{(B.27)}$$

$$\Delta P_{qq}^{(1)} = P_{qq}^{(1)} ,$$

$$\Delta P_{q\bar{q}}^{(1)} = -P_{q\bar{q}}^{(1)} ,$$

$$\Delta P_{qq,PS}^{(1)} = 2C_F T_f \left[1 - x - (1-3x)\ln x - (1+x)\ln^2 x\right] ,$$

$$\Delta P_{qg}^{(1)} = C_A T_f \left[24 - 22x + 2(1+8x)\ln x - 8(1-x)\ln(1-x) - 2(1+2x)\ln^2 x \right.$$

$$+ 2(1-2x)\ln^2(1-x) - 4(1+2x)\ln x\ln(1+x)$$

$$\left. - 4(1+2x)\mathrm{Li}_2(-x) - 4\zeta_2\right]$$

$$+ C_F T_f \left[-22 + 27x - 9\ln x + 8(1-x)\ln(1-x) - (1-2x)\ln^2 x \right.$$

$$\left. + 4(1-2x)\ln x\ln(1-x) - 2(1-2x)\ln^2(1-x) + 4(1-2x)\zeta_2\right] ,$$

$$\Delta P_{gq}^{(1)} = C_A C_F \left[\frac{41}{9} + \frac{35}{9}x + (4-13x)\ln x + \left(\frac{10}{3} + \frac{1}{3}x\right)\ln(1-x) \right.$$

$$- (4-2x)\ln x\ln(1-x) + (2+x)\ln^2 x + (4+2x)\ln x\ln(1+x)$$

$$\left. + (2-x)\ln^2(1-x) + (4+2x)\mathrm{Li}_2(-x) + 2x\zeta_2\right]$$

$$
+C_F^2 \left[-\frac{17}{2} + 4x - \left(2 - \frac{1}{2}x\right)\ln x - (2+x)\ln(1-x) + \left(1 - \frac{1}{2}x\right)\ln^2 x \right.
$$

$$
\left. -(2-x)\ln^2(1-x) \right]
$$

$$
+C_F T_f \left[-\frac{16}{9} - \frac{4}{9}x - \left(\frac{8}{3} - \frac{4}{3}x\right)\ln(1-x) \right] ,
$$

$$
\Delta P_{gg}^{(1)} = \quad C_A^2 \left[\left(\frac{67}{9} - 2\zeta_2\right)\left(\frac{1}{1-x}\right)_+ - \frac{37}{18} - \frac{97}{18}x + \left(\frac{29}{3} - \frac{67}{3}x\right)\ln x \right.
$$

$$
+ \left(8x - \frac{4}{1-x} - 4\right)\ln x\ln(1-x) + \left(8x + \frac{4}{1+x} + 4\right)\ln x\ln(1+x)
$$

$$
+ \left(\frac{1}{1-x} - \frac{1}{1+x} + 4\right)\ln^2 x + \left(8x + \frac{2}{1+x}\right)\zeta_2
$$

$$
\left. + \left(8x + \frac{4}{1+x} + 4\right)\mathrm{Li}_2(-x) + \left(3\zeta_3 + \frac{8}{3}\right)\delta(1-x) \right]
$$

$$
+C_A T_f \left[-\frac{20}{9}\left(\frac{1}{1-x}\right)_+ - \frac{56}{9} + \frac{76}{9}x - \frac{4}{3}(1+x)\ln x - \frac{4}{3}\delta(1-x) \right]
$$

$$
+C_F T_f \left[-10 + 10x - (10-2x)\ln x - (2+2x)\ln^2 x - \delta(1-x) \right]. \qquad \text{(B.28)}
$$

Recall the QCD colour factors (2.3): $C_F = 4/3$, $C_A = 3$ and $T_f = n_f/2$.

B.2.2 n-space

The DGLAP evolution equations, formulated in x-space, are a coupled system of integro–differential equations. If the equations are transformed to n-space, they reduce to a system of coupled differential equations, which can be solved analytically. Instead of using the Mellin-transformations of the above splitting function matrix, one can alternatively consider the matrix of the anomalous dimensions of the parton operators

$$
(\Delta)\gamma_{ji}(x,\alpha_s) = \frac{\alpha_s}{4\pi}(\Delta)\gamma_{ji}^{(0)} + \left(\frac{\alpha_s}{4\pi}\right)^2 (\Delta)\gamma_{ji}^{(1)} + \ldots,
$$

which are related to the moments of the splitting functions

$$
(\Delta)\gamma_{ji}^{(0)} = -4 \int_0^1 x^{n-1} (\Delta)P_{ji}^{(0)}(x)\mathrm{d}x ,
$$

168

$$(\Delta)\gamma_{ji}^{(1)} = -8\int_0^1 x^{n-1} (\Delta)P_{ji}^{(1)}(x)\mathrm{d}x.$$

The leading order anomalous dimensions are [31, 74, 166]

$$\gamma_{qq}^{(0)} = 4\,C_F\left[2S_1(n) - \frac{1}{n(n+1)} - \frac{3}{2}\right],$$

$$\gamma_{qg}^{(0)} = -8\,T_f\frac{n^2+n+2}{n(n+1)(n+2)},$$

$$\gamma_{gq}^{(0)} = -4\,C_F\frac{n^2+n+2}{(n-1)n(n+1)},$$

$$\gamma_{gg}^{(0)} = 4\,C_A\left[2S_1(n) - 4\frac{n^2+n+1}{(n^2-1)n(n+2)} - \frac{11}{6} + \frac{2}{3}\frac{T_f}{C_A}\right]; \qquad (B.29)$$

$$\Delta\gamma_{qq}^{(0)} = 4\,C_F\left[2S_1(n) - \frac{1}{n(n+1)} - \frac{3}{2}\right],$$

$$\Delta\gamma_{qg}^{(0)} = -8\,T_f\frac{n-1}{n(n+1)},$$

$$\Delta\gamma_{gq}^{(0)} = -4\,C_F\frac{n+2}{n(n+1)},$$

$$\Delta\gamma_{gg}^{(0)} = 4\,C_A\left[2S_1(n) - 4\frac{1}{n(n+1)} - \frac{11}{6} + \frac{2}{3}\frac{T_f}{C_A}\right]. \qquad (B.30)$$

A decomposition of the next-to-leading order quark–to–quark anomalous dimensions into qq, $q\bar{q}$ and qq, PS contributions – although possible – appears not to be adequate, as the resulting expressions are far more complicated than the $(+)$, $(-)$ and (S) combinations appearing in the evolution equation. In the following expressions [35, 167], we denote the non-singlet signatures by the variable $\eta = \pm 1$:

$$\gamma_{qq,\eta}^{(1)} = C_F^2\left[16S_1(n)\frac{(2n+1)}{n^2(n+1)^2} + 16\left(2S_1(n) - \frac{1}{n(n+1)}\right)(S_2(n) - S_2'(n/2))\right.$$

$$+24S_2(n) + 64\tilde{S}(n) - 8S_3'(n/2) - 3 - 8\frac{3n^3+n^2-1}{n^3(n+1)^3}$$

$$\left.-16\eta\frac{2n^2+2n+1}{n^3(n+1)^3}\right]$$

169

$$+C_F C_A \left[\frac{536}{9} S_1(n) - 8 \left(2S_1(n) - \frac{1}{n(n+1)} \right) (2S_2(n) - S_2'(n/2)) \right.$$

$$-\frac{88}{3} S_2(n) - 32\tilde{S}(n) + 4S_3'(n/2) - \frac{17}{3}$$

$$\left. -\frac{4}{9} \frac{151n^4 + 236n^3 + 88n^2 + 3n + 18}{n^3(n+1)^3} + 8\eta \frac{2n^2 + 2n + 1}{n^3(n+1)^3} \right]$$

$$+C_F T_f \left[-\frac{160}{9} S_1(n) + \frac{32}{3} S_2(n) + \frac{4}{3} + \frac{16}{9} \frac{11n^2 + 5n - 3}{n^2(n+1)^2} \right] , \tag{B.31}$$

$$\gamma_{qq,S}^{(1)} = \gamma_{qq,+}^{(1)} - 16\, C_F T_f \frac{5n^5 + 32n^4 + 49n^3 + 38n^2 + 28n + 8}{(n-1)n^3(n+1)^3(n+2)^2} ,$$

$$\gamma_{gg}^{(1)} = -8 C_A T_f \left[-2 \left(S_1^2(n) - S_2(n) + S_2'(n/2) \right) \frac{n^2 + n + 2}{n(n+1)(n+2)} \right.$$

$$+8 S_1(n) \frac{2n+3}{(n+1)^2(n+2)^2}$$

$$\left. +2 \frac{n^9 + 6n^9 + 15n^7 + 25n^6 + 36n^5 + 85n^4 + 128n^3 + 104n^2 + 64n + 16}{(n-1)n^3(n+1)^3(n+2)^3} \right]$$

$$-8 C_F T_f \left[\left(2S_1^2(n) - 2S_2(n) + 5 \right) \frac{n^2 + n + 2}{n(n+1)(n+2)} - 4S_1(n) \frac{1}{n^2} \right.$$

$$\left. +\frac{11n^4 + 26n^3 + 15n^2 + 8n + 4}{n^3(n+1)^3(n+2)} \right] ,$$

$$\gamma_{gq}^{(1)} = -4 C_F^2 \left[\left(10 S_1(n) + 2S_1^2(n) - 2S_2(n) \right) \frac{n^2 + n + 2}{(n-1)n(n+1)} - 4S_1(n) \frac{1}{(n+1)^2} \right.$$

$$\left. -\frac{12n^6 + 30n^5 + 43n^4 + 28n^3 - n^2 - 12n - 4}{(n-1)n^3(n+1)^3} \right]$$

$$-8 C_F C_A \left[\left(S_1^2(n) + S_2(n) - S_2'(n/2) \right) \frac{n^2 + n + 2}{(n-1)n(n+1)} \right.$$

$$-S_1(n) \frac{17n^4 + 41n^2 - 22n - 12}{3(n-1)^2 n^2(n+1)}$$

$$\left. +\frac{109n^9 + 621n^8 + 1400n^7 + 1678n^6 + 695n^5 - 1031n^4 - 1304n^3 - 152n^2 + 432n + 144}{9(n-1)^2 n^3(n+1)^3(n+2)^2} \right]$$

$$-\frac{32}{3} C_F T_f \left[\left(S_1(n) - \frac{8}{3} \right) \frac{n^2 + n + 2}{(n-1)n(n+1)} + \frac{1}{(n+1)^2} \right] ,$$

$$\gamma_{gg}^{(1)} = C_A^2 \left[\frac{536}{9} S_1(n) + 64 S_1(n) \frac{2n^5 + 5n^4 + 8n^3 + 7n^2 - 2n - 2}{(n-1)^2 n^2 (n+1)^2 (n+2)^2} - \frac{64}{3} + 32 \tilde{S}(n) \right.$$

$$+ 32 S_2'(n/2) \frac{n^2 + n + 1}{(n-1)n(n+1)(n+2)} - 16 S_1(n) S_2'(n/2) - 4 S_3'(n/2)$$

$$\left. - \frac{4}{9} \frac{457n^9 + 2742n^8 + 6040n^7 + 6098n^6 + 1567n^5 - 2344n^4 - 1632n^3 + 560n^2 + 1488n + 576}{(n-1)^2 n^3 (n+1)^3 (n+2)^3} \right]$$

$$+ C_A T_f \left[-\frac{160}{9} S_1(n) + \frac{32}{3} + \frac{16}{9} \frac{38n^4 + 76n^3 + 94n^2 + 56n + 12}{(n-1)n^2(n+1)^2(n+2)} \right]$$

$$+ C_F T_f \left[8 + 16 \frac{2n^6 + 4n^5 + n^4 - 10n^3 - 5n^2 - 4n - 4}{(n-1)n^3(n+1)^3(n+2)} \right] ; \tag{B.32}$$

$$\Delta \gamma_{qq,\eta}^{(1)} = \gamma_{qq,-\eta}^{(1)} , \tag{B.33}$$

$$\Delta \gamma_{qq,S}^{(1)} = \gamma_{qq,-}^{(1)} + 16 C_F T_f \frac{n^4 + 2n^3 + 2n^2 + 5n + 2}{n^3(n+1)^3} ,$$

$$\Delta \gamma_{qg}^{(1)} = 8 C_F T_f \left[2 \frac{n-1}{n(n+1)} \left(S_2(n) - S_1^2(n) \right) + 4 \frac{n-1}{n^2(n+1)} S_1(n) \right.$$

$$\left. - \frac{5n^5 + 5n^4 - 10n^3 - n^2 + 3n - 2}{n^3(n+1)^3} \right]$$

$$+ 16 C_A T_f \left[\frac{n-1}{n(n+1)} \left(S_1^2(n) - S_2(n) + S_2'(n/2) \right) - 4 \frac{1}{n(n+1)^2} S_1(n) \right.$$

$$\left. - \frac{n^5 + n^4 - 4n^3 + 3n^2 - 7n - 2}{n^3(n+1)^3} \right] ,$$

$$\Delta \gamma_{gq}^{(1)} = 32 C_F T_f \left[-\frac{n+2}{3n(n+1)} S_1(n) + \frac{5n^2 + 12n + 4}{9n(n+1)^2} \right]$$

$$+ 4 C_F^2 \left[\frac{2n+4}{n(n+1)} \left(S_1^2(n) + S_2(n) \right) - \frac{6n^2 + 14n + 4}{n(n+1)^2} S_1(n) \right.$$

$$\left. \frac{9n^5 + 30n^4 + 24n^3 - 7n^2 - 16n - 4}{n^3(n+1)^3} \right]$$

$$+ 8 C_A C_F \left[\frac{n+2}{n(n+1)} \left(-S_1^2(n) - S_2(n) + S_2'(n/2) \right) + \frac{11n^2 + 22n + 12}{3n^2(n+1)} S_1(n) \right.$$

$$\left. - \frac{76n^5 + 271n^4 + 254n^3 + 41n^2 + 72n + 36}{9n^3(n+1)^3} \right] ,$$

$$\Delta\gamma_{gg}^{(1)} = 4C_A^2\left[-4S_1(n)S_2'(n/2) + \frac{8}{n(n+1)}S_2'(n/2) - S_3'(n/2) + 8\tilde{S}(n)\right.$$

$$+\frac{134n^4 + 268n^3 + 134n^2 + 288n + 144}{9n^2(n+1)^2}S_1(n)$$

$$\left.-\frac{48n^6 + 144n^5 + 469n^4 + 698n^3 + 7n^2 + 258n + 144}{9n^3(n+1)^3}\right]$$

$$+32C_AT_f\left[-\frac{5}{9}S_1(n) + \frac{3n^4 + 6n^3 + 16n^2 + 13n - 3}{9n^2(n+1)^2}\right]$$

$$+8C_FT_f\frac{n^6 + 3n^5 + 5n^4 + n^3 - 8n^2 + 2n + 4}{n^3(n+1)^3}. \tag{B.34}$$

It was outlined in Section A.4 that the analytic continuation of some of the finite sums occurring in the above expressions is different for odd and even moments. The analytic continuation of the above quantities is nevertheless well defined. A formal treatment of lepton–hadron scattering in the operator product expression (e.g. [39]) shows that in the singlet case only the even moments of the unpolarized scattering amplitude and the odd moments of the polarized scattering amplitude are well defined. The remaining integer singlet moments are fixed by analytic continuation. In the unpolarized non-singlet case, one finds that the flavour non-singlet combinations have only even physical moments while the valence non-singlet combinations have only odd. This situation is inverted in the polarized case. In the above equations, one has therefore to use $\eta = 1$ in (B.32) and $\eta = -1$ in (B.34), the value of η in (B.31) and (B.33) depends on the non-singlet combination under consideration.

B.3 Solution in n-space

The numerical programme used to obtain the parton distributions presented in this thesis is based on an analytic solution of the DGLAP equations in n-space, which is inverted into x-space numerically. We outline a brief derivation of the solution in n-space below, which follows closely the approach of Furmanski and Petronzio [168].

The evolution equation for any[1] non-singlet combination of parton distributions with signature η reads

$$\frac{\partial}{\partial \ln Q^2} q_\eta(x, Q^2) = \int_x^1 \frac{dy}{y} \left[\frac{\alpha_s(Q^2)}{2\pi} P_{qq}^{(0)}(y) + \left(\frac{\alpha_s(Q^2)}{2\pi} \right)^2 P_{qq,\eta}^{(1)}(y) + \ldots \right] q_\eta(x/y, Q^2),$$

(B.35)

which transforms to[2]

$$\frac{\partial}{\partial \ln Q^2} q_\eta(n, Q^2) = -\frac{1}{2} \left[\frac{\alpha_s(Q^2)}{4\pi} \gamma_{qq}^{(0)} + \left(\frac{\alpha_s(Q^2)}{4\pi} \right)^2 \gamma_{qq,\eta}^{(1)} + \ldots \right] q_\eta(n, Q^2).$$

(B.36)

Using the evolution equation (2.4) for the running coupling

$$\frac{\partial}{\partial \ln Q^2} \ln \alpha_s(Q^2) = -\left[\frac{\alpha_s(Q^2)}{4\pi} \beta_0 + \left(\frac{\alpha_s(Q^2)}{4\pi} \right)^2 \beta_1 + \ldots \right],$$

we can rewrite the above equation as

$$\frac{\partial \ln q_\eta(n, Q^2)}{\partial \ln \alpha_s(Q^2)} = \frac{1}{2} \frac{\gamma_{qq}^{(0)} + \dfrac{\alpha_s(Q^2)}{4\pi} \gamma_{qq,\eta}^{(1)}}{\beta_0 + \dfrac{\alpha_s(Q^2)}{4\pi} \beta_1},$$

which can be expanded in $\alpha_s(Q^2)$

$$\frac{\partial \ln q_\eta(n, Q^2)}{\partial \ln \alpha_s(Q^2)} = \frac{1}{2\beta_0} \left[\gamma_{qq}^{(0)} + \frac{\alpha_s(Q^2)}{4\pi} \left(\gamma_{qq,\eta}^{(1)} - \frac{\beta_1}{\beta_0} \gamma_{qq}^{(0)} \right) \right].$$

Integration of this equation yields the solution for non-singlet combinations of parton distributions

$$q_\eta(n, Q^2) = \left(\frac{\alpha_s(Q^2)}{\alpha_s(Q_0^2)} \right)^{\frac{\gamma_{qq}^{(0)}}{2\beta_0}} \left[1 + \frac{\alpha_s(Q^2) - \alpha_s(Q_0^2)}{8\pi\beta_0} \left(\gamma_{qq,\eta}^{(1)} - \frac{\beta_1}{\beta_0} \gamma_{qq}^{(0)} \right) \right] q_\eta(n, Q_0^2).$$

(B.37)

The solution at leading order can be obtained from the above by omitting the second term in the brackets.

---

[1] The derivation below applies to flavour and valence non-singlet combinations of unpolarized and polarized parton distributions. We will omit the polarization index in the following.

[2] All anomalous dimensions in the remainder of the section are functions of n: $\gamma \equiv \gamma(n)$.

173

The solution in the quark singlet sector is more complicated as quark and gluon distributions are mixed in the evolution process. The evolution equations read

$$
\frac{\partial}{\partial \ln Q^2} \begin{pmatrix} \Sigma(x,Q^2) \\ G(x,Q^2) \end{pmatrix} = \int_x^1 \frac{dy}{y} \mathcal{P}(y) \begin{pmatrix} \Sigma(x/y,Q^2) \\ G(x/y,Q^2) \end{pmatrix}, \tag{B.38}
$$

with

$$
\mathcal{P}(y) = \frac{\alpha_s(Q^2)}{2\pi} \begin{pmatrix} P_{qq}^{(0)}(y) + \frac{\alpha_s(Q^2)}{2\pi} P_{qq,S}^{(1)}(y) + \dots \; ; & P_{qg}^{(0)}(y) + \frac{\alpha_s(Q^2)}{2\pi} P_{qg}^{(1)}(y) + \dots \\ P_{gq}^{(0)}(y) + \frac{\alpha_s(Q^2)}{2\pi} P_{gq}^{(1)}(y) + \dots \; ; & P_{gg}^{(0)}(y) + \frac{\alpha_s(Q^2)}{2\pi} P_{gg}^{(1)}(y) + \dots \end{pmatrix}.
$$

Transformation into moment space yields

$$
\frac{\partial}{\partial \ln Q^2} \begin{pmatrix} \Sigma(n,Q^2) \\ G(n,Q^2) \end{pmatrix} = -\frac{1}{2} \left[\frac{\alpha_s}{4\pi} \gamma^{(0)} + \left(\frac{\alpha_s}{4\pi} \right)^2 \gamma^{(1)} + \dots \right] \begin{pmatrix} \Sigma(n,Q^2) \\ G(n,Q^2) \end{pmatrix}, \tag{B.39}
$$

with

$$
\gamma^{(0)} = \begin{pmatrix} \gamma_{qq}^{(0)} & \gamma_{qg}^{(0)} \\ \gamma_{gq}^{(0)} & \gamma_{gg}^{(0)} \end{pmatrix},
$$

$$
\gamma^{(1)} = \begin{pmatrix} \gamma_{qq,S}^{(1)} & \gamma_{qg}^{(1)} \\ \gamma_{gq}^{(1)} & \gamma_{gg}^{(1)} \end{pmatrix}. \tag{B.40}
$$

Which again yields

$$
\frac{\partial}{\partial \ln \alpha_s(Q^2)} \begin{pmatrix} \Sigma(n,Q^2) \\ G(n,Q^2) \end{pmatrix} = \frac{1}{2\beta_0} \left[\gamma^{(0)} + \frac{\alpha_s(Q^2)}{4\pi} \gamma^R \right] \begin{pmatrix} \Sigma(n,Q^2) \\ G(n,Q^2) \end{pmatrix}. \tag{B.41}
$$

$$
\gamma^R \equiv \gamma^{(1)} - \frac{\beta_1}{\beta_0} \gamma^{(0)} \tag{B.42}
$$

Let us first consider the leading order equation

$$
\frac{\partial}{\partial \ln \alpha_s(Q^2)} \begin{pmatrix} \Sigma(n,Q^2) \\ G(n,Q^2) \end{pmatrix} = \frac{1}{2\beta_0} \gamma^{(0)} \begin{pmatrix} \Sigma(n,Q^2) \\ G(n,Q^2) \end{pmatrix}. \tag{B.43}
$$

The eigenvalues of $\gamma^{(0)}$ are given by

$$\lambda_{1,2} = \frac{1}{2}\left[\gamma_{qq}^{(0)} + \gamma_{gg}^{(0)} \pm \sqrt{\left(\gamma_{qq}^{(0)} - \gamma_{gg}^{(0)}\right)^2 + 4\gamma_{gq}^{(0)}\gamma_{qg}^{(0)}}\right]. \tag{B.44}$$

If we introduce projection matrices

$$e_1 = \frac{1}{\lambda_1 - \lambda_2}\left[\gamma^{(0)} - \lambda_2\, \mathbf{1}\right],$$

$$e_2 = \frac{1}{\lambda_1 - \lambda_2}\left[-\gamma^{(0)} + \lambda_1\, \mathbf{1}\right], \tag{B.45}$$

with the properties

$$e_i \cdot e_j = \delta_{ij}e_i,$$

$$\mathbf{1} = e_1 + e_2,$$

$$\gamma^{(0)} = \lambda_1 e_1 + \lambda_2 e_2,$$

(B.43) can be diagonalized

$$\frac{\partial}{\partial \ln \alpha_s(Q^2)}\begin{pmatrix} \Sigma(n,Q^2) \\ G(n,Q^2) \end{pmatrix} = \frac{1}{2\beta_0}\left(\lambda_1 e_1 + \lambda_2 e_2\right)\begin{pmatrix} \Sigma(n,Q^2) \\ G(n,Q^2) \end{pmatrix}$$

and integrated

$$\begin{pmatrix} \Sigma(n,Q^2) \\ G(n,Q^2) \end{pmatrix} = E^{(0)}(Q^2,Q_0^2)\begin{pmatrix} \Sigma(n,Q_0^2) \\ G(n,Q_0^2) \end{pmatrix},$$

$$E^{(0)}(Q^2,Q_0^2) = \left(\frac{\alpha_s(Q^2)}{\alpha_s(Q_0^2)}\right)^{\frac{\lambda_1}{2\beta_0}} e_1 + \left(\frac{\alpha_s(Q^2)}{\alpha_s(Q_0^2)}\right)^{\frac{\lambda_2}{2\beta_0}} e_2. \tag{B.46}$$

For the solution of (B.41), we can now make the ansatz

$$\frac{\partial}{\partial \ln \alpha_s(Q^2)}\begin{pmatrix} \Sigma(n,Q^2) \\ G(n,Q^2) \end{pmatrix} = (1+U)\, E^{(0)}(Q^2,Q_0^2)\begin{pmatrix} \Sigma(n,Q_0^2) \\ G(n,Q_0^2) \end{pmatrix}, \tag{B.47}$$

which yields an evolution equation for the matrix U:

$$\frac{\partial U}{\partial \ln \alpha_s(Q^2)} = \frac{1}{2\beta_0}\left[\frac{\alpha_s(Q^2)}{4\pi}\gamma^R + \gamma^{(0)}U - U\gamma^{(0)}\right].$$

175

Using the fact that the matrices e_i form an orthonormal basis, we can decompose any matrix

$$M = e_1 M e_1 + e_2 M e_2 + e_1 M e_2 + e_2 M e_1$$

into its components. Applying this to the above equation, we obtain evolution equations for individual projections of U:

$$\frac{\partial}{\partial \ln \alpha_s(Q^2)} (e_i U e_j) = \frac{\alpha_s(Q^2)}{8\pi\beta_0} e_i \gamma^R e_j + \frac{1}{2\beta_0}(\lambda_i - \lambda_j) e_i U e_j .$$

With the solution of the inhomogeneous differential equation $f'(x) = Ae^x + Bf(x)$:

$$f(x) = \frac{A}{1-B}\left[e^x - e^{x_0 + B(x - x_0)}\right] + f(x_0)e^{B(x - x_0)}$$

we obtain

$$e_i U e_j = \frac{1}{4\pi(2\beta_0 - \lambda_i + \lambda_j)}\left[\alpha_s(Q^2) - \alpha_s(Q_0^2)\left(\frac{\alpha_s(Q^2)}{\alpha_s(Q_0^2)}\right)^{\frac{\lambda_i - \lambda_j}{2\beta_0}}\right] e_i \gamma^R e_j.$$

Insertion into (B.47) yields the solution

$$\begin{pmatrix} \Sigma(n, Q^2) \\ G(n, Q^2) \end{pmatrix} =$$

$$\left\{\left(\frac{\alpha_s(Q^2)}{\alpha_s(Q_0^2)}\right)^{\frac{\lambda_1}{2\beta_0}}\left[e_1 + \frac{1}{8\pi\beta_0}\left(\alpha_s(Q^2) - \alpha_s(Q_0^2)\right) e_1 \gamma^R e_1\right.\right.$$

$$\left.+ \frac{\alpha_s(Q^2)}{4\pi(2\beta_0 - \lambda_2 + \lambda_1)} e_2 \gamma^R e_1 - \frac{\alpha_s(Q_0^2)}{4\pi(2\beta_0 - \lambda_1 + \lambda_2)} e_1 \gamma^R e_2\right]$$

$$+ \left(\frac{\alpha_s(Q^2)}{\alpha_s(Q_0^2)}\right)^{\frac{\lambda_2}{2\beta_0}}\left[e_2 + \frac{1}{8\pi\beta_0}\left(\alpha_s(Q^2) - \alpha_s(Q_0^2)\right) e_2 \gamma^R e_2\right.$$

$$\left.\left.+ \frac{\alpha_s(Q^2)}{4\pi(2\beta_0 - \lambda_1 + \lambda_2)} e_1 \gamma^R e_2 - \frac{\alpha_s(Q_0^2)}{4\pi(2\beta_0 - \lambda_2 + \lambda_1)} e_2 \gamma^R e_1\right]\right\} \begin{pmatrix} \Sigma(n, Q_0^2) \\ G(n, Q_0^2) \end{pmatrix} ,$$

$$(\text{B.48})$$

where γ^R is defined in (B.42).

Given the moments of parton distributions at a scale Q_0^2, (B.37) and (B.48) enable us to evolve these to some different scale Q^2.

B.3.1 Heavy flavour thresholds

The number of 'active' quark flavours n_f appears both in the anomalous dimensions and the coefficients of the QCD β-function. At scales of $Q^2 \sim M_p^2$, the number of active quark flavours is obviously three: u, d, s. The situation becomes more complicated as Q^2 increases; if $Q^2(1 - x)/x = W^2 > 4m_c^2$, one is able to produce a pair of charm quarks, above this threshold the c quark has become 'active'. If Q^2 is increased even further, the b quark will become 'active' as well. These thresholds can be incorporated into the running of $\alpha_s(Q^2)$ by increasing the number of flavours in the β-function and changing Λ in (2.5) at each threshold $Q^2 = m_q^2$, requiring that $\alpha_s(m_q^2)$ is continuous. For $\alpha_s(M_Z^2) = 0.112$, as used in Chapter 5 and [41] this procedure yields

$$\Lambda^{\text{NLO}}_{n_f=3,4,5,6} = 281, 231, 154, 59 \text{ MeV}.$$

So far, it has not been possible to incorporate the flavour threshold behaviour consistently into the evolution equations. Two different approaches are possible, each has advantages and drawbacks:

(1) The heavy flavours are assumed to be an intrinsic part of the proton structure. Their distribution is zero for $Q^2 < m_q^2$, and starts to evolve like any other massless distribution for $Q^2 > m_q^2$. This is implemented by changing the number of active flavours in the splitting functions as well as in the running coupling and the β-function. Furthermore, a new flavour non-singlet distribution

$$q_{+,NS} = \Sigma - (n_f - 1)(q_{n_f} + \bar{q}_{n_f})$$

starts evolving at each threshold. This approach yields the correct behaviour of the distributions at $Q^2 \to \infty$, where quark mass effects vanish.

177

(2) The heavy flavours are assumed to be not intrinsically present in the proton. They are only generated via a photon–gluon fusion in the DIS interaction. Therefore, the number of flavours in the splitting functions and anomalous dimensions is fixed to $n_f = 3$, while it increases at each threshold in the running coupling and the β-function. This approach allows a correct treatment of the heavy quark content of structure functions around threshold.

In practice, the difference between both approaches is only sizable around the threshold. Throughout this thesis, we have used the second approach, which is incorporated by applying (B.37) and (B.48) repeatedly for $Q_0^2 \rightarrow m_q^2$, $m_q^2 \rightarrow Q^2$ with the appropriate β and Λ in each interval.

B.3.2 Coefficient functions

A global fit of parton distributions to experimental data requires the evaluation of structure functions and related quantities for a large number of points in (x, Q^2). If the evolution is performed in x-space (e.g. [42]), one usually creates large grids with the parton distributions $f(x, Q^2)$. Any observable to be fitted can then be computed as convolution integral of coefficient functions and parton distributions.

Evolution in n-space has the advantage that the moments of splitting functions and initial parton distributions have only to be computed once along the contour of inversion. The distributions at a particular value of (x, Q^2) are then obtained by inverting (B.37, B.48). The computation time needed for a fit is further optimized by computing the moments of the experimental observables, which reduces the convolution of coefficient functions and parton densities to a product of their moments. The coefficient functions for the unpolarized and polarized structure functions (3.15–3.17) read in n-space:

$$
\begin{aligned}
C_{2,q}(n, \alpha_s) &= 1 + \frac{\alpha_s}{2\pi} C_F \Bigg[S_1^2(n) - S_2(n) + \frac{3}{2} S_1(n) - \frac{1}{n(n+1)} S_1(n) \\
&\quad - \frac{9n^3 + 2n^2 - 5n - 2}{2n^2(n+1)} \Bigg],
\end{aligned}
$$

178

$$C_{2,g}(n,\alpha_s) = \frac{\alpha_s}{2\pi}T_f\left[-2\frac{n^2+n+2}{n(n+1)(n+2)}S_1(n) - \frac{2n^3-8n^2-2n-4}{n^2(n+1)(n+2)}\right], \quad (B.49)$$

$$C_{L,q}(n,\alpha_s) = \frac{\alpha_s}{2\pi}C_F\frac{2}{n+1},$$

$$C_{L,g}(n,\alpha_s) = \frac{\alpha_s}{2\pi}T_f\frac{8}{(n+1)(n+2)}, \quad (B.50)$$

$$\Delta C_q(n,\alpha_s) = 1 + \frac{\alpha_s}{2\pi}C_F\left[S_1^2(n) - S_2(n) + \frac{3}{2}S_1(n) - \frac{1}{n(n+1)}S_1(n)\right.$$
$$\left. - \frac{9n^3+6n^2-3n-2}{2n^2(n+1)}\right],$$

$$\Delta C_g(n,\alpha_s) = \frac{\alpha_s}{2\pi}T_f\left[-2\frac{n-1}{n(n+1)}S_1(n) - \frac{2n^2-4n+2}{n^2(n+1)}\right]. \quad (B.51)$$

B.4 Inversion into x-space

Once the parton distributions or structure functions in n-space have been computed according to the above formulae, the expressions in x-space can in principle be regained by use of (B.2). It turns out that this is rather difficult in practice, as most functions appearing are strongly oscillating along the contour $]a - i\infty; a + i\infty[$ used in (B.2), while falling off only very slowly for large absolute values of n. Instead of using a dedicated integration algorithm for oscillating functions, we decided to deform the contour of integration in the complex n-plane such that an ordinary integration algorithm can be applied. Such a deformation of the contour does not change the value of the integral, provided the integrand is free of singularities in the area enclosed by the old and new contour (Cauchy's integration law).

The results of the n-space evolution contain the following singularities:

(1) All anomalous dimensions are singular for $\{n = -i \mid i \in \mathbb{N}_0\}$.

(2) The unpolarized singlet anomalous dimensions are furthermore singular for $n = +1$ (soft gluon singularity).

(3) If the initial distributions are singular like x^α ($\alpha < 0$) for $x \to 0$, their Mellin transformations are singular for $n = -\alpha$.

As all singularities are located on the real axis, we are free to choose any contour in the complex plane which crosses the real axis to the left of all singular points. Spurious singularities occur where the eigenvalues (B.44) of the leading order anomalous dimension matrix degenerate. To guarantee numerical stability, the integration contour should not touch these singularities either.
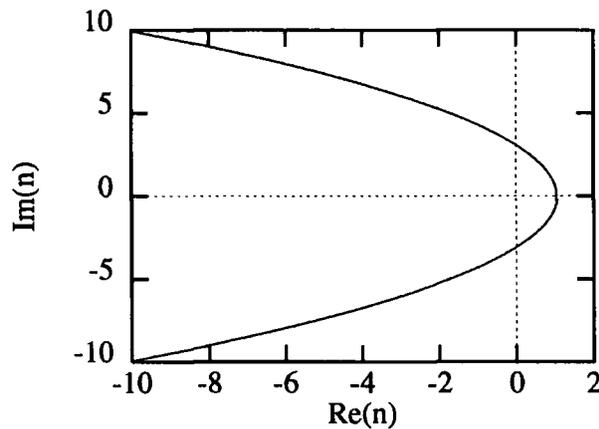

Figure B.1: Inversion contour used in the polarized evolution.

The results presented in this thesis were obtained with the contour

$$\text{Re}(n) = a - \tan^2 \phi$$

$$\text{Im}(n) = b \tan \phi, \tag{B.52}$$

in which (B.2) reads

$$f(x) = \frac{1}{2\pi} \int_{-\pi/2}^{\pi/2} \frac{\mathrm{d}\phi}{\cos^2 \phi} \left[b \,\text{Re} \left(x^{-n(\phi)} f(n(\phi)) \right) - 2 \tan \phi \,\text{Im} \left(x^{-n(\phi)} f(n(\phi)) \right) \right]. \tag{B.53}$$

We have chosen $a = 1.05, b = 3$ for the polarized and $a = 2.05, b = 3$ for the unpolarized evolution. The ϕ-integration was performed using Simpson's rule; to avoid sampling of

180

the integrand in irrelevant regions, we have cut $|\phi| < 1.48$ for $x \geq 0.4$ and $|\phi| < 1.37$ for $x < 0.4$.

Bibliography

[1] See for example: A. Sommerfeld, *Lectures on Theoretical Physics, Vol. IV: Optics"*, Academic Press (New York, 1954).

[2] F. Halzen and A.D. Martin, *Quarks and Leptons*, John Wiley & Sons, Inc. (New York, 1984).

[3] R. Hofstadter and R.W. McAllister, Phys. Rev. **98** (1955) 217.

[4] A review of these experiments can be found in: R. Hofstadter, Rev. Mod. Phys. **28** (1956) 217.

[5] M.N. Rosenbluth, Phys. Rev. **79** (1950) 615.

[6] R.G. Sachs, Phys. Rev. **126** (1962) 2256.

[7] F. Borkowski, G.G. Simon, V.H. Walther and R.D. Wendling, Nucl. Phys. **B93** (1975) 461 and refrences therein.

[8] R.G. Roberts, *The Structure of the Proton*, Cambridge University Press (Cambridge, 1990).

[9] S.D. Drell and J. Walecka, Ann. Phys. (N.Y.) **28** (1964) 18.

[10] W.K.H. Panofsky, Proceedings of the "14th International Conference on High Energy Physics", Vienna, 1968, eds. J. Prentki and J. Steinberger (CERN, 1968), p.23; E.D. Bloom *et al.*, Phys. Rev. Lett. **23** (1969) 930; M. Breidenbach *et al.*, Phys. Rev. Lett. **23** (1969) 935.

[11] A. Milsztajn and M. Virchaux, Proceedings of the "32. Universitätswochen für Kern- und Teilchenphysik", Schladming, Austria, 1993, eds. L. Mathelitsch and W. Plessas, Springer Verlag (Berlin, 1994), p.257.

[12] B. Badelek *et al.*, Proceedings of the "HERA workshop on proton, photon and pomeron structure", St. John's College, Durham, 1995, J. Phys. **G22** (1996) 815.

[13] SLAC-Yale collaboration: M.J. Alguard *et al.*, Phys. Rev. Lett. **37** (1976) 1261; G. Baum *et al.*, Phys. Rev. Lett. **45** (1980) 2000; **51** (1983) 1135.

[14] SMC collaboration: D. Adams *et al.*, Phys. Lett. **B336** (1994) 125.

[15] H. Yukawa, Proc. Phys. Math. Soc. Japan **17** (1935) 48.

[16] C.M.G. Lattes *et al.*, Nature **159** (1947) 694, **160** (1947) 453.

[17] R. Bjorkund *et al.*, Phys. Rev. **77** (1950) 213,
J. Steinberger, W.K.H. Panofsky, J.S. Steller, Phys. Rev. **78** (1950) 802.

[18] Y. Ne'eman, Nucl. Phys. **26** (1961) 22; M. Gell–Mann, Phys. Rev. **126** (1962) 1067; M. Gell-Mann and Y. Ne'eman, *The Eightfold Way*, Benjamin (New York, 1964).

[19] M. Gell-Mann, Phys. Lett. **8** (1964) 214; G. Zweig, CERN preprints CERN-TH-401 (1964), CERN-TH-412 (1964).

[20] O.W. Greenberg: Phys. Rev. Lett. **13** (1964) 598; M.Y. Han and Y. Nambu, Phys. Rev. **139B** (1965) 1006.

[21] H. Fritzsch, M. Gell-Mann and H. Leutwyler, Phys. Lett. **47B** (1973) 365.

[22] G. Sterman, *Introduction to Quantum Field Theory*, Cambridge University Press (Cambridge, 1993).

[23] M. Gell-Mann and F.E. Low, Phys. Rev. **95** (1954) 1300.

[24] D.J. Gross and F. Wilczek, Phys. Rev. Lett. **30** (1973) 1342;
H.D. Politzer, Phys. Rev. Lett. **30** (1973) 1346;
W.E. Caswell, Phys. Rev. Lett. **33** (1974) 244;
O.V. Tarasov, A.A. Vladimirov and A.Yu. Zharkov, Phys. Lett. **93B** (1980) 429.

[25] R.K. Ellis, W.J. Stirling and B.R. Webber, *QCD and Collider Physics*, Cambridge University Press (Cambridge, 1996).

[26] J.D. Bjorken, Phys. Rev. **179** (1969) 1547.

[27] J.D. Bjorken and E.A. Paschos, Phys. Rev. **185** (1969) 1975.

[28] S.D. Drell and T.M. Yan, Phys. Rev. Lett. **25** (1970) 316; Ann. Phys. **66** (1971) 578.

[29] J.H. Christenson *et al.*, Phys. Rev. Lett. **25** (1970) 1523, Phys. Rev. **D8** (1973) 2016.

[30] QCD corrections to deep inelastic structure functions have been calculated in numerous places in the literature, the derivation given in this section follows closely: E.B. Zijlstra and W.L. van Neerven, Nucl. Phys. **B383** (1992) 525, which contains the complete $\mathcal{O}(\alpha_s^2)$ corrections to $F_2(x, Q^2)$.

[31] V.N. Gribov and L.N. Lipatov, Sov. J. Nucl. Phys. **15** (1972) 438, 675.
G. Altarelli and G. Parisi, Nucl. Phys. **B126** (1977) 298.
Yu.L. Dokshitzer, Sov. Phys. JETP **46** (1977) 641.

[32] C. Chang *et al.*, Phys. Rev. Lett. **35** (1975) 901;
E.M. Riordan *el al.*, Phys. Lett. **52B** (1974) 249.

[33] G. Curci, W. Furmanski and R. Petronzio, Nucl. Phys. **B175** (1980) 27;
W. Furmanski and R. Petronzio, Phys. Lett. **97B** (1980) 437.
E.G. Floratos, C. Kounnas and R. Lacaze, Nucl. Phys. **B192** (1981) 417.
E.G. Floratos, D.A. Ross and C.T. Sachrajda, Nucl. Phys. **B129** (1977) 66; Errata

B139 (1978) 545, **B152** (1979) 493.

A. Gonzales–Arroyo, C. Lopez and F.J. Yndurain, Nucl. Phys. **B153** (1979) 161.

[34] The derivation sketched here follows closely: E.B. Zijlstra and W.L. van Neerven, Nucl. Phys. **B417** (1994) 61; Erratum **B426** (1994) 245.

[35] R. Mertig and W.L. van Neerven, Z. Phys. **C70** (1996) 637.
W. Vogelsang, Phys. Rev. **D54** (1996) 2023.

[36] W.A. Bardeen, A.J. Buras, D.W. Duke and T. Muta, Phys. Rev. **D18** (1978) 3998.

[37] J. Kodaira, S. Matsuda, T. Muta, K. Sasaki and T. Uematsu, Phys. Rev. **D20** (1979) 627.

[38] J. Kodaira, Nucl Phys. **B165** (1980) 129.

[39] S.A. Larin, P. Nogueira, T. van Ritbergen, J.A.M. Vermaseren, NIKHEF preprint 96-010 (1996).

[40] M. Göckeler et al., Phys. Rev. **D53** (1996) 2317.

[41] A.D. Martin, R.G. Roberts and W.J. Stirling, Phys. Lett. **B354** (1995) 155.

[42] A.D. Martin, R.G. Roberts and W.J. Stirling, Phys. Rev. **D50** (1994) 6734.

[43] CTEQ collaboration: H.L. Lai et al., Phys. Rev. **D51** (1995) 4763.

[44] M. Glück, E. Reya and A. Vogt, Z. Phys. **C67** (1995) 433.

[45] EMC collaboration: J. Ashman et al., Nucl. Phys. **B328** (1989) 1.

[46] SMC collaboration: B. Adeva et al., Phys. Lett. **B302** (1993) 533.

[47] SMC collaboration: D. Adams et al., Phys. Lett. **B329** (1994) 399.

[48] SMC collaboration: D. Adams et al., Phys. Lett. **B357** (1995) 248.

[49] SLAC-E142 collaboration: D.L. Anthony *et al.*, Phys. Rev. Lett. **71** (1993) 959.

[50] SLAC-E143 collaboration: K. Abe *et al.*, Phys. Rev. Lett. **74** (1995) 346.

[51] SLAC-E143 collaboration: K. Abe *et al.*, Phys. Rev. Lett. **75** (1995) 25.

[52] M. Düren (HERMES collaboration), Proceedings of the "XXXI Rencontres de Moriond, QCD and High Energy Hadronic Interactions", Les Arcs, 1996, to appear.

[53] SLAC-E143 collaboration: K. Abe *et al.*, Phys. Rev. Lett. **76** (1996) 584.

[54] SLAC-E143 collaboration: K. Abe *et al.*, Phys. Lett. **B364** (1995) 61.

[55] J.D. Bjorken, Phys. Rev. **148** (1966) 1467, Phys. Rev. **D1** (1970) 1376.

[56] M. Gourdin, Nucl. Phys. **B38** (1972) 418.

[57] J. Ellis and R.L. Jaffe, Phys. Rev. **D9** (1974) 1444; Erratum **D10** (1974) 1669.

[58] Particle Data Group, Phys. Rev. **D50** (1994) 1173; **D54** (1996) 1.

[59] F.E. Close and R.G. Roberts, Phys. Lett. **B316** (1993) 165.

[60] S. Gorishny and S.A. Larin, Phys. Lett. **B172** (1986) 109;
S.A. Larin and J.A.M. Vermaseren, Phys. Lett. **B259** (1991) 345.

[61] Corrections to this sum rule up to $\mathcal{O}(\alpha_s^2)$ are found in: S.A. Larin, Phys. Lett. **B334** (1994) 192.

[62] C.S. Lam and Bing-An Li, Phys. Rev. **D25** (1982) 683.

[63] R.D. Ball, S. Forte and G. Ridolfi, Phys. Lett. **B378** (1996) 255.

[64] G. Altarelli and W.J. Stirling, Particle World **1** (1989) 40.

[65] T. Gehrmann and W.J. Stirling, Z. Phys. **C65** (1995) 461.

186

[66] S.J. Brodsky, M. Burkardt and I. Schmidt, Nucl. Phys. **B441** (1995) 197.

[67] A.D. Martin, R.G. Roberts and W.J. Stirling, Durham preprint DTP/96/44 (1996).

[68] R.D. Ball, S. Forte and G. Ridolfi, Nucl. Phys. **B444** (1995) 287; Erratum **B449** (1995) 680.

[69] T. Gehrmann and W.J. Stirling, Phys. Rev. **D53** (1996) 6100.

[70] M. Abramowitz and I.A. Stegun, *Handbook of Mathematical Functions*, National Bureau of Standards Applied Mathematics Series **55** (1964).

[71] S.D. Bass and P.V. Landshoff, Phys. Lett. **B336** (1994) 537.

[72] F.E. Close and R.G. Roberts, Phys. Lett. **B336** (1994) 257.

[73] J. Bartels, B.I. Ermolaev and M.G. Ryskin, Z. Phys. **C70** (1996) 273.
J. Kwieciński, Acta Physica Polonica **B27** (1996) 893.

[74] M.A. Ahmed and G.G. Ross, Phys. Lett. **56B** (1975) 385.

[75] A. Berera, Phys. Lett. **B293** (1992) 445.

[76] D.A. Ross and C.T. Sachrajda, Nucl. Phys. **B149** (1979) 497.
M. Stratmann, W. Vogelsang and A. Weber, Phys. Rev. **D53** (1996) 138.

[77] T. Gehrmann and W.J. Stirling, Phys. Lett. **B365** (1996) 347.

[78] A.D. Watson, Z. Phys. **C12** (1982) 123.

[79] M. Glück, E. Reya and W. Vogelsang, Nucl. Phys. **B351** (1991) 579,
S. Frixione and G. Ridolfi, Genoa preprint GEF-TH-95-078,
M. Stratmann and W. Vogelsang, Rutherford Laboratory preprint RAL-TR-96-033.

[80] NMC collaboration: P. Amaudruz *et al.*, Phys. Lett. **B295** (1992) 159.

[81] L.W. Whitlow *et al.*, Phys. Lett. **B282** (1992) 159.

[82] F. James, *MINUIT: Function Minimization and Error Analysis*, Refrence Manual, Version 94.1, CERN Program Library Long Writeup D506, CERN (Geneva, 1994).

[83] M. Virchaux and A. Milsztajn, Phys. Lett. **B274** (1992) 221.

[84] HERMES collaboration: Technical Design report, DESY (1993).

[85] M. Glück, E. Reya and W. Vogelsang, Phys. Lett. **B359** (1995) 201.
M. Glück, E. Reya, M. Stratmann and W. Vogelsang, Phys. Rev. **D53** (1996) 4775.

[86] RHIC-SPIN collaboration proposal (1993).

[87] COMPASS collaboration proposal, CERN/SPSLC 96-14 (1996).

[88] SLAC-E154/E155 collaborations: proposals (1993).

[89] V. Breton, SLAC proposal (1994), S.E. Rock, ref. [90], p.259.

[90] Proceedings of the "Workshop on the Prospects of Spin Physics at HERA", Zeuthen, 1995, eds. J. Blümlein and W.D. Nowak, DESY (Hamburg, 1995).

[91] Proceedings of the workshop "Future Physics at HERA", DESY, Hamburg, September 1995 - May 1996, eds. A. De Roeck, G. Ingelman and R. Klanner, to appear.

[92] W.D. Nowak, Proceedings of "High Energy Spin Physics, 11th International Symposium", Bloomington, Indiana, 1994, eds. K. Heller and S. Smith, AIP conference Proceedings No. 343, AIP (New York, 1995), p.412.

[93] NMC collaboration: M. Arneodo *et al.*, Phys. Lett. **B309** (1993) 222.

[94] H1 collaboration: S. Aid *et al.*, Phys. Lett. **B354** (1995) 494.
ZEUS collaboration: M. Derrick *et al.*, Phys. Lett. **B345** (1995) 576.

[95] M. Klein, Proceedings of the workshop "Physics at HERA", Hamburg, October 1991, eds. W. Buchmüller and G. Ingelman, DESY (Hamburg, 1991), p.71.

[96] J. Blümlein, ref. [90], p.179.

[97] M. Maul and A. Schäfer, ref. [91].

[98] P. Ratcliffe, Nucl. Phys. **B223** (1983) 45.

[99] G. Altarelli, R.K. Ellis and G. Martinelli, Nucl. Phys. **B143** (1978) 521; **B146** (1978) 544(E); **B157** (1979) 461.
J. Kubar-André and F.E. Paige, Phys. Rev. **D19** (1979) 221.
J. Kubar, M. le Bellac, J.L. Meunier and G. Plaut, Nucl. Phys. **B175** (1980) 251.

[100] B. Kamal, Phys. Rev. **D53** (1996) 1142.

[101] H. Fritzsch and K.Streng, Phys. Lett. **72B** (1978) 385.

[102] EMC collaboration: J.J. Aubert *et al.*, Nucl. Phys. **B213** (1983) 31.

[103] J.J. Aubert *et al.*, Phys. Rev. Lett. **33** (1974) 1404; J.-E. Augustin *et al.*, Phys. Rev. Lett. **33** (1974) 1406.

[104] E.L. Berger and D. Jones, Phys. Rev. **D23** (1981) 1521.
R. Baier and R. Rückl, Nucl. Phys. **B218** (1983) 289.

[105] EMC collaboration: J. Ashman *et al.*, Z. Phys. **C56** (1992) 21.

[106] NMC collaboration: D. Allasia *et al.*, Phys. Lett. **B258** (1991) 493.

[107] M. Kramer, J. Zunft, J. Steegborn and P.M. Zerwas, Phys. Lett. **B348** (1995) 657.

[108] J.Ph. Guillet, Z. Phys. **C39** (1988) 75.

[109] A. Borissov and W.D. Nowak, HERMES–Zeuthen internal note 01/95 (1995).

[110] B. Humpert and P. Mery, Z. Phys. **C20** (1983) 83, Phys. Lett. **124B** (1983) 265.

[111] S.P. Baranov and H. Jung, Z. Phys. **C66** (1995) 647.

[112] J.F. Owens, Phys. Lett. **B266** (1991) 126.

[113] M. Glück, E. Reya and W. Vogelsang, ref. [85].

[114] ZEUS collaboration: M. Derrick *et al.*, Phys. Lett. **B315** (1993) 481; **B332** (1994) 228; **B338** (1994) 483.

[115] H1 collaboration: T. Ahmed *et al.*, Nucl. Phys. **B429** (1994) 477.

[116] I.Ya. Pomeranchuk, Sov. Phys. JETP **7** (1958) 499.

[117] T. Gehrmann and W.J. Stirling, Z. Phys. **C70** (1996) 89.

[118] T. Regge, Nuovo Cimento, **14** (1959) 951; **18** (1960) 947.

[119] P.D.B. Collins, *An Introduction to Regge Theory and High Energy Physics*, Cambridge Unversity Press (Cambridge, 1977).

[120] WA91 collaboration: S. Abatzis *et al.*, Phys. Lett. **B324** (1994) 509.

[121] A. Donnachie and P.V. Landshoff, Nucl. Phys. **B244** (1984) 322; **B267** (1986) 690.

[122] P.V. Landshoff and J.C. Polkinghorne, Nucl. Phys. **B32** (1971) 541.
G.A. Jaroskiewicz and P.V. Landshoff, Phys. Rev. **D10** (1974) 170.

[123] G. Ingelman and P. Schlein, Phys. Lett. **B152** (1985) 256.

[124] UA8 collaboration: R. Bonino *et al.*, Phys. Lett. **B211** (1988) 239; A. Brandt *et al.*, Phys. Lett. **B297** (1992) 417.

[125] P. Schlein, Proceedings of the "International Europhysics Conference on High Energy Physics", Marseille, 1993, eds. J. Carr and M. Perrottet, Editions Frontieres (Paris, 1994), p.592.

[126] A. Donnachie and P.V. Landshoff, Phys. Lett. **B191** (1987) 309; Erratum **B198** (1987) 590.

[127] G. Ingelman and K. Janson-Prytz, Proceedings of the Workshop "Physics at HERA", Hamburg, October 1991, eds. W. Buchmüller and G. Ingelman, DESY (Hamburg, 1991), p.233.

G. Ingelman and K. Prytz, Z. Phys. **C58** (1993) 285.

[128] A.H. Mueller and H. Navelet, Nucl. Phys. **B282** (1987) 727.

M. Genovese, N.N. Nikolaev and B.G. Zakharov, JETP **81** (1995) 625.

[129] L.N. Lipatov, Sov. J. Nucl. Phys. **23** (1976) 338.

E.A. Kuraev, L.N. Lipatov and V.S. Fadin, Sov. Phys. JETP **45** (1977) 199.

Ya.Ya. Baltitsky and L.N. Lipatov, Sov. J. Nucl. Phys. **28** (1978) 822.

[130] H1 collaboration: T. Ahmed *et al.*, Phys. Lett. **B348** (1995) 681.

[131] H. Fritzsch and K.H. Streng, Phys. Lett. **B164** (1985) 391.

E.L. Berger, J.C. Collins, D.E. Soper and G. Sterman, Nucl. Phys. **B286** (1987) 704.

A. Donnachie and P.V. Landshoff, Nucl. Phys. **B303** (1988) 634.

J. Bartels and G. Ingelman, Phys. Lett. **B235** (1990) 175.

A. Donnachie, Proceedings of the "International Workshop on Deep Inelastic Scattering and Related Subjects", Eilat, 1994, ed. A.Levy, World Scientific (Singapore, 1994), p.136.

[132] F.E. Low, Phys. Rev. **D12** (1975) 163.

S. Nussinov, Phys. Rev. Lett. **34** (1975) 1286; Phys. Rev. **D14** (1976) 246.

[133] B.A. Kniehl, H.G. Kohrs and G. Kramer, Z. Phys. **C65** (1995) 657.

[134] G. Altarelli, N. Cabibbo, L. Maiani and R. Petronzio, Nucl. Phys. **B69** (1974) 531.

M. Glück and E. Reya, Nucl. Phys. **B130** (1977) 76.

[135] M. Glück, E. Reya and A. Vogt, Z. Phys. **C48** (1990) 471.

[136] M. Glück, E. Reya and M. Stratmann, Nucl. Phys. **B422** (1994) 37.

[137] H1 Collaboration: T. Ahmed *et al.*, Nucl. Phys. **B439** (1995) 471; ZEUS Collaboration: M. Derrick *et al.*, Z. Phys. **C65** (1995) 379.

[138] ZEUS Collaboration: M. Derrick *et al.*, Z. Phys. **C68** (1995) 569.

[139] S. Tapprogge (H1 collaboration), Proceedings of "XXXI Rencontres de Moriond: QCD and High Energy Hadronic Interactions", Les Arcs, 1996, to appear.

[140] ZEUS collaboration: M. Derrick *et al.*, Z. Phys. **C70** (1996) 391.

[141] K. Golec–Biernat and J. Kwieciński, Krakow preprint INP-1734-PH (1996).

[142] The LEP collaborations ALPEH, DELPHI, L3, OPAL and the LEP electroweak working group, preprint CERN-PPE/95-172 (1995).

[143] E. Etzion (SLD collaboration), Proceedings of "XXXI Rencontres de Moriond: Electroweak Interactions and Unified Theories", Les Arcs, 1996, to appear.

[144] CDF collaboration: F. Abe *et al.*, Phys. Rev. Lett. **77** (1996) 438.

[145] E.W.N. Glover, A.D. Martin, R.G. Roberts and W.J. Stirling, Phys. Lett. **B381** (1996) 353.

[146] CTEQ collaboration: J. Huston *et al.*, Phys. Rev. Lett. **77** (1996) 444.

[147] J. Blazey (D0 collaboration), Proceedings of "XXXI Rencontres de Moriond: QCD and High Energy Hadronic Interactions", Les Arcs, 1996, to appear.

[148] G. Altarelli, N. Di Bartolomeo, F. Feruglio, R. Gatto and M.L. Mangano, Phys. Lett. **B375** (1996) 292.

[149] P. Chiappetta, J. Layssac, F.M. Renard and C. Verzegnassi, Phys. Rev. **D54** (1996) 789.

[150] C.T. Hill and S.J. Parke, Phys. Rev. **D49** (1994) 4454.

E. Eichten and K. Lane, Phys. Lett. **B327** (1994) 129.

V. Barger and R.J.N. Phillips, Phys. Lett. **B335** (1994) 510.

Jin Min Yang and Chong Sheng Li, Phys. Rev. **D52** (1995) 1541.

K. Lane, Phys. Rev. **D52** (1995) 1546.

K. Whisnant, Bing-Lin Young and X. Zhang, Phys. Rev. **D52** (1995) 3115.

D. Atwood, A. Kagan and T.G. Rizzo, Phys. Rev. **D52** (1995) 6264.

P. Haberl, O. Nachtmann and A. Wilch, Phys. Rev. **D53** (1996) 4875.

[151] CDF collaboration: F. Abe *et al.*, Phys. Rev. Lett. **73** (1994) 225; Phys. Rev. **D50** (1994) 2966.

[152] P. Nason, S. Dawson and R.K. Ellis, Nucl. Phys. **B303** (1988) 607.

W. Beenakker, H. Kuijf, W.L. van Neerven and J. Smith, Phys. Rev. **D40** (1989) 54.

[153] G. Altarelli, R.K. Ellis and G. Martinelli, Nucl. Phys. **B143** (1978) 521; **B146** (1978) 544(E); **B157** (1979) 461.

J. Kubar-André and F.E. Paige, Phys. Rev. **D19** (1979) 221.

J. Kubar, M. le Bellac, J.L. Meunier and G. Plaut, Nucl. Phys. **B175** (1980) 251.

[154] J. Jersàk, E. Laermann and P.M. Zerwas, Phys. Rev. **D25** (1982) 1218., **D36** (1987) 310(E).

L. Reinders, H. Rubinstein and S. Yazaki, Phys. Rep. **127** (1985) 1.

[155] J.H. Kühn and P.M. Zerwas, in: *Heavy Flavours*, eds. A.J. Buras and M. Lindner, World Scientific (Singapore, 1992), p.434.

[156] J. Schwinger, *Particles, Sources and Fields*, Addison-Wesley (New York, 1973).

[157] CDF collaboration: F. Abe *et al.*, Phys. Rev. Lett. **74** (1995) 2626; Phys. Rev. **D52** (1995) 2605; preliminary results: A. Caner, presented at "Les rencontres de Physique de la Vallée d'Aoste", March 1996

[158] D0 collaboration: S. Abachi *et al.*, Phys. Rev. Lett. **74** (1995) 2632; Phys. Rev. **D52** (1995) 4877; preliminary results: M. Narain, presented at "Les rencontres de Physique de la Vallée d'Aoste", March 1996

[159] S. Catani, M.L. Mangano, P. Nason and L. Trentadue, Phys. Lett. **B378** (1996) 329.

[160] W.J. Stirling, Proceedings of the "Workshop on Deep Inelastic Scattering and QCD", Paris, 1995, eds. J.-F. Laporte and Y. Sirois, Ecole Polytechnique (Paris, 1995), p.91.
R.K. Ellis, Proceedings of the "XXVII Int. Conf. on High Energy Physics", Glasgow, 1994, eds. P.J. Bussey and I.G. Knowles, IOP Publishing (Bristol, 1995), Vol.II, p.1203.

[161] K. Lane, Ref. [150].

[162] Wiliam H. Press *et al.*, *Numerical Recipes: The Art of Scientific Computing*, Cambridge University Press (Cambridge, 1986).

[163] Bruce W. Char *et al.*, *Maple V Library Reference Manual*, Springer Verlag (New York, 1991), p.259.

[164] A. Devoto and D.W. Duke, Riv. Nuovo Cimento **7** (1984) 1.

[165] A. Gonzales–Arroyo, C. Lopez and F.J. Yndurain, ref. [33].

[166] H. Georgi and H.D. Politzer, Phys. Rev. **D9** (1974) 416;
D.J. Gross and F.A. Wilczek, Phys. Rev. **D9** (1974) 980.

[167] E.G. Floratos, C. Kounnas and R. Lacaze, ref. [33].

[168] W. Furmanski and R. Petronzio, Z. Phys. **C11** (1982) 293.

194